Measurement of Chiral Susceptibility in Lattice QCD with Wilson Fermion using Gradient Flow

Atsushi Baba

February 2021

Measurement of Chiral Susceptibility in Lattice QCD with Wilson Fermion using Gradient Flow

Atsushi Baba
Doctoral Program in Physics

Submitted to the Graduate School of
Pure and Applied Sciences
in Partial Fulfillment of Requirements
for the Degree of Doctor of Philosophy in
Science

at the
University of Tsukuba

Abstract

In this thesis, I present a study on finite temperature QCD transition by numerical simulation adopting lattice formulation of QCD. In finite temperature QCD, it is widely believed that the phase transition is related to spontaneously symmetry breaking of the chiral symmetry. Here, the effective restoration of anomalous $U(1)_A$ symmetry in the high temperature phase is also important in understanding the global structure of the QCD phase diagram. On the other hand, it is known that the chiral symmetry is difficult to implement when we formulate the quarks on the lattice avoiding the fermion doubling problem. Actually, the Wilson-type quark used in our numerical simulation explicitly breaks the chiral symmetry and this requires nontrivial renormalizations to obtain physical quantities including the chiral and $U(1)_A$ susceptibilities, which are important to clarify the fate of the $U(1)_A$ symmetry. To avoid this problem, we adopt the small flow-time expansion (SFtX) method based on gradient flow as a renormalization procedure of the chiral and $U(1)_A$ susceptibilities. For the SFtX method, we use the renormalization scale not only the traditional one but also the recently proposed one to reduce the systematic error. We found that the connected part of chiral susceptibility does not show a peak at the transition temperature, while the disconnected part has a clear peak. From the $U(1)_A$ susceptibility, we found that the $U(1)_A$ symmetry breaking is highly suppressed but remains nonzero at the temperatures in the high temperature phase we measured. The temperature dependence of the $U(1)_A$ susceptibility in the high temperature phase is qualitatively consistent with a previous domain-wall fermion result.

Contents

Chapter 1

Introduction

QCD phase diagram has various structures in finite temperature and density as shown in Fig. 1.1. The high temperature and low density region of the phase diagram would be related to the early universe while the low temperature and high density would be related to the neutron stars. Heavy-ion collision experiments scan the high temperature and density region to detect first-order transition line and its critical endpoint. Therefore, exploring the QCD phase diagram has attracted much attention both from theoretical and experimental perspective. Since the QCD phase transition is a non-perturbative phenomenon, the first principle calculation on the basis of the lattice QCD plays an indispensable role in those studies.

In this thesis, I study the QCD phase transition in finite temperature QCD by numerical simulation adopting latticeQCD. In finite temperature QCD, it is widely considered that the phase transition that occurred between the low-temperature hadronic phase and high-temperature quark-gluon plasma (QGP) phase is related to the chiral symmetry. The phase transition is thus referred to as the chiral transition. In the study of chiral transition, chiral condensate is the order parameter of the phase transition. In numerical simulation, its susceptibility is often used to define the transition temperature. The chiral susceptibility can be decomposed into the disconnected contribution and connected contribution. In many of previous studies, disconnected chiral susceptibility has been used to estimate the transition temperature. Though this quantity is not a physical quantity, disconnected susceptibility shows a clear peak at the transition and has been used to estimate the transition temperature. On the other hand, previous studies of connected chiral susceptibility reported that the connected part does not show singular behavior around the transition temperature. Besides the restoration of the chiral symmetry, effective restoration of the $U(1)_A$ symmetry in finite temperature is also important in understanding the QCD phase diagram. This symmetry is explicitly broken by anomaly but expected to restore in the high temperature limit. The fate

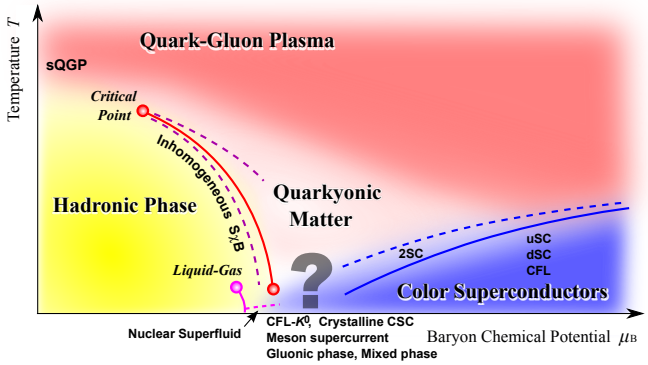

Figure 1.1: Conjectured QCD phase diagram [1]: horizontal axis is the baryon chemical potential and vertical axis is the temperature T. Some conjecture is included.

of the $U(1)_A$ symmetry at the QCD transition temperature is considered to be related to the order of the phase transition and universality class in the chiral limit. However, studies from different groups show different results about the effective restoration of the $U(1)_A$ symmetry. Whether the $U(1)_A$ symmetry is effectively restored or not at the chiral transition temperature is still an open question.

As shown above, effective restorations of chiral and $U(1)_A$ symmetry are very important in finite temperature QCD. However, lattice QCD has a subtle problem with chiral symmetry due to the fermion doubling problem. In this thesis, I employ Wilson-type quark in the numerical simulation. Wilson-type quarks explicitly break the chiral symmetry to avoid the doubling problem. This requires the nontrivial renormalizations to obtain physical quantities related to the chiral symmetry. To avoid this problem, we adopt the small flow-time expansion (SFtX) method based on the gradient flow as a renormalization procedure of the chiral and $U(1)_A$ susceptibilities. The SFtX method provides us many advantages to lattice QCD. For example, the energy-momentum tensor (EMT) is defined even on the lattice avoiding the violation of the translation symmetry.

In the SFtX method, we are free to choose the renormalization scale of the matching coefficients, which bridge the gradient flow to the $\overline{\text{MS}}$ scheme. In this thesis, we choose the newly suggested one. Because the newly suggested renormalization scale is about 1.5 times larger than the traditional one, the perturbative behavior gets improved due to the asymptotic freedom. With this improvement, systematic errors can be reduced to those from the traditional renormalized scale. Our results for chiral and $U(1)_A$ susceptibilities are qualitatively consistent with previous results. For the chiral susceptibility, the connected part has no peak around the transition temperature but the amplitude is significantly larger than the disconnected part. For the $U(1)_A$ susceptibility, our result is also quantitatively consistent with the result from the domain-wall fermion. Details are discussed in later.

This thesis is organized as follows. The lattice formulation and fermion doubler problems are presented in chapter 2. In the chapter 3, we review previous results about chiral phase transition and the fate of the $U(1)_A$ susceptibility. In the chapter 4, we review the gradient flow method and small flow-time expansion method briefly. Numerical results of chiral susceptibility and $U(1)_A$ susceptibility by SFtX method are shown in chapter 5. Finally, summary of the results are presented in chapter 6.

Chapter 2

Lattice QCD

2.1 Lattice gauge theory

2.1.1 QCD in continuum space-time

In the continuum theory, QCD action in 4-dimensional space-time is given as

$$S_{\rm QCD} = S_{\rm YM}[A] + S_F[\psi, \bar{\psi}, A], \tag{2.1}$$

$$S_{\rm YM}[A] = -\frac{1}{2g_0^2}\int {\rm d}^4x\, {\rm tr}\left\{F_{\mu\nu}(x)F_{\mu\nu}(x)\right\}, \tag{2.2}$$

$$S_F[\psi, \bar{\psi}, A] = \int {\rm d}^4x \sum_f \bar{\psi}_f(x)\left(\not{D} + m_{f,0}\right)\psi_f(x), \tag{2.3}$$

where $F_{\mu\nu}(x)$ is the field strength of the $SU(3)$ gauge field $A_\mu(x)$,

$$F_{\mu\nu}(x) = \partial_\mu A_\nu(x) - \partial_\nu A_\mu(x) + [A_\mu(x), A_\nu(x)], \tag{2.4}$$

with $A_\mu = A_\mu^a(x)T^a$, where the T^a is the generator of the $SU(N)$ gauge group. $\psi_f(x)$ and $\bar{\psi}_f(x)$ are the quark fields for flavor f and $\not{D} = \gamma_\mu D_\mu$ indicates covariant derivative

$$D_\mu = \left(\partial_\mu + iA(x)\right). \tag{2.5}$$

This action is invariant under the gauge transformation

$$A_\mu(x) \to \frac{1}{ig}\Omega(x)\partial_\mu\Omega^\dagger(x) + \Omega(x)A_\mu(x)\Omega^\dagger(x), \tag{2.6}$$

$$\psi_f(x) \to \Omega(x)\psi_f(x), \tag{2.7}$$

$$\bar{\psi}_f(x) \to \bar{\psi}_f(x)\Omega^\dagger(x). \tag{2.8}$$

where Ω is element of $SU(N)$ gauge group.

Let us consider a non-local quark bilinear operator

$$\bar{\psi}_f(x)\psi_f(x + \Delta x). \tag{2.9}$$

For small Δx, we can construct a quantity,

$$\begin{aligned}
\bar{\psi}_f(x)\left[1 + i\Delta x_\mu A_\mu(x)\right]\psi_f(x + \Delta x) &= \bar{\psi}_f(x)\left[1 + i\Delta x_\mu A_\mu(x)\right]\left(1 + \Delta x_\mu\partial_\mu + O(\Delta x^2)\right)\psi_f(x) \\
&= \bar{\psi}_f(x)\left[1 + i\Delta x_\mu\left(\partial_\mu + A_\mu(x)\right)\right]\psi_f(x) + O(\Delta x^2) \\
&= \bar{\psi}_f(x)\left[1 + i\Delta x_\mu D_\mu\right]\psi_f(x) + O\left((\Delta x)^2\right),
\end{aligned} \tag{2.10}$$

which is gauge invariant up to $O((\Delta x))$. A generalization to finite interval is given by

$$\bar{\psi}_f(x) P \exp\left[i \int_x^y \mathrm{d}z_\mu \, A_\mu(z) \right] \psi_f(y) \equiv \bar{\psi}_f(x) U(x,y) \psi_f(y), \tag{2.11}$$

where P denotes path ordering

$$U(x,y) = P \exp\left[i \int_x^y \mathrm{d}z_\mu \, A_\mu(z) \right] = \lim_{N\to\infty} \prod_{n=0}^{N-1} \left[1 + i\Delta x_\mu A_\mu(x + n\Delta x) \right], \tag{2.12}$$

where $\Delta x = |y - x|/N$. Using the gauge transformation for a product elements at $x_n = x + n\Delta x$,

$$\begin{aligned} 1 + i\Delta x_\mu A_\mu(x_n) &\to 1 + i\Delta x_\mu \left\{ \Omega(x_n) \partial_\mu \Omega^\dagger(x_n) + i\Omega(x_n) A_\mu(x_n) \Omega^\dagger(x_n) \right\} \\ &= \Omega(x_n)\Omega^\dagger(x_{n+1}) + i\Delta x_\mu \Omega(x_n) A_\mu(x_n) \Omega^\dagger(x_{n+1}) + O(\Delta x^2) \\ &= \Omega(x_n) \left(1 + i\Delta x_\mu A_\mu(x_n) \right) \Omega^\dagger(x_{n+1}) + O\left((\Delta x)^2 \right), \end{aligned} \tag{2.13}$$

we can calculate the the gauge transformation for $U(x,y)$ as

$$\begin{aligned} U(x,y) &= \lim_{N\to\infty} \prod_{n=0}^{N-1} \left[1 + i\Delta x_\mu A_\mu(x_n) \right] \\ &\to \lim_{N\to\infty} \left(\prod_{n=0}^{N-1} \Omega(x_n) \left[1 + i\Delta x_\mu A_\mu(x_n) \right] \Omega^\dagger(x_{n+1}) + O\left((\Delta x)^2 \right) \right) \\ &= \lim_{N\to\infty} \Omega(x) \left(\prod_{n=0}^{N-1} \left[1 + i\Delta x_\mu A_\mu(x_n) \right] + O\left((\Delta x)^2 \right) \right) \Omega^\dagger(y) \\ &= \Omega(x) U(x,y) \Omega^\dagger(y). \end{aligned} \tag{2.14}$$

Using this factor, we can constract the gauge invariant non-local quark bilinear operator,

$$\begin{aligned} \bar{\psi}_f(x) U(x,y) \psi_f(y) &\to \bar{\psi}_f(x) \Omega^\dagger(x) \Omega(x) U(x,y) \Omega^\dagger(y) \Omega(y) \psi_f(y) \\ &= \bar{\psi}_f(x) U(x,y) \psi_f(y). \end{aligned} \tag{2.15}$$

2.1.2 Wilson's plaquette action

In the lattice gauge theory, gauge fields are put on links. We introduce the link variable $U_{n,\mu}$ as a $U(x, x + \hat{\mu}a)$ with small lattice spacing a,

$$U_{n,\mu} \simeq \exp[ia A_\mu(n + \hat{\mu}/2)], \tag{2.16}$$

where $\hat{\mu}$ denotes the unit vector toward μ-direction.

The minimal choice of gauge invariant non-local quantity constructed of link variable $U_{\nu,\mu}$ is the plaquette $\mathrm{tr}\, U^{\mathrm{plaq}}_{n,\mu\nu}$, the minimal square on the lattice,

$$\begin{aligned} \mathrm{tr}\, U^{\mathrm{plaq}}_{n,\mu\nu} &= \mathrm{tr}\left[U_{n,\mu} U_{n+\hat{\mu},\nu} U^\dagger_{n+\hat{\nu},\mu} U^\dagger_{n,\nu} \right] \\ &\to \mathrm{tr}\left[\Omega(n) U_{n,\mu} U_{n+\hat{\mu},\nu} U^\dagger_{n+\hat{\nu},\mu} U^\dagger_{n,\nu} \Omega^\dagger(n) \right] \\ &= \mathrm{tr}\left[U_{n,\mu} U_{n+\hat{\mu},\nu} U^\dagger_{n+\hat{\nu},\mu} U^\dagger_{n,\nu} \right]. \end{aligned} \tag{2.17}$$

The plaquette can be written as

$$\operatorname{tr} U^{\text{plaq}}_{n,\mu\nu} = \operatorname{tr}\left[1 - \frac{a^4}{2} F_{\mu\nu}(n_c) F_{\mu\nu}(n_c) + O(a^6)\right]. \tag{2.18}$$

Here, we neglect the A_μ-odd terms because these terms vanish in the trace due to $\operatorname{tr} T^a = 0$. Using the plaquette, we can construct the plaquette action [2],

$$S_g[U] = \beta \sum_n \sum_{\mu\neq\nu} \operatorname{tr}\left[1 - U^{\text{plaq}}_{n,\mu\nu}\right], \tag{2.19}$$

$$= \beta \sum_n \sum_{\mu<\nu} \operatorname{Re}\operatorname{tr}\left[1 - U^{\text{plaq}}_{n,\mu\nu}\right], \tag{2.20}$$

where β is a constant specified below. It is easy to see that the plaquette action is consistent with the Yang-Mills action in the continuum limit,

$$\lim_{a\to 0} S_g[U] = \lim_{a\to 0} \beta \sum_n \sum_{\mu<\nu} \operatorname{Re}\operatorname{tr}\left[1 - U^{\text{plaq}}_{n,\mu\nu}\right]$$

$$= \frac{\beta}{4} \int \mathrm{d}^4x \sum_{\mu,\nu} \operatorname{tr}\left[F_{\mu\nu}(x) F_{\mu\nu}(x)\right]. \tag{2.21}$$

Therefore, we find that $\beta = 2/g_0$.

2.1.3 Naïve discretization of fermion action

In this section, we consider the discretization of fermion action. For simplicity, we drop the flavor index in the following sections.

The free fermion action S^0_F with mass m in continuum theory is given by

$$S^0_F[\psi, \bar\psi] = \int \mathrm{d}^4x\, \bar\psi(x) \left(\not\partial + m_0\right) \psi(x), \tag{2.22}$$

where $\not\partial = \gamma_\mu \partial_\mu$. We employ the discretization of partial derivative as symmetric expression

$$\partial_\mu \psi(x) \to \frac{1}{2a} \left(\psi_{n+\hat\mu} - \psi_{n-\hat\mu}\right), \tag{2.23}$$

where ψ_n denotes the fermion field on discretized space-time lattice cite $na = x$ and replace the space-time integral to sum over all space-time sites Λ

$$\int \mathrm{d}^4x \to a^4 \sum_{n\in\Lambda}. \tag{2.24}$$

Thus, discretized free fermion action reads

$$S^0_F[\psi, \bar\psi] = a^4 \sum_{n\in\Lambda} \bar\psi_n \left(\sum_{\mu=1}^4 \gamma_\mu \frac{\psi_{n+\hat\mu} - \psi_{n-\hat\mu}}{2a} + m_0 \psi_n\right). \tag{2.25}$$

As discussed before, we obtain the gauge invariant quark bilinear operator by introducing the link variables,

$$S_F[\psi, \bar\psi] = a^4 \sum_{n\in\Lambda} \bar\psi_n \left(\sum_{\mu=1}^4 \gamma_\mu \frac{U_{n,\mu}\psi_{n+\hat\mu} - U^\dagger_{n,\mu}\psi_{n-\hat\mu}}{2a} + m_0 \psi_n\right), \tag{2.26}$$

this is called *naïve fermion action*.

Table 2.1: List of lattice fermions.

Fermion	Chiral symmetry	Continuum limit	Numerical cost
Wilson	×	✓	Moderate
Staggerd	△	△	Cheap
Domain-Wall	✓	✓	Expensive
Overlap	✓	✓	Expensive

2.1.4 Doubler problem

In the momentum space, free fermion action S_F^0 can be written as

$$S_F^0 = \int \frac{\mathrm{d}^4 p}{(2\pi)^2} \bar{\psi}(-p) \left[i\gamma_\mu \sin(p_\mu a) + M \right] \psi(p), \tag{2.27}$$

where M is the dimension-less mass $M = am_0$. The fermion propagator of this action is given as

$$G_F(p) = \frac{1}{i\gamma_\mu \sin(p_\mu a) + M} = \frac{-i\gamma_\mu \sin(p_\mu a) + M}{\sin^2(p_\mu a) + M^2}. \tag{2.28}$$

Even though the fermion doubling problem exists, we can understand this problem as the natural property of the lattice formulation. Such property is known as the Nielsen-Ninomiya theorem [3–5]. According to the theorem, when the lattice fermion satisfies the assumptions below,

- Translational invariance,
- Chiral symmetry,
- Hermitian property,
- Bi-linear form in fermion field,
- Locality,

the doubling problem must occur.

2.1.5 Wilson fermion formulation

To avoid the doubling problem, we can add the chirality-violating term called the *Wilson term* [6]:

$$S_W = -ar \int \mathrm{d}^4 x \, \bar{\psi} D^2 \psi \tag{2.29}$$

$$\to -\frac{1}{2} r \sum_{n,\mu} \left[\bar{\psi}_n U_{n,\mu} \psi_{n+\hat{\mu}} + \bar{\psi}_{n+\hat{\mu}} U_{n,\mu}^\dagger \psi_n - 2\bar{\psi}_n \psi_n \right], \tag{2.30}$$

where r is the Wilson parameter. This term obviously vanishes in naïve continuum limit.

In the momentum space, free part of Wilson term is

$$\begin{aligned} S_W^0 &= -\frac{1}{2} r \sum_{n,\mu} \left[\bar{\psi}_n \psi_{n+\hat{\mu}} + \bar{\psi}_{n+\hat{\mu}} \psi_n - 2\bar{\psi}_n \psi_n \right] \\ &= r \int \frac{\mathrm{d}^4 p}{(2\pi)^4} \bar{\psi}(-p) \sum_\mu \left[1 - \cos(p_\mu a) \right] \psi(p), \end{aligned} \tag{2.31}$$

thus, the fermion propagator becomes

$$G_F(p) = \frac{-i\gamma_\mu \sin(p_\mu a) + M(p)}{\sin^2(p_\mu a) + M^2(p)}, \tag{2.32}$$

$$M(p) = M + r\sum_\mu \left[1 - \cos(p_\mu a)\right]. \tag{2.33}$$

The pole mass of doublers diverge in the $a \to 0$ limit, while the mass of physical degrees of freedom stays finite value m. Thus, doublers can not contribute to the low energy dynamics. This is called the *decoupling of doublers at low energy*.

The lattice fermion shown in this section is called Wilson fermion. Some other lattice fermions are also used. Other lattice fermions and those properties are listed in Table 2.1

2.2 Improvement of lattice action

2.2.1 Iwasaki gauge action

To construct the improved gauge action, we can add the rectangle action. This is the $O(a^2)$-improvement of gauge action because the $O(a)$-term vanishes in the trace of color indices.

Rectangle term is

$$U_{\rm rect}(n) = R_{\mu\mu\nu}(n) + R_{\mu\nu\nu}(n), \tag{2.34}$$

$$R_{\mu\mu\nu} = U_{n,\mu}U_{n+\hat{\mu},\mu}U_{n+2\hat{\mu},\nu}U^\dagger_{n+\hat{\mu}+\hat{\nu},\mu}U^\dagger_{n+\hat{\nu},\mu}U^\dagger_{n,\nu}. \tag{2.35}$$

Combining this term, we can use the improved lattice action

$$S_I = \beta \sum_{n,\mu\neq\nu} \left[c_0 \,\mathrm{tr}\, U_{\rm plaq}(n) + c_1 \,\mathrm{tr}\, U_{\rm rect}(n)\right], \tag{2.36}$$

with $c_0 + 8c_1 = 1$.

$$c_1 = -0.331, \qquad c_0 = 1 - 8c_1 = 3.648, \tag{2.37}$$

for renormalization group improved Iwasaki gauge action [7].

2.2.2 Wilson clover fermion

The $O(a)$-improvement of Wilson fermion is given as [8][1]

$$S_{\rm clover} = S_W + c_{\rm sw} a^5 \sum_{n\in\Lambda}\sum_{\mu<\nu} \bar{\psi}_n \frac{1}{2}\sigma_{\mu\nu}\hat{F}_{\mu\nu}(n)\psi_n, \tag{2.38}$$

where

$$\hat{F}_{\mu\nu}(n) = \frac{-i}{8a}\left(Q_{\mu\nu}(n) - Q_{\nu\mu}(n)\right), \tag{2.39}$$

$$Q_{\mu\nu}(n) \equiv U_{\mu,\nu}(n) + U_{\nu,-\mu}(n) + U_{-\mu,-\nu}(n) + U_{-\nu,\mu}(n), \tag{2.40}$$

and $c_{\rm sw}$ is referred to Sheikoleslami-Wohlert coefficient. The term is often referred to as the clover term and the action Eq. (2.38) is called Wilson clover action.

[1] Here, we continuously drop the flavor index.

Chapter 3

QCD Phase Transition

In finite temperature QCD, the phase transition between low- and high-temperature phases corresponding to confinement and deconfinement phases occurs. These phases are denoted as hadronic phase and quark-gluon plasma (QGP) phase, respectively. It is widely believed that this transition is related to the chiral symmetry.

3.1 Chiral phase transition

The phase transition in finite temperature QCD is referred to as the chiral phase transition because this phase transition is related to the effective restoration of the spontaneously breaking of chiral symmetry. The chiral condensate

$$\Sigma_f = \frac{1}{V_4}\int \mathrm{d}^4x \left\langle \bar{\psi}_f(x)\psi_f(x)\right\rangle, \tag{3.1}$$

where V_4 is the four-dimensional space-time volume and the flavor index f is not summed over, is often used as an order parameter of the chiral phase transition. Ideally, the transition temperature is defined as the temperature at which the order parameter changes significantly. In the numerical simulation, the susceptibility, the fluctuation of the order parameter, is often used to define the transition temperature. The peak of the susceptibility indicate the transition temperature. Actually, the chiral susceptibility is often used to estimate the chiral phase transition temperature.

The chiral susceptibility χ_f^{full} is defined as the fluctuation of the chiral condensate,

$$\chi_f^{\mathrm{full}} = \left\langle \left\{ \frac{1}{V_4}\int \mathrm{d}^4x \left(\bar{\psi}_f(x)\psi_f(x) - \left\langle \bar{\psi}_f(x)\psi_f(x)\right\rangle\right)\right\}^2\right\rangle \tag{3.2}$$

$$= \left\langle \left\{ \frac{1}{V_4}\int \mathrm{d}^4x\, \bar{\psi}_f(x)\psi_f(x)\right\}^2\right\rangle - \left\langle \frac{1}{V_4}\int \mathrm{d}^4x\, \bar{\psi}_f(x)\psi_f(x)\right\rangle^2, \tag{3.3}$$

where also the flavor index f is not summed over. The chiral susceptibility can be further decomposed into the connected and disconnected parts as

$$\chi_f^{\mathrm{full}} = \chi_f^{\mathrm{conn}} + \chi_f^{\mathrm{disc}}, \tag{3.4}$$

$$\chi_f^{\mathrm{conn}} = \left\langle \frac{1}{V_4}\int \mathrm{d}^4x\, \overbrace{\bar{\psi}_f(x)\overbrace{\psi_f(x)\bar{\psi}_f(0)}\psi_f(0)}\right\rangle, \tag{3.5}$$

$$\chi_f^{\mathrm{disc}} = \left\langle \left\{ \frac{1}{V_4}\int \mathrm{d}^4x\, \overbrace{\bar{\psi}_f(x)\psi_f(x)}\right\}^2\right\rangle - \left\langle \frac{1}{V_4}\int \mathrm{d}^4x\, \bar{\psi}_f(x)\psi_f(x)\right\rangle^2. \tag{3.6}$$

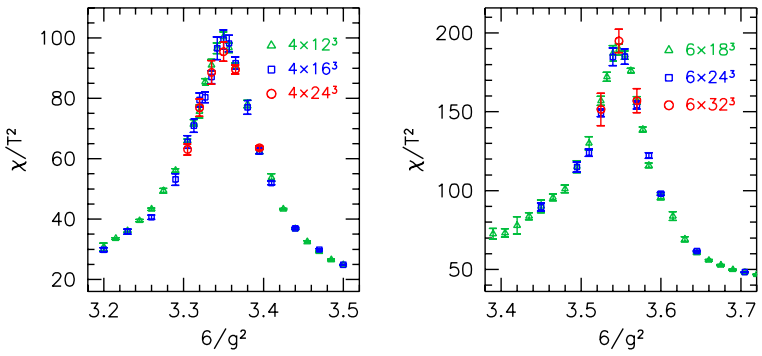

Figure 3.1: Disconnected chiral susceptibilities for the light quarks as a function of the gauge coupling [9]. They used the staggered-type quarks at physical point.

Here, connected and disconnected are classification based on the way to take the quark lines between the two scalar density operators in the diagrammatic representation.

Though the disconnected part of the chiral susceptibility is not a physical observable, it is used in many studies in exploring the chiral phase transition temperature. In the Ref. [9], The order of the chiral phase transition of $2+1$-flavor QCD are studied by the finite size scaling using the disconnected chiral susceptibility $\chi_f^{\rm disc}$ at physical point. As shown in Fig. 3.1, the disconnected chiral susceptibility shows no volume dependence. This suggests that the transition is an analytic crossover at the quark masses the physical quark mass. In that study, they took continuum limit and show the crossover scaling in the continuum limit.

Previous studies of chiral susceptibility including connected part contribution suggests the the connected chiral susceptibility shows a mild or no pronounced peak around the QCD transition/crossover. In the study with HISQ at $m_\pi \sim$ 80-160 MeV [10], connected part varies monotonically around the the transition temperature with "no contribution to the singular behavior of the chiral phase transition". A study with improved Wilson quarks at $m_\pi \sim 400$ MeV [11], they also found that the bare connected susceptibility shows "no singular behavior" around the phase transition as shown in Fig. 3.2. Note here that the chiral susceptibility measured in this study is not renormalized. Though both studies show no singular connected part, full chiral susceptibility has a peak around the transition.

In the recent study with HISQ at the physical point [12], chiral phase transition temperature is studied with high precision. In this study, various sorts of susceptibilities are measured including disconnected and full chiral susceptibilities. Estimated chiral phase transition temperatures from five different susceptibilities are consistent with each other in the continuum limit.

In this thesis, I measure the renormalized chiral susceptibility including the connected part contribution with Wilson-type quark.

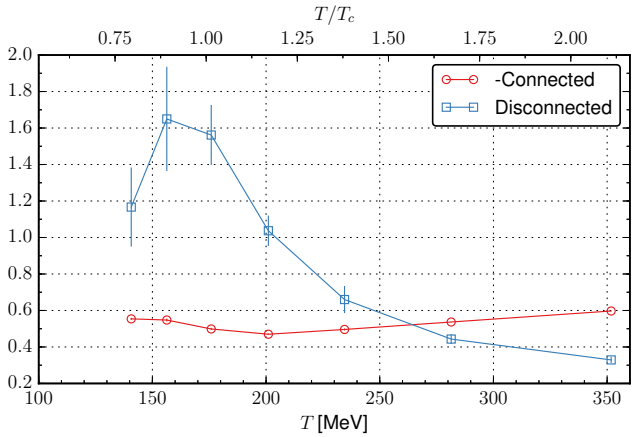

Figure 3.2: Unrenormalized chiral susceptibility as a function of temperature [11]. Blue box denotes the disconnected part and Red circle denotes the connected part of the chiral susceptibility. Expect for the singular in disconnected part, both parts contribute same order. They used Wilson-type quarks at $m_\pi \sim 400$ MeV.

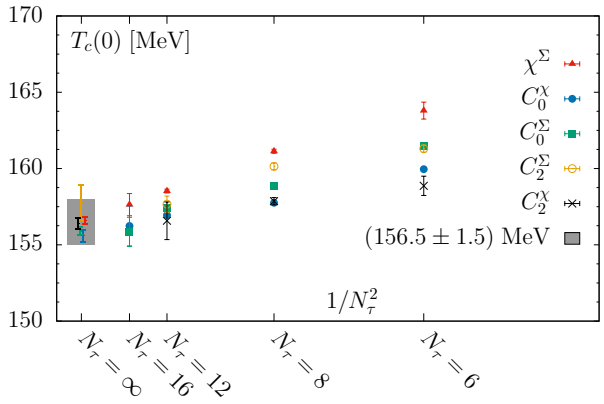

Figure 3.3: Various sorts of susceptibility including the disconnected chiral susceptibility (blue filled circle) and the full chiral susceptibility (red triangle) as a function of temporal direction lattice size [12]. The solid gray band at $N_\tau = \infty$ is the continuum-extrapolated result of pseudo-critical temperature T_{pc}.

3.2 Axial $U(1)$ anomaly

It is known that the $U(1)_A$ symmetry is broken at zero temperature by anomaly. The effective restoration of anomalous $U(1)_A$ symmetry is also an interesting topic in finite temperature QCD.

To explore the effective restoration of the $U(1)_A$ symmetry, chiral multiplets are used. In Fig. 3.4, chiral multiplets of meson scalar-pseudoscalar sector are shown. These operators connected by arrows are those that transform each other with the symmetry shown nearby.

Under the infinitesimal $U(1)_A$ transformation,

$$\begin{aligned}\psi_f(x) &\to e^{i\gamma_5\theta(x)}\psi_f(x)\\ &\sim (1+i\gamma_5\theta(x))\psi_f(x),\end{aligned} \tag{3.7}$$

$$\begin{aligned}\bar{\psi}_f(x) &\to \bar{\psi}_f(x)e^{i\gamma_5\theta(x)}\\ &\sim \bar{\psi}_f(x)(1+i\gamma_5\theta(x)),\end{aligned} \tag{3.8}$$

where $\theta(x)$ is the local parameter of $U(1)_A$ transformation. The operators shown in Fig. 3.4 are transformed as

$$\begin{aligned}\eta(x)=\bar{\psi}(x)\gamma_5\psi(x) &\to \bar{\psi}(x)(1+i\gamma_5\theta(x))\gamma_5(1+i\gamma_5\theta(x))\psi(x)\\ &= \bar{\psi}(x)\gamma_5\psi(x)+2i\theta(x)\bar{\psi}(x)\psi(x)\\ &= \eta(x)+2i\theta(x)\sigma_(x),\end{aligned} \tag{3.9}$$

$$\begin{aligned}\delta^a(x)=\bar{\psi}(x)T^a\psi(x) &\to \bar{\psi}(x)(1+i\gamma_5\theta(x))T^a(1+i\gamma_5\theta(x))\psi(x)\\ &= \bar{\psi}(x)T^a\psi(x)+2i\theta(x)\bar{\psi}(x)\gamma_5T^a\psi(x)\\ &= \delta^a(x)+2i\theta(x)\pi^a(x),\end{aligned} \tag{3.10}$$

where T^a is the generator of the degenerate flavor space with $a \geq 1$ and ψ and $\bar{\psi}$ are the multiplet of the degenerate flavors. When we write the flavor indiex explicitly, flavor indices are naïvely summed over. As shown in the Fig. 3.4, scalar and pseudoscalar mesons transform each other with flavor singlet and non-singlet parts independently.

The deviation of the corresponding susceptibilities are,

$$\begin{aligned}\chi^{\pi-\delta} &= \chi^{\pi}-\chi^{\delta}\\ &= \int \mathrm{d}^4x\,\langle\pi^a(x)\pi^a(0)-\delta^a(x)\delta^a(0)\rangle\,,\end{aligned} \tag{3.11}$$

$$\chi^{\eta-\sigma} = \chi^{\eta}-\chi^{\sigma}, \tag{3.12}$$

where no sum over a is taken. In the non-singlet part, the disconnected contribution and one-point function vanishes in the trace of flavor index. These are referred to as the $U(1)_A$ susceptibility. In this thesis, we only consider the case that $a = 1$ or 2 *i.e.* we concentrate only on the ud quark part for

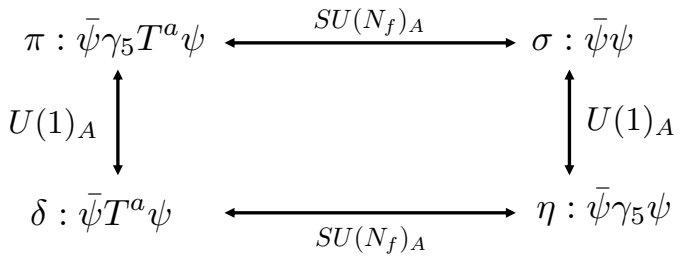

Figure 3.4: Scalar chiral multiplets. We use the T^a as the generator of flavor symmetry.

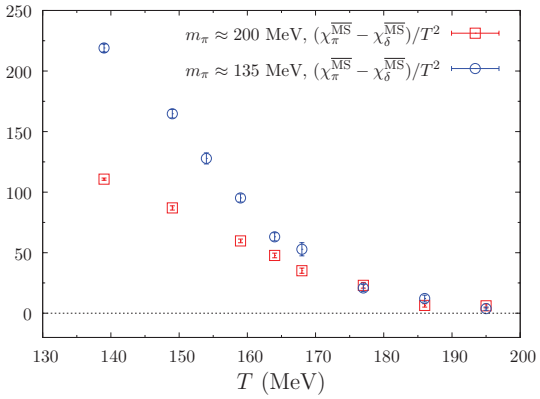

Figure 3.5: $U(1)_A$ susceptibility as a function of temperature [13]. They use the domain-wall fermion at $m_{pi} = 135$ MeV and 200 MeV.

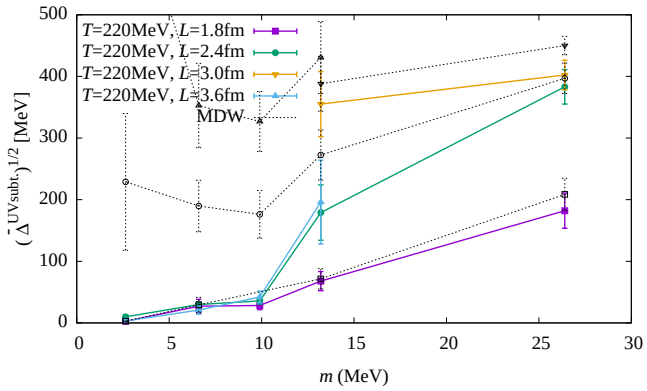

Figure 3.6: $U(1)_A$ susceptibility as a function of quark mass [14]. This result is obtained from two-flavor QCD at 220 MeV. Colored results indicate the results from overlap Dirac eigenvalue and gray results is the result from domain-wall Dirac eigenvalue.

the $U(1)_A$ susceptibility. In the massless QCD, these quantities vanish when the $U(1)_A$ symmetry is restored. Here, we note that the non-singlet scalar susceptibility is identical to the connected part of chiral susceptibility, $\chi^\delta = \chi_{ud}^{\rm conn}$.

In the study with (2+1)-flavors of domain-wall fermion at $m_\pi = 135$ MeV and 200 MeV [13], $\chi^{\pi-\delta}$ was measured as a $U(1)_A$ susceptibility. At the chiral transition temperature, $U(1)_A$ susceptibility remains non-zero value. Above the transition temperature, it is also shown that the $U(1)_A$ susceptibility measured on two different quark masses shows consistent value within error bars. This means that the $U(1)_A$ symmetry breaking at high temperature is due to the axial anomaly.

The authors of Ref. [14] aim to take the chiral limit in the two-flavor QCD to explore the Columbia plot. The fate of the $U(1)_A$ susceptibility at the transition temperature affects the order of transition and universality class. Measurements are performed on domain-wall configuration and apply the reweighting of the domain-wall fermion determinant to the overlap fermion. In this study, not only $U(1)_A$ susceptibility but also topological susceptibility and meson and baryon screening mass are measured. The authors of Ref. [14] conclude that "the remaining anomaly of the axial $U(1)$ symmetry at the physical point for $T \geq T_c$ is at most a few MeV level, which is $\sim 1\%$ of the simulated temperatures".

As shown above, results from different groups lead to different conclusion. Therefore, the fate of $U(1)_A$ symmetry still open question. In this thesis, I attack this problem with Wilson-type quark. To care the chiral symmetry breaking of Wilson fermion, we use the SFtX method based on the gradient flow as a

renormalization procedure.

Chapter 4

Gradient Flow

Over the past decade, gradient flow has been shown to provide many advantages in lattice QCD calculations, *e.g.* scale setting, definition of the topological density, and renormalization by removing UV divergences from any operators [15–19]

4.1 Definition of flow equations

In the gradient flow method, we consider a time evolution along a fictitious time. This fictitious time is often called "flow-time". For a D-dimensional space-time theory with a fields $\phi(x)$, we consider a $D+1$-dimensional "flowed" fields $\Phi(t,x)$, where t indicates the flow-time. We impose the initial condition at the vanishing flow time,

$$\Phi(t=0,x)=\phi(x). \tag{4.1}$$

The time evolution toward finite flow-time is defined by the variation of the action,

$$\partial_t\Phi(t,x)\sim-\frac{\delta S[\Phi(t,x)]}{\delta\Phi(t,x)}. \tag{4.2}$$

This method was first applied to Yang-Mills theory [17] to determine the topological sector on the lattice calculation and was shown that flowed fields are free from UV divergences at $t>0$ by using the one-loop perturbative calculation. The proof of UV finiteness was extended to all orders of perturbation theory by Ref. [18]. This idea is also extended to the quark fields immediately with slight modification [19].

4.1.1 Flow equation for gauge field

As shown above, flowed fields are defined through the flow equation such as Eq. (4.2). The flow equation for $SU(N)$ Yang–Mills theory,

$$S_{\mathrm{YM}}[A]=-\frac{1}{2g_0^2}\int \mathrm{d}^Dx\,\mathrm{tr}\left\{F_{\mu\nu}(x)F_{\mu\nu}(x)\right\}, \tag{4.3}$$

$$F_{\mu\nu}(x)=\partial_\mu A_\nu(x)-\partial_\nu A_\nu(x)+[A_\mu(x),A_\nu(x)], \tag{4.4}$$

is defined as [17]

$$\begin{aligned}\partial_tB_\mu(t,x)&=D_\nu G_{\nu\mu}(t,x)\\&=\partial^2B_\mu(t,x)-\partial_\mu\partial_\nu B_\nu(t,x)+R_\mu(t,x),\end{aligned} \tag{4.5}$$

where the initial condition, flowed field strength $G_{\mu\nu}(t,x)$ and covariant derivative for the flowed gauge fields $B_\mu(t,x)$ are

$$B_\mu(0,x) = A_\mu(x), \tag{4.6}$$
$$G_{\mu\nu}(t,x) = \partial_\mu B_\nu(t,x) - \partial_\nu B_\nu(t,x) + [B_\mu(t,x), B_\nu(t,x)], \tag{4.7}$$
$$D_\mu = \partial_\mu + [B_\mu(t,x), \cdot\,], \tag{4.8}$$

and the inhomogeneous terms $R_\mu(t,x)$ is

$$R_\mu(t,x) = 2[B_\nu, \partial_\nu B_\mu] - [B_\nu, \partial_\mu B_\nu] - [B_\mu, \partial_\nu B_\nu] + [B_\nu, [B_\nu, B_\mu]]. \tag{4.9}$$

Note that the t is for the flow-time and x means four-dimensional coordinates. We distinguish between flow-time t and ordinal time, zeroth component of space-time, x_0 explicitly.

Under the flow-time dependent infinitesimal gauge transformation,

$$\delta B_\mu(t,x) = D_\mu \omega(t,x), \tag{4.10}$$

gauge flow equation Eq. (4.5) is consistent with the modified gauge flow equation

$$\begin{aligned}\partial_t B_\mu(t,x) &= D_\nu G_{\nu\mu}(t,x) + \alpha_0 D_\mu \partial_\nu B_\nu(t,x) \\ &= \partial^2 B_\mu(t,x) + (\alpha_0 - 1)\partial_\mu \partial_\nu B_\nu(t,x) + R'_\mu(t,x), \qquad (4.11)\\ R'_\mu &= 2[B_\nu, \partial_\nu B_\mu] - [B_\nu, \partial_\mu B_\nu] + (\alpha_0 - 1)[B_\mu, \partial_\nu B_\nu] + [B_\nu, [B_\nu, B_\mu]]. \qquad (4.12)\end{aligned}$$

where the gauge transformation parameter $\omega(t,x)$ satisfies

$$(\partial_t - \alpha_0 D_\mu \partial_\mu)\omega(t,x) = -\delta\alpha_0 \partial_\nu B_\nu(t,x). \tag{4.13}$$

The gauge parameter α_0 transforms as $\alpha_0 \to \alpha_0 + \delta\alpha_0$ under the infinitesimal gauge transformation Eq. (4.10). The second term in the right hand side of Eq. (4.11) with $\alpha_0 \neq 0$ damps the gauge degrees of freedom of the field and this term is referred to as a gauge fixing term. Due to the existence of the gauge fixing term, we can avoid some subtlty in perturbative calculations as long as we concentrate on the gauge-invariant observables.

The formal solution of Eq. (4.11) is given by [18],

$$B_\mu(t,x) = \int \mathrm{d}^D y \left\{ K_t(x-y)_{\mu\nu} A_\nu(y) + \int_0^t \mathrm{d}s\, K_{t-s}(x-y)_{\mu\nu} R_\nu(s,y) \right\}, \tag{4.14}$$

where the $K_t(x)_{\mu\nu}$ is the heat kernel

$$K_t(x)_{\mu\nu} = \int \frac{\mathrm{d}^D p}{(2\pi)^D} \frac{1}{p^2} \left\{ \left(\delta_{\mu\nu} p^2 - p_\mu p_\nu\right) e^{-tp^2} + p_\mu p_\nu e^{-\alpha_0 t p^2} \right\} e^{ipx}. \tag{4.15}$$

When we choose the gauge parameter $\alpha_0 = 1$, the heat kernel reduces to a Gaussian damping factor,

$$K_t(x)_{\mu\nu} = \delta_{\mu\nu} K_t(x) = \delta_{\mu\nu} \int \frac{\mathrm{d}^D p}{(2\pi)^D} e^{-tp^2} e^{ipx} = \delta_{\mu\nu} \frac{e^{-x^2/4t}}{(4\pi t)^{D/2}}. \tag{4.16}$$

This shows the smoothing property of the gradient flow. In four dimension space-time, flowed field is smeared over a spherical range $x \sim \sqrt{8t}$.

4.1.2 Application of perturbation theory

In perturbation theory, it is useful to rescale the gauge field by the bare coupling,

$$A_\mu(x) \to g_0 A_\mu(x). \tag{4.17}$$

Here, perturbative expansion is expanded in terms of the bare gauge coupling. The flowed gauge field $B_\mu(t,x)$ become a function of the gauge coupling with an asymptotic expansion,

$$B_\mu(t,x) = \sum_{k=1}^{\infty} g_0^k B_{\mu,k}(t,x), \qquad B_{\mu,k}(t=0,x) = \delta_{k1} A_\mu(x). \tag{4.18}$$

Inserting this expansion into Eq. (4.11) and the gauge parameter α_0 set to unity, flow equations for the $B_{\mu,k}(t,x)$ are,

$$\partial_t B_{\mu,k}(t,x) - \partial^2 B_{\mu,k}(t,x) = R_{\mu,k}(t,x), \tag{4.19}$$

where the inhomogeneous terms are given by

$$R_{\mu,1} = 0, \tag{4.20}$$
$$R_{\mu,2} = 2[B_{\nu,1}, \partial_\nu B_{\mu,1}] - [B_{\nu,1}, \partial_\mu B_{\nu,1}], \tag{4.21}$$
$$R_{\mu,3} = 2[B_{\nu,2}, \partial_\nu B_{\mu,1}] + 2[B_{\nu,1}, \partial_\nu B_{\mu,2}] - [B_{\nu,2}, \partial_\mu B_{\nu,1}] - [B_{\nu,1}, \partial_\mu B_{\nu,2}] + [B_{\nu,1}, [B_{\nu,1}, B_{\mu,1}]], \tag{4.22}$$

and so on. The leading order equation can be solved as

$$B_{\mu,1}(t,x) = \int \mathrm{d}^D y \, K_t(x-y) A_\mu(y), \tag{4.23}$$
$$K_t(z) = \int \frac{\mathrm{d}^D p}{(2\pi)^D} e^{ipz} e^{-tp^2} = \frac{e^{-z^2/4t}}{(4\pi t)^D}, \tag{4.24}$$

and higher order equations can be solved formally,

$$B_{\mu,k}(t,x) = \int_0^t \mathrm{d}s \int \mathrm{d}^D y \, K_{t-s}(x-y) R_{\mu,k}(s,y). \tag{4.25}$$

As we can see, higher order flowed gauge fields can be obtained using these equations recursively.

Using these expansion, we calculate the flowed energy

$$E(t) = \frac{1}{4} \int \mathrm{d}^D x \left\langle G^a_{\mu\nu}(t,x) G^a_{\mu\nu}(t,x) \right\rangle \tag{4.26}$$
$$= \frac{1}{2} \left\langle \partial_\mu B^a_\nu(t,x) \partial_\mu B^a_\nu(t,x) - \partial_\mu B^a_\nu(t,x) \partial_\nu B^a_\mu(t,x) \right\rangle + f^{abc} \left\langle \partial_\mu B^a_\nu(t,x) B^b_\mu B^c_\nu(t,x) \right\rangle + \frac{1}{4} f^{abe} f^{cde} \left\langle B^a_\mu(t,x) B^b_\nu(t,x) B^c_\mu(t,x) B^d_\nu(t,x) \right\rangle. \tag{4.27}$$

These terms are expanded up to one-loop order,

$$\mathcal{E}_0 = \frac{1}{2} g_0^2 \left\langle \partial_\mu B^a_{\nu,1} \partial_\mu B^a_{\nu,1} - \partial_\mu B^a_{\nu,1} \partial_\nu B^a_{\mu,1} \right\rangle, \tag{4.28}$$

$$\mathcal{E}_1 = g_0^3 f^{abc} \left\langle \partial_\mu B^a_{\nu,1} B^b_{\mu,1} B^c_{\nu,1} \right\rangle, \tag{4.29}$$

$$\mathcal{E}_2 = \frac{1}{2} g_0^3 \left\langle \partial_\mu B^a_{\nu,1} \partial_\mu B^a_{\nu,2} - \partial_\mu B^a_{\nu,1} \partial_\nu B^a_{\mu,2} \right\rangle, \tag{4.30}$$

$$\mathcal{E}_3 = \frac{1}{4} g_0^4 f^{abe} f^{cde} \left\langle B^a_{\mu,1} B^b_{\nu,1} B^c_{\mu,1} B^d_{\nu,1} \right\rangle, \tag{4.31}$$

$$\mathcal{E}_4 = \frac{1}{2} g_0^4 \left\langle \partial_\mu B^a_{\nu,1} \partial_\mu B^a_{\nu,3} - \partial_\mu B^a_{\nu,1} \partial_\nu B^a_{\mu,3} \right\rangle, \tag{4.32}$$

$$\mathcal{E}_5 = \frac{1}{2} g_0^4 \left\langle \partial_\mu B^a_{\nu,2} \partial_\mu B^a_{\nu,2} - \partial_\mu B^a_{\nu,2} \partial_\nu B^a_{\mu,2} \right\rangle, \tag{4.33}$$

where $\mathcal{E}_0$ is the lowest order contribution.

As caclulated in [17],

$$E(t) = \frac{1}{2} \frac{N^2-1}{(8\pi t)^{D/2}} (D-1) g_0^2 \left[1 + \frac{1}{(4\pi)^{D/2}} (8t)^\varepsilon g_0^2 \left\{ \frac{1}{\varepsilon} \left(\frac{11}{3} N - \frac{2}{3} N_f \right) + (\text{finite}) \right\} + O(g_0^4) \right]. \tag{4.34}$$

The divergent part is cancelled with the gauge coupling renormalization,

$$g_0^2 = \bar{g}^2 \mu^{2\varepsilon} \left(4\pi e^{-\gamma_E} \right)^{-\varepsilon} \left\{ 1 - \frac{1}{(4\pi)^2} \bar{g}^2 \left(\frac{11}{3} N - \frac{2}{3} N_f \right) \frac{1}{\varepsilon} + O\left(\bar{g}^4 \right) \right\}. \tag{4.35}$$

In the Ref. [18], UV finiteness for the all orders in perturbation theory is discussed.

4.1.3 Flow equations for quark fields

We have considered the Yang-Mills gradient flow in the previous sections. We also need to consider flowed quark fields for the application in QCD. Flow equations for quark fields are also considered in Ref. [19]. Here, flow equations for quark fields do not need to be a gradient flow of the original fermion action. We employ the minimal choice, the gauge covariant diffusion equation as flow equations for quark fields,

$$\partial_t \chi_f(t,x) = D^2 \chi_f(t,x), \quad \chi_f(0,x) = \psi_f(x), \tag{4.36}$$

$$\partial_t \bar{\chi}_f(t,x) = \bar{\chi}_f(t,x) \overleftarrow{D}^2, \quad \bar{\chi}_f(0,x) = \bar{\psi}_f(x), \tag{4.37}$$

where $D^2 = D_\mu D_\mu$ denotes flowed covariant derivative for fermion fields,

$$D_\mu = \partial_\mu + B_\mu(t,x), \quad \overleftarrow{D}_\mu = \overleftarrow{\partial}_\mu - B_\mu(t,x). \tag{4.38}$$

These are consistent with modified equations,

$$\begin{aligned} \partial_t \chi_f(t,x) &= D^2 \chi_f(t,x) - \alpha_0 \partial_\nu B_\nu(t,x) \chi_f(t,x) \\ &= \partial^2 \chi_f(t,x) + (1-\alpha_0) \partial_\nu B_\nu(t,x) \chi_f(t,x) + 2 B_\nu(t,x) \partial_\nu(t,x) \chi_f(t,x) + B^2(t,x) \chi_f(t,x), \end{aligned} \tag{4.39}$$

$$\begin{aligned} \partial_t \bar{\chi}_f(t,x) &= \bar{\chi}_f(t,x) \overleftarrow{D}^2 + \alpha_0 \bar{\chi}_f(t,x) \partial_\nu B_\nu(t,x) \\ &= \partial^2 \bar{\chi}_f(t,x) - (1-\alpha_0) \partial_\nu B_\nu(t,x) \bar{\chi}_f(t,x) - 2 B_\nu(t,x) \partial_\nu \bar{\chi}_f(t,x) - B^2(t,x) \bar{\chi}_f(t,x), \end{aligned} \tag{4.40}$$

under the flow-time dependent infinitesimal gauge transformations

$$\chi_f(t,x) \to (1 + i\omega(t,x)) \chi_f(t,x), \tag{4.41}$$

$$\bar{\chi}_f(t,x) \to \bar{\chi}_f(t,x) (1 - i\omega(t,x)). \tag{4.42}$$

Additional terms damp gauge modes as is the case for the gauge flow. The formal solutions of the flowed quark fields are

$$\chi_f(t,x) = \int \mathrm{d}^D y \left\{ K_t(x-y)\psi_f(y) + \int_0^t \mathrm{d}s\, K_{t-s}(x-y)\Delta'\chi_f(s,y) \right\}, \tag{4.43}$$

$$\bar{\chi}_f(t,x) = \int \mathrm{d}^D y \left\{ \bar{\psi}_f(y)K_t(x-y) + \int_0^t \mathrm{d}s\, \bar{\chi}_f(s,y)\overleftarrow{\Delta}'K_{t-s}(x-y) \right\}, \tag{4.44}$$

where Δ and $\overleftarrow{\Delta}'$ are the inhomogeneous tems,

$$\Delta' = (1-\alpha_0)\partial_\nu B_\nu + 2B_\nu\partial_\nu + B^2, \tag{4.45}$$

$$\overleftarrow{\Delta}' = -(1-\alpha_0)\partial_\nu B_\nu(t,x) - 2B_\nu(t,x)\partial_\nu - B^2(t,x), \tag{4.46}$$

and the heat kernel $K_t(z)$ is

$$K_t(z) = \int \frac{\mathrm{d}^D p}{(2\pi)^D} e^{ipz} e^{-tp^2} = \frac{e^{-z^2/4t}}{(4\pi t)^{D/2}}. \tag{4.47}$$

As shown in Ref. [19], we need wave function renormalization

$$\chi_f = Z_\chi^{-1/2}\chi_{f,R}, \qquad \bar{\chi} = \bar{\chi}_{f,R}Z_\chi^{-1/2}, \tag{4.48}$$

where the renormalization constant in $\overline{\mathrm{MS}}$ scheme is

$$Z_\chi = 1 + \frac{3C_F}{16\pi^2\varepsilon}\bar{g}^2 + O(\bar{g}^4). \tag{4.49}$$

Finally, we consider the Wick contraction of flowed quark fields. Basically, Wick contractions of fields are given explicitly by the action. Actually, in the D-dimensional QCD, Wick contraction of the quark fields are

$$\overbrace{\psi(x)_f\bar{\psi}}_f(y) = S_f(x,y), \tag{4.50}$$

$$(\not{D} + m_{f,0})S_f(x,y) = \delta(x-y). \tag{4.51}$$

On the other hand, we cannot adopt this strategy because we do not have the effective action of flowed field. At the flow-time zero, Wick contraction have to coincide with the one in D-dimensions. Thus, the contraction of time-dependent quark fields is written as

$$\overbrace{\chi(t,x)_f\bar{\chi}}_f(s,y) = \int \mathrm{d}^D v\, \mathrm{d}^D w\, K(t,x:0,v)S_f(v,w)K^\dagger(s,y:0,w), \tag{4.52}$$

where the fundamental solution

$$\left\{ \partial_t - D^2 - \alpha_0\partial_\nu B_\nu(t,x) \right\} K(t,x;s,y) = 0, \tag{4.53}$$

$$\lim_{t\to s} K(t,x:s,y) = \delta(x-y). \tag{4.54}$$

for the fermion flow equation is used.

4.2 Small flow-time expansion (SFtX) method

The small flow-time expansion (SFtX) method provides us a way to calculate the correctly renormalized operators in the sense of gradient flow. As the first step of the SFtX method, we relate the bare operator and flowed operator.

At a small flow-time, it is shown that the flowed operators are related to the bare operator as [18]

$$\mathcal{O}(\chi,\bar{\chi},B) = c_{\mathcal{O}}(t)\mathcal{O}(\psi,\bar{\psi},A) + O(t), \tag{4.55}$$

where $\mathcal{O}(\psi,\bar{\psi},A)$ is the bare operator and $\mathcal{O}(\chi,\bar{\chi},B)$ is the flowed operator. This means that, for instance, in the case of scalar density operator,

$$\bar{\chi}_f(t,x)\chi_f(t,x) \overset{t\to 0}{\sim} c_S(t)\bar{\psi}_f(x)\psi_f(x) + O(t). \tag{4.56}$$

To obtain the coefficient $c(t)$, we consider the one-particle irreducible vertex correction as [20]

$$\Big\langle \mathcal{O}(\chi,\bar{\chi},B) - \mathcal{O}(\psi,\bar{\psi},A) \Big\rangle_{\text{1PI}} = I_{GF}(t)\Gamma_{\mathcal{O}}, \tag{4.57}$$

where $\Gamma_{\mathcal{O}}$ is a related vertex function. At the small flow-time, the left hand side would be

$$\begin{aligned}\Big\langle \mathcal{O}(\chi,\bar{\chi},B) - \mathcal{O}(\psi,\bar{\psi},A) \Big\rangle_{\text{1PI}} &= (c(t)-1)\Big\langle \mathcal{O}(\psi,\bar{\psi},A) \Big\rangle_{\text{1PI}} \\ &= (c(t)-1)\, Z_{\mathcal{O}}\Gamma_{\mathcal{O}},\end{aligned} \tag{4.58}$$

up to $O(t)$. Combining these relations, we obtain the representation of small flow-time expansion as

$$\mathcal{O}(\chi,\bar{\chi},B) \sim (1 + I_{GF}(t))\,\mathcal{O}(\psi,\bar{\psi},A) + O(t). \tag{4.59}$$

As calculated in Ref. [19], quark fields need wave function renormalization. A useful choice is [21]

$$\mathring{\chi}_f(t,x) = \sqrt{\varphi_f(t)}\chi_f(t,x), \qquad \mathring{\bar{\chi}}_f(t,x) = \sqrt{\varphi_f(t)}\bar{\chi}_f(t,x), \tag{4.60}$$

$$\varphi_f(t) = \frac{-6}{(4\pi t)^2\Big\langle \bar{\chi}_f(t,x)\gamma_\mu \overrightarrow{D}_\mu \chi_f(t,x)\Big\rangle}, \tag{4.61}$$

where the wave function renormalization cancel out and denominator does not diverge in the $t\to 0$ limit. Therefore, flowed operators need to be rewritten in terms of ringed quarks, $\mathcal{O}(\mathring{\chi},\mathring{\bar{\chi}},B)$. Then,

$$\mathcal{O}(\mathring{\chi},\mathring{\bar{\chi}},B) = \varphi^{n/2}(t)\mathcal{O}(\chi,\bar{\chi},B), \tag{4.62}$$

$$\varphi^{n/2} \equiv \prod_{f\in\mathcal{O}} \varphi_f^{1/2}, \tag{4.63}$$

where n denotes the number of flowed quark fields χ and $\bar{\chi}$ in $\mathcal{O}(\chi,\bar{\chi},B)$. Therefore, the small flow-time representation becomes

$$\mathcal{O}(\mathring{\chi},\mathring{\bar{\chi}},B) = \varphi^{n/2}(t)\,(1 + I_{GF}(t))\,\mathcal{O}(\psi,\bar{\psi},A) + O(t). \tag{4.64}$$

On the other hand, bare operators is renormalized as

$$\mathcal{O}_{\overline{\text{MS}}}(\psi_{\overline{\text{MS}}},\bar{\psi}_{\overline{\text{MS}}},A) = Z_{\mathcal{O}}^{\overline{\text{MS}}}(Z_{\psi}^{\overline{\text{MS}}})^{n/2}\mathcal{O}(\psi,\bar{\psi},A), \tag{4.65}$$

where $Z_{\mathcal{O}}^{\overline{\text{MS}}}$ and $Z_{\psi}^{\overline{\text{MS}}}$ denote the renormalization constants. To summarize there relations, we obtain the relation between flowed and renormalized operator,

$$\mathcal{O}_{\overline{\text{MS}}}(\psi_{\overline{\text{MS}}},\bar{\psi}_{\overline{\text{MS}}},A) = \frac{Z_{\mathcal{O}}^{\overline{\text{MS}}}}{(1+I_{GF}(t))}\left(\frac{Z^{\overline{\text{MS}}}}{\varphi(t)}\right)^{n/2}\mathcal{O}(\mathring{\chi},\mathring{\bar{\chi}},B) + O(t) \tag{4.66}$$

$$\equiv Z^{\text{GF}\to\overline{\text{MS}}}\mathcal{O}(\mathring{\chi},\mathring{\bar{\chi}},B) + O(t), \tag{4.67}$$

where the $Z^{\text{GF}\to\overline{\text{MS}}}$ is the matching coefficient we need.

4.3 Some numerical results

In this section, we show some previous results by the SFtX method.

4.3.1 Thermodynamic quantities

Thermodynamic quantities can be extracted from energy-momentum tensorc(EMT) diagonal part under the assumption that the system is isotropic and uniform.

We can obtain thermodynamic quantities, the energy density ϵ and the pressure p, using the EMT as

$$\frac{\epsilon}{T^4} = -\frac{\langle T_{00}\rangle}{T^4}, \tag{4.68}$$

$$\frac{p}{T^4} = \sum_i \frac{\langle T_{ii}\rangle}{T^4}, \tag{4.69}$$

or the trace anomaly and the entropy density is given as

$$\frac{\epsilon - 3p}{T^4} = -\frac{\langle T_{\mu\mu}\rangle}{T^4}, \tag{4.70}$$

$$\frac{\epsilon + p}{T^4} = -\frac{4}{3T^4}\left\langle T_{00} - \frac{1}{4}T_{\mu\mu}\right\rangle. \tag{4.71}$$

The EMT is the Noether current with respect to the translational symmetry. However, there is many difficulties to determine the EMT on the lattice because translational symmetry is explicitly violated by the finite lattice spacing a. In continuum QCD, the EMT is written in terms of the four-dimensional gauge invariant second-rank symmetric tensors

$$\mathcal{O}_{1,\mu\nu}(x) = F^a_{\mu\rho}(x)F^a_{\nu\rho}(x), \tag{4.72}$$

$$\mathcal{O}_{2,\mu\nu}(x) = \delta_{\mu\nu}F^a_{\rho\sigma}(x)F^a_{\rho\sigma}(x), \tag{4.73}$$

$$\mathcal{O}_{3,\mu\nu}(x) = \sum_f \bar{\psi}_f(x)\Big(\gamma_\mu \overrightarrow{D}_\nu + \gamma_\nu \overrightarrow{D}_\nu\Big)\psi_f v(x), \tag{4.74}$$

$$\mathcal{O}_{4,\mu\nu}(x) = \delta_{\mu\nu}\sum_f \bar{\psi}_f(x)\overrightarrow{\not{D}}\psi_f(x), \tag{4.75}$$

$$\mathcal{O}_{5,\mu\nu}(x) = \delta_{\mu\nu}\sum_f m_{f,0}\bar{\psi}_f(x)\psi_f(x), \tag{4.76}$$

as

$$T_{\mu\nu}(x) = \frac{1}{g_0^2}\left[\mathcal{O}_{1,\mu\nu}(x) - \frac{1}{4}\mathcal{O}_{2,\mu\nu}(x)\right] + \frac{1}{4}\mathcal{O}_{3,\mu\nu}(x) - \frac{1}{2}\mathcal{O}_{4,\mu\nu}(x) - \mathcal{O}_{5,\mu\nu}(x). \tag{4.77}$$

In Refs. [20, 21], it is suggested that the SFtX method can be used to construct the EMT on the lattice. Using the flowed operators,

$$\tilde{\mathcal{O}}_{1\mu\nu}(t,x) = G^a_{\mu\rho}(t,x)G^a_{\nu\rho}(t,x), \tag{4.78}$$

$$\tilde{\mathcal{O}}_{2\mu\nu}(t,x) = \delta_{\mu\nu}G^a_{\rho\sigma}(t,x)G^a_{\rho\sigma}(t,x), \tag{4.79}$$

$$\tilde{\mathcal{O}}^f_{3\mu\nu}(t,x) = \mathring{\bar{\chi}}_f(t,x)(\gamma_\mu \overrightarrow{D}_\nu + \gamma_\nu \overrightarrow{D}_n u)\mathring{\chi}_f(t,x), \tag{4.80}$$

$$\tilde{\mathcal{O}}^f_{4\mu\nu}(t,x) = \delta_{\mu\nu}\mathring{\bar{\chi}}_f(t,x)\overrightarrow{\not{D}}\mathring{\chi}_f(t,x), \tag{4.81}$$

$$\tilde{\mathcal{O}}^f_{5\mu\nu}(t,x) = \delta_{\mu\nu}m_{f,0}\mathring{\bar{\chi}}_f(t,x)\mathring{\chi}_f(t,x), \tag{4.82}$$

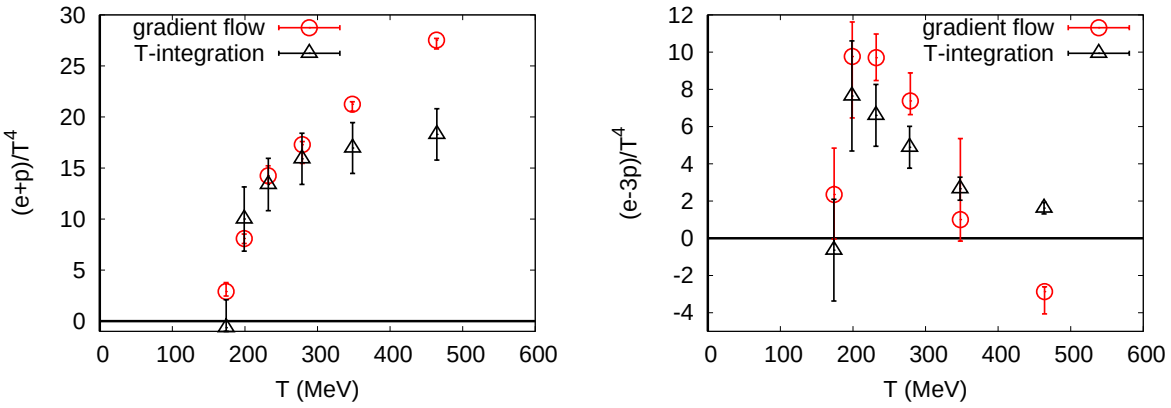

Figure 4.1: Entropy density(left) and trace anomaly(right) as a function of temperature [23]. One-loop matching coefficients [21] are used.

the EMT is given by

$$T_{\mu\nu}(x) = \lim_{t\to 0}\left\{c_1(t)\left[\tilde{\mathcal{O}}_{1\mu\nu}(t,x) - \frac{1}{4}\tilde{\mathcal{O}}_{2\mu\nu}(t,x)\right] + c_2(t)\tilde{\mathcal{O}}_{2\mu\nu}(t,x) \right.$$
$$\left. + \sum_f \left\{c_3(t)\left[\tilde{\mathcal{O}}^f_{3\mu\nu}(t,x) - 2\tilde{\mathcal{O}}^f_{4\mu\nu}(t,x)\right] + c_4(t)\tilde{\mathcal{O}}^f_{4\mu\nu}(t,x) + c_5^f(t)\tilde{\mathcal{O}}^f_{5\mu\nu}(t,x)\right\}\right\}, \quad (4.83)$$

where the matching coefficients $c_i(t)$ are

$$c_1(t) = \frac{1}{\bar{g}^2(\mu')} - \frac{1}{(4\pi)^2}\left(9\left(\ln\left(2\mu'^2 t\right) + \gamma_E\right) + \frac{19}{4}\right), \quad (4.84)$$

$$c_2(t) = \frac{1}{8}\frac{1}{(4\pi)^2}\frac{11}{2}, \quad (4.85)$$

$$c_3(t) = \frac{1}{4}\left\{1 + \frac{\bar{g}^2(\mu')}{(4\pi)^2}\frac{4}{3}\left[\frac{3}{2} + \ln(432)\right]\right\}, \quad (4.86)$$

$$c_4(t) = \frac{\bar{g}^2(\mu')}{(4\pi)^2}, \quad (4.87)$$

$$c_5^f(t) = -\frac{\bar{m}_f(\mu')}{m_{f,0}}\left\{1 + \frac{\bar{g}^2}{(4\pi)^2}\left[4\left(\ln\left(2\mu'^2 t\right) + \gamma_E\right) + \frac{14}{3} + \frac{4}{3}\ln(432)\right]\right\}, \quad (4.88)$$

where the group factors are set to the case $(2+1)$-flavor QCD, $N = 3$ and $N_f = 3$. This is first applied to $SU(3)$ Yang-Mills theory [22] and subsequently to full QCD [23].

Fig. 4.1, shows the results of [23]. Red point denote the results of SFtX method and the black triangle denote the results of the T-integral method [24]. These results are consistent at low temperatures $T \leq 279$ MeV. However, at high temperatures $T \geq 348$ MeV, these results show the deviation due to the severe lattice artifact.

Fig. 4.2 shows the results of [25]. Latent heat and pressure gap in $SU(3)$ Yang-Mills theory are studied in this paper. The ordering of the double limit — continuum and vanishing flow-time limit — is also discussed. The result of different ordering of double limit is shown In the left panel. In the method 1, the double limit is taken as $t \to 0$ followed by $a \to 0$. In the method 2, ordering is reversed: $a \to 0$ followed by $t \to 0$. These results are consistent each other. This indicate that the ordering of double limit does not affect the final result.

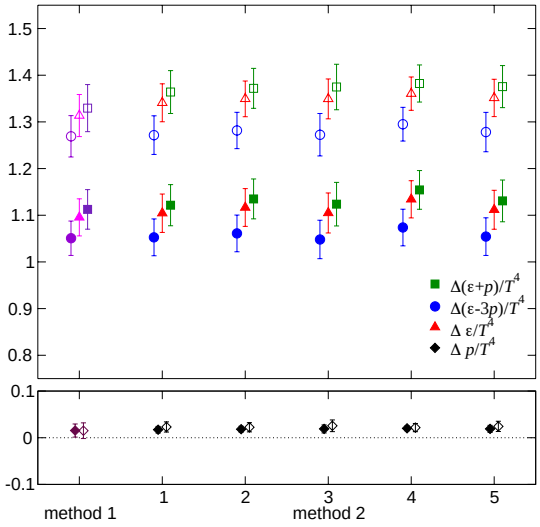

Figure 4.2: Study of latent heat and pressure gap in pure Yang-Mills theory [25]. Results of latent heat and pressure gap are shown. Filled symbol indicates the result of aspect ratio $N_s/N_t = 8$ and open symbol indicates the results of $N_s/N_t = 6$. In the method 1, the double limit is taken as $t \to 0$ followed by $a \to 0$. In the method 2, the double limit is taken as $a \to 0$ followed by $t \to 0$ and fit range dependence of $t \to 0$ extrapolation is shown in 1, 2, ... 5.

4.3.2 Topological susceptibility

Through the Peccei-Quinn mechanism [26], the axion, the candidate of the dark matter, is introduced into QCD to solve the strong CP problem. Since the axion mass relates to the topological susceptibility, the temperature dependence of the topological susceptibility also plays important role in the cosmology.

The topological susceptibility can be defined in two different ways. One is the straight forward way, define as the fluctuation of the topological charge. The most popular definition of the topological charge is using the gauge field strength

$$Q(x) = \int \mathrm{d}^4x\, q(x) = \frac{1}{64\pi^2} \int \mathrm{d}^4x\, \varepsilon^{\mu\nu\rho\sigma} F^a_{\mu\nu}(x) F^a_{\mu\nu}(x). \qquad \varepsilon^{0123} = 1, \tag{4.89}$$

Using the topological charge, gluonic definition of the topological susceptibility is defined by

$$\chi_{\mathrm{t}} = \frac{1}{V} \left(\left\langle Q^2 \right\rangle - \langle Q \rangle^2 \right). \tag{4.90}$$

In calculation of topological quantities on the lattice, gradient flow works as the cooling procedure [27].

The other way of defining the topological susceptibility is using the disconnected two-point function of the pseudoscalar density,

$$\chi_{\mathrm{t}} = \frac{1}{V} \left\langle Q^2 \right\rangle = \frac{m^2}{V N_{\mathrm{f}}^2} \left(\left\langle P^0 P^0 \right\rangle - N_{\mathrm{f}} \left\langle P^a P^a \right\rangle \right), \tag{4.91}$$

where N_{f} is the number of degenerate flavors. In the continuum QCD, this relation valid through the chiral Ward-Takahashi identities [28, 29]. The flavor non-singlet pseudoscalar density is also defined using SFtX method as [30]:

$$P^a = \lim_{t\,\to 0} P^a(t) = \lim_{t \to 0} \int \mathrm{d}^4x\, c_S(t) \mathring{\bar{\chi}}(t,x) \gamma_5 T^a \mathring{\chi}(t,x), \tag{4.92}$$

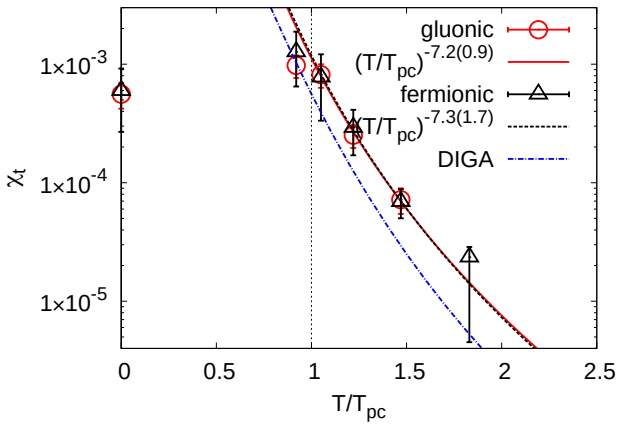

Figure 4.3: Topological susceptibility as a function of temperature [31]. Red circle denotes calculation via gluonic definition Eq. (4.90) and black triangle denotes calculation via fermionic definition Eq. (4.91)

where the matching coefficient $c_S(t)$ is

$$c_S(t) = \left\{1 + \frac{\bar{g}^2(\mu')}{(4\pi)^2}\left[4\left(\ln 2t\mu'^2 + \gamma_E\right) + 8 + \frac{4}{3}\ln 432\right]\right\}\frac{\bar{m}_f(\mu')}{\bar{m}_f(2\mathrm{GeV})}, \tag{4.93}$$

where the group factors are also set to the case $(2+1)$-flavor QCD.

Results are shown in Fig. 4.3. The red point and black triangle denote gluonic and fermionic definition, respectively. The gluonic and fermionic definitions show good agreement with each other. This result indicates that the SFtX method works well for the chiral Ward-Takahashi identity even with the Wilson-type quark.

Chapter 5

Numerical Results

5.1 Lattice setup

We use the configurations generated by Refs. [24,32]. We employ $(2+1)$-flavor QCD with slightly heavy u and d quarks ($m_\pi/m_\rho \sim 0.63$) and approximately physical s quark ($m_{\eta_{ss}}/m_\phi \sim 0.74$) on a relatively fine lattice with the lattice spacing $a \sim 0.07$ fm ($a^{-1} \sim 2.79$ GeV) [24,32]. We adopt the renormalization-group improved Iwasaki gauge action [7, 33] and $O(a)$-improved Wilson fermion [8]. The bare gauge coupling parameter is set to $\beta = 2.05$, which corresponds to $a \sim 0.07$ fm ($a^{-1} \sim 2.79$ GeV). The hopping parameters are set to $(\kappa_{ud}, \kappa_s) = (0.1356, 0.1351)$ respectively.

In this study, we adopt the fixed-scale approach [34,35] in which the temperature $T = 1/(N_t a)$ is varied by changing the temporal lattice size N_t with a fixed lattice spacing a. In the original paper [24], finite temperature configurations have been generated on lattice with the temperature range of 174 – 697 MeV corresponding to the temporal lattice size of $N_t = 16, 14, \cdots, 4$. In the study of [24], pseudocritical temperature is estimated as $T_{pc} \simeq 190$ MeV using renormalized Polyakov loop, etc. In the previous study applying the SFtX method to these comfigurations [23], it turns out that the lattice with $N_t \leq 8$ suffer from the lattice artifact $O(a^2T^2) = O(1/N_t^2)$. Therefore, in this study, we use the configurations with the range $N_t \geq 8$ corresponding to $T \simeq 174$ – 348 MeV.

In this study, observables are measured every 50 trajectories at $T > 0$ and every 100 trajectories at $T = 0$. This corresponds to one measurement for every ten original configurations both in $T = 0$ and $T > 0$. Number of configurations used for measurements are summarized in Table 5.1.

Table 5.1: Lattice parameters: The temporal lattice size N_t, temperature T in MeV unit, $T/T_{\rm pc}$ assuming $T_{\rm pc} = 190$ MeV, $t_{1/2}$ defined in Eq. (5.9), and the number of configurations used in measurments. Spatial box size is 32^3 for $T > 0$ and 28^3 for $T = 0$.

N_t	T [MeV]	T/T_c	$t_{1/2}$	Configurations
56	0	0	24.5	65
16	174	0.92	8	144
14	199	1.05	6.125	127
12	232	1.22	4.5	129
10	279	1.47	3.125	78
8	348	1.83	2	51

5.2 Renormalization scale

In general, matching coefficients are functions of renormalization scale μ', the $\overline{\text{MS}}$ running coupling constant $\bar{g}(\mu')$ and running mass $\bar{m}(\mu')$. We have the freedom in choosing of the renormalization scale as long as μ' is proportional to $1/\sqrt{t}$ and perturbative expansion of the matching coefficients are valid because the physical quantities does not depend on μ'.

The conventional choice is

$$\mu' = \mu_d(t) \equiv \frac{1}{\sqrt{8t}}, \tag{5.1}$$

which is a natural scale for flowed operators because $x \sim \sqrt{8t}$ is the physical smearing extent of flowed fields. The μ_d-scale have been used since the early time of the SFtX method, and provide good results in the previous studies [22, 23, 31, 36].

Recently, an alternative choice is proposed in Ref. [37],

$$\mu' = \mu_0(t) \equiv \frac{e^{-\gamma_E/2}}{\sqrt{2t}}. \tag{5.2}$$

This renormalization scale has been chosen to remove the constant appearing in perturbative calculation of matching coefficients, $L(\mu, t) = \ln(2\mu'^2 t) + \gamma_E$. These two choices are numerically related as

$$\mu_0(t) = \sqrt{\frac{8t}{2e^{\gamma_E} t}}\, \mu_d \sim 1.5\mu_d(t). \tag{5.3}$$

Because the new renormalization scale is larger than the conventional scale, it would improve the perturbative behavior of matching coefficients in the asymptotic free theory. In the Ref. [37], it is also discussed that the renormalization scale dependence are reduced in the two-loop order than the one-loop order. However, μ_0-scale provides many advantages not only for two-loop matching coefficients but also one-loop matching coefficients [38].

As a result of improvement of perturbation behavior by the μ_0-scale, we can use the longer flow-time than the μ_d-scale. This also helps to stabilize the $t \to 0$ extrapolation.

5.3 $t \to 0$ extrapolation

We need to take the $t \to 0$ extrapolation to extract the physical quantities using data at finite flow-time. At the small flow-time, flowed observables would typically behaves as

$$\langle \mathcal{O}(t) \rangle = \langle \mathcal{O} \rangle_{\overline{\rm MS}} + tS + O(t^2), \tag{5.4}$$

where $\langle \mathcal{O}(t) \rangle$ is the measured observable at flow-time t and S is the sum of the dimension-eight[1] operators with the same quantum number, and $O(t^2)$ is the contamination from the higher-dimensional operators.

On finite lattices, lattice artifacts due to finite lattice spacing a contaminate additionally. Since we employ $O(a)$-improved Wilson quarks, the lattice artifacts are conjectured to start from $O(a^2)$ and we expect that

$$\begin{aligned}\langle \mathcal{O}(t,a) \rangle &= \langle \mathcal{O}(t) \rangle + O(a^2) \\ &= \langle \mathcal{O} \rangle_{\overline{\rm MS}} + tS + O(t^2) \\ &\quad + A \cdot \frac{a^2}{t} + \sum_f B_f \cdot (am_f)^2 + C \cdot (aT)^2 + D \cdot (a\Lambda_{\rm QCD})^2 + O(a^4),\end{aligned} \tag{5.5}$$

where $\mathcal{O}(t,a)$ is the flowed operator on the finite lattice spacing. A, B_f, C and D are the contamination from dimension-six operators as a lattice artifact.

If we can take the continuum limit before taking the $t \to 0$ limit, additional terms as $O(a^2)$ vanish. Thus, theoretically, we can carry out the $t \to 0$ extrapolation safely. On the other hand, when we take the $t \to 0$ limit before taking the continuum limit, there exists singular terms at $t \sim 0$ like $1/t$, $1/t^2, \ldots$ and so on. We need to remove these singular behavior around $t \sim 0$ in the procedure of taking the $t \to 0$ extrapolation.

In the studies of Refs. [23, 31, 38], *linear fit*

$$\langle \mathcal{O}(t,a) \rangle = \langle \mathcal{O} \rangle_{\overline{\rm MS}} + tS, \tag{5.6}$$

works well even at finite lattice spacings when we obtain a *linear window* in which the linear behavior looks dominating. We follow this strategy. In the small flow-time region, singular behavior $O(1/t)$ is dominating. On the other hand, there exists the non-linear behavior $O(t^2)$ at large flow-time region. We need to find a proper linear window avoiding these nonlinear behaviors.

To find the linear window, we employ the χ^2/d.o.f as a cut-off of the fit ranges. Because we could not measure the reliable correlation of the data among different flow-times, the absolute value of the χ^2/d.o.f have no definite meanings. We thus adopt the following procedures to obtain a reasonable linear window:

1. Fitting all available ranges by linear fit and check the χ^2/d.o.f of each ranges
2. Finding out the longest range under the condition that χ^2/d.o.f is smaller than the cut-off value.
3. Choosing the moderate cut-off by consulting the quality and stability of the resulting fits.

To estimate the systematic error due to the choice of the linear window, we also perform the *nonlinear fit*:

$$\langle \mathcal{O}(t,a) \rangle = \langle \mathcal{O} \rangle_{\overline{\rm MS}} + tS + t^2 R + A\frac{a^2}{t}. \tag{5.7}$$

This is inspired by Eq. (5.5). Higher term of small flow-time expansion t^2 and leading singular term from lattice artifact a^2/t are taken into account.

[1] Chiral and $U(1)_A$ susceptibilities are dimension-six operators.

To estimate the possible higher order correction of matching coefficient, we also perform *linear+log fit*,

$$\langle \mathcal{O} \rangle_{\overline{\rm MS}} + tA + \frac{Q}{\log^2(\sqrt{8t}\Lambda_{\rm QCD})}. \tag{5.8}$$

The exponent two correspond to the matching coefficient is calculated in one-loop perturbation theory [30]. These additional fits are performed on the linear window, chosen by using the linear fit.

In the searching the linear window, we need to take care of the oversmearing problem. To avoid boundary effects due to oversmearing, the smeared range of the gradient flow $x \sim \sqrt{8t}$ should not exceed $\min(N_s/2, N_t/2) \times a$. Thus, the measurements should be performed within flow-times

$$t/a^2 \leq t_{1/2} \equiv \frac{1}{8}\left[\min\left(\frac{N_s}{2}, \frac{N_t}{2}\right)\right]^2. \tag{5.9}$$

5.4 The Chiral susceptibility

In this section, we show the numerical results of the chiral susceptibility adopting μ_0-scale. The flow-time dependence of those in μ_d-scale are shown in Appendix B.

In the study of [23,38], disconnected part of the chiral susceptibilities using SFtX method are measure and show the clear peak around the transition temperature. In this study, we extend these study with measuring the connected part and obtain the full chiral susceptibility.

In the previous studies [23,38], they measured the flow-time up to $t/a^2 = 2.0$. As shown in Table 5.1, this is the same to the $t_{1/2}$ at $N_t = 8$. Even though we adopt the μ_0-scale, maximum value of flow-time is bounded by $t/a^2 = 2.0$ for $N_t = 8$. Thus, we do not perform the additional measurement for $N_t = 8$. Therefore, our measurement of $N_t = 8$ are limited to $t/a^2 \leq 2.0$ even though μ_0-scale is adopted.

The employed cut-offs and corresponding linear windows are listed at Appendix C.1.

5.4.1 The disconnected chiral susceptibility $\chi_f^{\mathbf{disc}}$

Before showing the full chiral susceptibility, we show the disconnected part of chiral susceptibility as a consistency check, because the disconnected chiral susceptibility is measured using SFtX method on the same configuration in Refs. [23, 38]. In Ref. [23], the μ_d-scale was adopted and they found a good linear window at $N_t \geq 8$. They found a clear peak at $T \sim 199$ MeV which is consistent to previous estimation $T_{pc} \simeq 190$ MeV. In the [38], the μ_0 scale was adopted, however, using the same data to [23] with maximum value of flow-time is $t/a^2 = 2.0$, which is suitable for μ_d-scale. As expected, linear behavior is highly improved than the μ_d-scale at large t/a^2. In the $t \to 0$ limit, though systematic errors due to the nonlinear fits become somewhat larger than [23], they found a clear peak at $T \sim 199$ MeV.

In this study, we show the disconnected chiral susceptibility adopting the μ_0-scale with maximum value of flow-time $t/a^2 = 6.0$.[2] In the Figs. 5.1 and 5.2, flow-time dependence of the disconnected chiral susceptibilities for the each temperatures are shown. Linear windows are denoted by the pair of dashed vertical lines and filled black, blue and red symbols at $t \sim 0$ are the results of $t \to 0$ extrapolations of linear, nonlinear, and linear+log fits.

Results fo ther disconnected chiral susceptibilities as a function of temperature are summarized in the first columns of Tables 5.2 and 5.3 and shown in Fig. 5.3. The ud quark and s quark results are shown in the left and right panel, respectively. We find clear peak at $T \sim 199$ MeV. This is consistent to the previous results for the transition/crossover temperature [23,38]. Comparing to the [38], systematic errors due to the fit ansatz are suppressed. This indicates that we need not only to change the renoemalization scale of the matching coefficient, but also to measure up to a suitable maximum value of the flow time to perform an optimum extrapolation to the vanishing flow-time limit.

5.4.2 The connected part of the chiral susceptibility $\chi_f^{\mathbf{conn}}$

Next, we show the connected part of the chiral susceptibility. Flow-time dependence of connected part of the chiral susceptibilities are shown in Figs. 5.4 and 5.5. Compared to the those with μ_d-scale (see, Figs. B.5 and B.6 in Appendix B.1.3), steep curvature shown in the μ_d-scale analysis become milder in the μ_0-scale and we obtain longer linear windows in which the flow-time dependence looks well linear.

Temperature dependence of connected the chiral susceptibilities are summarized in the middle columns of Tables 5.2 and 5.3 and in Fig 5.5. As expected from other studies [10,11], no singular behavior is visible within the range of temperature we measured. On the other hand, our results increase monotonically as temperature increase. This behavior is quite different from other studies. However, as mentioned in previous work [23], measurement on $N_t = 8$ would suffer from the lattice artifact $O(a^2T^2)$. Thus, the the

[2] Even though we measured up to $t/a^2 = 6.0$, the maximum value for linear window is bounded by $t_{1/2}$.

Table 5.2: Results for the chiral susceptibility for ud quarks by SFtX method c All values are in lattice unit. The first parenthesis is for the statistical error. The second parenthesis is for the systematic error due to the fit ansatz using nonlinear and linear+log fits.

T [MeV]	$a^6\chi_{ud}^{\rm disc} \times 10^8$	$a^6\chi_{ud}^{\rm conn} \times 10^8$	$a^6\chi_{ud}^{\rm full} \times 10^8$
174	$0.94(28)(^{32}_{32})$	$4.91(52)(^{2.59}_{2.62})$	$5.85(67)(^{3.03}_{3.06})$
199	$2.63(80)(^{82}_{84})$	$6.35(68)(^{3.41}_{3.40})$	$9.3(1.13)(^{4.42}_{4.46})$
232	$0.71(19)(^{21}_{21})$	$8.20(81)(^{3.59}_{3.56})$	$9.23(75)(^{3.71}_{3.66})$
279	$0.46(5)(^{15}_{17})$	$11.25(23)(^{3.39}_{3.28})$	$11.62(26)(^{3.53}_{3.42})$
348	$0.51(9)(^{16}_{24})$	$17.41(49)(^{4.27}_{4.93})$	$17.81(56)(^{4.43}_{5.12})$

Table 5.3: The same as Table 5.2 but for s quark.

T [MeV]	$a^6\chi_{s}^{\rm disc} \times 10^8$	$a^6\chi_{s}^{\rm conn} \times 10^8$	$a^6\chi_{s}^{\rm full} \times 10^8$
174	$0.51(16)(^{19}_{19})$	$4.15(42)(^{2.30}_{2.35})$	$4.56(53)(^{2.62}_{2.67})$
199	$1.54(53)(^{55}_{55})$	$5.41(56)(^{2.99}_{2.99})$	$7.16(85)(^{3.72}_{3.74})$
232	$0.48(15)(^{20}_{19})$	$7.40(26)(^{3.43}_{3.46})$	$7.75(2.6)(^{3.73}_{3.75})$
279	$0.40(5)(^{15}_{15})$	$10.25(21)(^{3.21}_{3.09})$	$10.84(22)(^{3.35}_{3.24})$
348	$0.53(10)(^{16}_{24})$	$16.87(47)(^{4.13}_{4.78})$	$17.28(55)(^{4.29}_{4.96})$

increasing property of our result may the unphysical effect from lattice artifact. To confirm this effect, we need take continuum limit to verify this behavior.

Note here that the vertical scale of the plots are different from those for the disconnected chiral susceptibility. The amplitude of connected part is ten times larger than the disconnected chiral susceptibility expect for the peak in the disconnected chiral susceptibility.

5.4.3 The full chiral susceptibility $\chi_f^{\rm full}$

So far, we have shown the disconnected and the connected chiral susceptibility. Combining these component, we obtain the full chiral susceptibility. In Figs. 5.7, and 5.8, results of the full chiral susceptibilities are shown as a function of flow-time. By virtue of the new adopted scale μ_0, the flow-time dependences are significantly improved and we can take wider linear window than the μ_d-scale discussed in Appendix B.1.1.

Results of the temperature dependence of the full chiral susceptibilities are summarized in the last columns of Tables 5.2 and 5.3 and in Fig. 5.9. The full chiral susceptibility have no singular behavior within the errors even though disconnected part have the a clear peak at $T \sim 199$ MeV. The full chiral susceptibility is increase monotonically with slight bump at $T \sim 199$ MeV.

As noted before, the connected part contribution is typically larger than those of disconnected part. The peak structure of the disconnected chiral susceptibility is smeared by the large nonsingular behavior of the connected part. In the physical point, preliminary result of the disconnected chiral susceptibility is reported in [39] and it is reported that the peak hight is ten times larger than our result. This imply that the in the lighter ud quarks, the full chiral susceptibility may have a peak at the transition temperature. Physical point simulation needed to conform this suggestion is a future work.

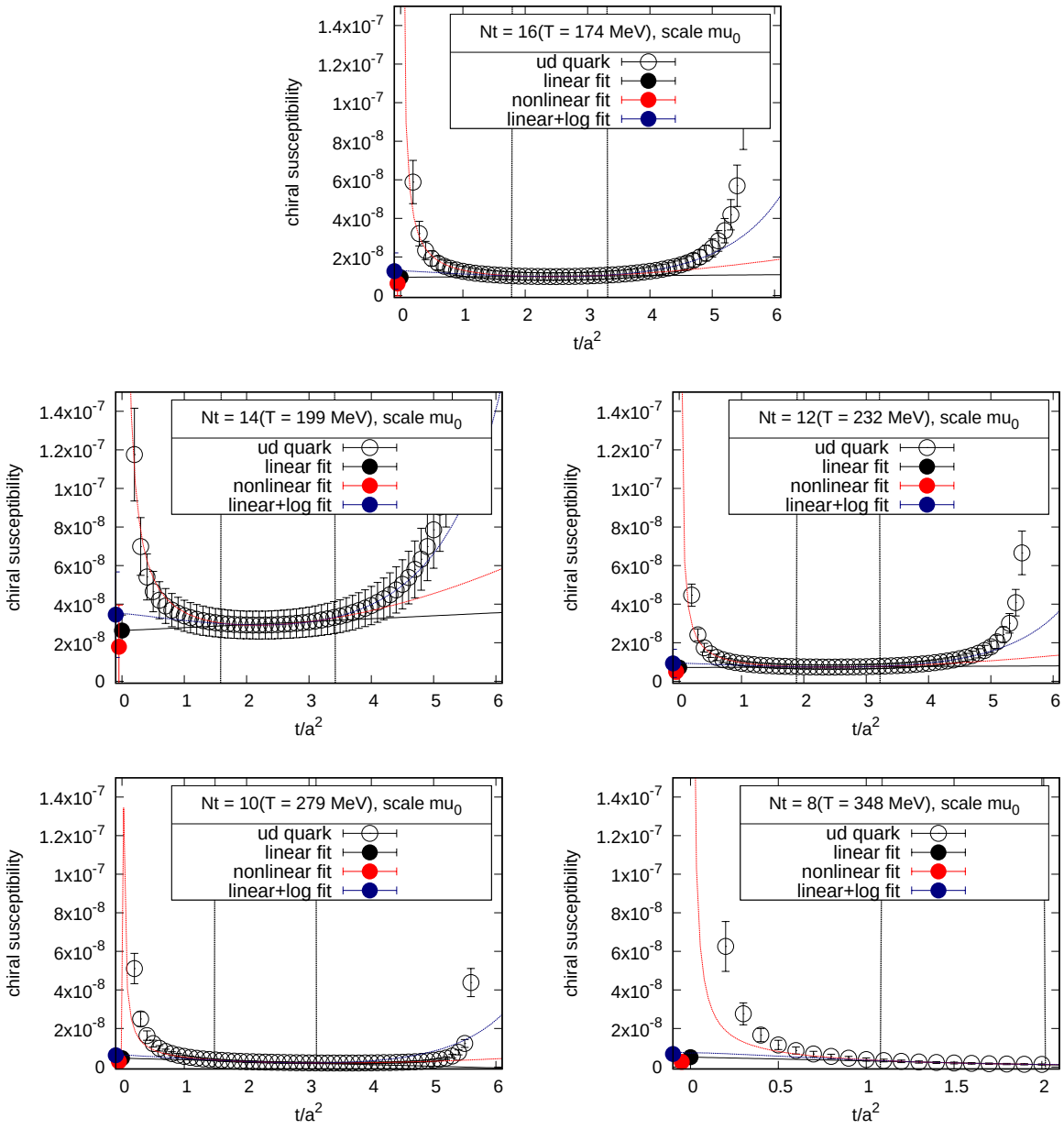

Figure 5.1: The disconnected chiral susceptibility for ud quark $\chi_{ud}^{\rm disc}$ with μ_0-scale as function of the flow-time. The vertical axis is in lattice unit. The dashed vertical lines indicates the linear window used for the fits at each T. Black solid lines are the fit results of the linear fit and filled circles at $t = 0$ are the full chiral susceptibility extracted from the fits. Red and blue dashed lines and filled circle at $t \sim 0$ are the fit results of nonlinear fit (5.7) and linear+log fit (5.8), respectively.

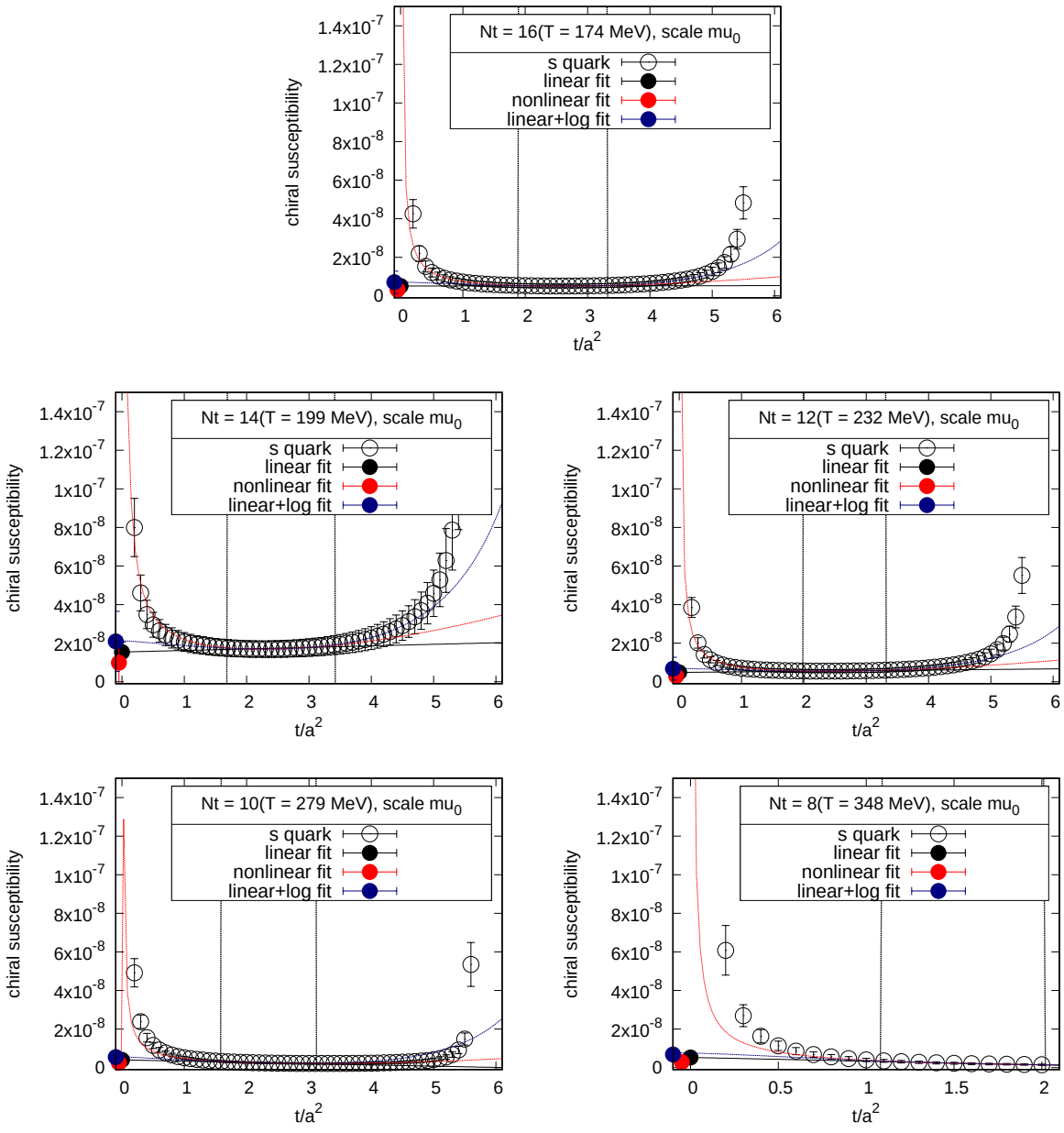

Figure 5.2: The same as 5.1 but for s quark χ_s^{disc}.

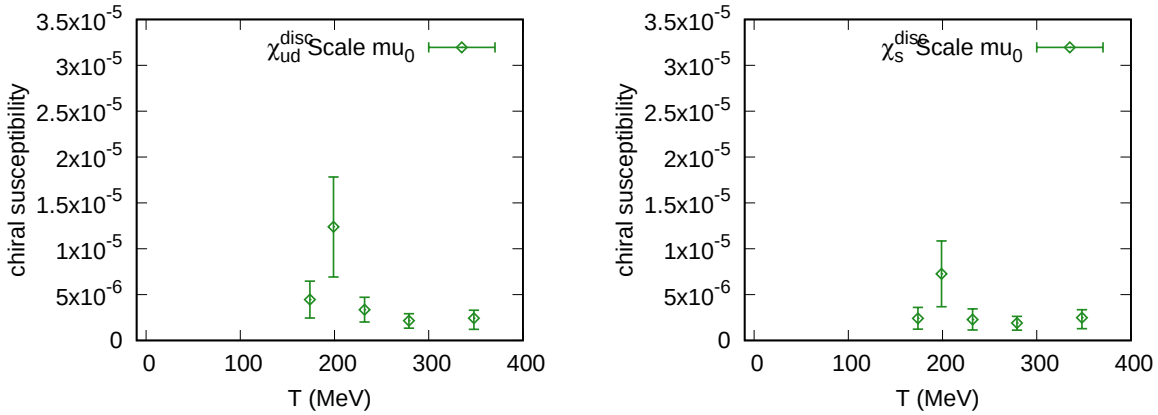

Figure 5.3: Results of the disconnected chiral susceptibility for ud quark (**Left**) and s quark (**Right**) as function of temperature. The vertical axis is in unit of GeV^6.

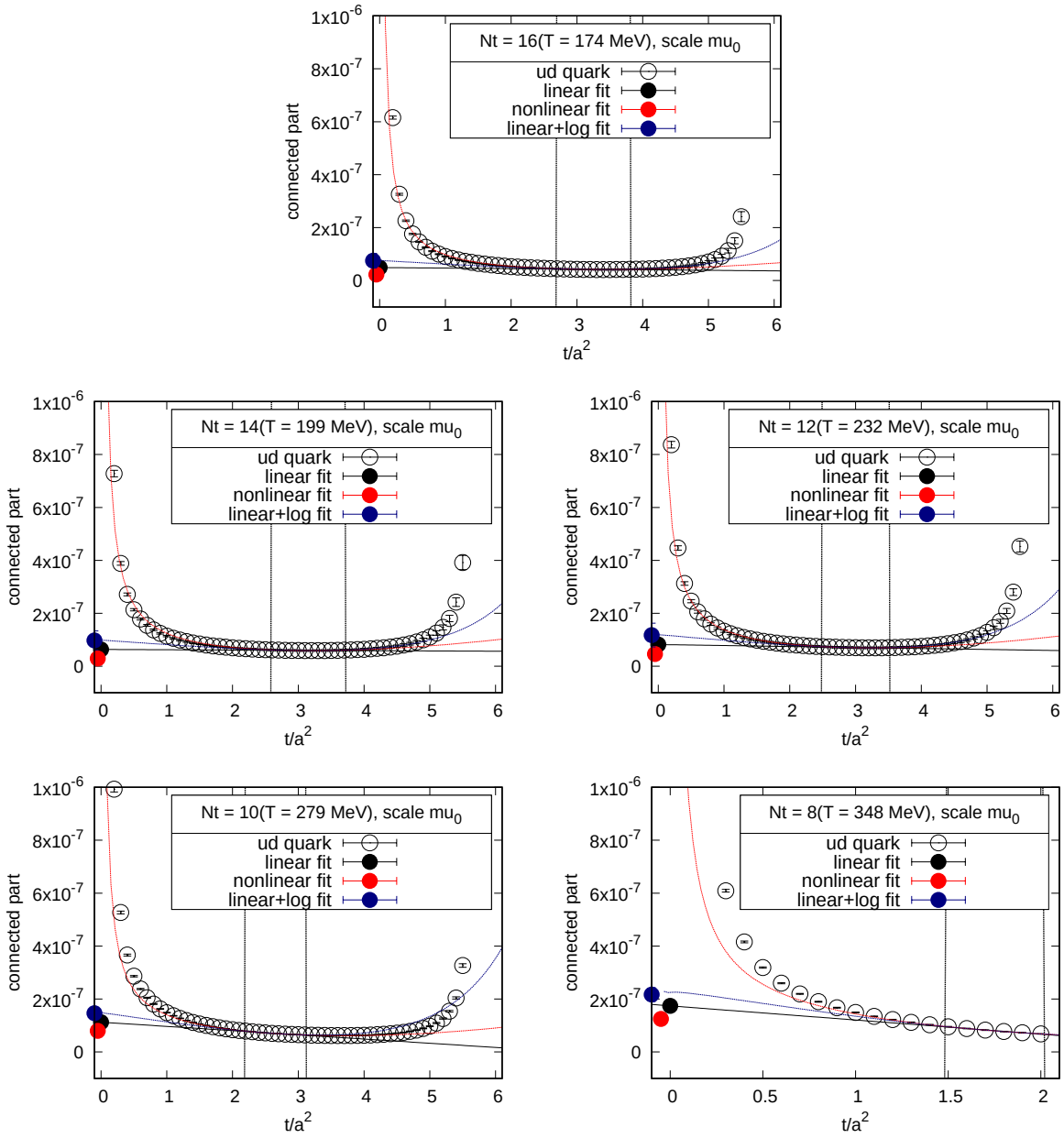

Figure 5.4: Connected part of the chiral susceptibility for ud quark $\chi_{ud}^{\rm conn}$ with μ_0-scale as function of the flow-time. The vertical axis is in lattice unit. The dashed vertical lines indicates the linear window used for the fits at each T. Black solid lines are the fit results of the linear fit and filled circles at $t = 0$ are the full chiral susceptibility extracted from the fits. Red and blue dashed lines and filled circle at $t \sim 0$ are the fit results of nonlinear fit (5.7) and linear+log fit (5.8), respectively.

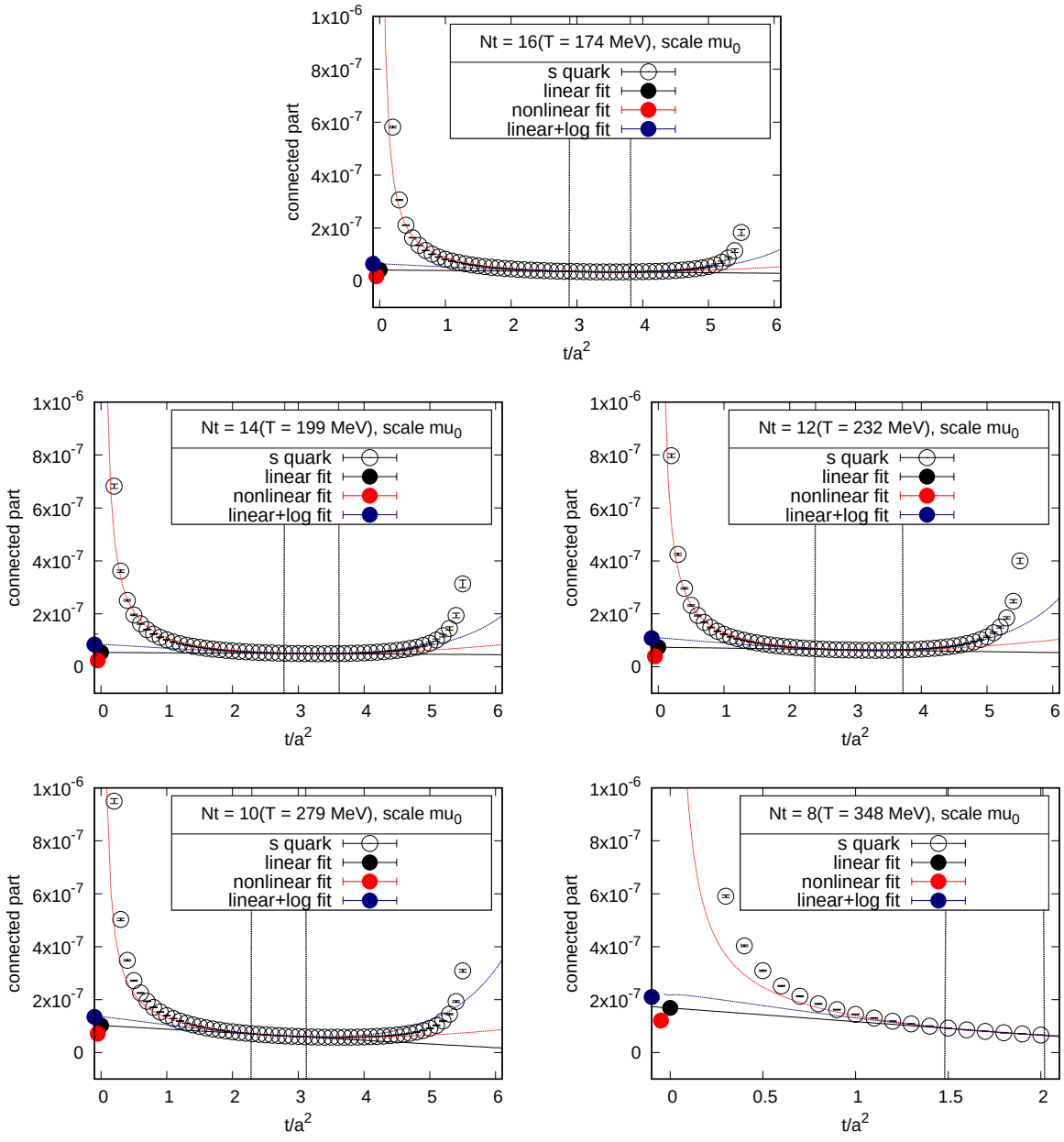

Figure 5.5: The same as 5.4 but for s quark χ_s^{conn}.

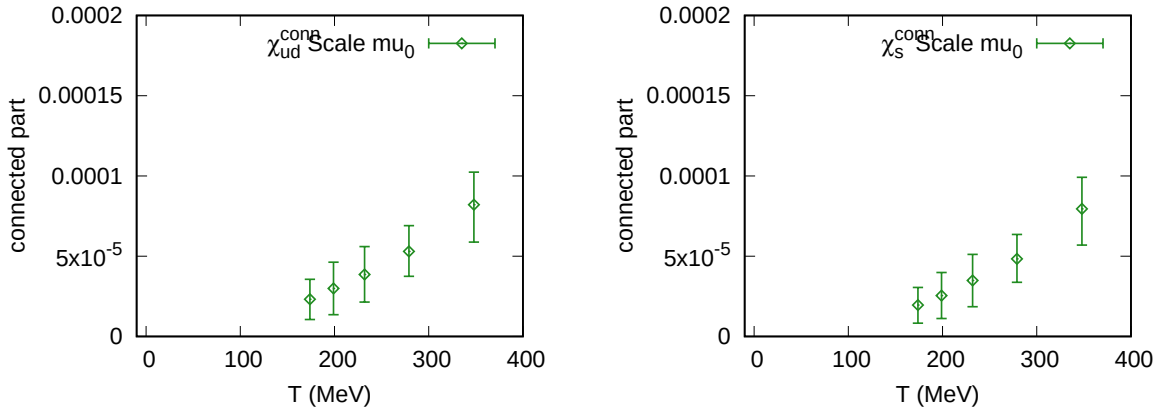

Figure 5.6: Results of connected part of the chiral susceptibility for *ud* quark (**Left**) and *s* quark (**Right**) as function of temperature. The vertical axis is in unit of GeV^6.

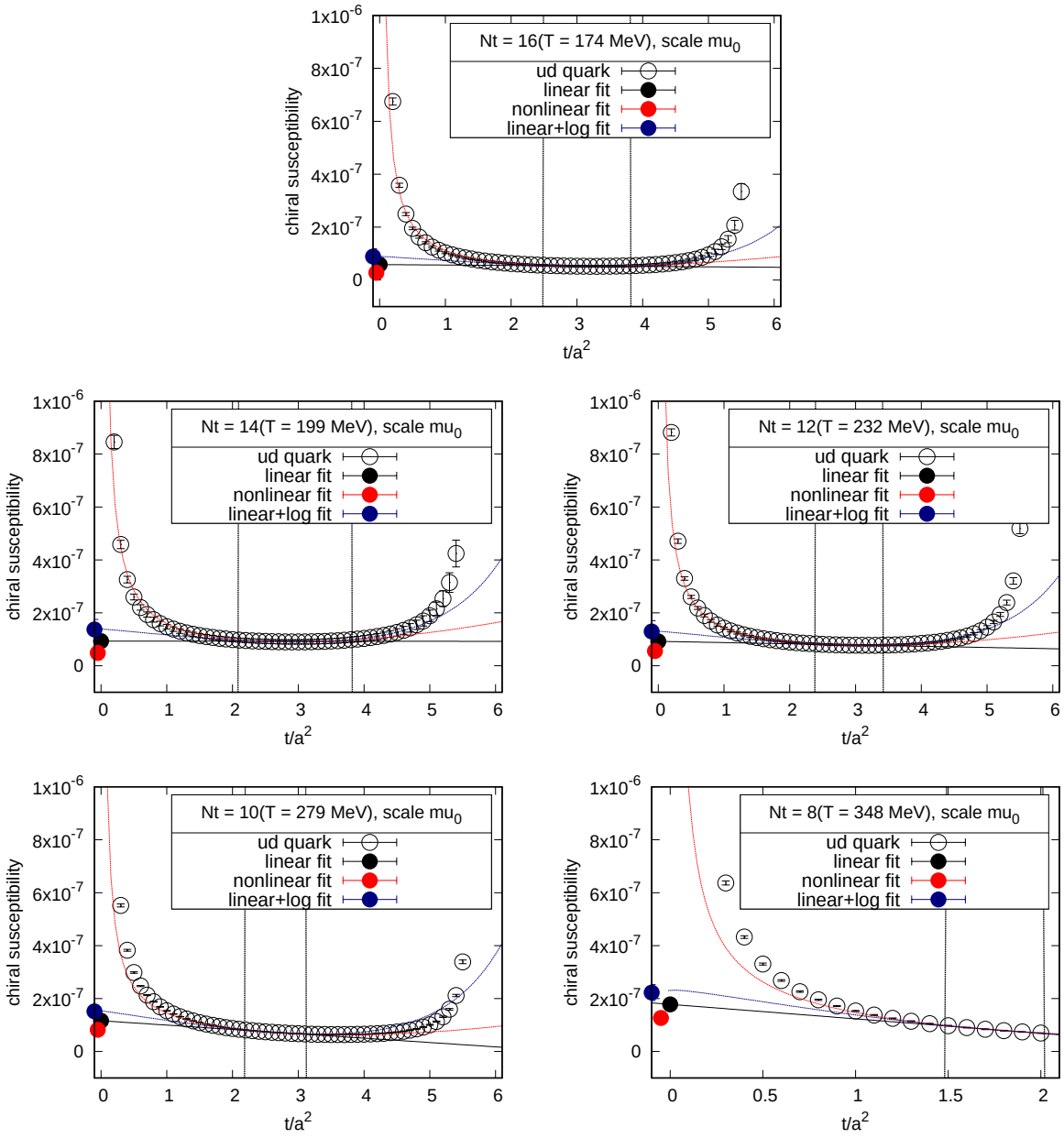

Figure 5.7: The full chiral susceptibility for ud quark χ_{ud}^{full} with μ_0-scale as function of the flow-time. The vertical axis is in lattice unit. The dashed vertical lines indicates the linear window used for the fits at each T. Black solid lines are the fit results of the linear fit and filled circles at $t = 0$ are the full chiral susceptibility extracted from the fits. Red and blue dashed lines and filled circle at $t \sim 0$ are the fit results of nonlinear fit (5.7) and linear+log fit (5.8), respectively.

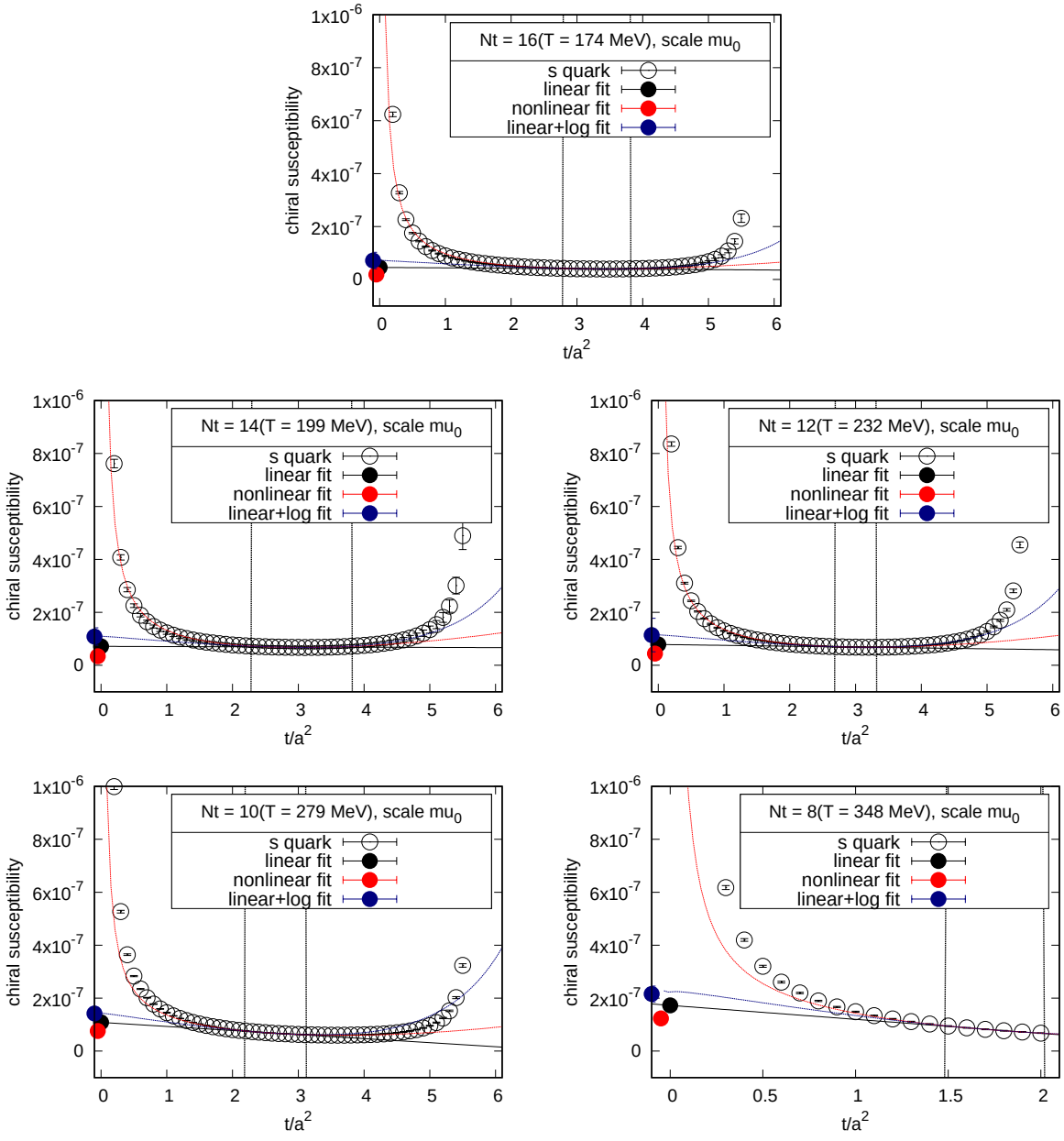

Figure 5.8: The same as Fig. 5.7 but for s quark $\chi_s^{\rm full}$.

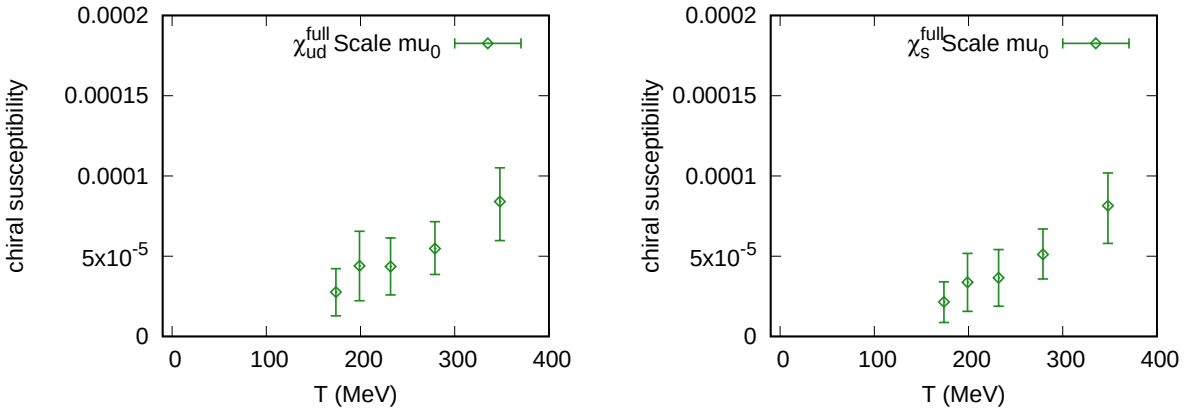

Figure 5.9: Results of the full chiral susceptibility for *ud* quark (**Left**) and *s* quark (**Right**) as function of temperature. The vertical axis is in unit of GeV^6.

5.5 The $U(1)_A$ susceptibility

In this section, we show the numerical results of $\chi^{\pi-\delta}$ as the $U(1)_A$ susceptibility adopting the μ_0-scale. In Fig. 5.10, results of the $U(1)_A$ susceptibility as a function of flow-time is shown. The pair of dashed vertical lines indicates the linear window we choose. As shown in Appendix B.2, flow-time dependence of the $U(1)_A$ susceptibility with the μ_d-scale shows well linear behavior like the disconnected chiral susceptibility, however, that with μ_0-scale shows wider linear windows and thus lesser systematic errors, especially at low temperatures $N_t = 16, 18$. The employed cut-offs and corresponding linear windows are listed at Appendix C.1.

Temperature dependence of the $U(1)_A$ susceptibility is sumamrized in the Table 5.4 and in Fig. 5.11. Green diamond indicates the $U(1)_A$ susceptibility $\chi^{\pi-\delta}/T^2$ and black triangle denotes the topological susceptibility obtained previously on the same configurations using gradient flow method as a smearing procedure [31]. The $U(1)_A$ symmetry seems to be restored at very high temperatures

Above the transition temperature, the $U(1)_A$ susceptibility $\chi^{\pi-\delta}/T^2$ and the topological susceptibility $\chi_{\rm t}/m_{ud}^2T^2$ show good agreement. Though this agreement is justified only in the limit $m \to 0$ and $T \to \infty$, our results at finite quark masses show good consistency at $T \geq T_{pc}$.

In Fig. 5.12, we compare the our results with the same quantity measured by other group with the domain-wall fermion at $m_\pi \sim 200$ MeV [40]. In the previous study [13], it is indicated that the quark mass dependence of the $U(1)_A$ susceptibility vanishes at high temperatures. In this study, our result seems consistent with the previous one. However, no concrete evidence obtained due to the slight overlap of the temperature ranges.

Table 5.4: Results for the $U(1)_A$ susceptibility $\chi^{\pi-\delta}/T^2$ by SFtX method with the mu_0-scale. The first parenthesis is for the statistical error. The second parenthesis is for the systematic error due to the fit ansatz using nonlinear and linear+log fits.

T [MeV]	$\chi^{\pi-\delta}/T^2$
174	$9.52(74)(^{2.35}_{2.38})$
199	$4.16(95)(^{1.23}_{1.19})$
232	$1.44(40)(^{45}_{46})$
279	$0.28(2)(^{9}_{9})$
348	$0.19(3)(^{5}_{6})$

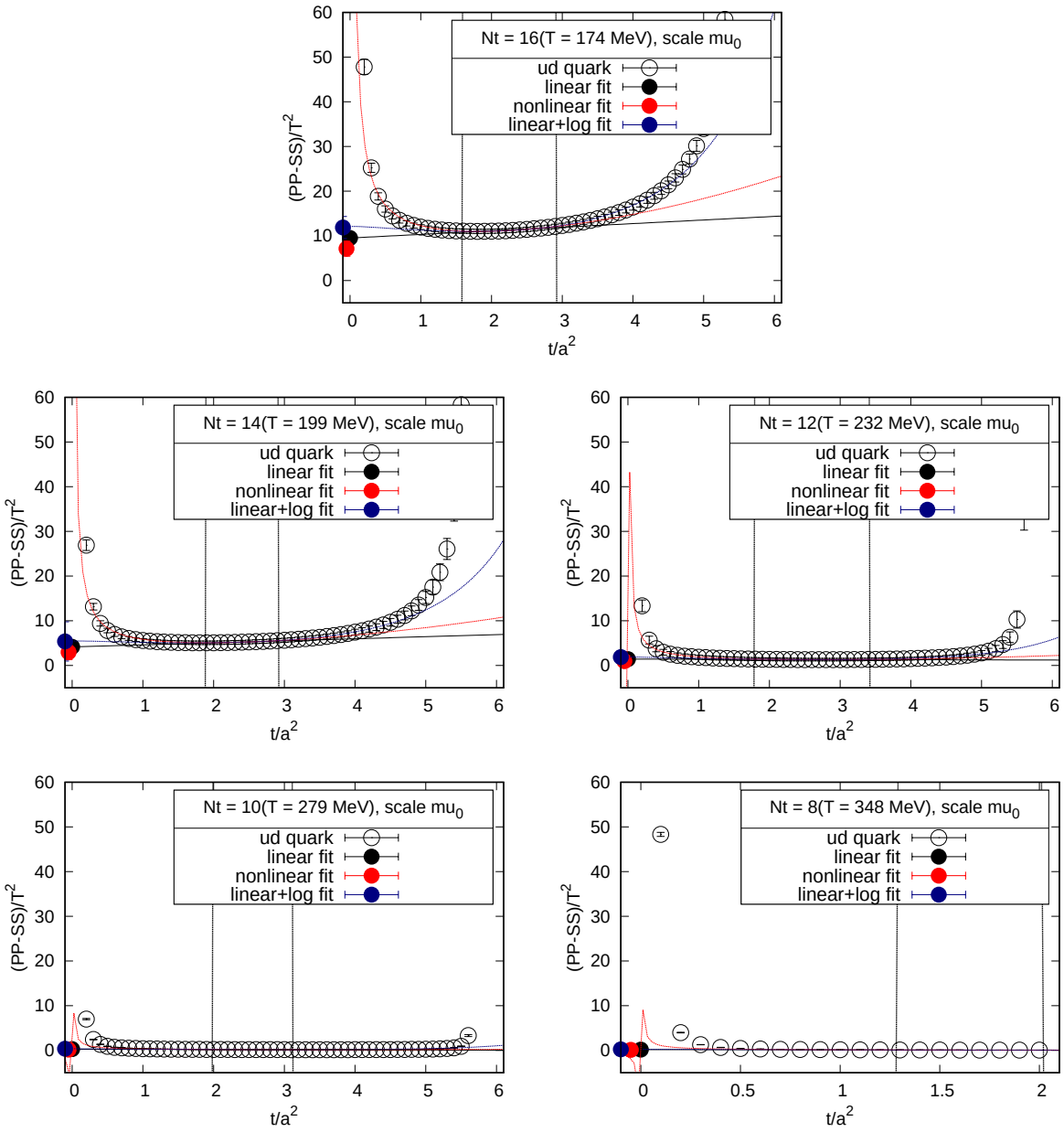

Figure 5.10: The $U(1)_A$ susceptibility $\chi^{\pi-\delta}/T^2$ with μ_0-scale as function of the flow-time. The dashed vertical lines indicates the linear window used for the fits at each T. Black solid lines are the fit results of the linear fit and filled circles at $t = 0$ are the full chiral susceptibility extracted from the fits. Red and blue dashed lines and filled circle at $t \sim 0$ are the fit results of nonlinear fit (5.7) and linear+log fit (5.8), respectively.

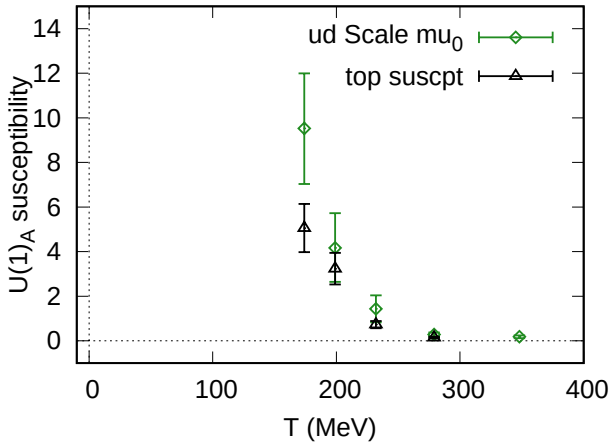

Figure 5.11: Results of the $U(1)_A$ susceptibility $\chi^{\pi-\delta}/T^2$ with μ_0-scale as function of the temperature. Green diamond denotes the $U(1)_A$ susceptibility. Black triangle denotes the topological susceptibility χ_t/T^2 measured in [31].

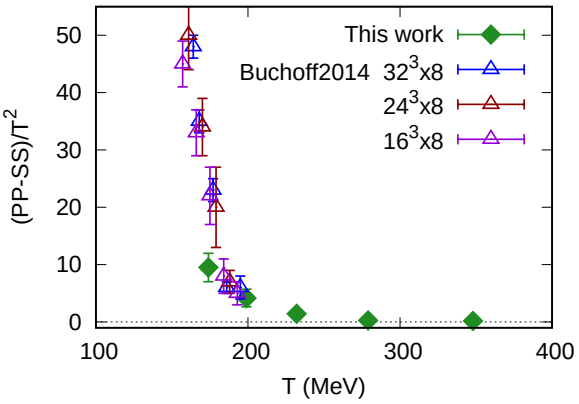

Figure 5.12: The $U(1)_A$ susceptibility as a function of temperature. Green diamond denotes our result and triangles are those measured in [40].

Chapter 6

Summery and Outlook

In this thesis, I present results of chiral susceptibility and the $U(1)_A$ susceptibility in finite temperature lattice QCD with $(2+1)$-flavor Wilson-type quarks using small flow-time expansion method based on gradient flow. On our simulation point, degenerate heavy u and d quarks and almost physical s quark at a fine lattice spacing $a \sim 0.07$ fm. Exploring the QCD phase structure is the one of the most important problem in QCD and has been studied for a long time. At finite temperature, it is considered that the phase transition between the high- and low-temperature phase, called QGP and hadronic phase, is chiral phase transition. At the same time, it is said that the $U(1)_A$ symmetry, broken by anomaly at zero temperature, is effectively restored at very high temperatures. The degree of $U(1)_A$ symmetry breaking has interesting physical consequences both in theoretical and phenomenological view point.

For the chiral susceptibility, we measure not only the disconnected part but also the connected part to evaluate the full chiral susceptibility. Though the disconnected chiral susceptibility shows a pronounced peak, the connected part shows no singular behavior. These behaviors are consistent with previous studies. Moreover, the connected part turned out to be about typically ten times larger than the disconnected part. As a result, the full chiral susceptibilities have no pronounced peak within errors though the slight bump is seen at $T \sim 199$ MeV. This is different from previous works. In Ref. [39], the preliminary result of disconnected chiral susceptibility at the physical point has shown that this difference is owing to the heavy u and d quark mass. The peak height of the disconnected chiral susceptibility at the physical point is reported to be much higher than that of ours.

We also measure $\chi^{\pi-\delta}$ as the $U(1)_A$ susceptibility. Previous studies of the $U(1)_A$ susceptibility require a chiral symmetry preserving formulation of quarks because they are very sensitive to the chiral symmetry breaking due to lattice quarks. We attack this problem by using SFtX method. We found that anomalous $U(1)_A$ symmetry breaking would be effectively restored at very high temperature. We compared our result with the topological susceptibility measured on the same configuration. They are expected to coincide in the limit of the vanishing quark mass and high temperatures. Our results shows a good agreement above T_{pc} even with finite quark masses. We also compared our results with those from other group [40] which measured with the domain-wall fermion at $m_\pi \sim 200$ MeV. Our measurements are performed on the temperature range $T \simeq 174$–348 MeV, while in the Ref. [40], the measurements are on the temperature range of $T \simeq 139$–195 MeV. In the previous study [13], it is indicated that quark mass dependence of $U(1)_A$ susceptibility vanishes in high temperatures. The agreement between our measurement and that from other groiup [40] seems to start around $T \sim 199$ MeV, which is above the transition temperature of our simulation point. These results indicate that the SFtX method provides the good chiral property equivalent to the domain-wall fermion even with the Wilson-type quarks.

acknowledgements

I would like to thank Prof. Yoshinobu Kuramashi for his encouragement. I am also grateful to all the members of WHOT-QCD Collaboration, Professor Kazuyuki Kanaya, Professor Hiroshi Suzuki, Associate Professor Yusuke Taniguchi, Associate Professor Shinji Ejiri, Associate Professor Takashi Umeda, Assistant Professor Masakiyo Kitazawa, and Dr. Asobu Suzuki for their helpful discussion. Finally, I would thank to all staffs and students of Particle Theory Group of the University of Tsukuba.

This research used computational resources of COMA, Oakforest-PACS, and Cygnus provided by the Interdisciplinary Computational Science Program of Center for Computational Sciences, University of Tsukuba, K and other computers of JHPCN through the HPCI System Research Projects (Project ID: hp17208, hp190028, hp190036) and JHPCN projects (jh190003, jh190063), OCTOPUS at Cybermedia Center, Osaka University, and ITO at R.I.I.T., Kyushu University. The simulations were in part based on the lattice QCD code set Bridge++ [41].

Appendix A

Running coupling and running mass

In the matching coefficients of the SFtX method, we need to use the running coupling $\bar{g}(\mu)$ and the running mass $\bar{m}(\mu)$, where μ is the renormalization scale. The renormalization group invariant scale Λ, so called the Lambda parameter, is defined as

$$\frac{\Lambda}{\mu} = \left[b_0\bar{g}^2(\mu)\right]^{-b_1/2b_0^2} \exp\left[-\frac{1}{2b_0\bar{g}^2(\mu)}\right] \cdot \exp\left\{-\int_0^{\bar{g}(\mu)} \mathrm{d}g \left[\frac{1}{\beta(g)} + \frac{1}{b_0 g^3} - \frac{b_1}{b_0^2 g}\right]\right\}, \tag{A.1}$$

while the running mass and the RG invariant mass M are related by

$$\bar{m}(\mu) = M\left[2b_0\bar{g}^2(\mu)\right]^{d_0/2b_0} \exp\left\{\int_0^{\bar{g}(\mu)} \mathrm{d}g \left[\frac{\tau(g)}{\beta(g)} - \frac{d_0}{b_0 g}\right]\right\}. \tag{A.2}$$

The renormalization group functions, $\beta(g)$ and $\tau(g)$, are known to the five-loop order in MS or $\overline{\mathrm{MS}}$ scheme.For the $SU(N)$ gauge theory with N_f flavor fundamental fermions, setting

$$\beta(g) = -g^3 \sum_{k=0}^{\infty} b_k g^{2k}, \tag{A.3}$$

$$\tau(g) = -g^2 \sum_{k=0}^{\infty} d_k g^{2k}, \tag{A.4}$$

the first two coefficients are given by [42, 43]

$$b_0 = \frac{1}{(4\pi)^2}\left(\frac{11}{3}N - \frac{2}{3}N_f\right), \tag{A.5}$$

$$b_1 = \frac{1}{(4\pi)^4}\left[\frac{34}{3}N^2 - \left(\frac{13}{3}N - N^{-1}\right)N_f\right], \tag{A.6}$$

and [44, 45]

$$d_0 = \frac{3}{(4\pi)^2}\left(N - N^{-1}\right), \tag{A.7}$$

$$d_1 = \frac{1}{(4\pi)^4}\left(N - N^{-1}\right)\left(\frac{203}{12}N - \frac{3}{4}N^{-1} - \frac{5}{3}N_f\right). \tag{A.8}$$

For higher orders ($k \geq 2$), setting

$$b_k = \frac{1}{(4\pi)^{2k+2}} \sum_{l=0}^{k} b_{k,l} N_f^l, \tag{A.9}$$

$$d_k = \frac{1}{(4\pi)^{2k+2}}\left(N - N^{-1}\right) \sum_{l=0}^{k} d_{k,l} N_f^l, \tag{A.10}$$

we have [46–50]

$$b_{2,0} = \frac{2857}{54}N^3, \tag{A.11}$$
$$b_{2,1} = -\frac{1709}{54}N^2 + \frac{187}{36} + \frac{1}{4}N^{-2}, \tag{A.12}$$
$$b_{2,2} = \frac{56}{27}N - \frac{11}{18}N^{-1}, \tag{A.13}$$
$$b_{3,0} = \frac{150473}{486}N^4 - \frac{40}{3}N^2 + \frac{44}{9}\zeta(3)N^4 + 352\zeta(3)N^2, \tag{A.14}$$
$$b_{3,1} = -\frac{485513}{1944}N^3 + \frac{58583}{1944}N - \frac{2341}{216}N^{-1} - \frac{23}{8}N^{-3} - \frac{20}{9}\zeta(3)N^3 - \frac{548}{9}\zeta(3)N + \frac{44}{9}\zeta(3)N^{-1}, \tag{A.15}$$
$$b_{3,2} = \frac{8654}{243}N^2 - \frac{2477}{243} - \frac{623}{54}N^{-2} + \frac{28}{3}\zeta(3)N^2 - \frac{64}{9}\zeta(3) + \frac{244}{9}\zeta(3)N^{-2}, \tag{A.16}$$
$$b_{3,3} = \frac{130}{243}N - \frac{77}{243}N^{-1}, \tag{A.17}$$
$$\tag{A.18}$$

and [51–56]

$$d_{2,0} = \frac{11413}{108}N^2 - \frac{129}{8} + \frac{129}{8}N^{-2}, \tag{A.19}$$
$$d_{2,1} = -\frac{1177}{54}N + \frac{23}{2}N^{-1} - 12\zeta(3)N - 12\zeta(3)N^{-1}, \tag{A.20}$$
$$d_{2,2} = -\frac{35}{27}, \tag{A.21}$$
$$\begin{aligned} d_{3,0} = {} & \frac{460151}{576}N^3 - \frac{66577}{576}N + \frac{50047}{192}N^{-1} + \frac{1261}{64}N^{-3} \\ & + \frac{1157}{9}\zeta(3)N^3 + 104\zeta(3)N - 47\zeta(3)N^{-1} + 42\zeta(3)N^{-3} \\ & - 220\zeta(5)N^3 - 220\zeta(5)N, \end{aligned} \tag{A.22}$$
$$\begin{aligned} d_{3,1} = {} & -\frac{23816}{81}N^2 + \frac{10475}{108} + \frac{37}{3}N^{-2} \\ & - \frac{889}{3}\zeta(3)N^2 - 170\zeta(3) - 111\zeta(3)N^{-2} + 66\zeta(4)N^2 + 66\zeta(4) \\ & + 160\zeta(5)N^2 + 100\zeta(5) - 60\zeta(5)N^{-2}, \end{aligned} \tag{A.23}$$
$$d_{3,2} = \frac{899}{162}N - \frac{38}{27}N^{-1} + 20\zeta(3)N + 20\zeta(3)N^{-1} - 12\zeta(4)N - 12\zeta(4)N^{-1}, \tag{A.24}$$
$$d_{3,3} = -\frac{83}{81} + \frac{16}{9}\zeta(3). \tag{A.25}$$
$$\tag{A.26}$$

For $(2+1)$-flavor QCD, $N = 3$ and $N_f = 3$, we have

$$b_0 = \frac{1}{(4\pi)^2}\,9, \tag{A.27}$$
$$b_1 = \frac{1}{(4\pi)^4}\,64, \tag{A.28}$$
$$b_2 = \frac{1}{(4\pi)^6}\frac{3863}{6}, \tag{A.29}$$
$$b_3 = \frac{1}{(4\pi)^8}\left[3560\zeta(3) + \frac{140599}{18}\right], \tag{A.30}$$

$$b_4 = \frac{1}{(4\pi)^{10}}\left[\frac{139857733}{1296} - \frac{801}{2}\pi^4 + \frac{11059213}{54}\zeta(3) - \frac{534385}{3}\zeta(5)\right] \tag{A.31}$$

and

$$d_0 = \frac{1}{(4\pi)^2}\,8, \tag{A.32}$$

$$d_1 = \frac{1}{(4\pi)^4}\frac{364}{3}, \tag{A.33}$$

$$d_2 = \frac{1}{(4\pi)^6}\left[\frac{17770}{9} - 320\zeta(3)\right], \tag{A.34}$$

$$d_3 = \frac{1}{(4\pi)^8}\left[-\frac{297440}{27}\zeta(3) - \frac{16000}{3}\zeta(5) + 48\pi^4 + \frac{2977517}{81}\right]. \tag{A.35}$$

$$d_4 = \frac{1}{(4\pi)^{10}}\left[\frac{156509815}{486} + \frac{9506}{9}\pi^4 + \frac{4000}{63}\pi^6 - \frac{47327494}{243}\zeta(3) + 87040\zeta^2(3) - \frac{90501860}{243}\zeta(5) + \frac{3031168}{9}\zeta(7)\right] \tag{A.36}$$

Appendix B

Numerical Results of μ_d-Scale

In this chapter, we show the numerical results of μ_d-scale. We show only the flow-time dependence of chiral and $U(1)_A$ susceptibilities. The cu-off values are listed in the Appendix C.1.

B.1 The Chiral susceptibility

B.1.1 The full chiral susceptibility $\chi_f^{\mathbf{full}}$

The flow-time dependence of full chiral susceptibility with μ_d-scale has a tight curve even at the linear window for all temperatures. This leads to ambiguous $t \to 0$ extrapolation. Furthermore, we obtain the large systematic errors due to the unstable nonlinear fits. In this thesis, we overcome this problem by adopting the μ_0-scale. This scale provide a longer and more stable linear window than μ_d-scale as shown in Chap. 5.

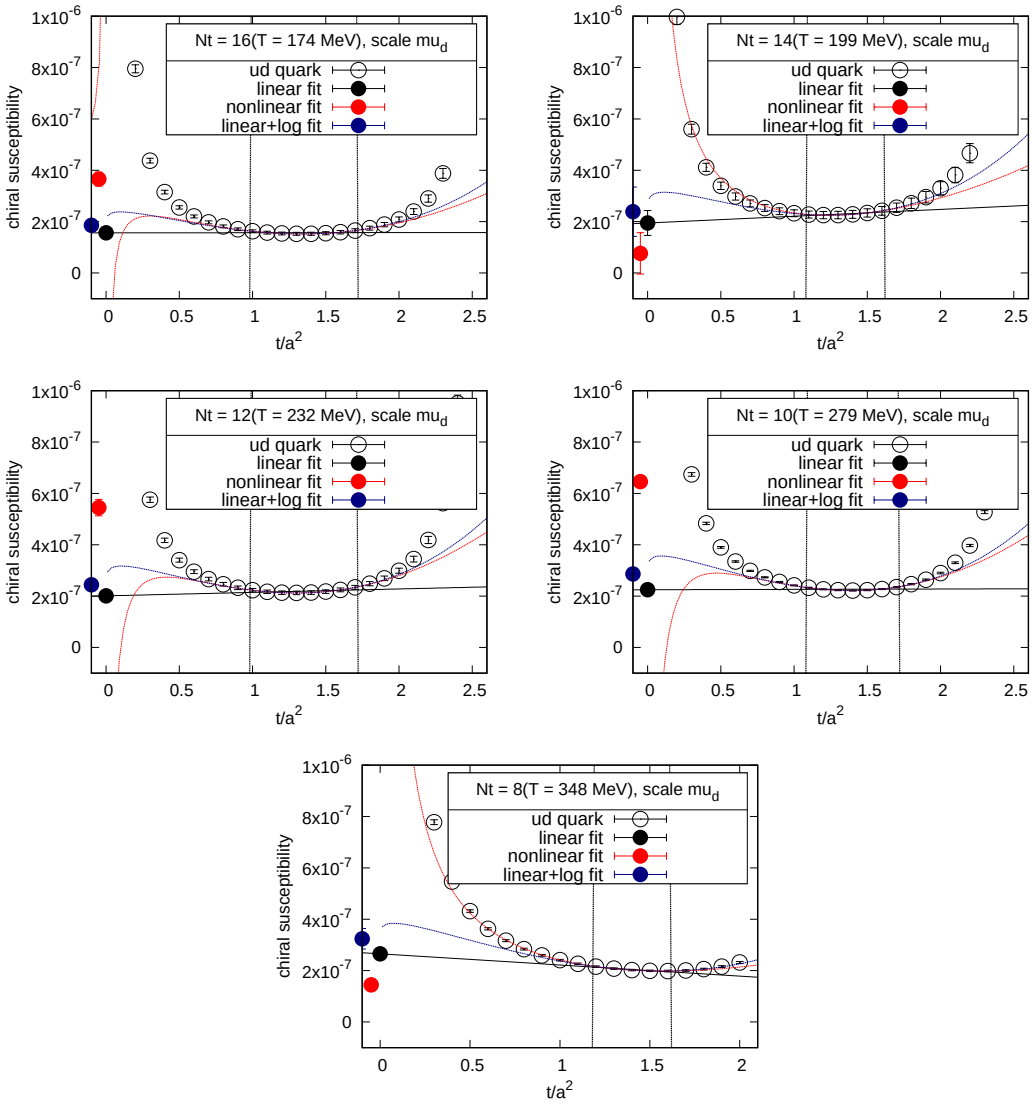

Figure B.1: The full chiral susceptibility for ud quark χ_{ud}^{full} with μ_D-scale as function of the flow-time. The vertical axis is in lattice unit.

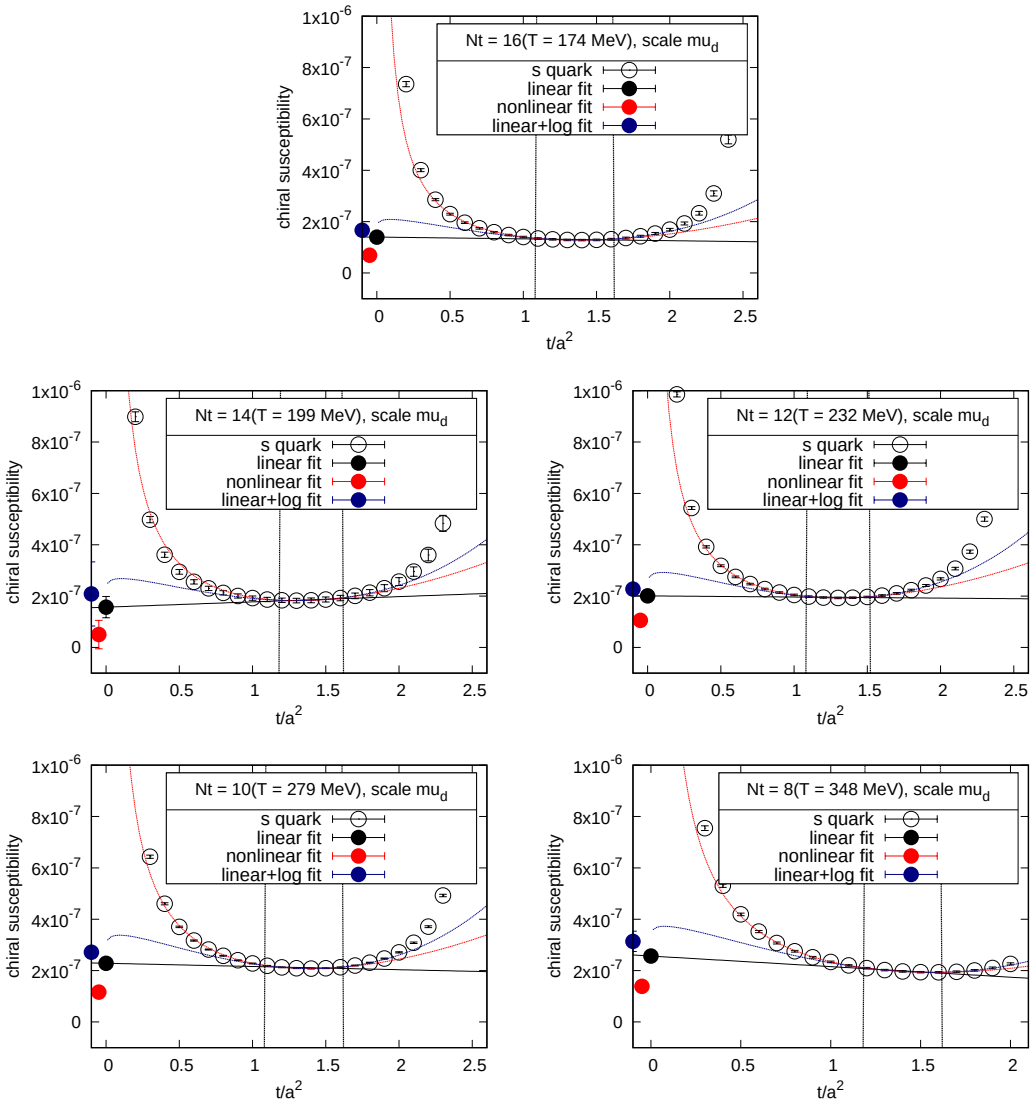

Figure B.2: The full chiral susceptibility for s quark χ_s^{full} with μ_d-scale as function of the flow-time. The vertical axis is in lattice unit.

B.1.2 The disconnected chiral susceptibility $\chi_f^{\mathbf{disc}}$

The disconnected chiral susceptibility with μ_d-scale also is studied in Ref. [23]. In this study, we also obtain the flat linear window for the disconnected chiral susceptibility even though the strategy for choosing the linear window is different from each other.

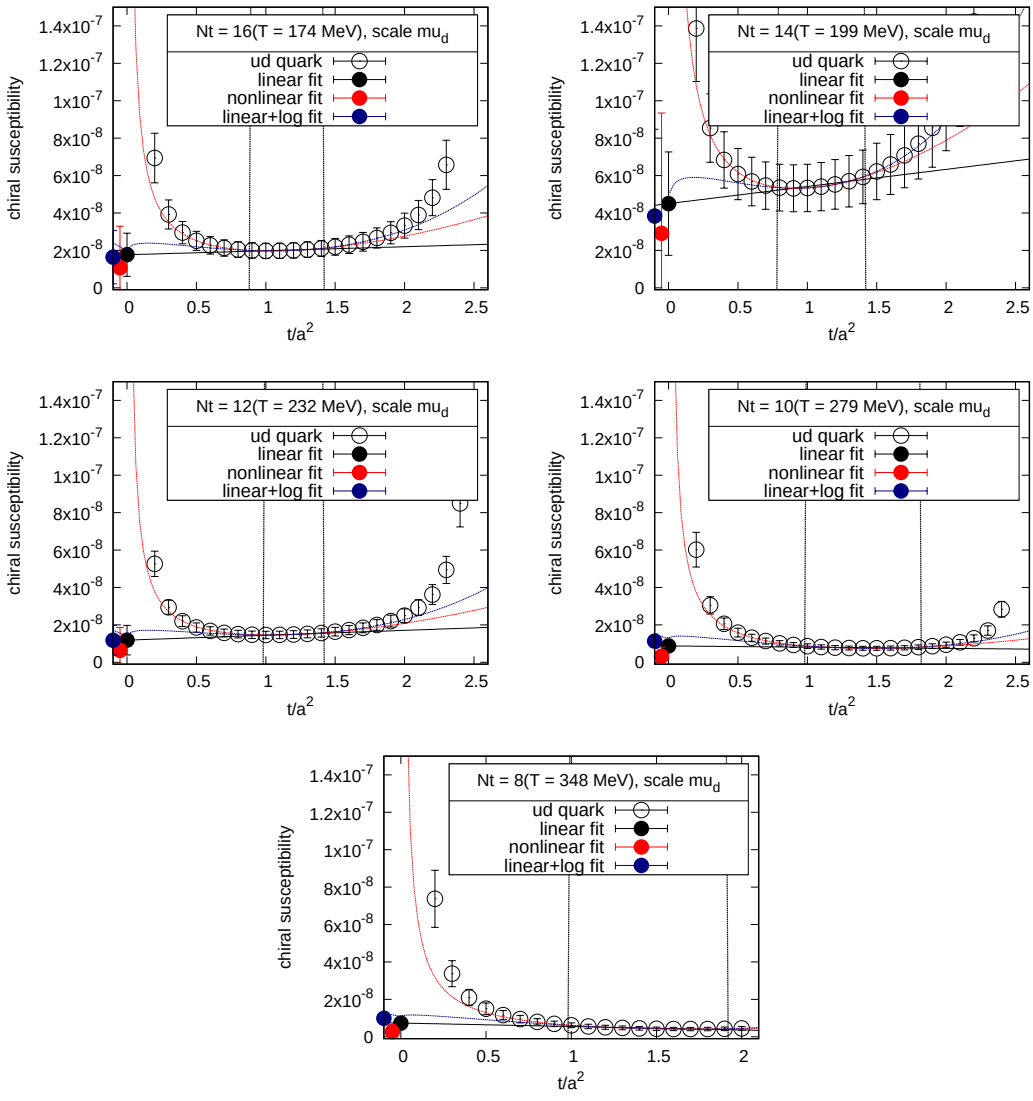

Figure B.3: The disocnnected chiral susceptibility for ud quark $\chi_{ud}^{\rm disc}$ with μ_D-scale as function of the flow-time. The vertical axis is in lattice unit.

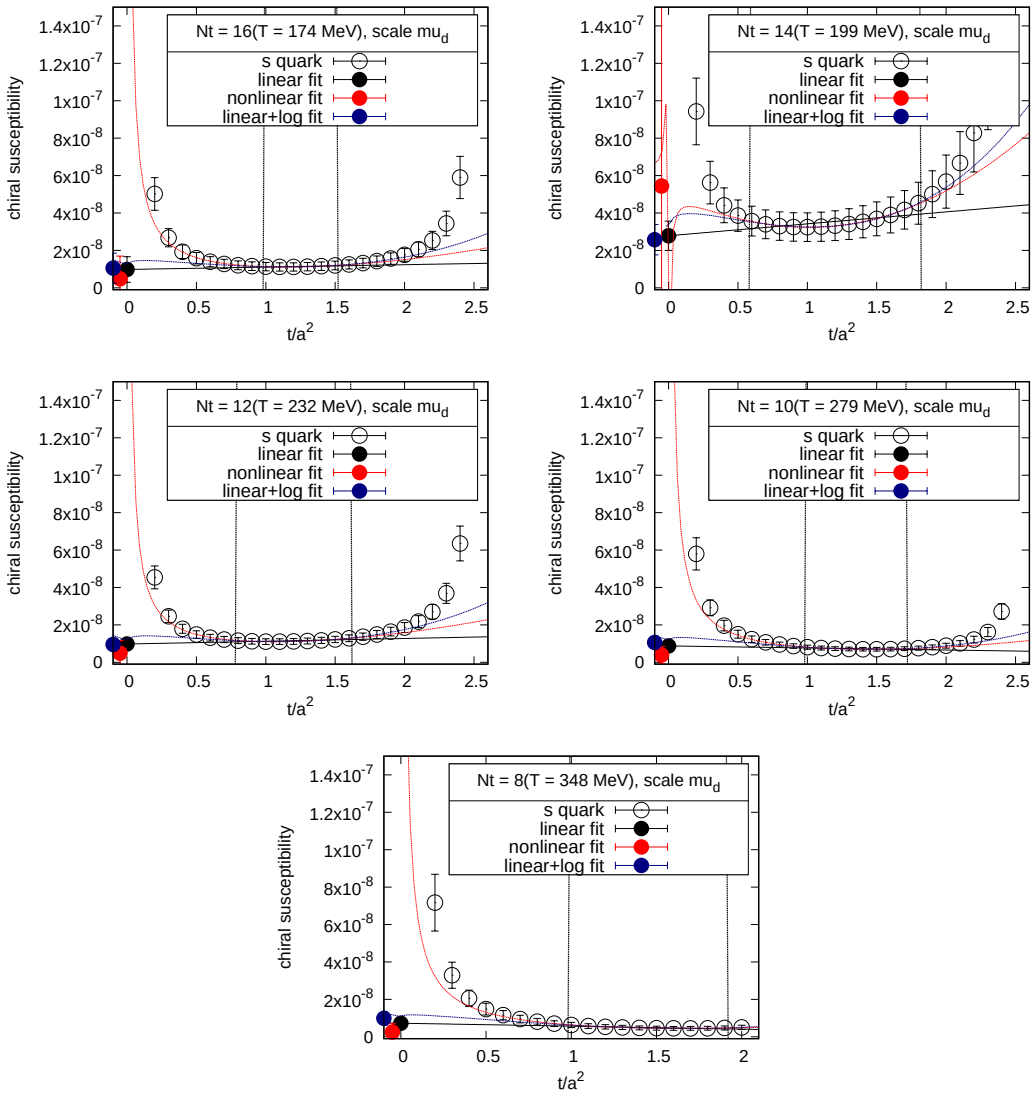

Figure B.4: The diconnected chiral susceptibility for s quark $\chi_s^{\rm disc}$ with μ_D-scale as function of the flow-time. The vertical axis is in lattice unit.

B.1.3 The connected part of chiral susceptibility $\chi_f^{\mathbf{conn}}$

As is the case with the full chiral susceptibility, flow-time dependence of the connected part of chiral susceptibility curves tightly. Due to the unstable linear window, the $t \to 0$ extrapolation become ambiguous. The nonlinear fit also unstable therefore the systematic error becomes large.

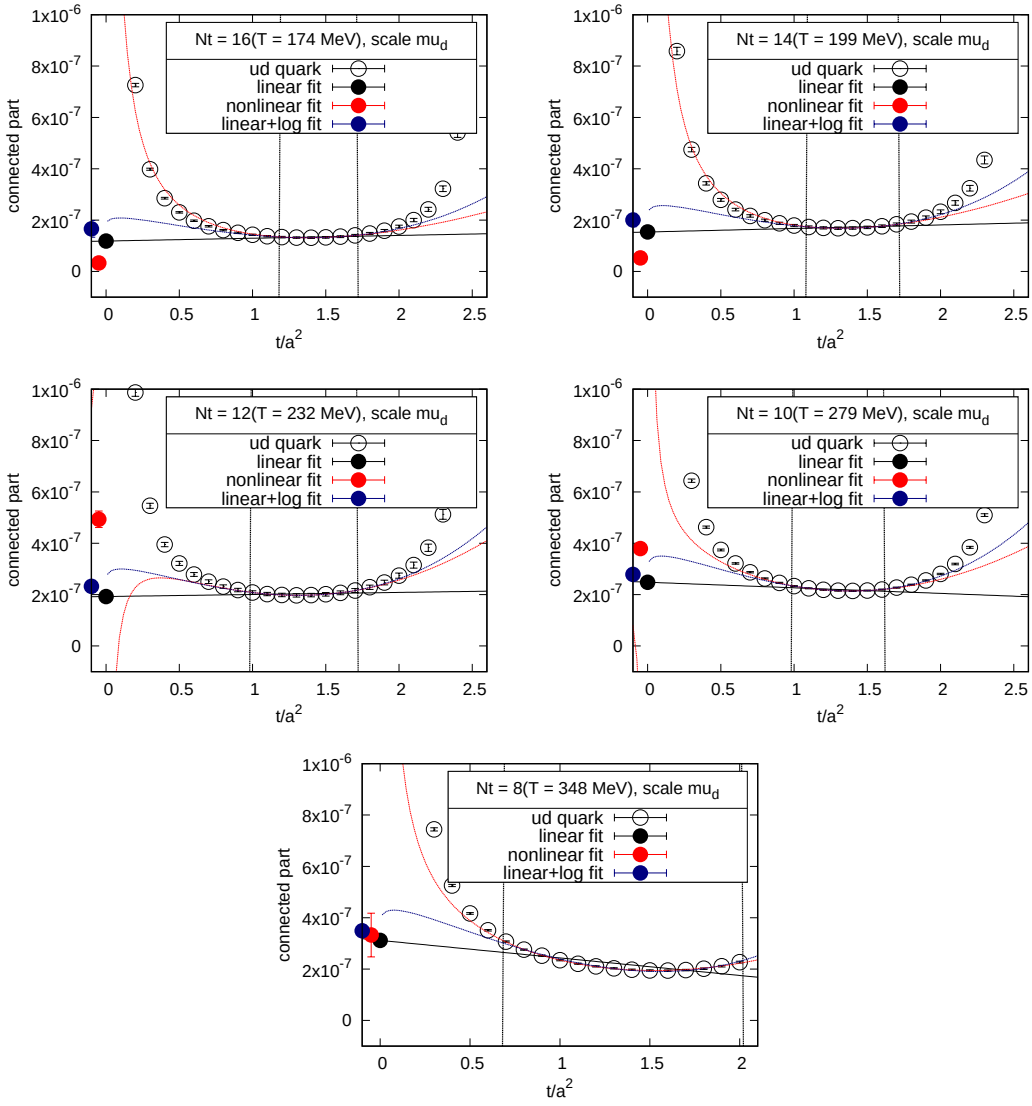

Figure B.5: Connected part of chiral susceptibility for ud quark $\chi_{ud}^{\rm conn}$ with μ_D-scale as function of the flow-time. The vertical axis is in lattice unit.

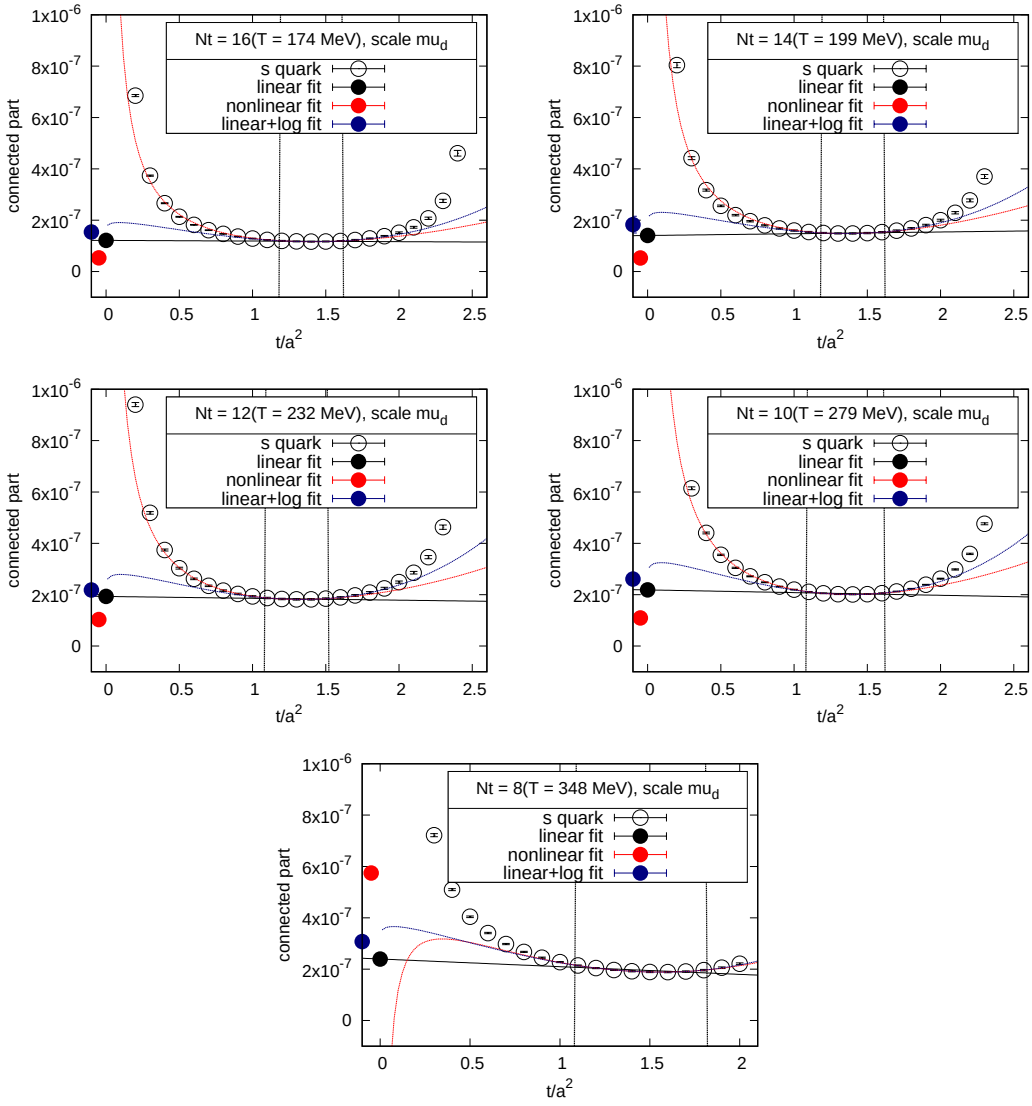

Figure B.6: Connected part of chiral susceptibility for s quark $\chi_s^{\rm conn}$ with μ_D-scale as function of the flow-time. The vertical axis is in lattice unit.

B.2 The $U(1)_A$ susceptibility

The $U(1)_A$ susceptibility $\chi^{\pi-\delta}$ with μ_d-scale have a highly flat linear behavior. At the high temperature, the $O(1/t)$ behavior become weaker than those of the low temperature. This lead us to find the stable linear window even at the high temperature.

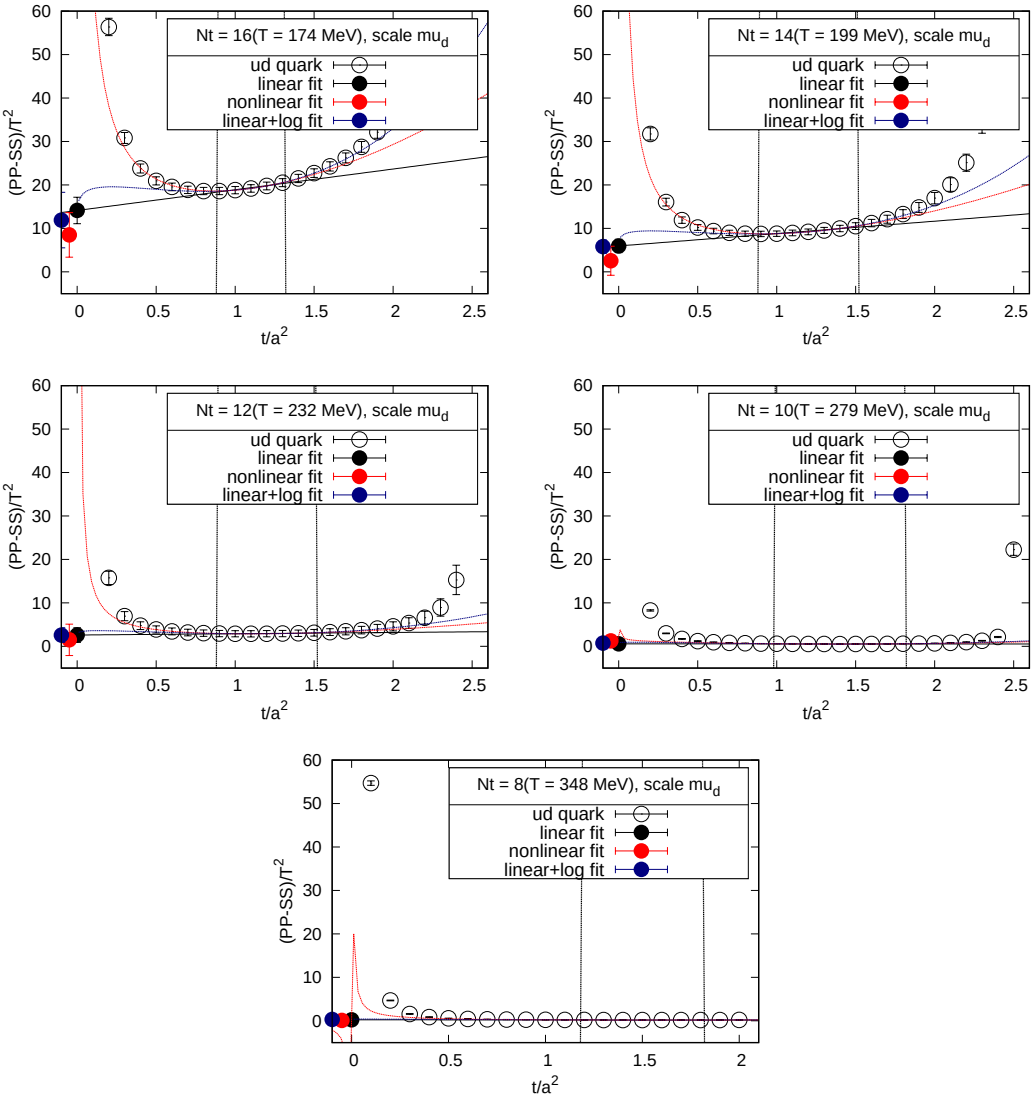

Figure B.7: The $U(1)_A$ susceptibility $\chi^{\pi-\delta}$ with μ_D-scale as function of the flow-time. The vertical axis is in lattice unit.

Appendix C

Some details of Measurements

In this chapter, we show some details of analysis — employed cut-off for linear fit and corresponding range of linear window.

C.1 Linear window

We have to take the $t \to 0$ extrapolation to obtain the correctly renormalized observables in the SFtX method. In the $t \to 0$ extrapolation, we respect the linear fit with the linear window, the linear behavior dominating region. The linear window is defined following the procedure presented in Sec. 5.3. In this procedure, we use the χ^2/d.o.f as a cut-off value of the linear fits and choose the moderate cut-off by consulting the quality and stability of the resulting fits. The chosen cut-off for each operators and temperatures are listed in the Tables C.2 and C.4. We list the result with μ_0-scale in Table C.1 and list in Table C.3 those of μ_d-scale. In this list, the cut-off values of χ^2/d.o.f for the linear fits a, b, c, d, e, f, g and h are 10^{-5}, 10^{-4}, 10^{-3}, 10^{-2}, 10^{-1}, 10^{0}, 10^{1} and 10^{2}, respectively. The corresponding range of the linear windows are listed in Tables C.2 and C.4.

Table C.1: The employed cut-off for each operators and temperatures. The cut-off values of χ^2/d.o.f for the linear fits a, b, c, ..., and h are 10^{-5}, 10^{-4}, 10^{-3}, ... and 10^{2}, respectively.

T [MeV]	χ_{ud}^{full}	χ_{ud}^{disc}	χ_{ud}^{conn}	χ_{s}^{full}	χ_{s}^{disc}	χ_{s}^{conn}	$\chi^{\pi-\delta}$
174	e	d	e	e	d	e	e
199	e	d	e	e	d	e	d
232	e	d	e	f	d	f	d
279	f	e	f	f	e	f	e
348	f	e	f	f	e	f	e

Table C.2: The linear windows for each operators and temperatures corresponding to the cut-off listed in the Table C.1. These values are dimension-less flow-time t/a^2.

T [MeV]	χ_{ud}^{full}	χ_{ud}^{disc}	χ_{ud}^{conn}	χ_{s}^{full}	χ_{s}^{disc}	χ_{s}^{conn}	$\chi^{\pi-\delta}$
174	2.5 – 3.8	1.8 – 3.3	2.7 – 3.8	2.7 – 3.8	2.8 – 3.8	1.4 – 3.9	1.6 – 2.9
199	2.1 – 3.8	1.6 – 3.4	2.6 – 3.7	2.3 – 3.8	1.7 – 3.4	2.8 – 3.6	1.9 – 2.9
232	2.4 – 3.4	1.9 – 3.2	2.5 – 3.5	2.4 – 3.7	2.0 – 3.3	2.4 – 3.7	1.8 – 3.4
279	2.2 – 3.1	1.5 – 3.1	2.2 – 3.1	2.2 – 3.1	1.6 – 3.1	2.3 – 3.1	2.0 – 3.1
348	1.5 – 2.0	1.1 – 2.0	1.5 – 2.0	1.5 – 2.0	1.1 – 2.0	1.5 – 2.0	1.3 – 2.0

Table C.3: The same as Table C.1 but for μ_d-scale.

T [MeV]	χ_{ud}^{full}	χ_{ud}^{disc}	χ_{ud}^{conn}	χ_{s}^{full}	χ_{s}^{disc}	χ_{s}^{conn}	$\chi^{\pi-\delta}$
174	f	d	f	f	d	f	e
199	e	d	f	e	e	f	e
232	g	d	f	f	e	f	d
279	g	e	g	g	e	g	f
348	f	e	g	f	e	g	e

Table C.4: The same as Table C.2 but for μ_d-scale.

T [MeV]	χ_{ud}^{full}	χ_{ud}^{disc}	χ_{ud}^{conn}	χ_{s}^{full}	χ_{s}^{disc}	χ_{s}^{conn}	$\chi^{\pi-\delta}$
174	1.0 – 1.7	0.9 – 1.4	1.2 – 1.7	1.1 – 1.6	1.0 – 1.5	1.2 – 1.6	0.9 – 1.3
199	1.1 – 1.6	0.8 – 1.4	1.1 – 1.7	1.2 – 1.6	0.6 – 1.8	1.2 – 1.6	0.9 – 1.5
232	0.7 – 1.9	1.0 – 1.4	1.0 – 1.7	1.1 – 1.5	0.8 – 1.6	1.1 – 1.5	0.9 – 1.5
279	1.1 – 1.7	1.0 – 1.8	1.0 – 1.6	1.1 – 1.6	1.0 – 1.7	1.1 – 1.6	1.0 – 1.8
348	1.2 – 1.6	1.0 – 1.9	1.1 – 1.8	1.2 – 1.6	1.0 – 1.9	1.1 – 1.8	1.2 – 1.8

C.2 Cut-off Dependence of Fit Range

In this section, we show all the

C.2.1 The full chiral susceptibility $\chi_{ud}^{\mathbf{full}}$, μ_d

$N_t = 16$

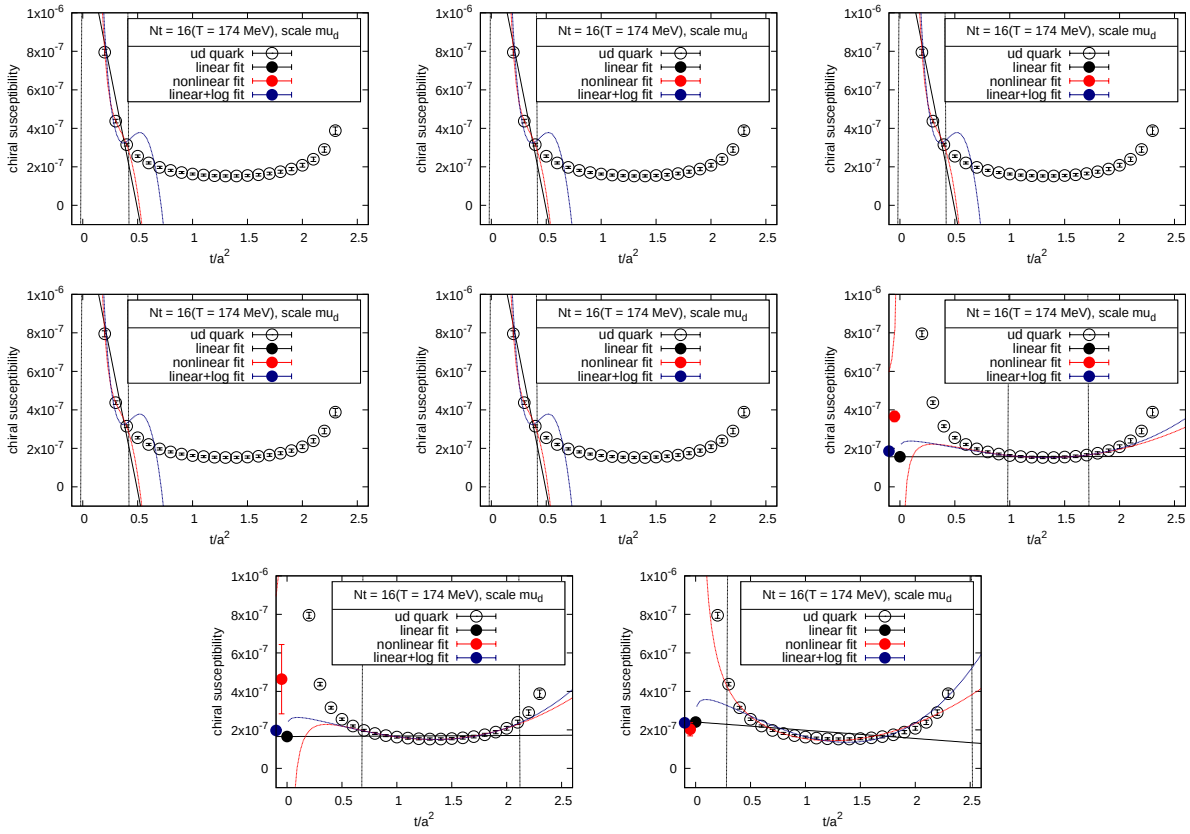

Figure C.1: The full chiral susceptibility χ_{ud}^{full} as a function of the flow-time. $N_t = 16$, μ_d. From top-left to the bottom: we vary the cut-off values of the linear fit as a, b, c, ..., h. The pair of dashed vertical lines indicates the window used for the fit at each cut-off. Black solid lines are the fit results of the linear fit and filled circles at $t = 0$ are the results extracted from the fits. Red and blue dashed lines and filled circle at $t \sim 0$ are the results of nonlinear and linear+log fit, respectively.

$N_t = 14$

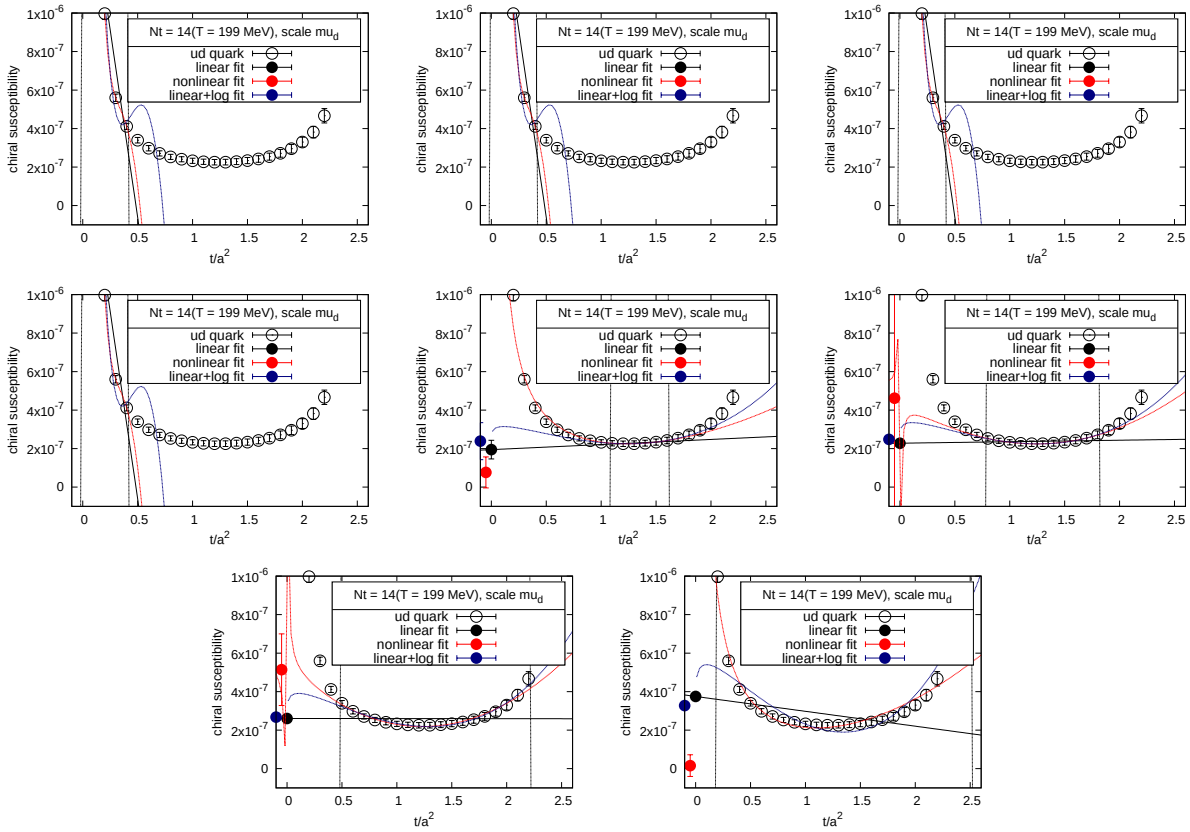

Figure C.2: The full chiral susceptibility χ_{ud}^{full} as a function of the flow-time. $N_t = 14$, μ_d. From top-left to the bottom: we vary the cut-off values of the linear fit as a, b, c, ..., h. The pair of dashed vertical lines indicates the window used for the fit at each cut-off. Black solid lines are the fit results of the linear fit and filled circles at $t = 0$ are the results extracted from the fits. Red and blue dashed lines and filled circle at $t \sim 0$ are the results of nonlinear and linear+log fit, respectively.

$N_t = 12$

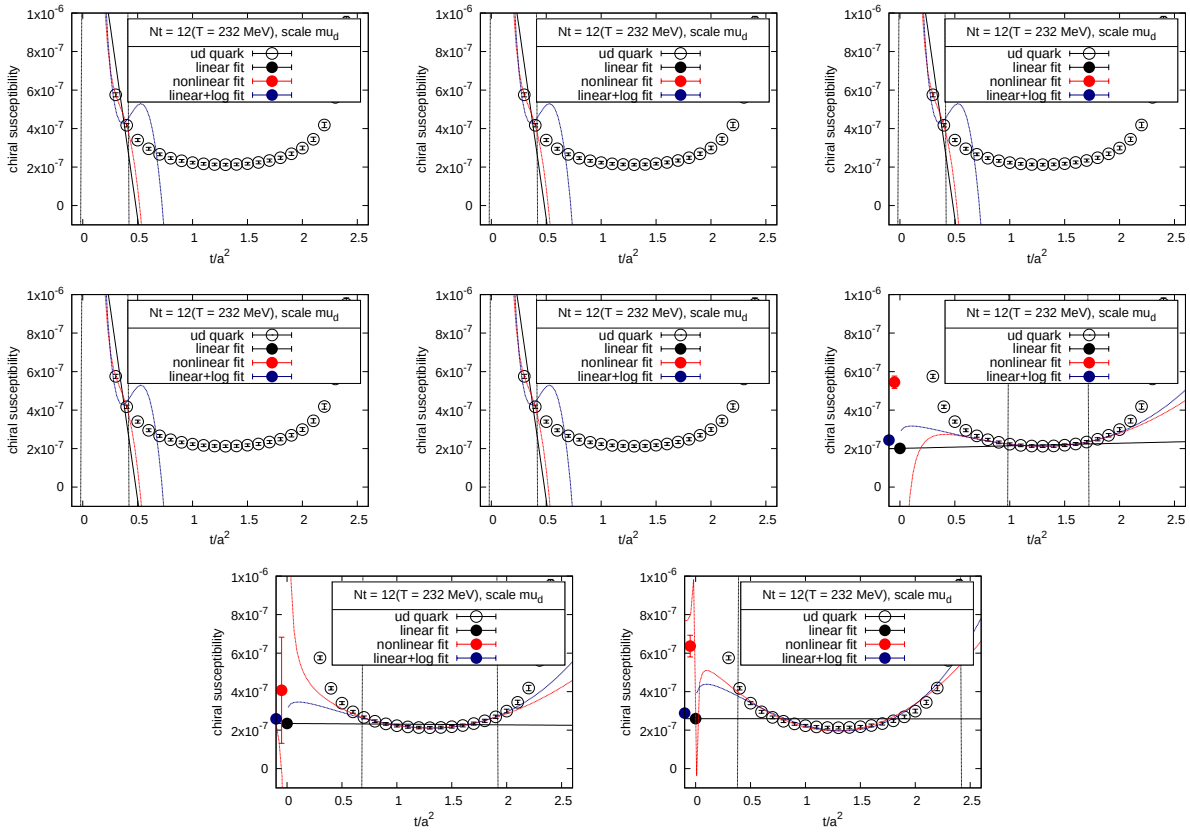

Figure C.3: The full chiral susceptibility χ_{ud}^{full} as a function of the flow-time. $N_t = 12$, μ_d. From top-left to the bottom: we vary the cut-off values of the linear fit as a, b, c, ..., h. The pair of dashed vertical lines indicates the window used for the fit at each cut-off. Black solid lines are the fit results of the linear fit and filled circles at $t = 0$ are the results extracted from the fits. Red and blue dashed lines and filled circle at $t \sim 0$ are the results of nonlinear and linear+log fit, respectively.

$N_t = 10$

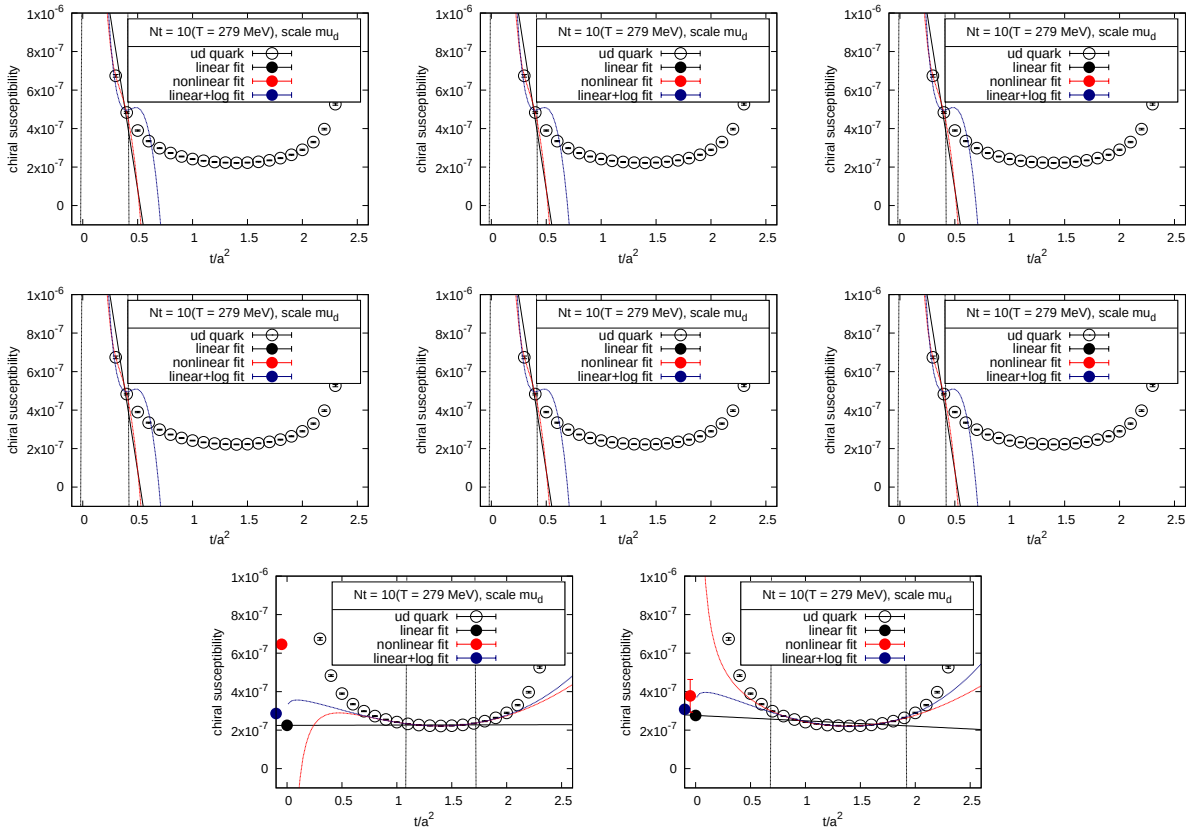

Figure C.4: The full chiral susceptibility χ_{ud}^{full} as a function of the flow-time. $N_t = 10$, μ_d. From top-left to the bottom: we vary the cut-off values of the linear fit as a, b, c, ..., h. The pair of dashed vertical lines indicates the window used for the fit at each cut-off. Black solid lines are the fit results of the linear fit and filled circles at $t = 0$ are the results extracted from the fits. Red and blue dashed lines and filled circle at $t \sim 0$ are the results of nonlinear and linear+log fit, respectively.

$N_t = 8$

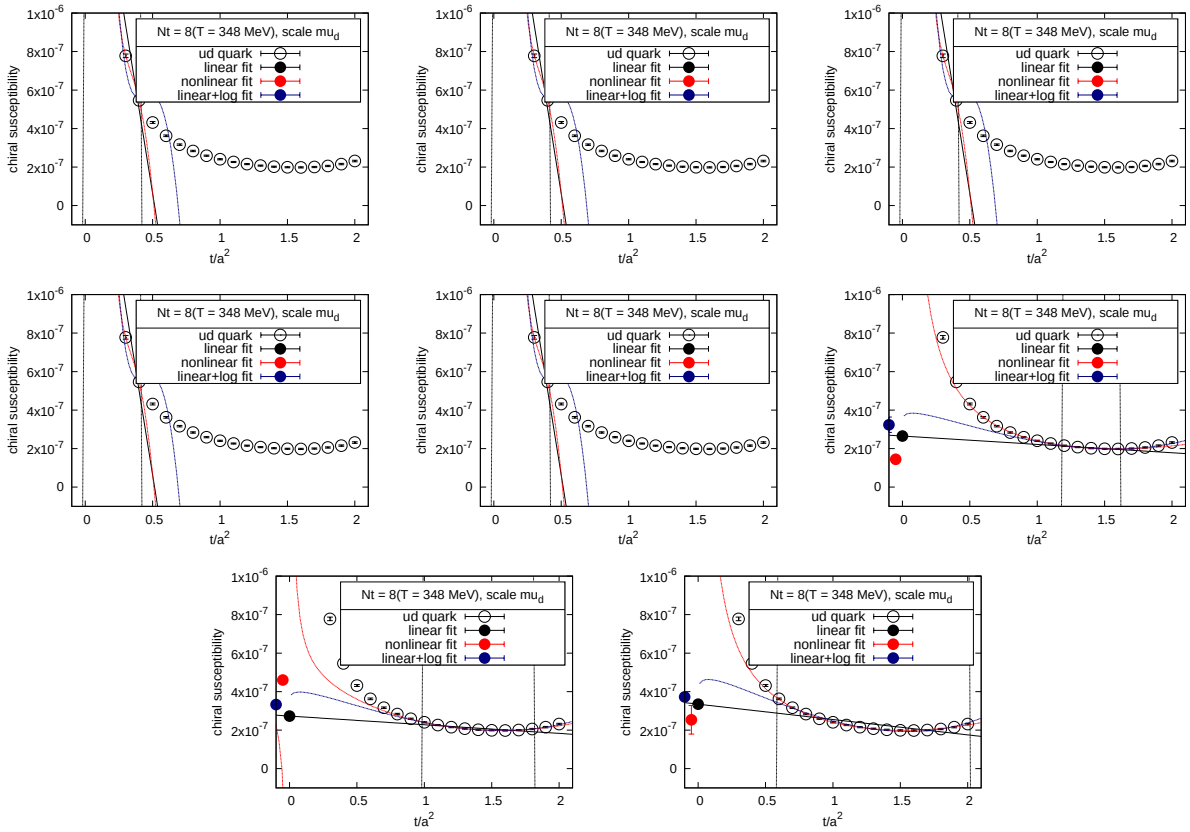

Figure C.5: The full chiral susceptibility χ_{ud}^{full} as a function of the flow-time. $N_t = 8$, μ_d. From top-left to the bottom: we vary the cut-off values of the linear fit as a, b, c, ..., h. The pair of dashed vertical lines indicates the window used for the fit at each cut-off. Black solid lines are the fit results of the linear fit and filled circles at $t = 0$ are the results extracted from the fits. Red and blue dashed lines and filled circle at $t \sim 0$ are the results of nonlinear and linear+log fit, respectively.

C.2.2 The full chiral susceptibility , μ_d

$N_t = 16$

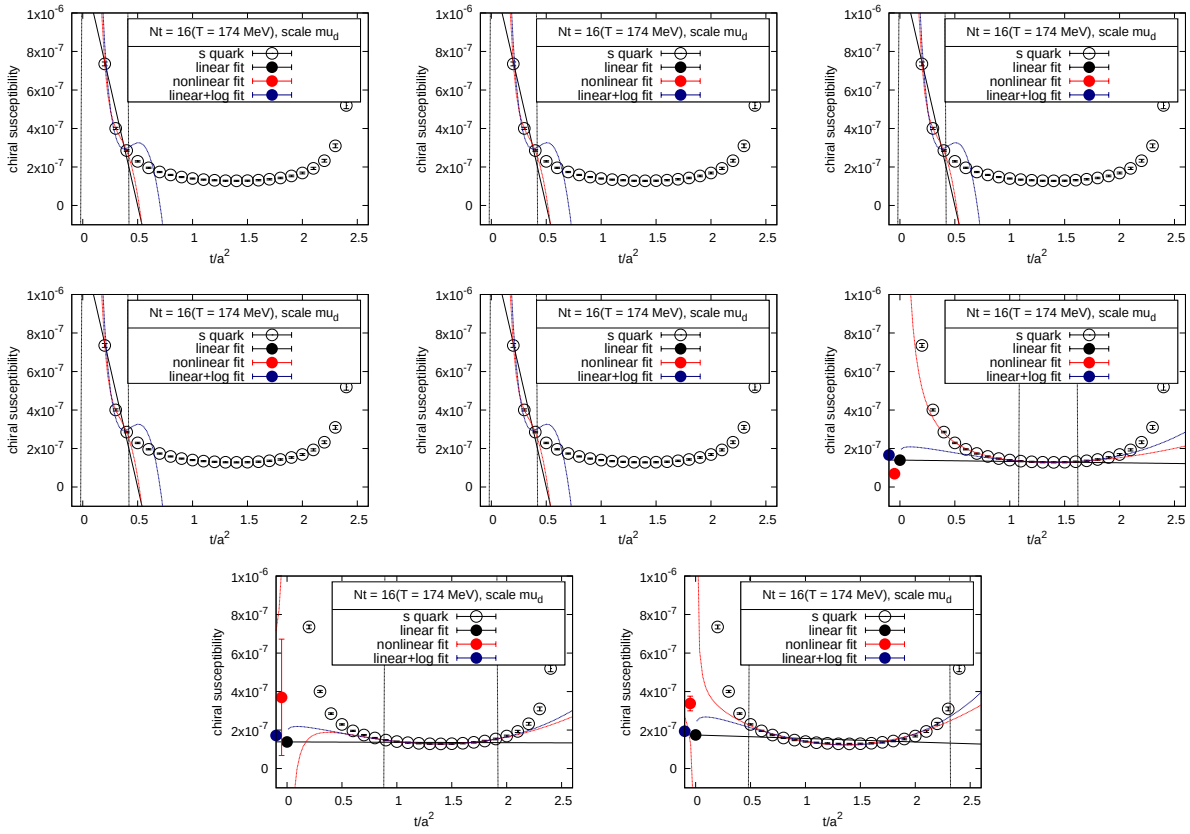

Figure C.6: The full chiral susceptibility χ_s^{full} as a function of the flow-time. $N_t = 16$, μ_d. From top-left to the bottom: we vary the cut-off values of the linear fit as a, b, c, ..., h. The pair of dashed vertical lines indicates the window used for the fit at each cut-off. Black solid lines are the fit results of the linear fit and filled circles at $t = 0$ are the results extracted from the fits. Red and blue dashed lines and filled circle at $t \sim 0$ are the results of nonlinear and linear+log fit, respectively.

$N_t = 14$

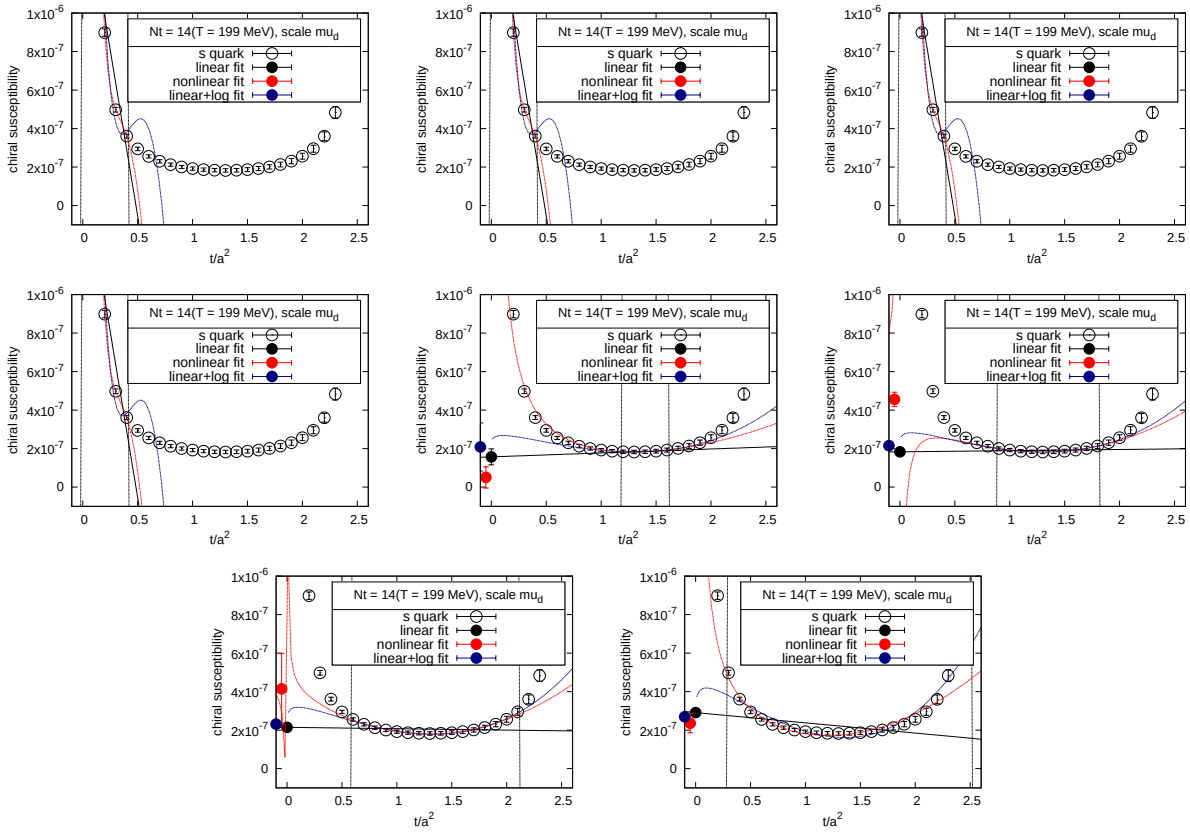

Figure C.7: The full chiral susceptibility χ_s^{full} as a function of the flow-time. $N_t = 14$, μ_d. From top-left to the bottom: we vary the cut-off values of the linear fit as a, b, c, ..., h. The pair of dashed vertical lines indicates the window used for the fit at each cut-off. Black solid lines are the fit results of the linear fit and filled circles at $t = 0$ are the results extracted from the fits. Red and blue dashed lines and filled circle at $t \sim 0$ are the results of nonlinear and linear+log fit, respectively.

$N_t = 12$

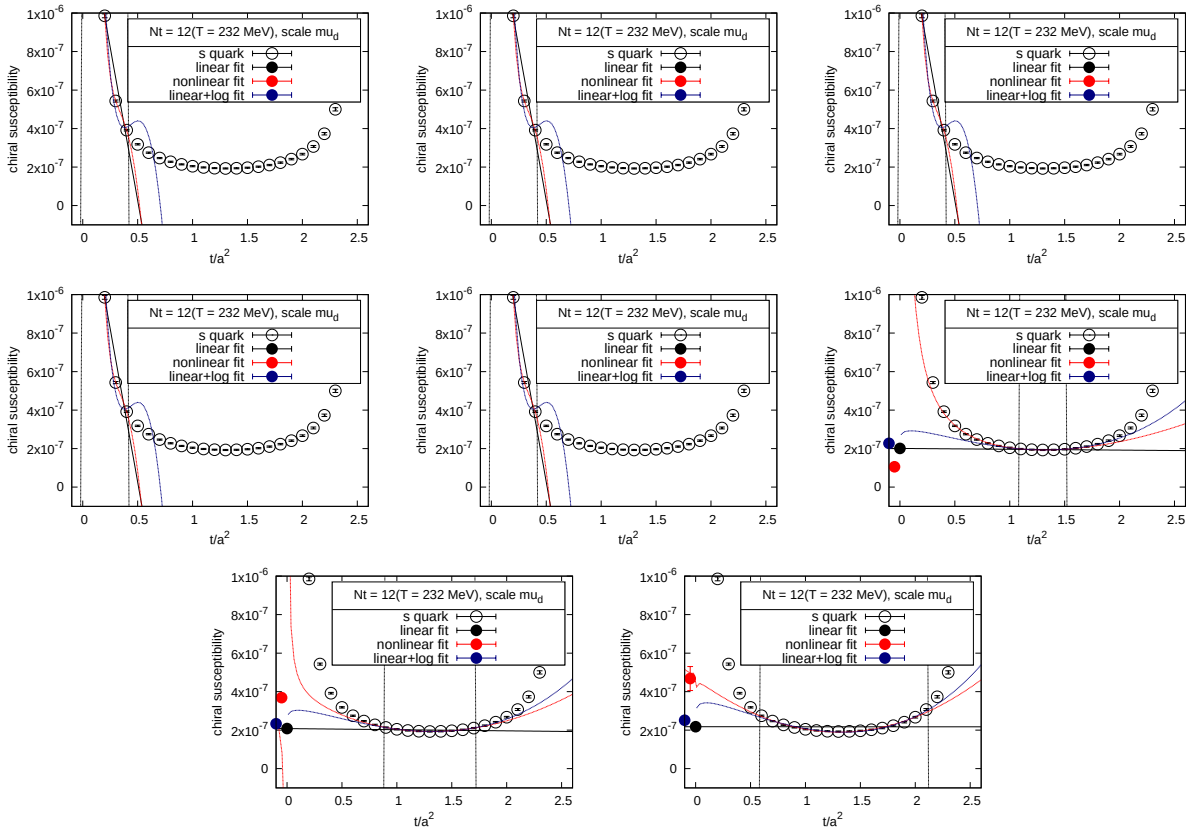

Figure C.8: The full chiral susceptibility χ_s^{full} as a function of the flow-time. $N_t = 12$, μ_d. From top-left to the bottom: we vary the cut-off values of the linear fit as a, b, c, ..., h. The pair of dashed vertical lines indicates the window used for the fit at each cut-off. Black solid lines are the fit results of the linear fit and filled circles at $t = 0$ are the results extracted from the fits. Red and blue dashed lines and filled circle at $t \sim 0$ are the results of nonlinear and linear+log fit, respectively.

$N_t = 10$

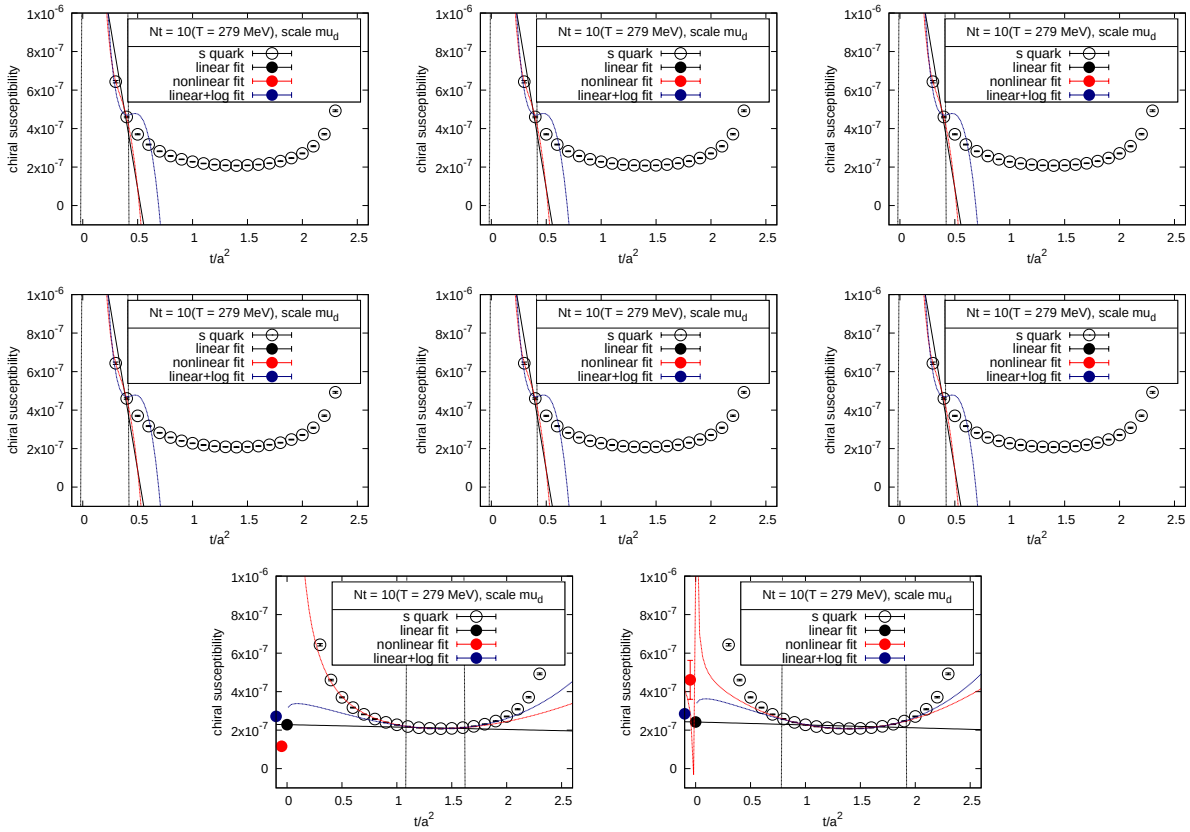

Figure C.9: The full chiral susceptibility χ_s^{full} as a function of the flow-time. $N_t = 10$, μ_d. From top-left to the bottom: we vary the cut-off values of the linear fit as a, b, c, ..., h. The pair of dashed vertical lines indicates the window used for the fit at each cut-off. Black solid lines are the fit results of the linear fit and filled circles at $t = 0$ are the results extracted from the fits. Red and blue dashed lines and filled circle at $t \sim 0$ are the results of nonlinear and linear+log fit, respectively.

renewcommand108

$N_t = 10$

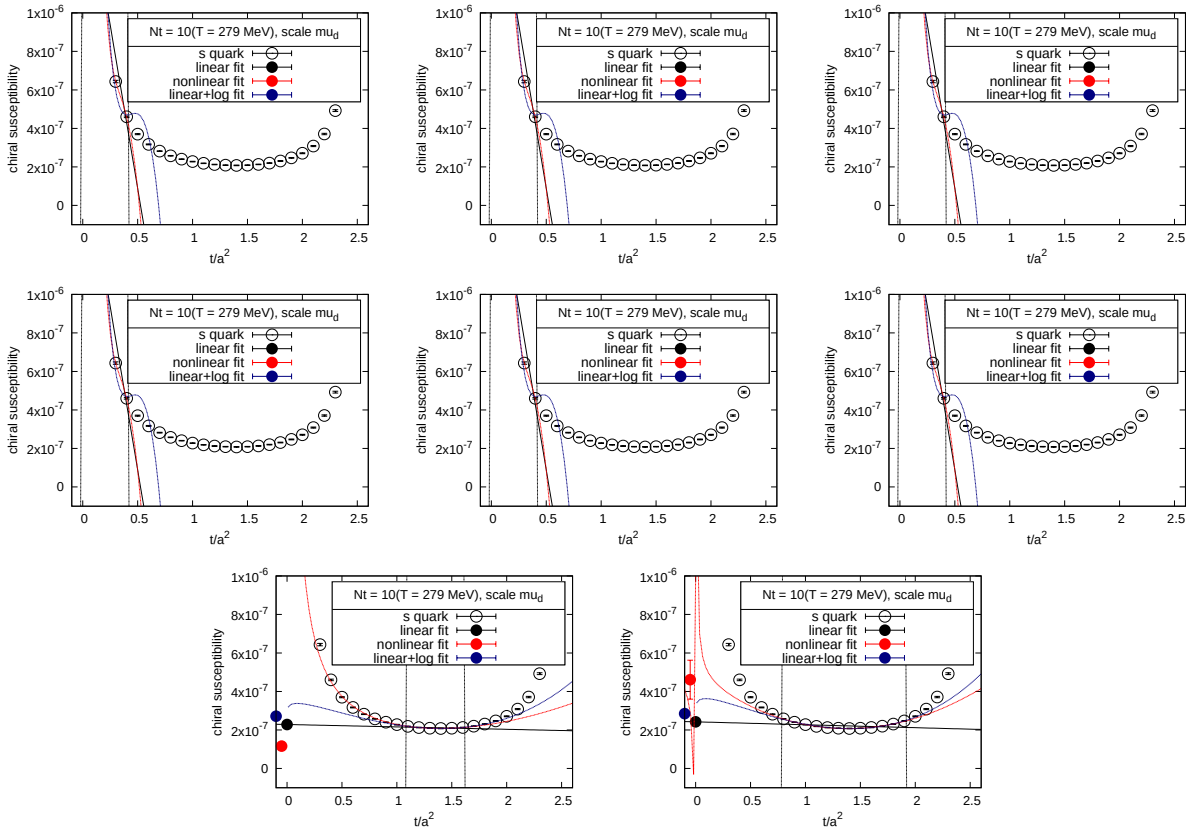

Figure C.10: The full chiral susceptibility χ_s^{full} as a function of the flow-time. $N_t = 10$, μ_d. From top-left to the bottom: we vary the cut-off values of the linear fit as a, b, c, ..., h. The pair of dashed vertical lines indicates the window used for the fit at each cut-off. Black solid lines are the fit results of the linear fit and filled circles at $t = 0$ are the results extracted from the fits. Red and blue dashed lines and filled circle at $t \sim 0$ are the results of nonlinear and linear+log fit, respectively.

C.2.3 The full chiral susceptibility , μ_0

$N_t = 16$

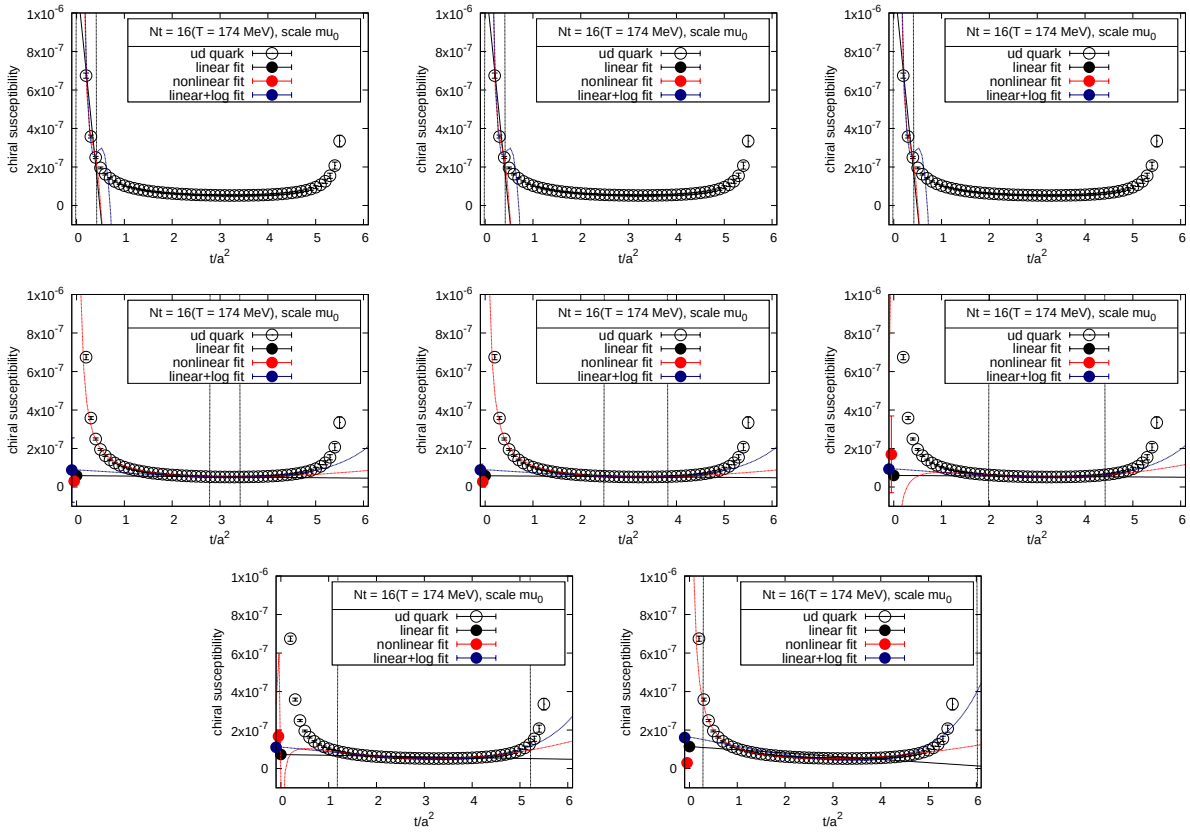

Figure C.11: The full chiral susceptibility χ_{ud}^{full} as a function of the flow-time. $N_t = 16$, μ_0. From top-left to the bottom: we vary the cut-off values of the linear fit as a, b, c, ..., h. The pair of dashed vertical lines indicates the window used for the fit at each cut-off. Black solid lines are the fit results of the linear fit and filled circles at $t = 0$ are the results extracted from the fits. Red and blue dashed lines and filled circle at $t \sim 0$ are the results of nonlinear and linear+log fit, respectively.

$N_t = 14$

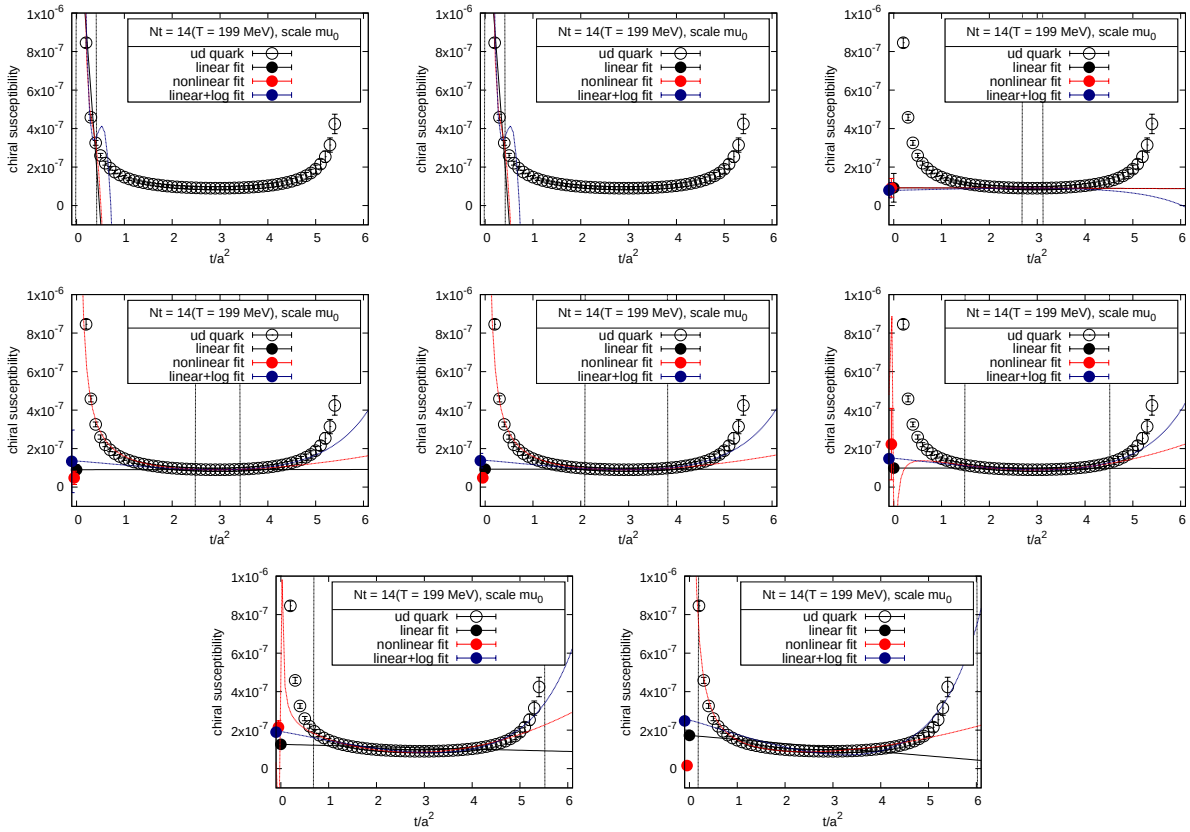

Figure C.12: The full chiral susceptibility χ_{ud}^{full} as a function of the flow-time. $N_t = 14$, μ_0. From top-left to the bottom: we vary the cut-off values of the linear fit as a, b, c, ..., h. The pair of dashed vertical lines indicates the window used for the fit at each cut-off. Black solid lines are the fit results of the linear fit and filled circles at $t = 0$ are the results extracted from the fits. Red and blue dashed lines and filled circle at $t \sim 0$ are the results of nonlinear and linear+log fit, respectively.

$N_t = 12$

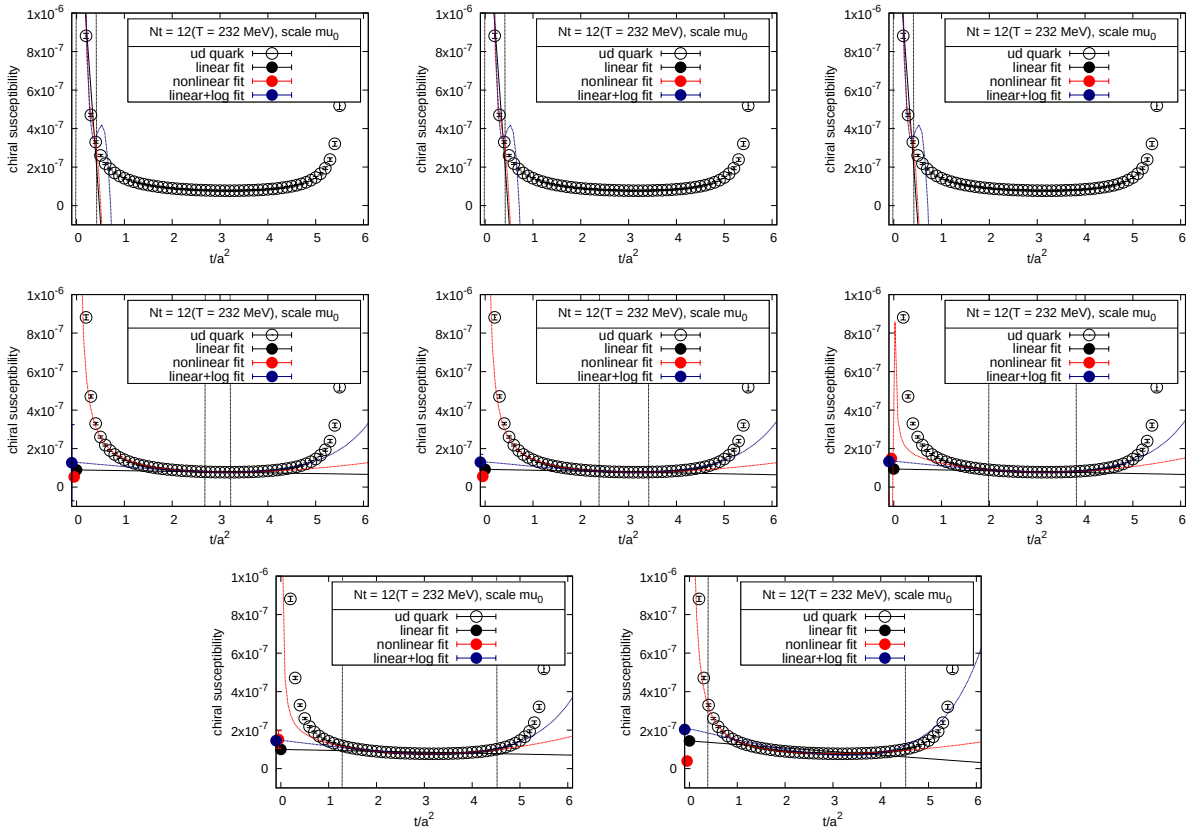

Figure C.13: The full chiral susceptibility χ_{ud}^{full} as a function of the flow-time. $N_t = 12$, μ_0. From top-left to the bottom: we vary the cut-off values of the linear fit as a, b, c, ..., h. The pair of dashed vertical lines indicates the window used for the fit at each cut-off. Black solid lines are the fit results of the linear fit and filled circles at $t = 0$ are the results extracted from the fits. Red and blue dashed lines and filled circle at $t \sim 0$ are the results of nonlinear and linear+log fit, respectively.

$N_t = 10$

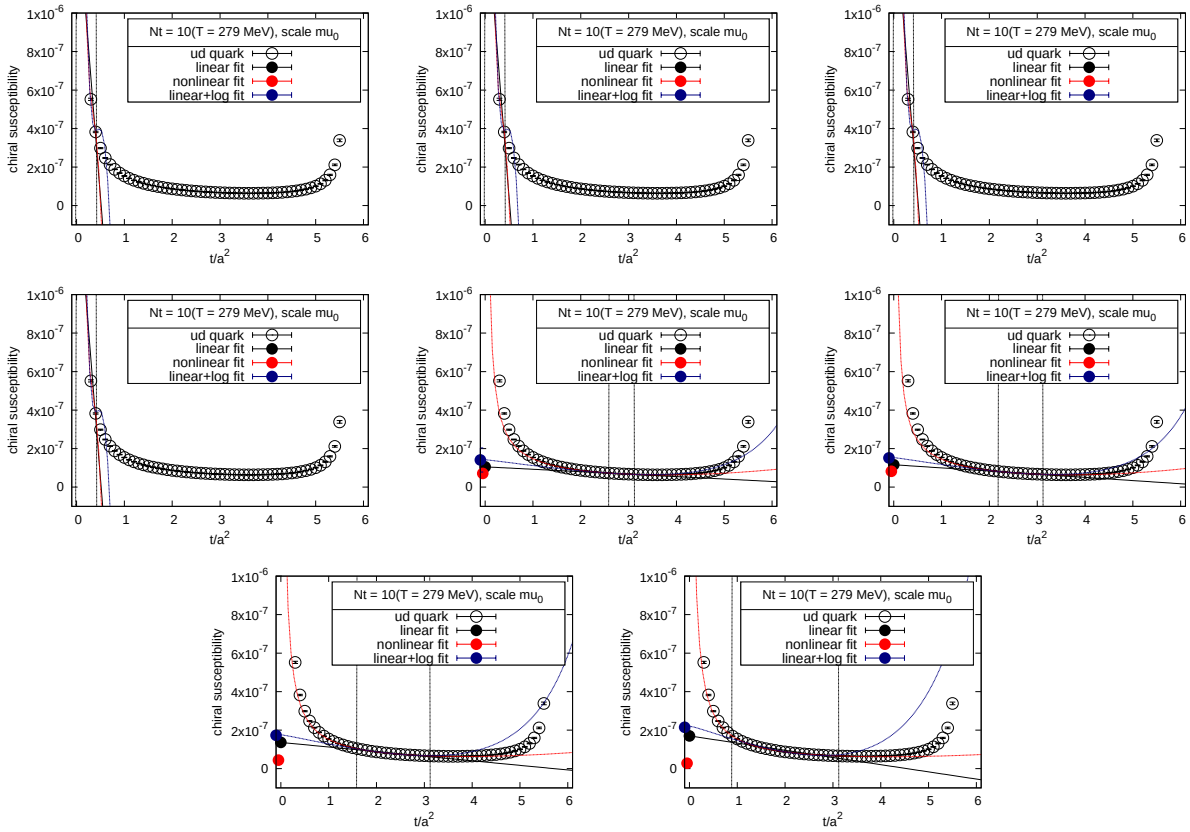

Figure C.14: The full chiral susceptibility χ_{ud}^{full} as a function of the flow-time. $N_t = 10$, μ_0. From top-left to the bottom: we vary the cut-off values of the linear fit as a, b, c, ..., h. The pair of dashed vertical lines indicates the window used for the fit at each cut-off. Black solid lines are the fit results of the linear fit and filled circles at $t = 0$ are the results extracted from the fits. Red and blue dashed lines and filled circle at $t \sim 0$ are the results of nonlinear and linear+log fit, respectively.

$N_t = 8$

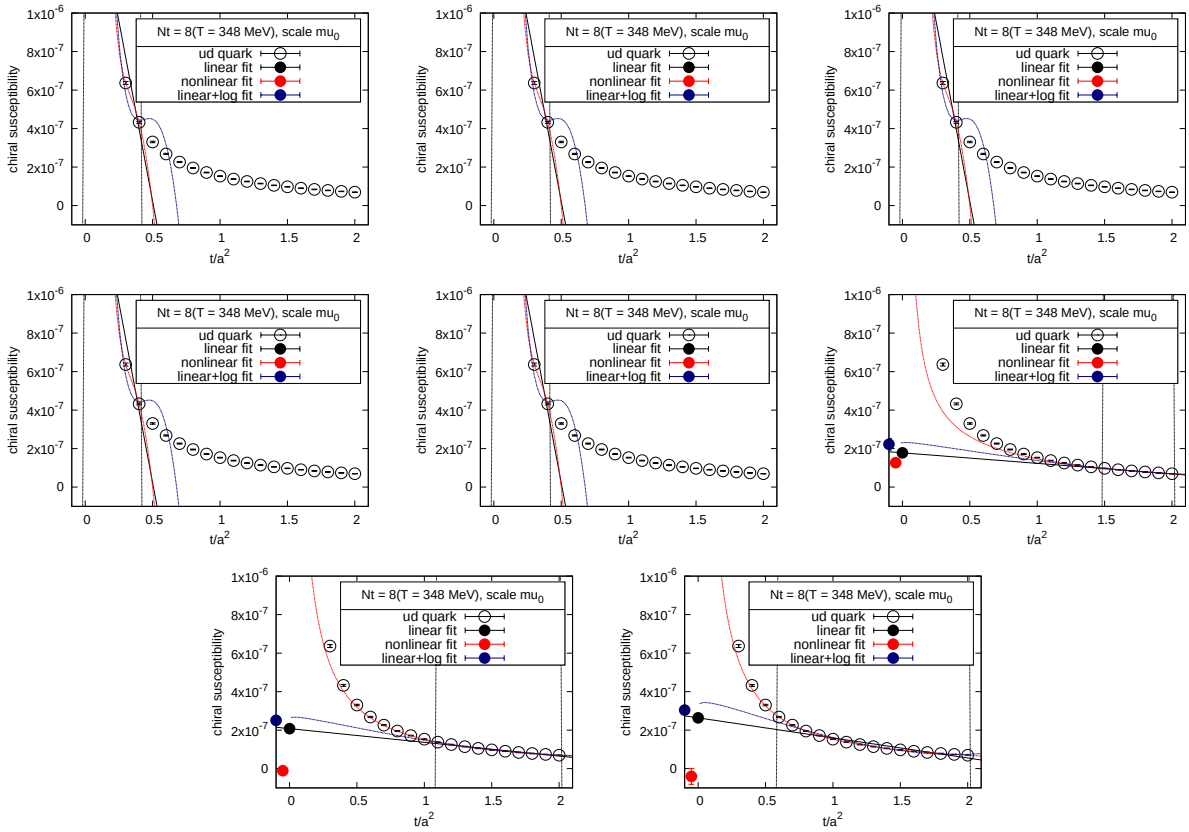

Figure C.15: The full chiral susceptibility χ_{ud}^{full} as a function of the flow-time. $N_t = 8$, μ_0. From top-left to the bottom: we vary the cut-off values of the linear fit as a, b, c, ..., h. The pair of dashed vertical lines indicates the window used for the fit at each cut-off. Black solid lines are the fit results of the linear fit and filled circles at $t = 0$ are the results extracted from the fits. Red and blue dashed lines and filled circle at $t \sim 0$ are the results of nonlinear and linear+log fit, respectively.

C.2.4 The full chiral susceptibility , μ_0

$N_t = 16$

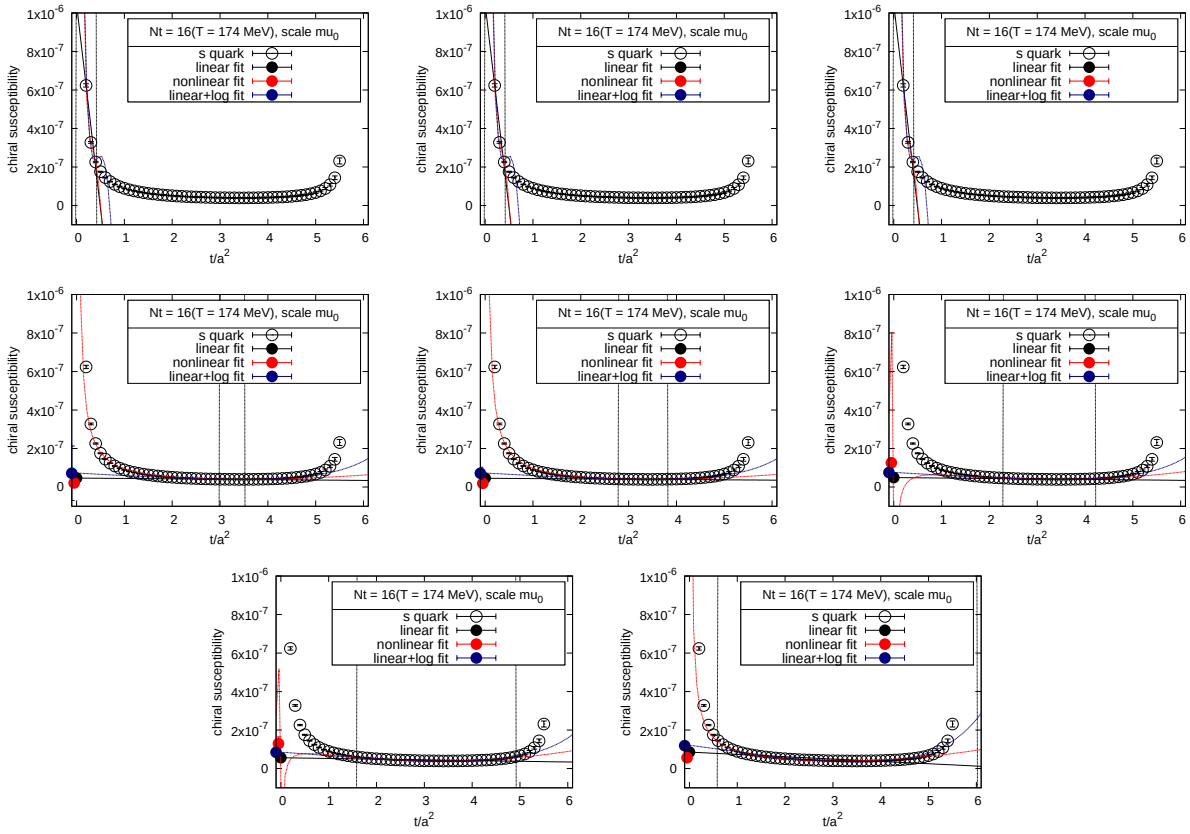

Figure C.16: The full chiral susceptibility χ_s^{full} as a function of the flow-time. $N_t = 16$, μ_0. From top-left to the bottom: we vary the cut-off values of the linear fit as a, b, c, ..., h. The pair of dashed vertical lines indicates the window used for the fit at each cut-off. Black solid lines are the fit results of the linear fit and filled circles at $t = 0$ are the results extracted from the fits. Red and blue dashed lines and filled circle at $t \sim 0$ are the results of nonlinear and linear+log fit, respectively.

$N_t = 14$

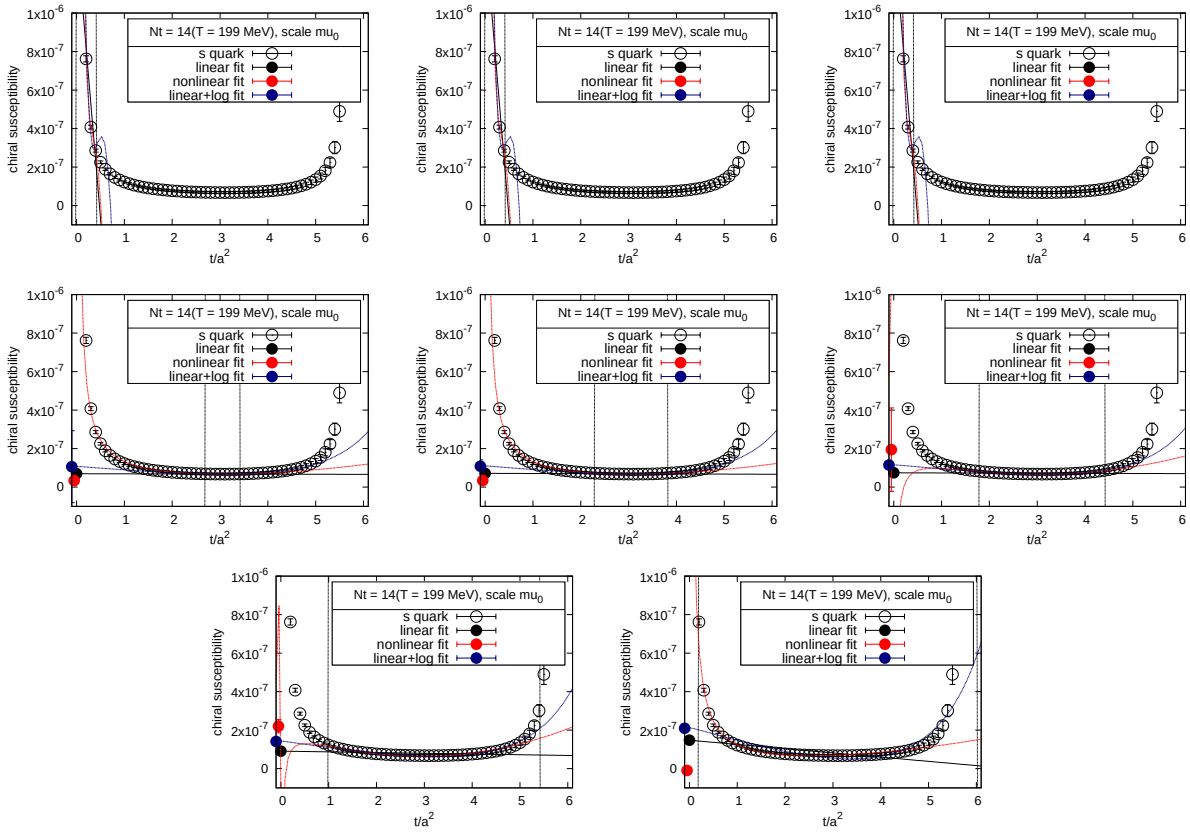

Figure C.17: The full chiral susceptibility χ_s^{full} as a function of the flow-time. $N_t = 14$, μ_0. From top-left to the bottom: we vary the cut-off values of the linear fit as a, b, c, ..., h. The pair of dashed vertical lines indicates the window used for the fit at each cut-off. Black solid lines are the fit results of the linear fit and filled circles at $t = 0$ are the results extracted from the fits. Red and blue dashed lines and filled circle at $t \sim 0$ are the results of nonlinear and linear+log fit, respectively.

$N_t = 12$

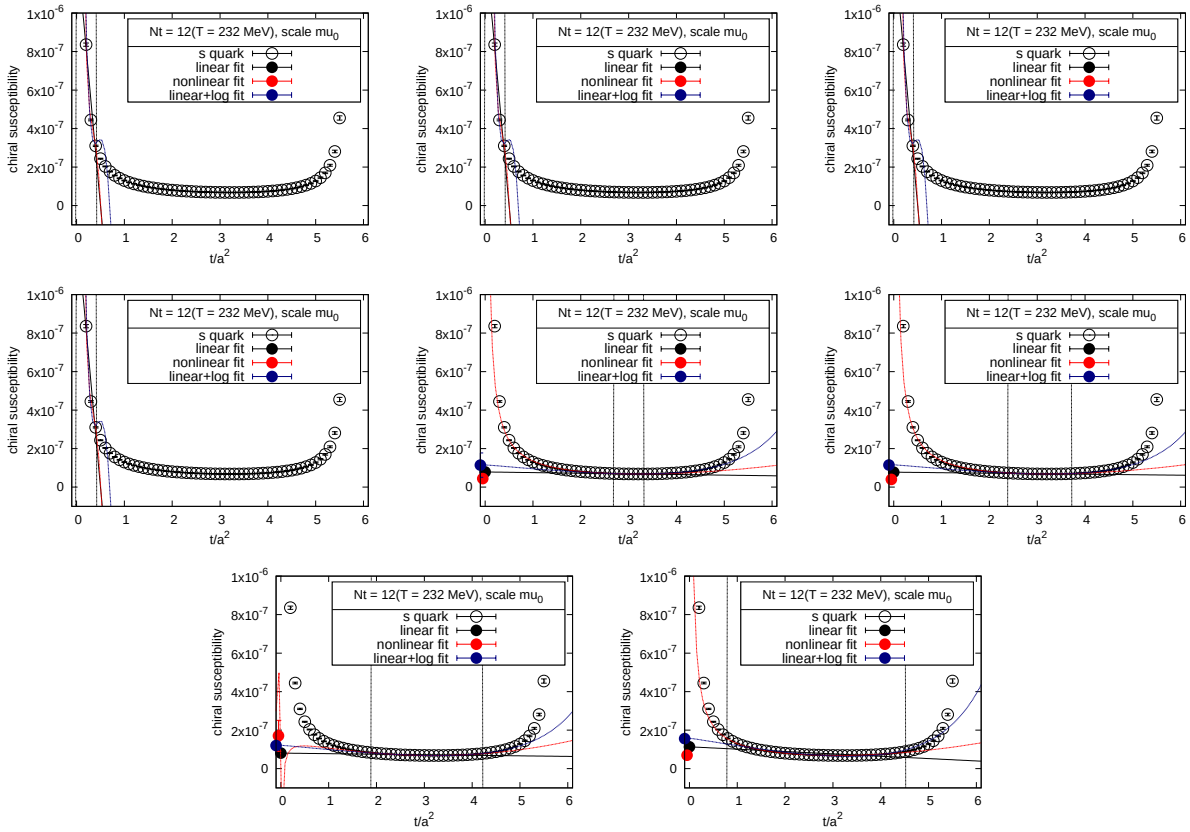

Figure C.18: The full chiral susceptibility χ_s^{full} as a function of the flow-time. $N_t = 12$, μ_0. From top-left to the bottom: we vary the cut-off values of the linear fit as a, b, c, ..., h. The pair of dashed vertical lines indicates the window used for the fit at each cut-off. Black solid lines are the fit results of the linear fit and filled circles at $t = 0$ are the results extracted from the fits. Red and blue dashed lines and filled circle at $t \sim 0$ are the results of nonlinear and linear+log fit, respectively.

$N_t = 10$

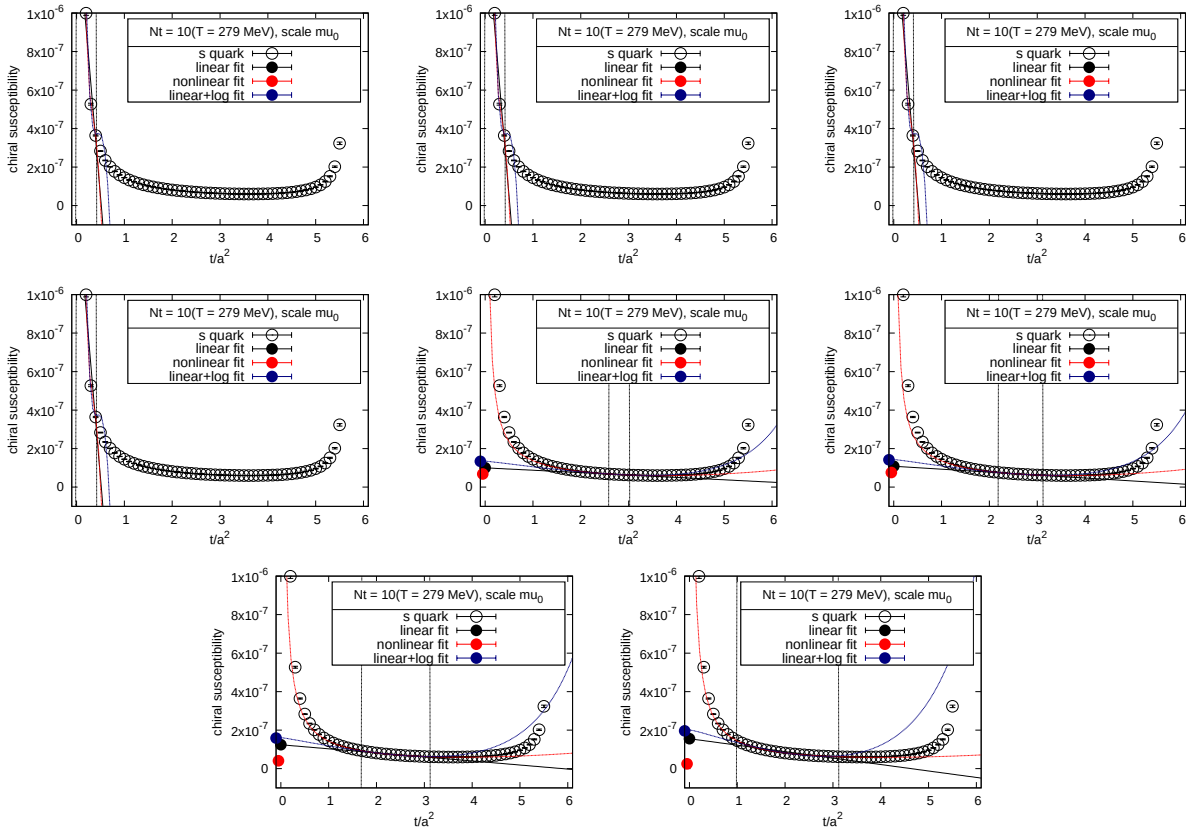

Figure C.19: The full chiral susceptibility χ_s^{full} as a function of the flow-time. $N_t = 10$, μ_0. From top-left to the bottom: we vary the cut-off values of the linear fit as a, b, c, ..., h. The pair of dashed vertical lines indicates the window used for the fit at each cut-off. Black solid lines are the fit results of the linear fit and filled circles at $t = 0$ are the results extracted from the fits. Red and blue dashed lines and filled circle at $t \sim 0$ are the results of nonlinear and linear+log fit, respectively.

$N_t = 8$

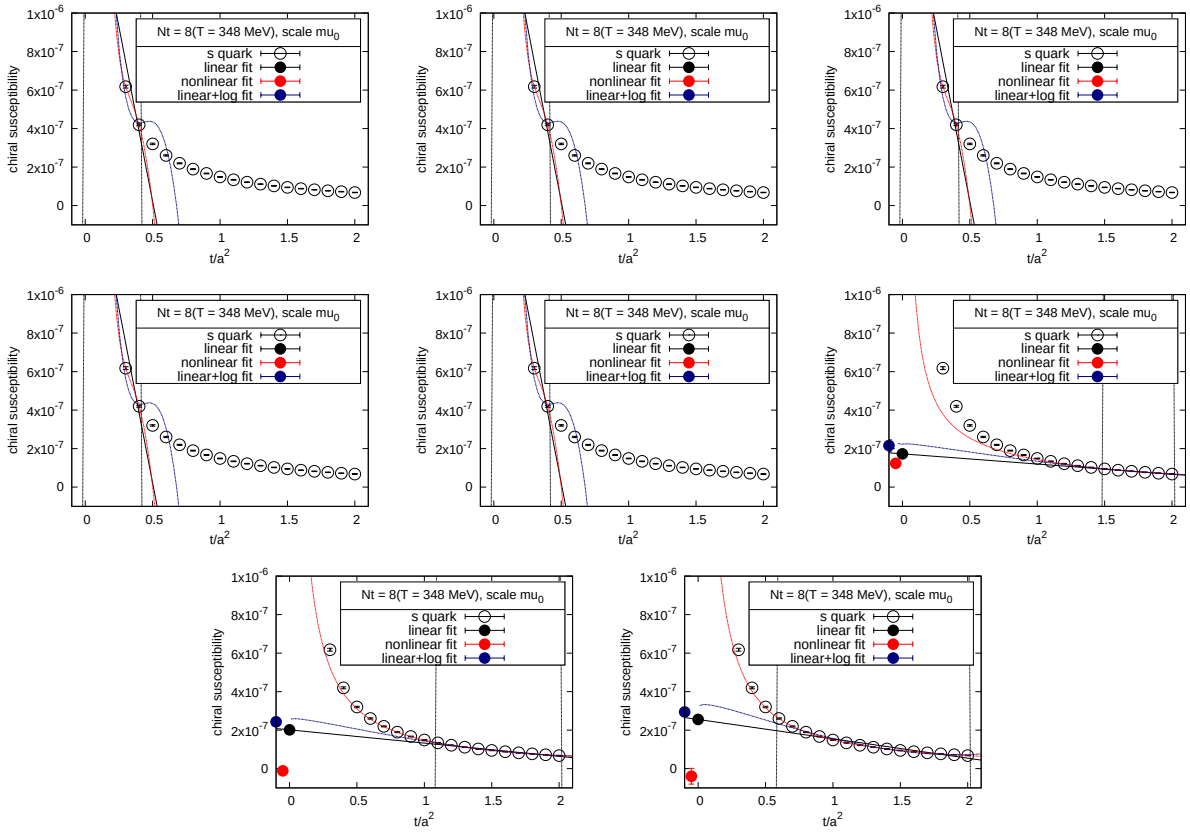

Figure C.20: The full chiral susceptibility χ_s^{full} as a function of the flow-time. $N_t = 8$, μ_0. From top-left to the bottom: we vary the cut-off values of the linear fit as a, b, c, ..., h. The pair of dashed vertical lines indicates the window used for the fit at each cut-off. Black solid lines are the fit results of the linear fit and filled circles at $t = 0$ are the results extracted from the fits. Red and blue dashed lines and filled circle at $t \sim 0$ are the results of nonlinear and linear+log fit, respectively.

C.2.5 The disconnected chiral susceptibility $\chi_{ud}^{\mathbf{disc}}$, μ_d

$N_t = 16$

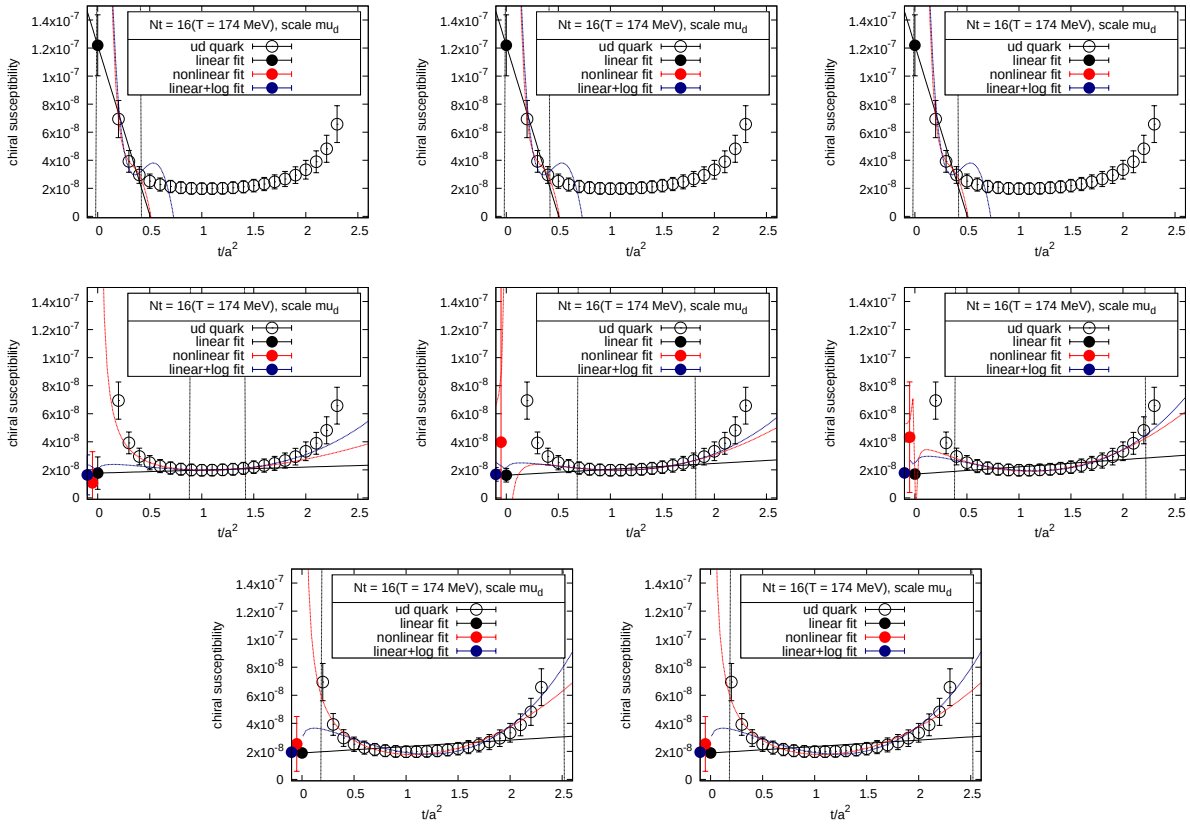

Figure C.21: The disconnected chiral susceptibility $\chi_{ud}^{\mathrm{disc}}$ as a function of the flow-time. $N_t = 16$, μ_d. From top-left to the bottom: we vary the cut-off values of the linear fit as a, b, c, ..., h. The pair of dashed vertical lines indicates the window used for the fit at each cut-off. Black solid lines are the fit results of the linear fit and filled circles at $t = 0$ are the results extracted from the fits. Red and blue dashed lines and filled circle at $t \sim 0$ are the results of nonlinear and linear+log fit, respectively.

$N_t = 14$

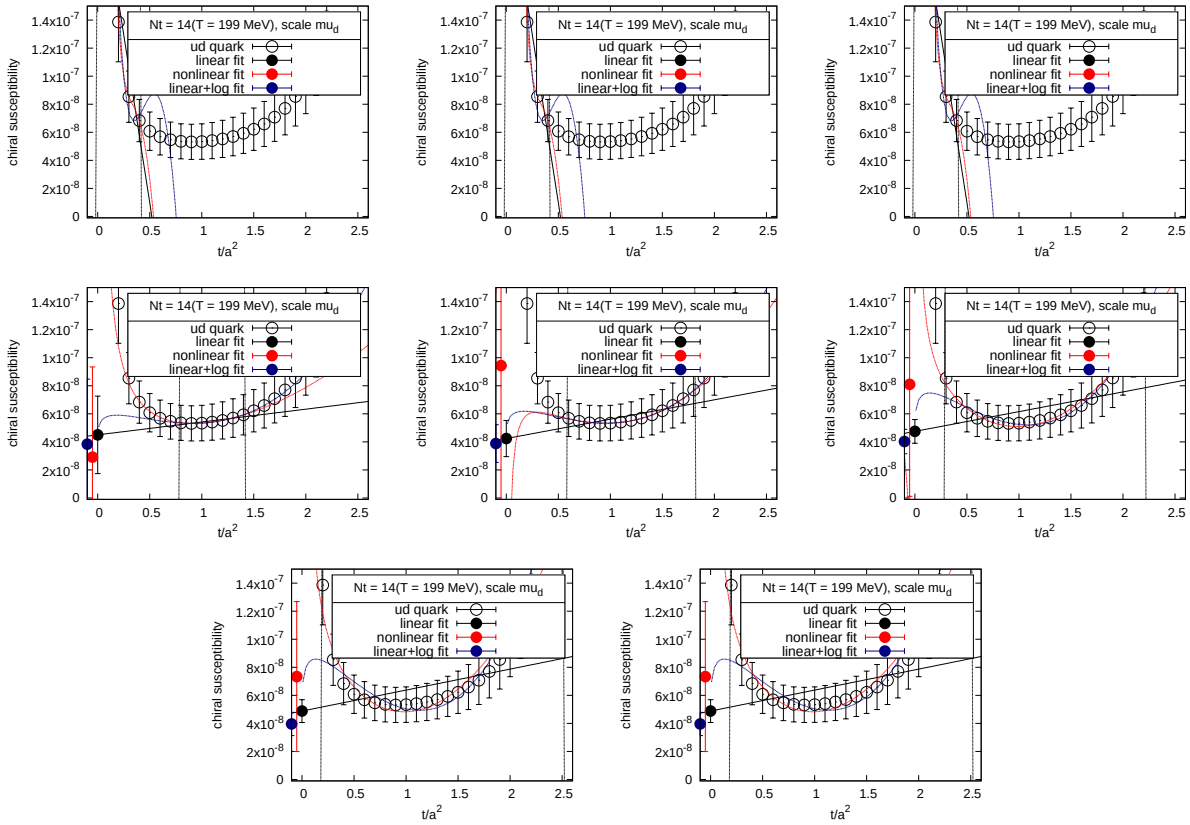

Figure C.22: The disconnected chiral susceptibility $\chi_{ud}^{\rm disc}$ as a function of the flow-time. $N_t = 14$, μ_d. From top-left to the bottom: we vary the cut-off values of the linear fit as a, b, c, ..., h. The pair of dashed vertical lines indicates the window used for the fit at each cut-off. Black solid lines are the fit results of the linear fit and filled circles at $t = 0$ are the results extracted from the fits. Red and blue dashed lines and filled circle at $t \sim 0$ are the results of nonlinear and linear+log fit, respectively.

$N_t = 12$

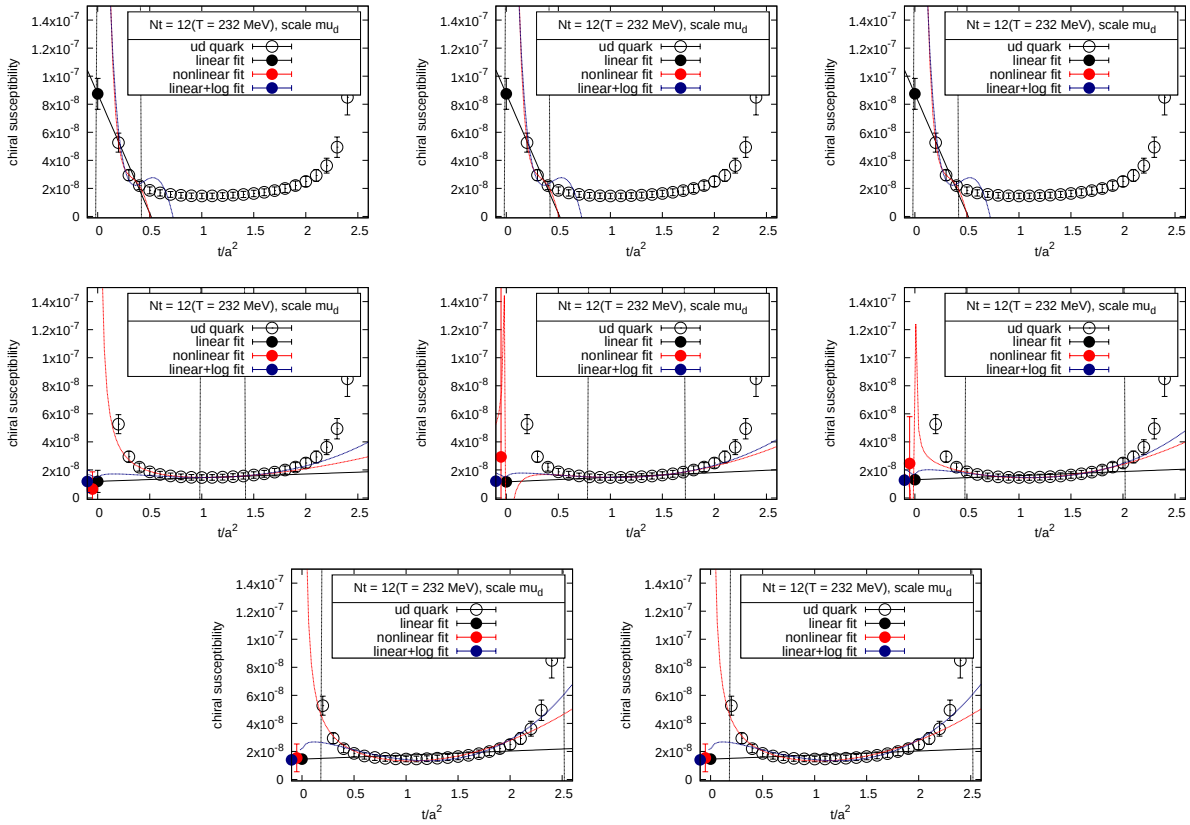

Figure C.23: The disconnected chiral susceptibility $\chi_{ud}^{\rm disc}$ as a function of the flow-time. $N_t = 12$, μ_d. From top-left to the bottom: we vary the cut-off values of the linear fit as a, b, c, ..., h. The pair of dashed vertical lines indicates the window used for the fit at each cut-off. Black solid lines are the fit results of the linear fit and filled circles at $t = 0$ are the results extracted from the fits. Red and blue dashed lines and filled circle at $t \sim 0$ are the results of nonlinear and linear+log fit, respectively.

$N_t = 10$

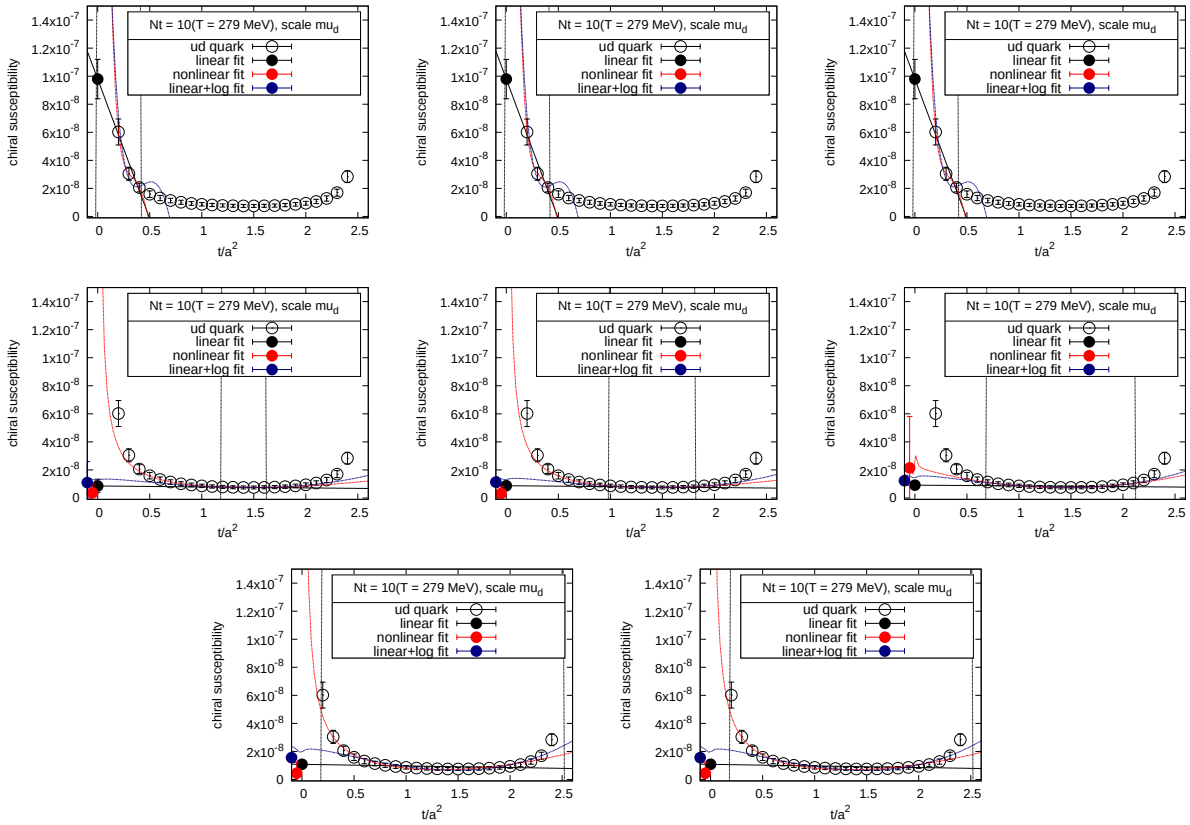

Figure C.24: The disconnected chiral susceptibility $\chi_{ud}^{\rm disc}$ as a function of the flow-time. $N_t = 10$, μ_d. From top-left to the bottom: we vary the cut-off values of the linear fit as a, b, c, ..., h. The pair of dashed vertical lines indicates the window used for the fit at each cut-off. Black solid lines are the fit results of the linear fit and filled circles at $t = 0$ are the results extracted from the fits. Red and blue dashed lines and filled circle at $t \sim 0$ are the results of nonlinear and linear+log fit, respectively.

$N_t = 8$

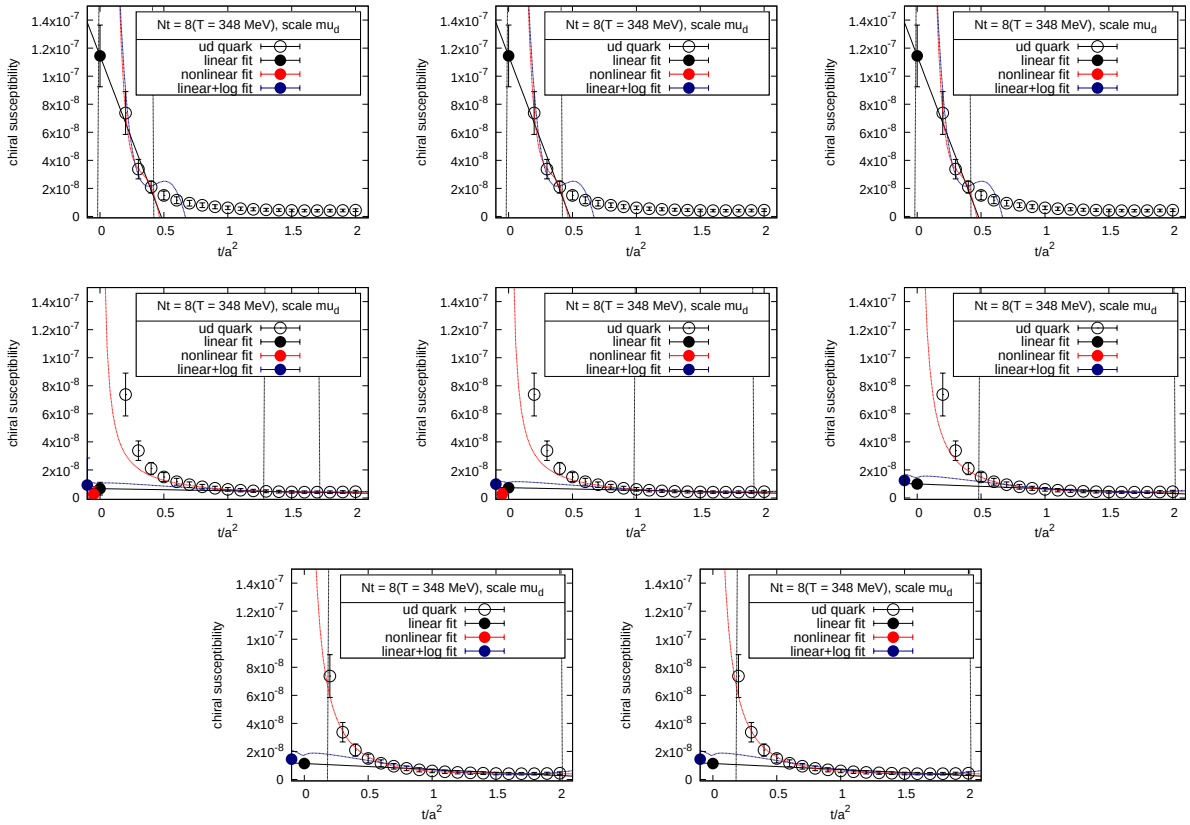

Figure C.25: The disconnected chiral susceptibility $\chi_{ud}^{\rm disc}$ as a function of the flow-time. $N_t = 8$, μ_d. From top-left to the bottom: we vary the cut-off values of the linear fit as a, b, c, ..., h. The pair of dashed vertical lines indicates the window used for the fit at each cut-off. Black solid lines are the fit results of the linear fit and filled circles at $t = 0$ are the results extracted from the fits. Red and blue dashed lines and filled circle at $t \sim 0$ are the results of nonlinear and linear+log fit, respectively.

C.2.6 The disconnected chiral susceptibility , μ_d

$N_t = 16$

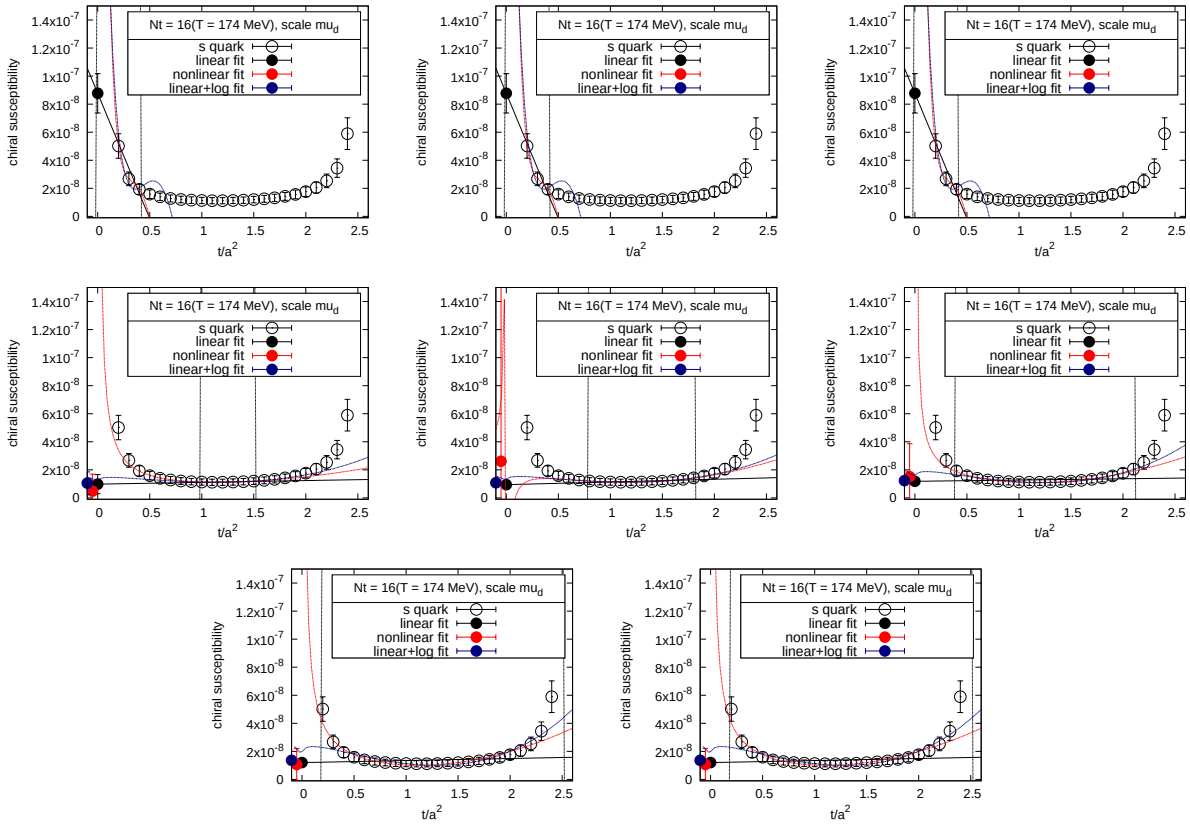

Figure C.26: The disconnected chiral susceptibility $\chi_s^{\rm disc}$ as a function of the flow-time. $N_t = 16$, μ_d. From top-left to the bottom: we vary the cut-off values of the linear fit as a, b, c, ..., h. The pair of dashed vertical lines indicates the window used for the fit at each cut-off. Black solid lines are the fit results of the linear fit and filled circles at $t = 0$ are the results extracted from the fits. Red and blue dashed lines and filled circle at $t \sim 0$ are the results of nonlinear and linear+log fit, respectively.

$N_t = 14$

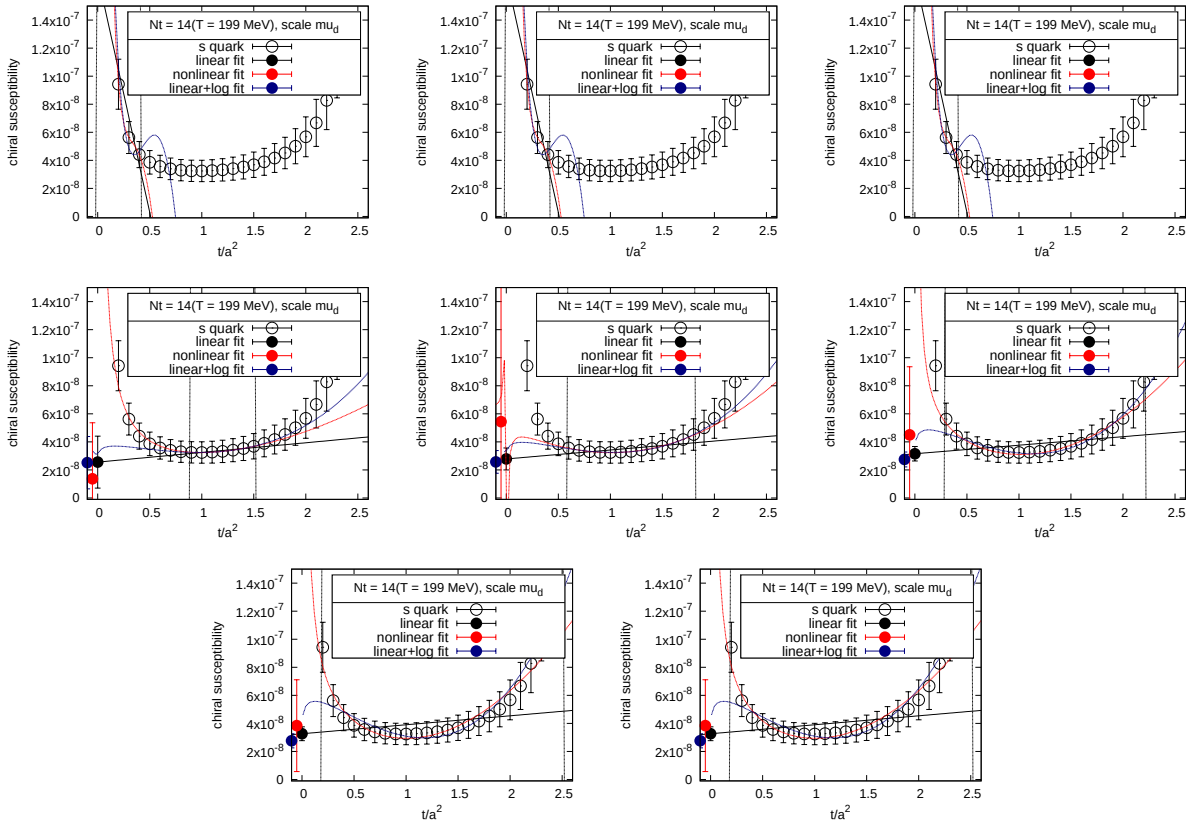

Figure C.27: The disconnected chiral susceptibility $\chi_s^{\rm disc}$ as a function of the flow-time. $N_t = 14$, μ_d. From top-left to the bottom: we vary the cut-off values of the linear fit as a, b, c, ..., h. The pair of dashed vertical lines indicates the window used for the fit at each cut-off. Black solid lines are the fit results of the linear fit and filled circles at $t = 0$ are the results extracted from the fits. Red and blue dashed lines and filled circle at $t \sim 0$ are the results of nonlinear and linear+log fit, respectively.

$N_t = 12$

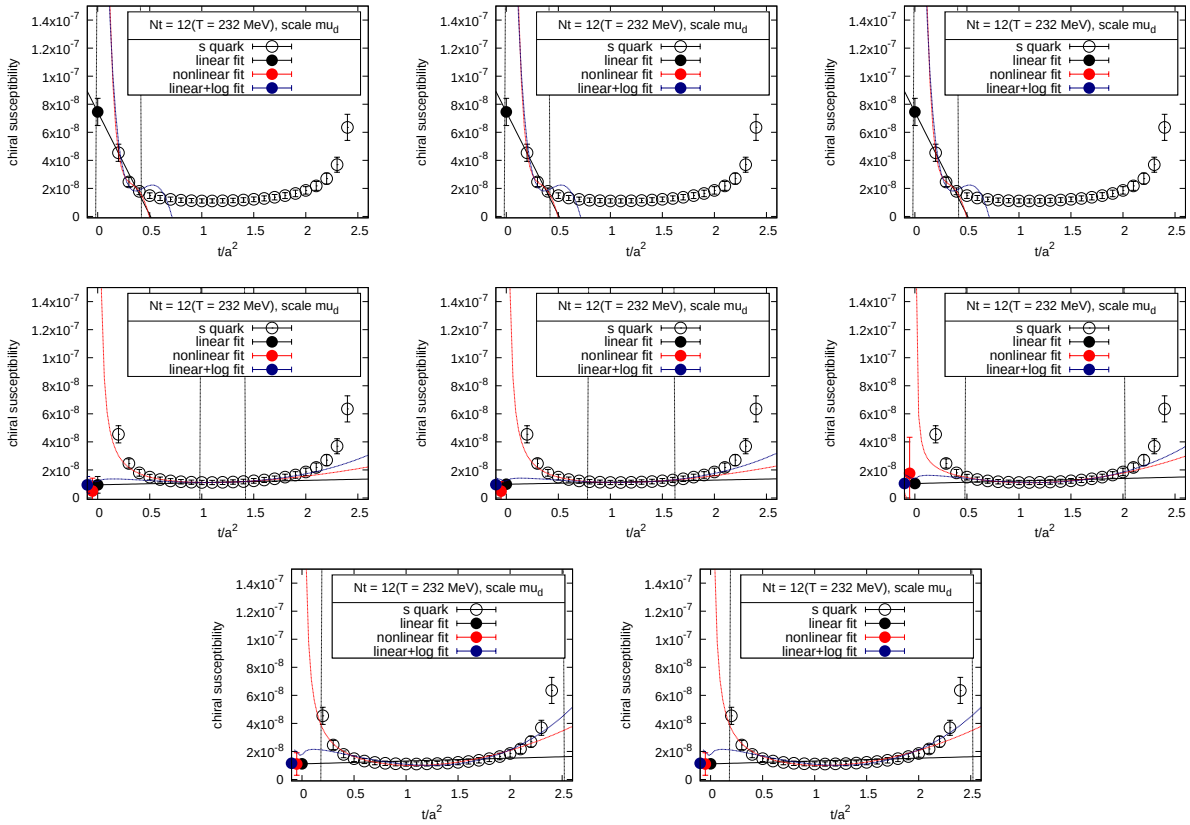

Figure C.28: The disconnected chiral susceptibility $\chi_s^{\rm disc}$ as a function of the flow-time. $N_t = 12$, μ_d. From top-left to the bottom: we vary the cut-off values of the linear fit as a, b, c, ..., h. The pair of dashed vertical lines indicates the window used for the fit at each cut-off. Black solid lines are the fit results of the linear fit and filled circles at $t = 0$ are the results extracted from the fits. Red and blue dashed lines and filled circle at $t \sim 0$ are the results of nonlinear and linear+log fit, respectively.

$N_t = 10$

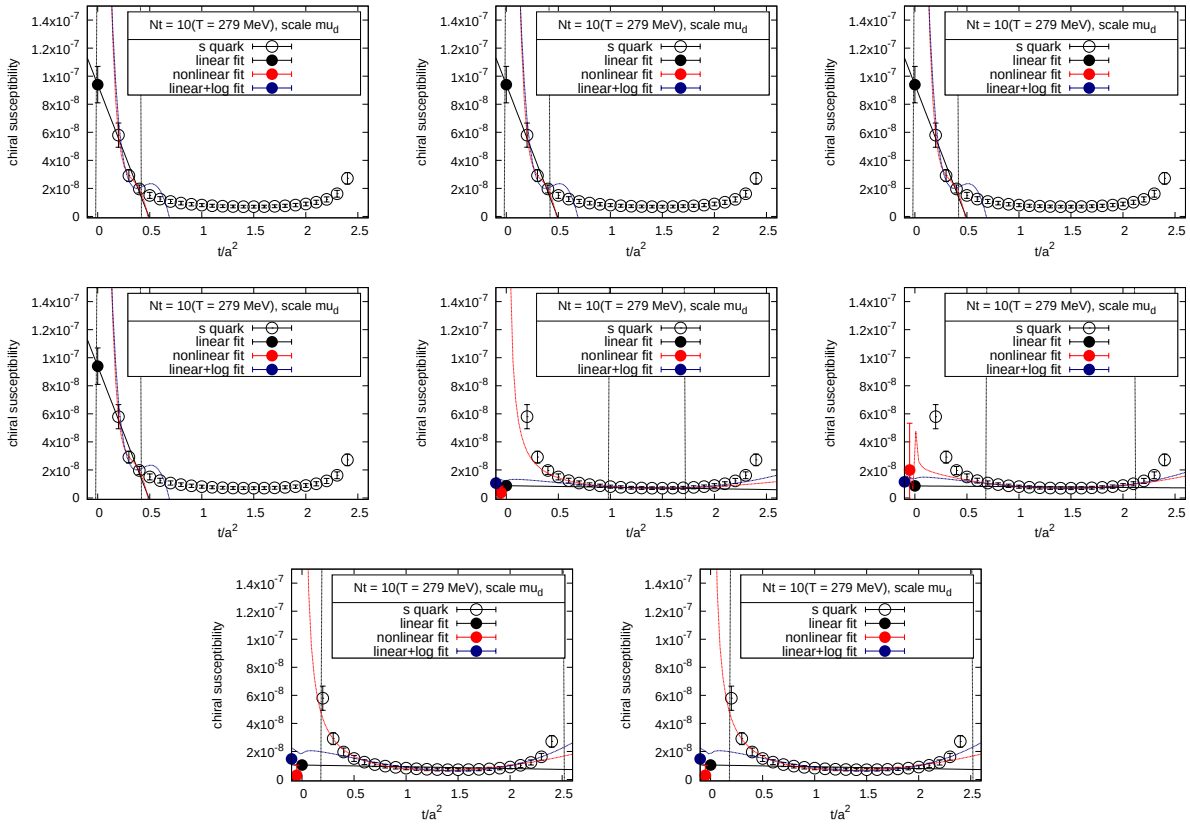

Figure C.29: The disconnected chiral susceptibility $\chi_s^{\rm disc}$ as a function of the flow-time. $N_t = 10$, μ_d. From top-left to the bottom: we vary the cut-off values of the linear fit as a, b, c, ..., h. The pair of dashed vertical lines indicates the window used for the fit at each cut-off. Black solid lines are the fit results of the linear fit and filled circles at $t = 0$ are the results extracted from the fits. Red and blue dashed lines and filled circle at $t \sim 0$ are the results of nonlinear and linear+log fit, respectively.

renewcommand108

$N_t = 10$

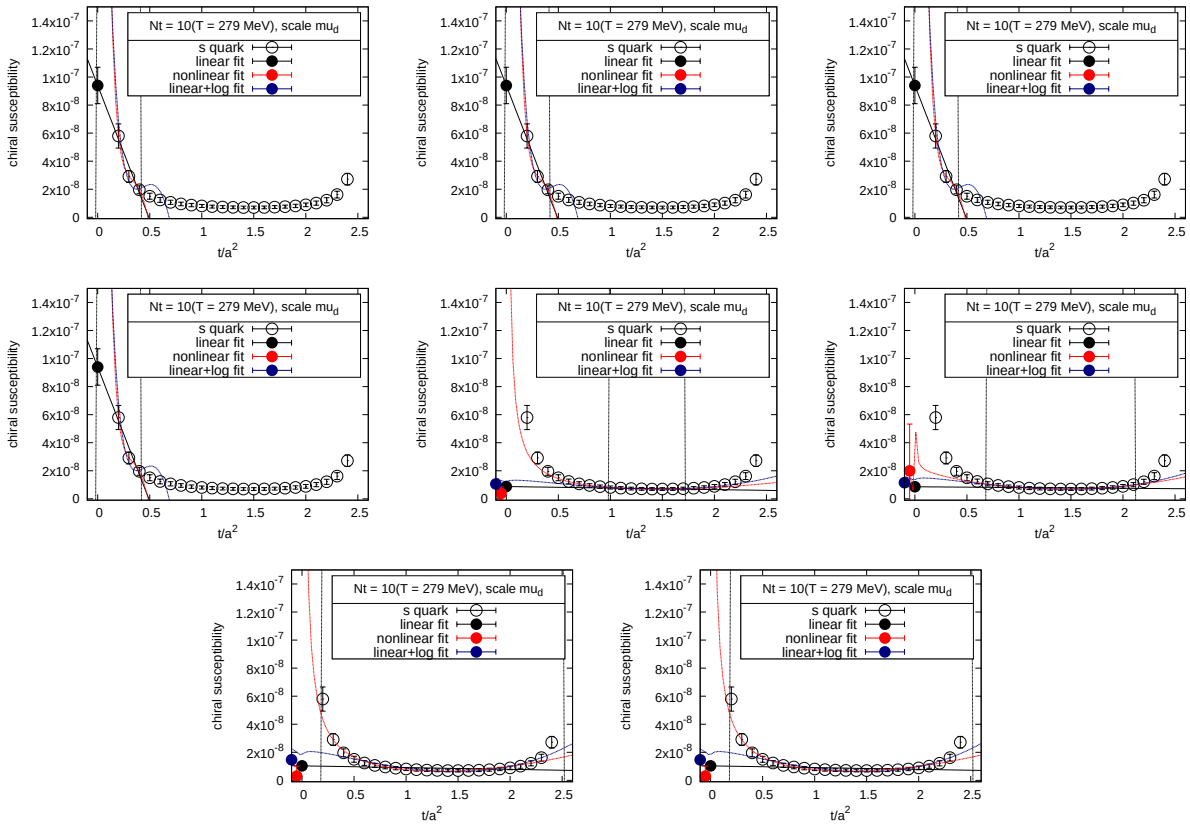

Figure C.30: The disconnected chiral susceptibility $\chi_s^{\rm disc}$ as a function of the flow-time. $N_t = 10$, μ_d. From top-left to the bottom: we vary the cut-off values of the linear fit as a, b, c, ..., h. The pair of dashed vertical lines indicates the window used for the fit at each cut-off. Black solid lines are the fit results of the linear fit and filled circles at $t = 0$ are the results extracted from the fits. Red and blue dashed lines and filled circle at $t \sim 0$ are the results of nonlinear and linear+log fit, respectively.

C.2.7 The disconnected chiral susceptibility , μ_0

$N_t = 16$

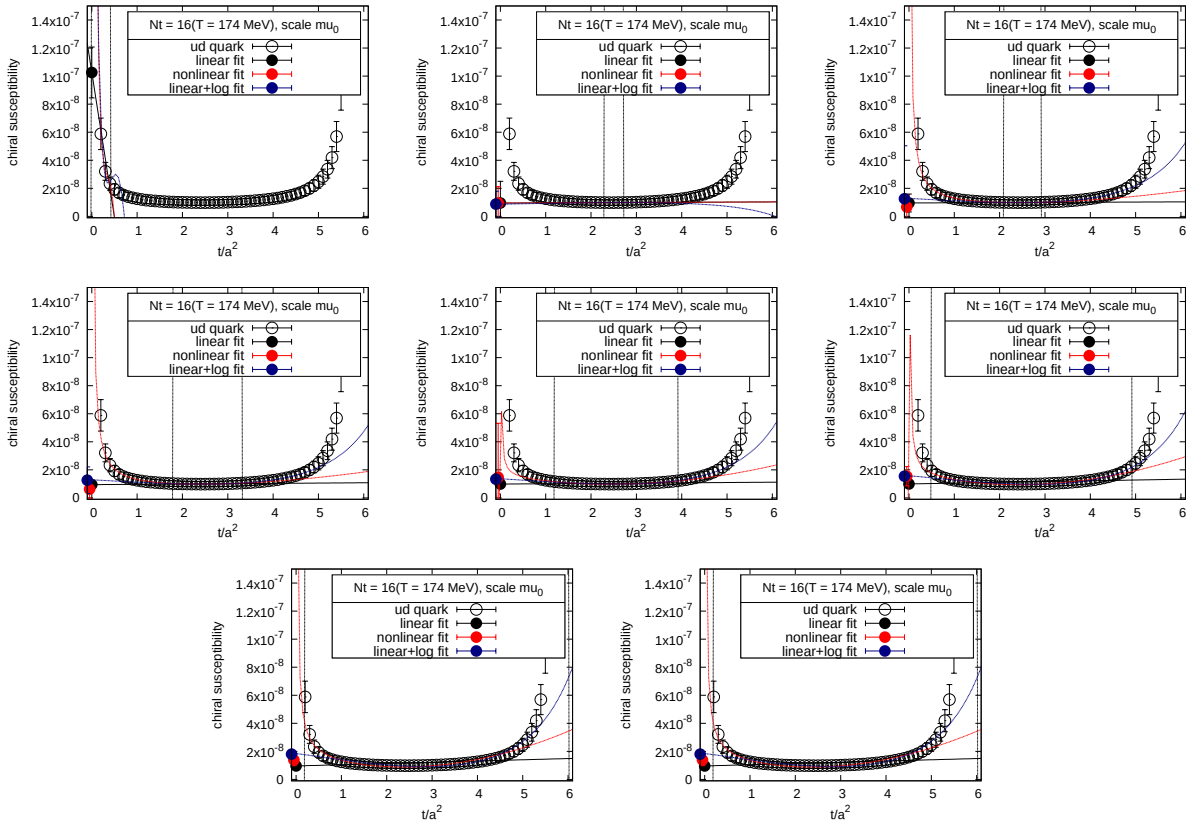

Figure C.31: The disconnected chiral susceptibility $\chi_{ud}^{\rm disc}$ as a function of the flow-time. $N_t = 16$, μ_0. From top-left to the bottom: we vary the cut-off values of the linear fit as a, b, c, ..., h. The pair of dashed vertical lines indicates the window used for the fit at each cut-off. Black solid lines are the fit results of the linear fit and filled circles at $t = 0$ are the results extracted from the fits. Red and blue dashed lines and filled circle at $t \sim 0$ are the results of nonlinear and linear+log fit, respectively.

$N_t = 14$

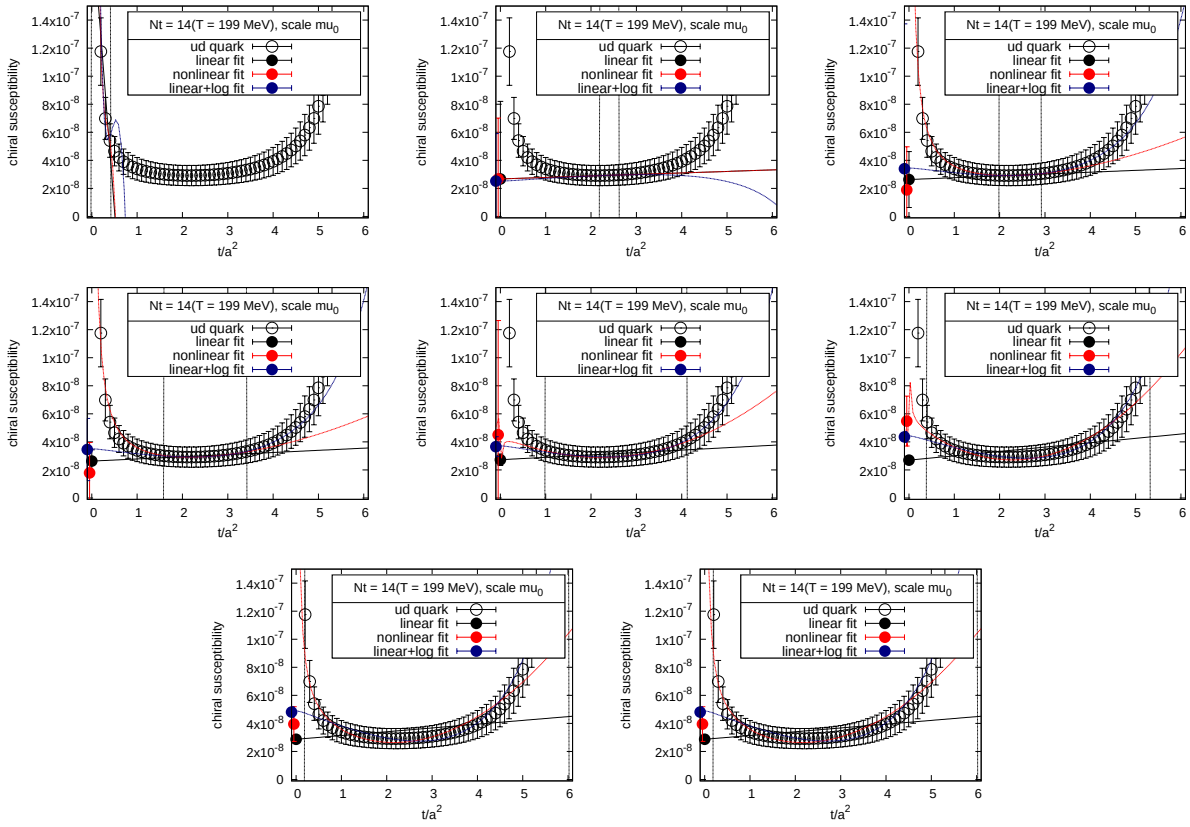

Figure C.32: The disconnected chiral susceptibility $\chi_{ud}^{\rm disc}$ as a function of the flow-time. $N_t = 14$, μ_0. From top-left to the bottom: we vary the cut-off values of the linear fit as a, b, c, ..., h. The pair of dashed vertical lines indicates the window used for the fit at each cut-off. Black solid lines are the fit results of the linear fit and filled circles at $t = 0$ are the results extracted from the fits. Red and blue dashed lines and filled circle at $t \sim 0$ are the results of nonlinear and linear+log fit, respectively.

$N_t = 12$

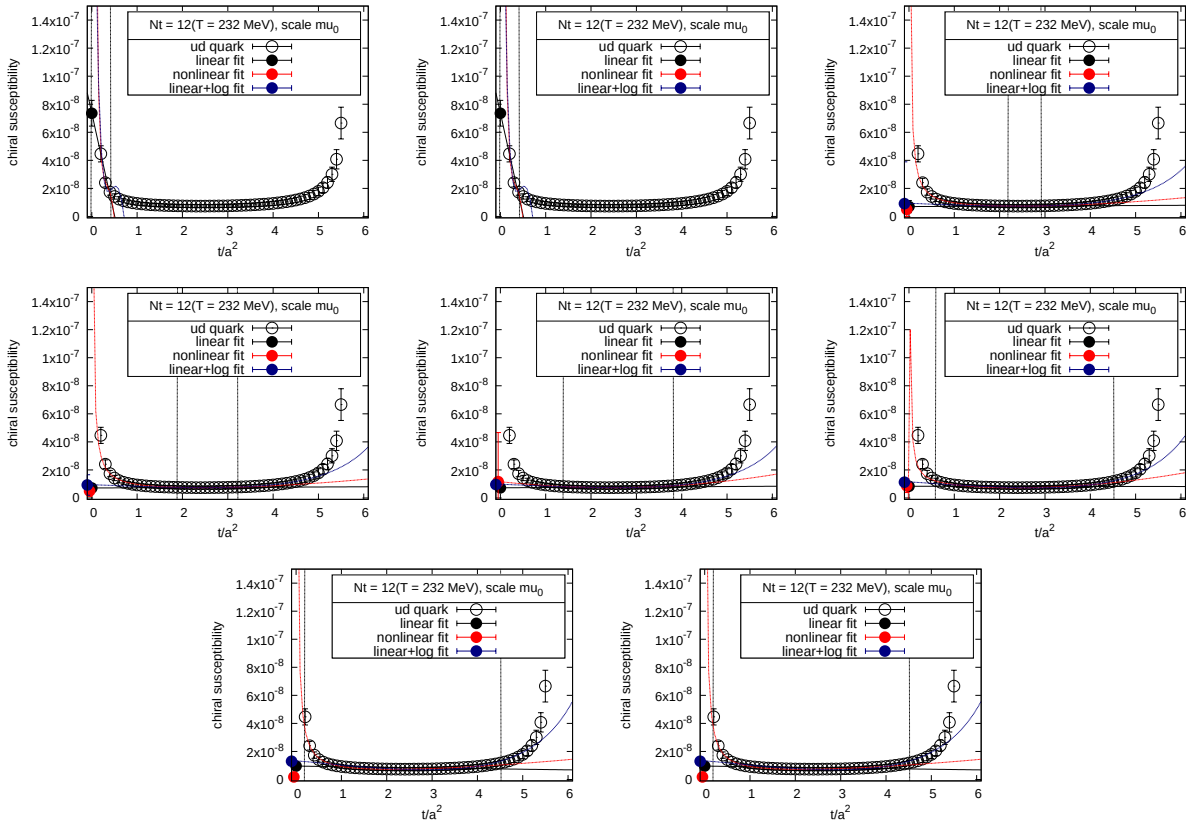

Figure C.33: The disconnected chiral susceptibility $\chi_{ud}^{\mathrm{disc}}$ as a function of the flow-time. $N_t = 12$, μ_0. From top-left to the bottom: we vary the cut-off values of the linear fit as a, b, c, ..., h. The pair of dashed vertical lines indicates the window used for the fit at each cut-off. Black solid lines are the fit results of the linear fit and filled circles at $t = 0$ are the results extracted from the fits. Red and blue dashed lines and filled circle at $t \sim 0$ are the results of nonlinear and linear+log fit, respectively.

$N_t = 10$

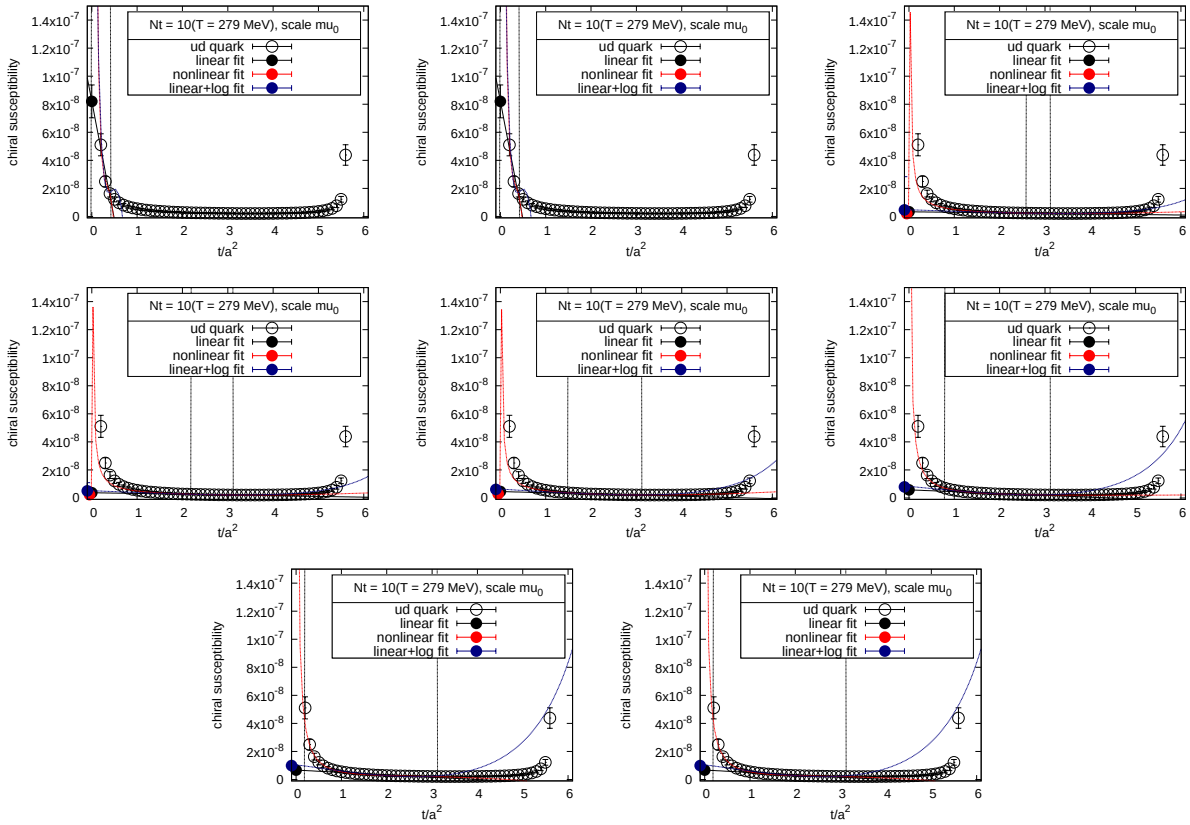

Figure C.34: The disconnected chiral susceptibility $\chi_{ud}^{\rm disc}$ as a function of the flow-time. $N_t = 10$, μ_0. From top-left to the bottom: we vary the cut-off values of the linear fit as a, b, c, ..., h. The pair of dashed vertical lines indicates the window used for the fit at each cut-off. Black solid lines are the fit results of the linear fit and filled circles at $t = 0$ are the results extracted from the fits. Red and blue dashed lines and filled circle at $t \sim 0$ are the results of nonlinear and linear+log fit, respectively.

$N_t = 8$

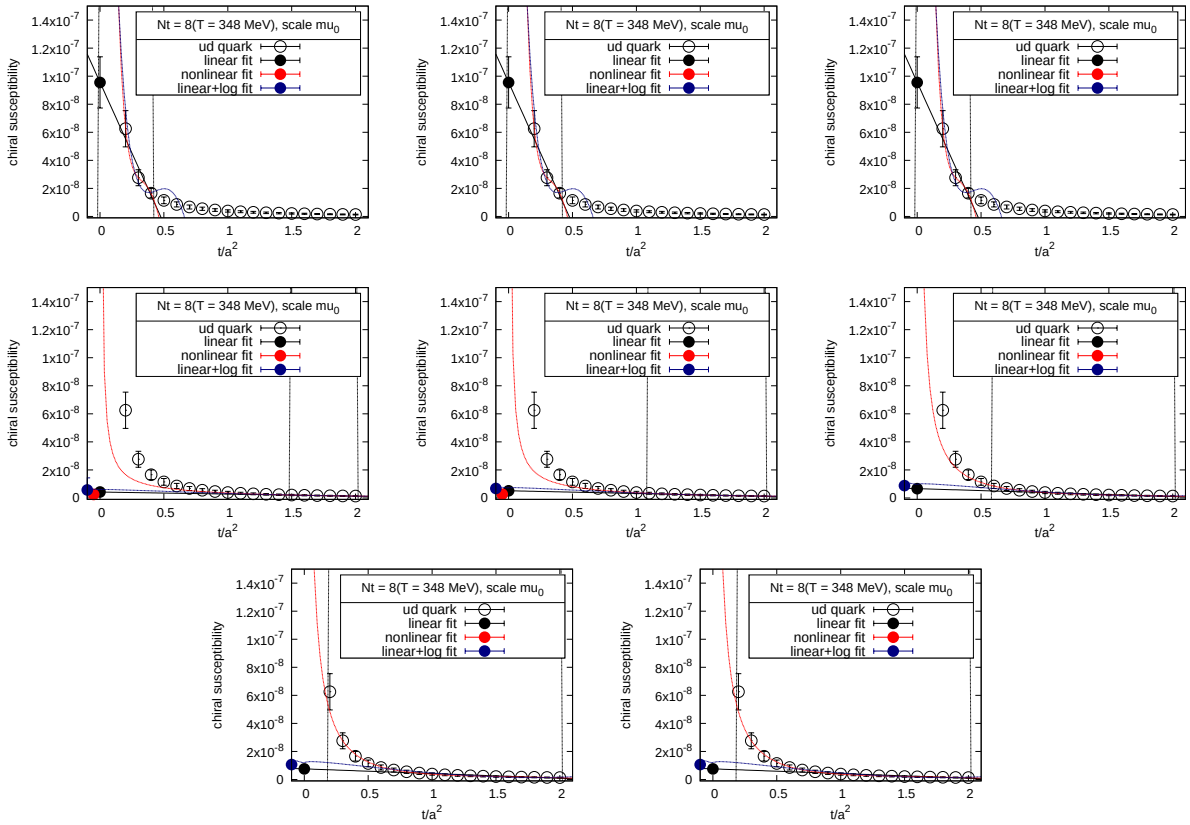

Figure C.35: The disconnected chiral susceptibility $\chi_{ud}^{\rm disc}$ as a function of the flow-time. $N_t = 8$, μ_0. From top-left to the bottom: we vary the cut-off values of the linear fit as a, b, c, ..., h. The pair of dashed vertical lines indicates the window used for the fit at each cut-off. Black solid lines are the fit results of the linear fit and filled circles at $t = 0$ are the results extracted from the fits. Red and blue dashed lines and filled circle at $t \sim 0$ are the results of nonlinear and linear+log fit, respectively.

C.2.8 The disconnected chiral susceptibility , μ_0

$N_t = 16$

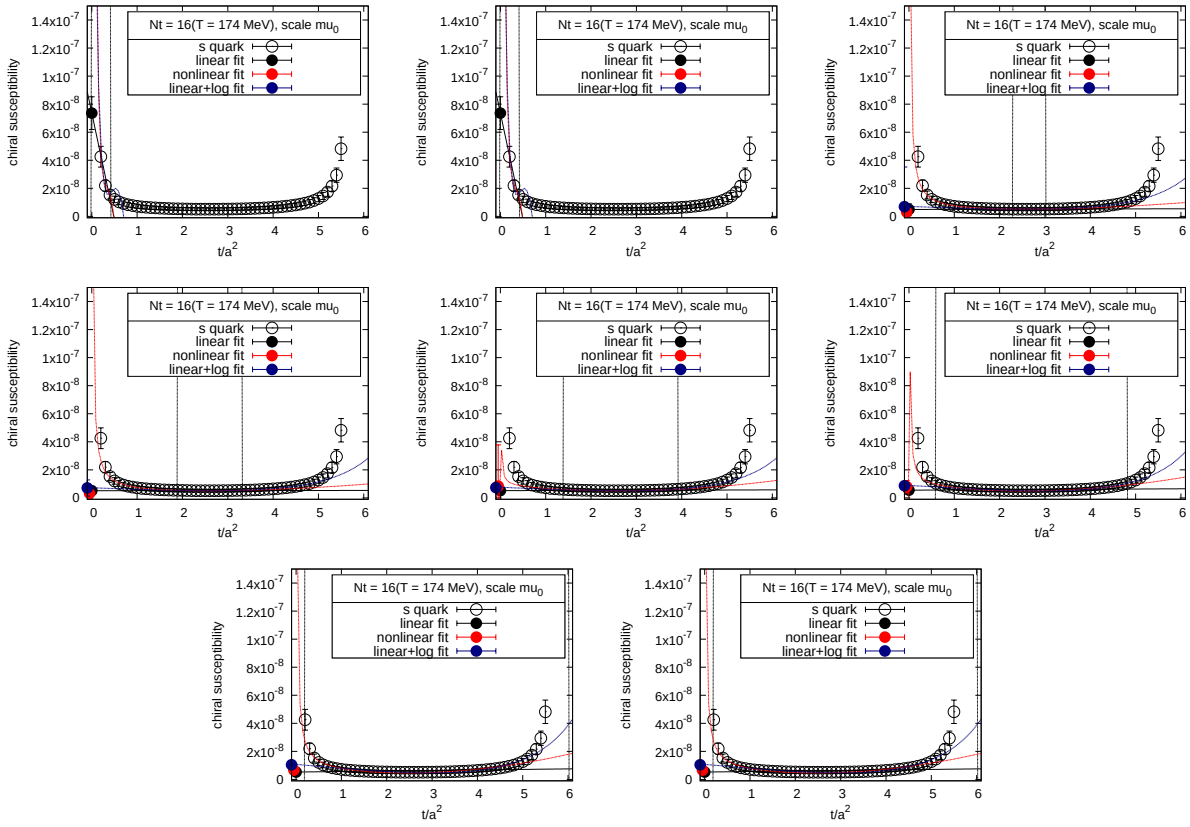

Figure C.36: The disconnected chiral susceptibility $\chi_s^{\rm disc}$ as a function of the flow-time. $N_t = 16$, μ_0. From top-left to the bottom: we vary the cut-off values of the linear fit as a, b, c, ..., h. The pair of dashed vertical lines indicates the window used for the fit at each cut-off. Black solid lines are the fit results of the linear fit and filled circles at $t = 0$ are the results extracted from the fits. Red and blue dashed lines and filled circle at $t \sim 0$ are the results of nonlinear and linear+log fit, respectively.

$N_t = 14$

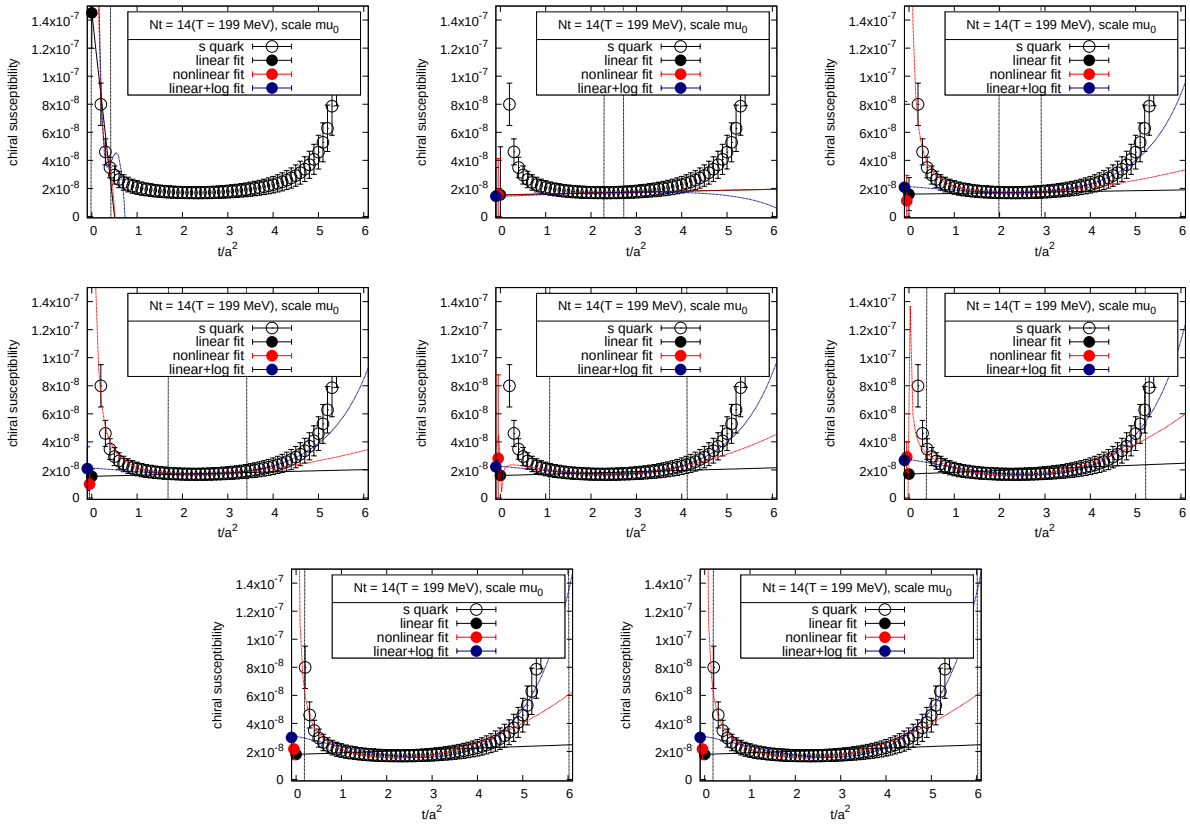

Figure C.37: The disconnected chiral susceptibility $\chi_s^{\rm disc}$ as a function of the flow-time. $N_t = 14$, μ_0. From top-left to the bottom: we vary the cut-off values of the linear fit as a, b, c, ..., h. The pair of dashed vertical lines indicates the window used for the fit at each cut-off. Black solid lines are the fit results of the linear fit and filled circles at $t = 0$ are the results extracted from the fits. Red and blue dashed lines and filled circle at $t \sim 0$ are the results of nonlinear and linear+log fit, respectively.

$N_t = 12$

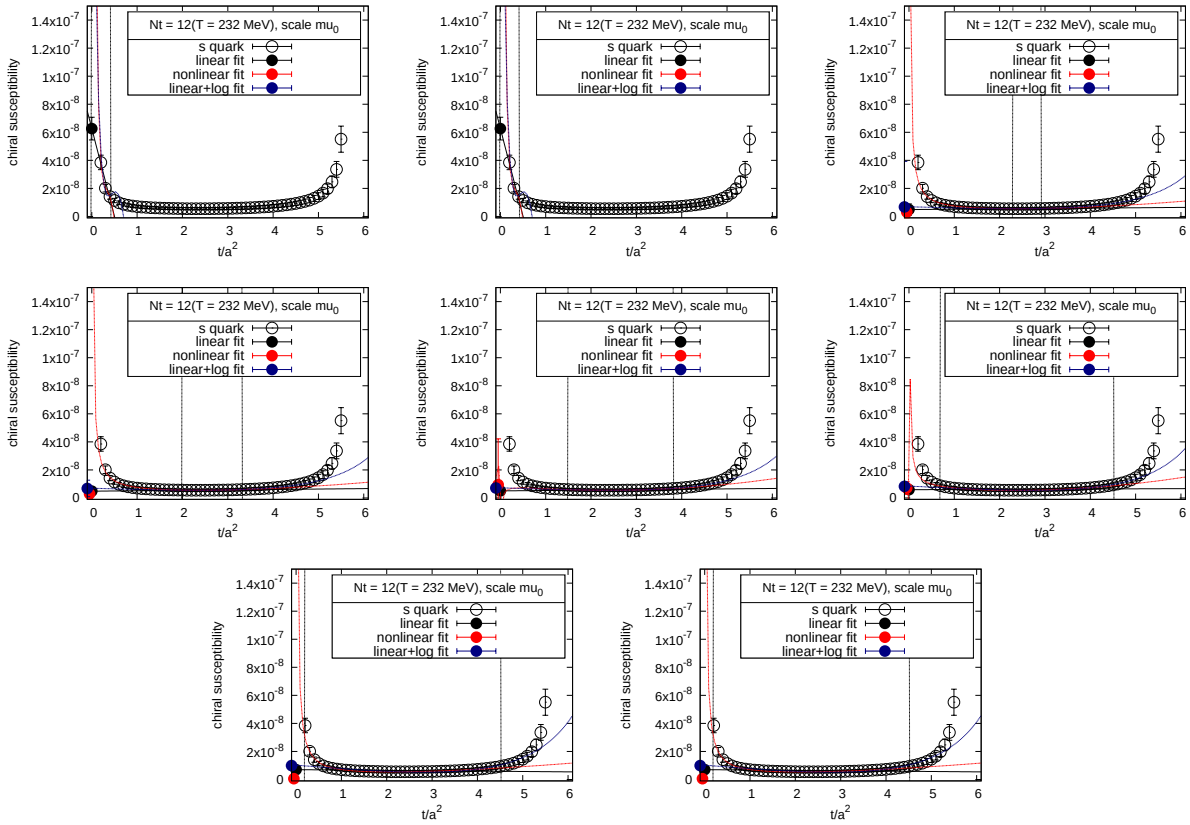

Figure C.38: The disconnected chiral susceptibility $\chi_s^{\rm disc}$ as a function of the flow-time. $N_t = 12$, μ_0. From top-left to the bottom: we vary the cut-off values of the linear fit as a, b, c, ..., h. The pair of dashed vertical lines indicates the window used for the fit at each cut-off. Black solid lines are the fit results of the linear fit and filled circles at $t = 0$ are the results extracted from the fits. Red and blue dashed lines and filled circle at $t \sim 0$ are the results of nonlinear and linear+log fit, respectively.

$N_t = 10$

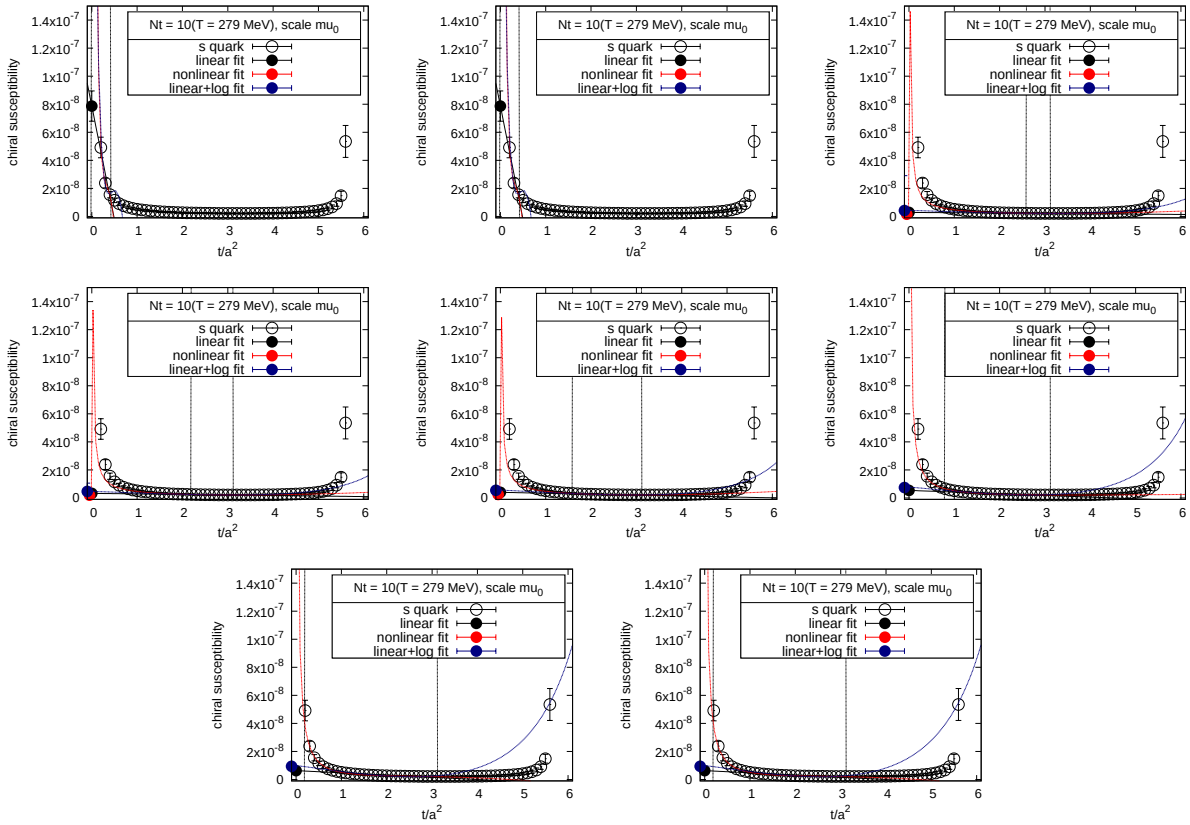

Figure C.39: The disconnected chiral susceptibility $\chi_s^{\rm disc}$ as a function of the flow-time. $N_t = 10$, μ_0. From top-left to the bottom: we vary the cut-off values of the linear fit as a, b, c, ..., h. The pair of dashed vertical lines indicates the window used for the fit at each cut-off. Black solid lines are the fit results of the linear fit and filled circles at $t = 0$ are the results extracted from the fits. Red and blue dashed lines and filled circle at $t \sim 0$ are the results of nonlinear and linear+log fit, respectively.

$N_t = 8$

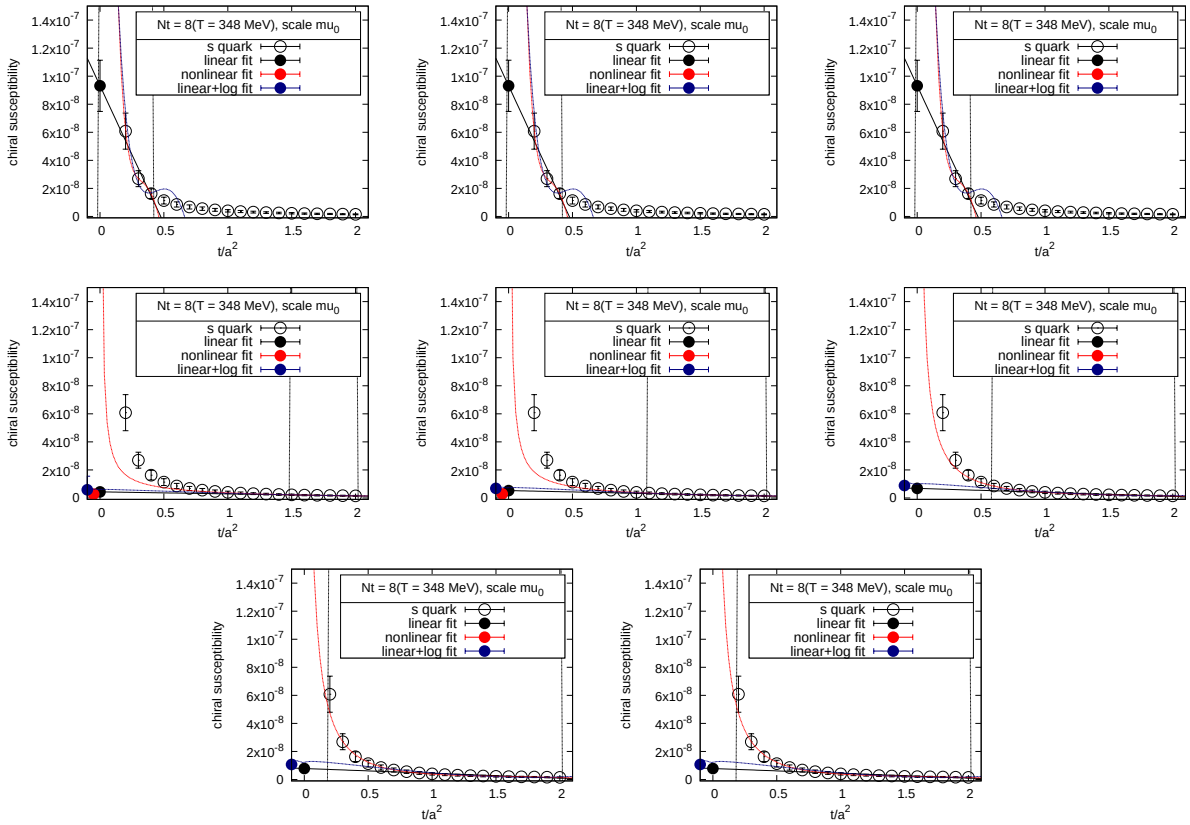

Figure C.40: The disconnected chiral susceptibility $\chi_s^{\rm disc}$ as a function of the flow-time. $N_t = 8$, μ_0. From top-left to the bottom: we vary the cut-off values of the linear fit as a, b, c, ..., h. The pair of dashed vertical lines indicates the window used for the fit at each cut-off. Black solid lines are the fit results of the linear fit and filled circles at $t = 0$ are the results extracted from the fits. Red and blue dashed lines and filled circle at $t \sim 0$ are the results of nonlinear and linear+log fit, respectively.

C.2.9 The connected part of chiral susceptibility $\chi_{ud}^{\mathrm{conn}}$, μ_d

$N_t = 16$

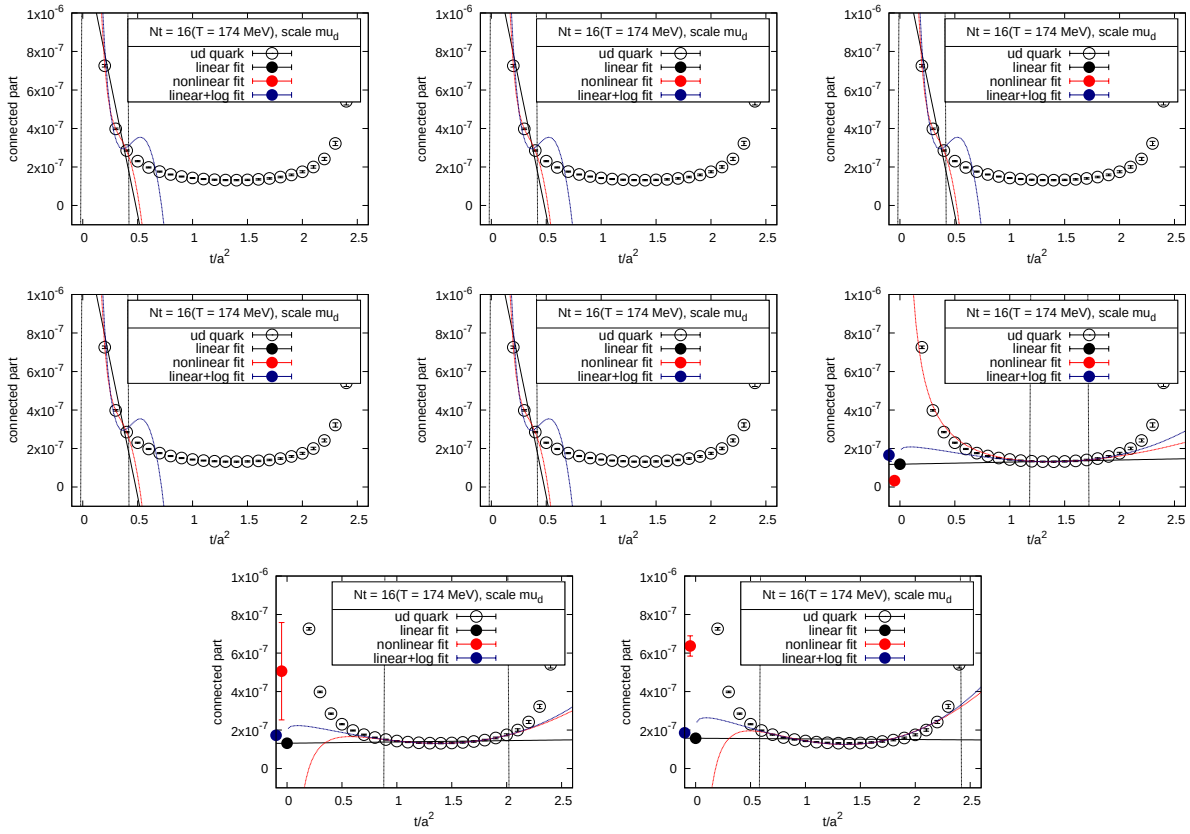

Figure C.41: The connected part of chiral susceptibility $\chi_{ud}^{\mathrm{conn}}$ as a function of the flow-time. $N_t = 16$, μ_d. From top-left to the bottom: we vary the cut-off values of the linear fit as a, b, c, ..., h. The pair of dashed vertical lines indicates the window used for the fit at each cut-off. Black solid lines are the fit results of the linear fit and filled circles at $t = 0$ are the results extracted from the fits. Red and blue dashed lines and filled circle at $t \sim 0$ are the results of nonlinear and linear+log fit, respectively.

$N_t = 14$

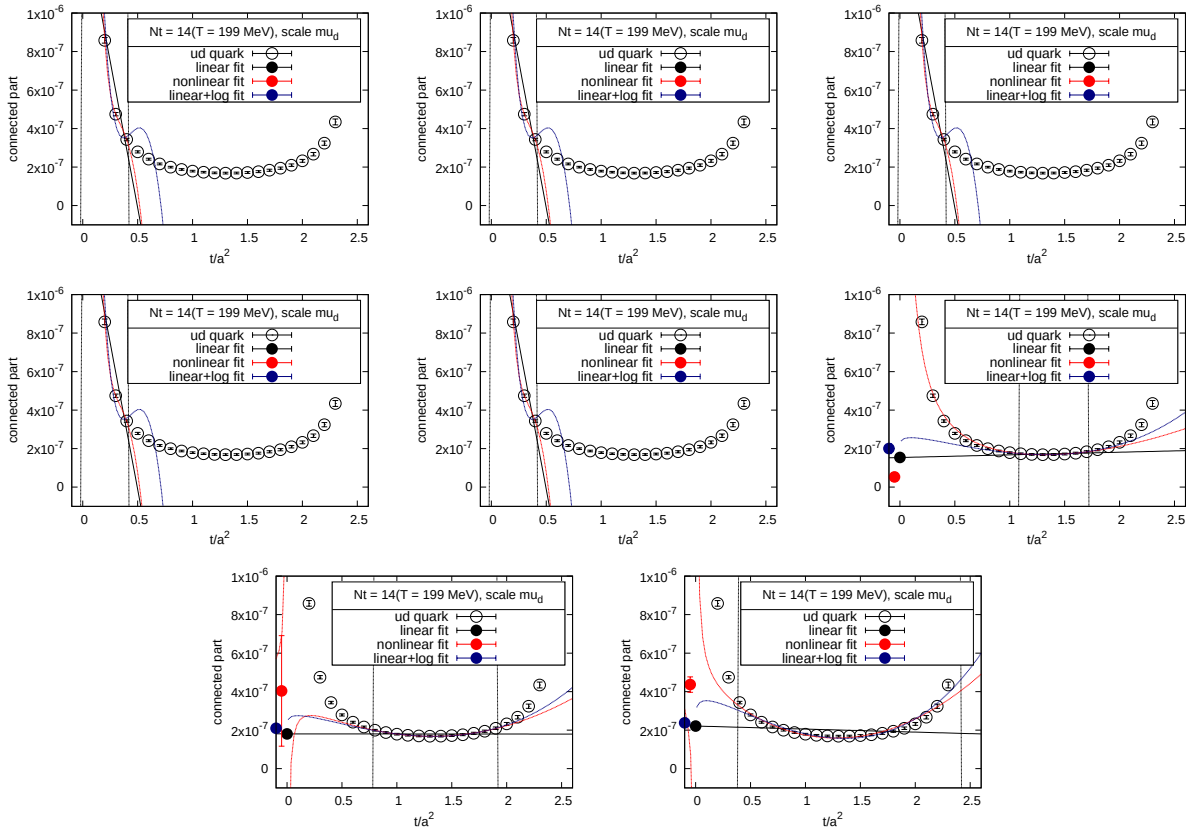

Figure C.42: The connected part of chiral susceptibility $\chi_{ud}^{\rm conn}$ as a function of the flow-time. $N_t = 14$, μ_d. From top-left to the bottom: we vary the cut-off values of the linear fit as a, b, c, ..., h. The pair of dashed vertical lines indicates the window used for the fit at each cut-off. Black solid lines are the fit results of the linear fit and filled circles at $t = 0$ are the results extracted from the fits. Red and blue dashed lines and filled circle at $t \sim 0$ are the results of nonlinear and linear+log fit, respectively.

$N_t = 12$

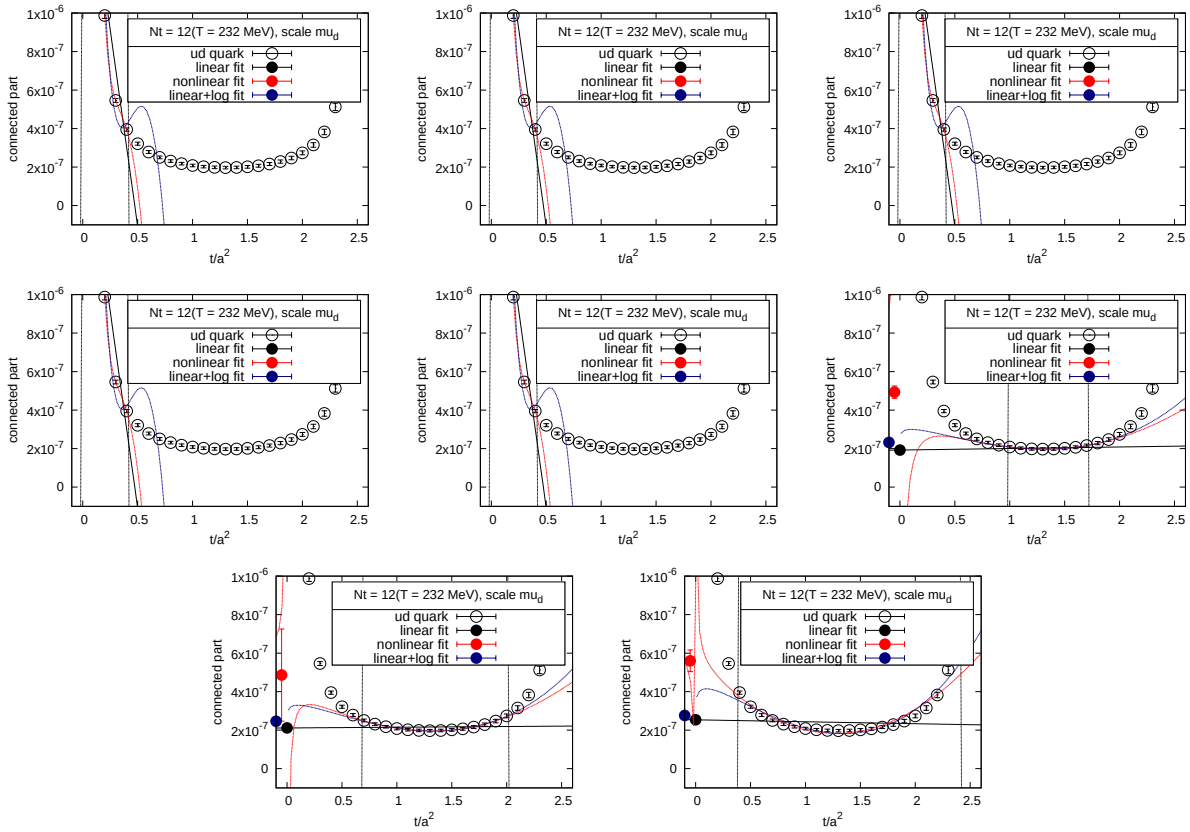

Figure C.43: The connected part of chiral susceptibility $\chi_{ud}^{\rm conn}$ as a function of the flow-time. $N_t = 12$, μ_d. From top-left to the bottom: we vary the cut-off values of the linear fit as a, b, c, ..., h. The pair of dashed vertical lines indicates the window used for the fit at each cut-off. Black solid lines are the fit results of the linear fit and filled circles at $t = 0$ are the results extracted from the fits. Red and blue dashed lines and filled circle at $t \sim 0$ are the results of nonlinear and linear+log fit, respectively.

$N_t = 10$

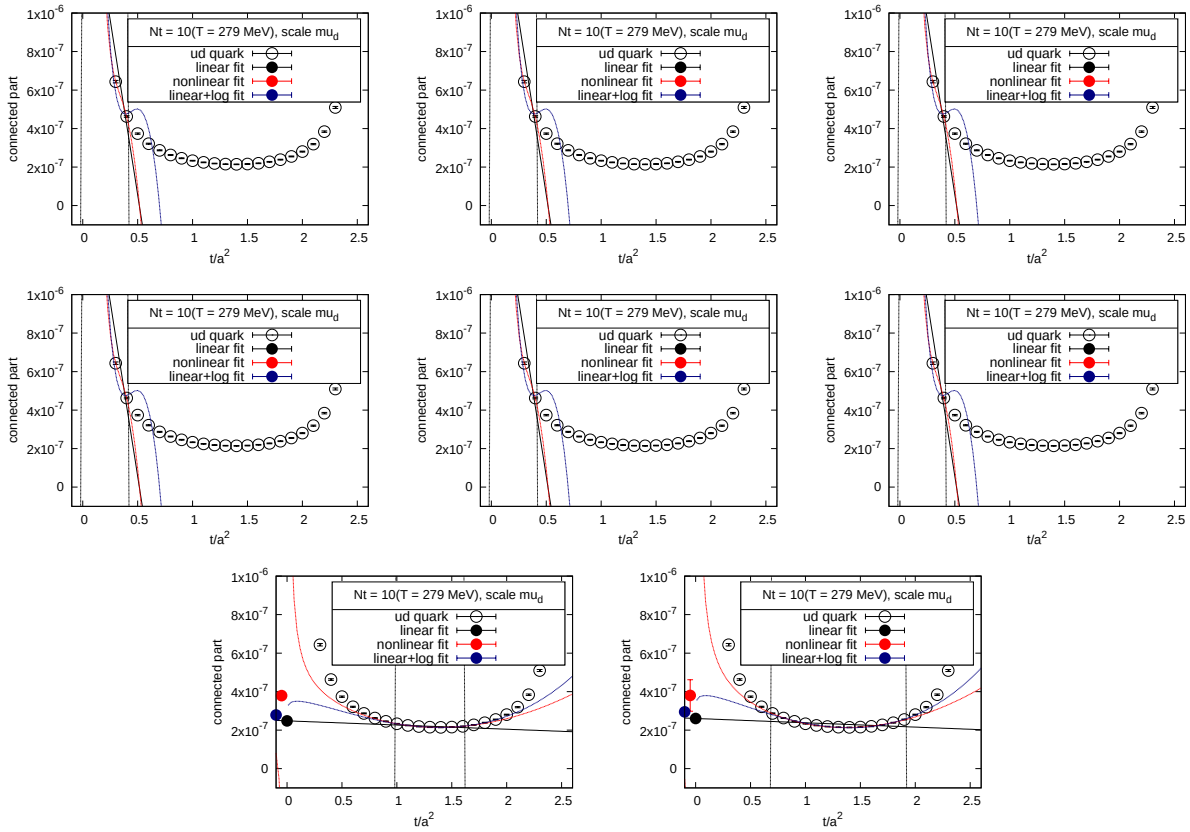

Figure C.44: The connected part of chiral susceptibility $\chi_{ud}^{\rm conn}$ as a function of the flow-time. $N_t = 10$, μ_d. From top-left to the bottom: we vary the cut-off values of the linear fit as a, b, c, ..., h. The pair of dashed vertical lines indicates the window used for the fit at each cut-off. Black solid lines are the fit results of the linear fit and filled circles at $t = 0$ are the results extracted from the fits. Red and blue dashed lines and filled circle at $t \sim 0$ are the results of nonlinear and linear+log fit, respectively.

$N_t = 8$

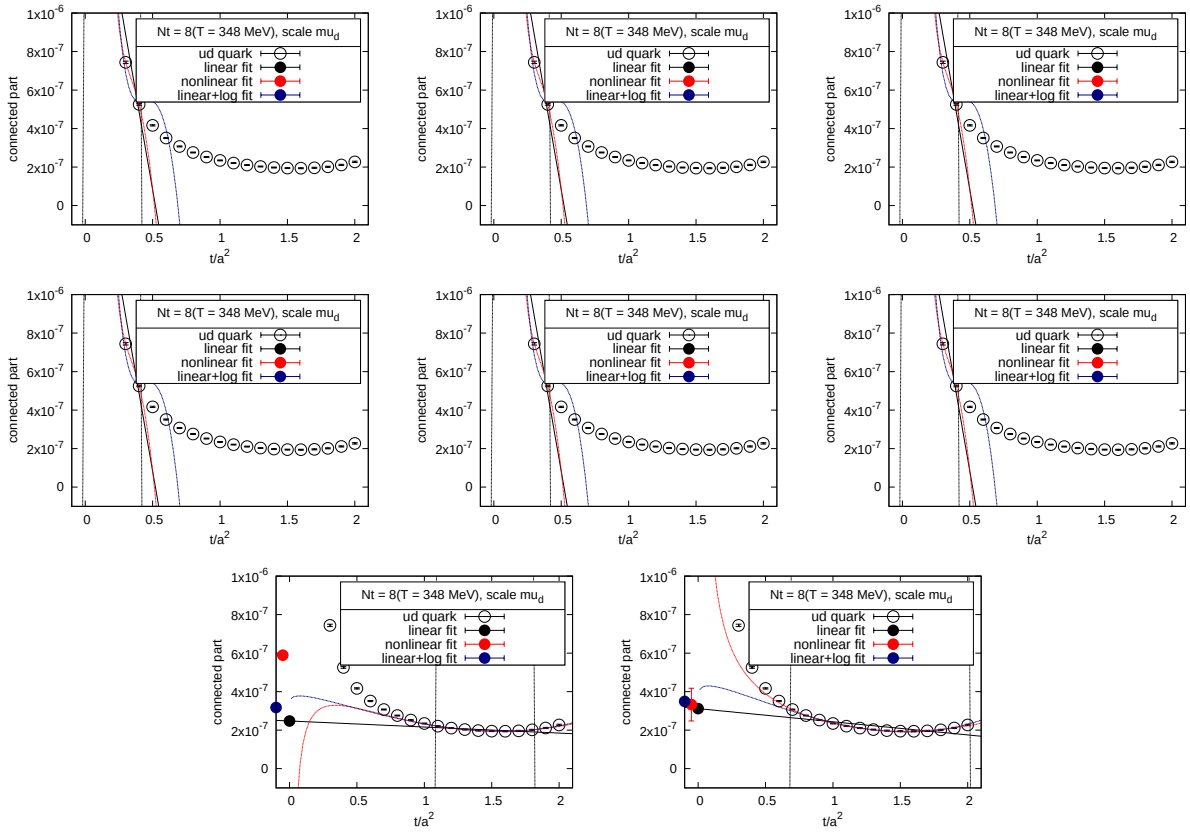

Figure C.45: The connected part of chiral susceptibility $\chi_{ud}^{\rm conn}$ as a function of the flow-time. $N_t = 8$, μ_d. From top-left to the bottom: we vary the cut-off values of the linear fit as a, b, c, ..., h. The pair of dashed vertical lines indicates the window used for the fit at each cut-off. Black solid lines are the fit results of the linear fit and filled circles at $t = 0$ are the results extracted from the fits. Red and blue dashed lines and filled circle at $t \sim 0$ are the results of nonlinear and linear+log fit, respectively.

C.2.10 The connected part of chiral susceptibility , μ_d

$N_t = 16$

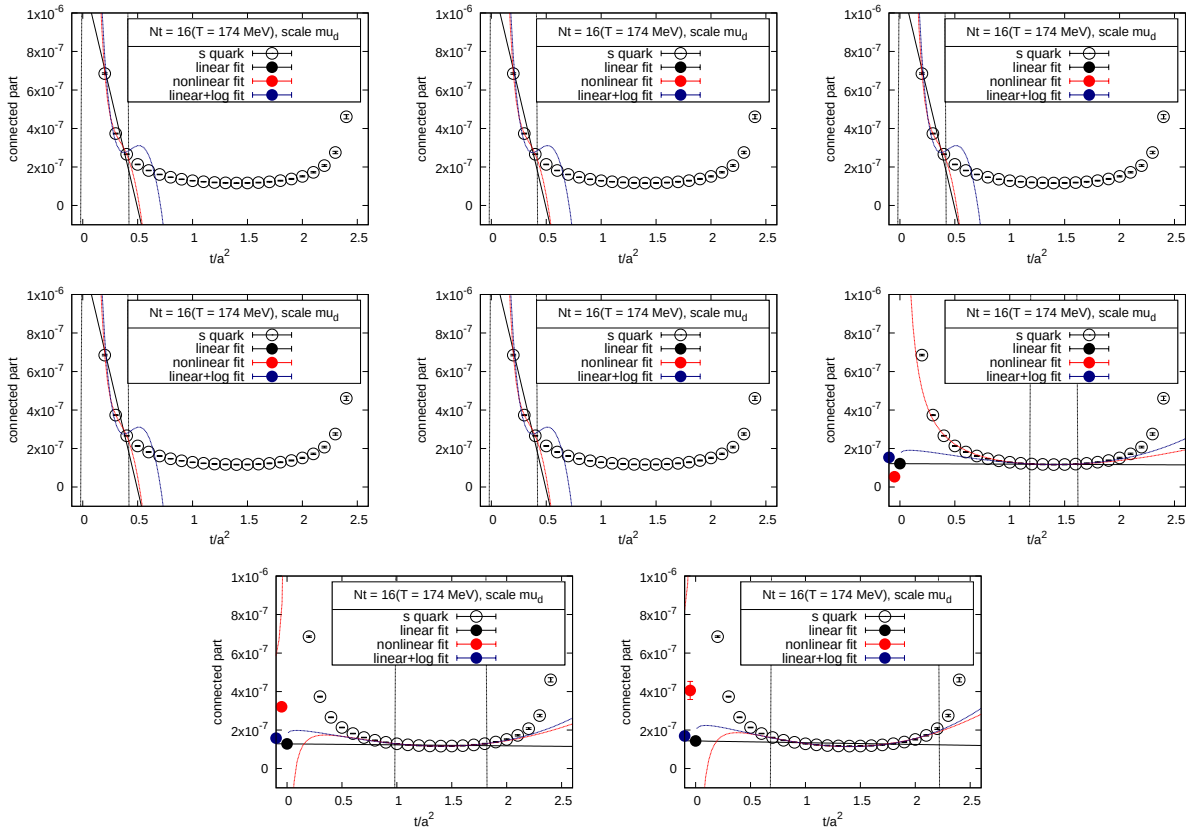

Figure C.46: The connected part of chiral susceptibility $\chi_s^{\rm conn}$ as a function of the flow-time. $N_t = 16$, μ_d. From top-left to the bottom: we vary the cut-off values of the linear fit as a, b, c, ..., h. The pair of dashed vertical lines indicates the window used for the fit at each cut-off. Black solid lines are the fit results of the linear fit and filled circles at $t = 0$ are the results extracted from the fits. Red and blue dashed lines and filled circle at $t \sim 0$ are the results of nonlinear and linear+log fit, respectively.

$N_t = 14$

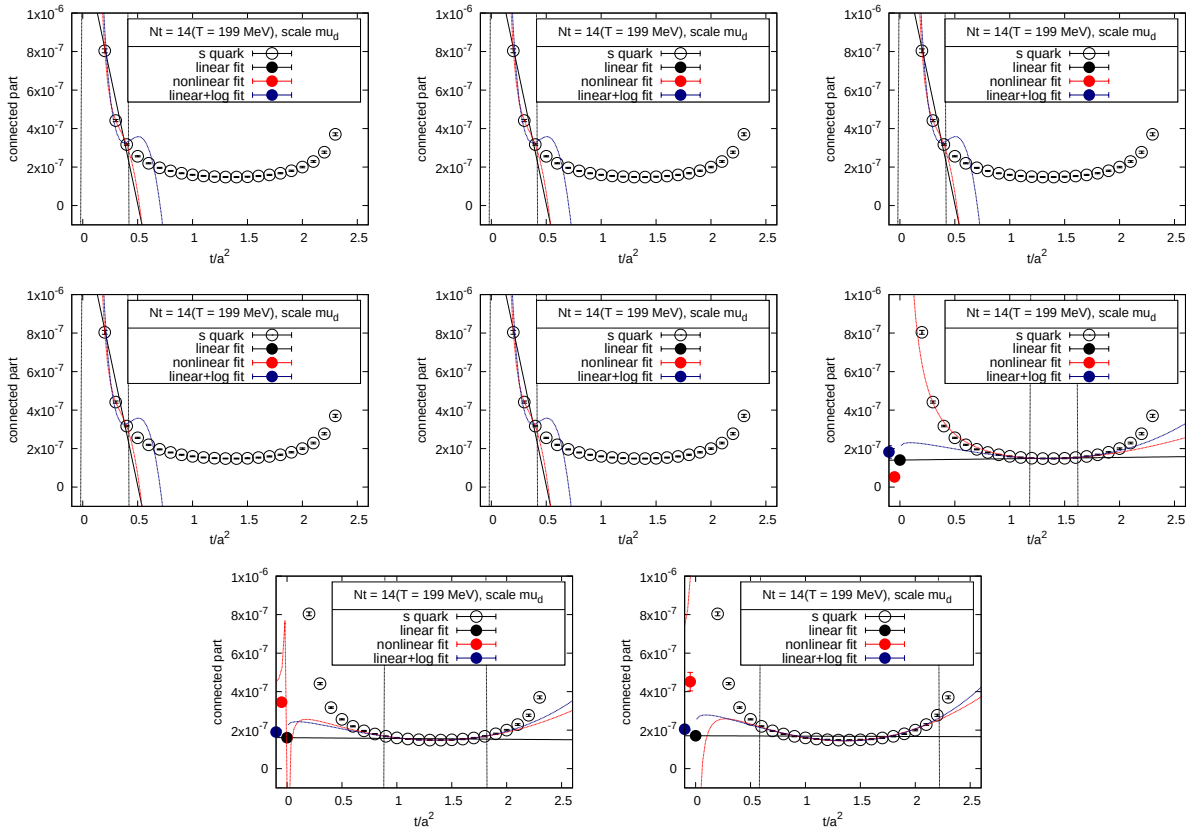

Figure C.47: The connected part of chiral susceptibility $\chi_s^{\rm conn}$ as a function of the flow-time. $N_t = 14$, μ_d. From top-left to the bottom: we vary the cut-off values of the linear fit as a, b, c, ..., h. The pair of dashed vertical lines indicates the window used for the fit at each cut-off. Black solid lines are the fit results of the linear fit and filled circles at $t = 0$ are the results extracted from the fits. Red and blue dashed lines and filled circle at $t \sim 0$ are the results of nonlinear and linear+log fit, respectively.

$N_t = 12$

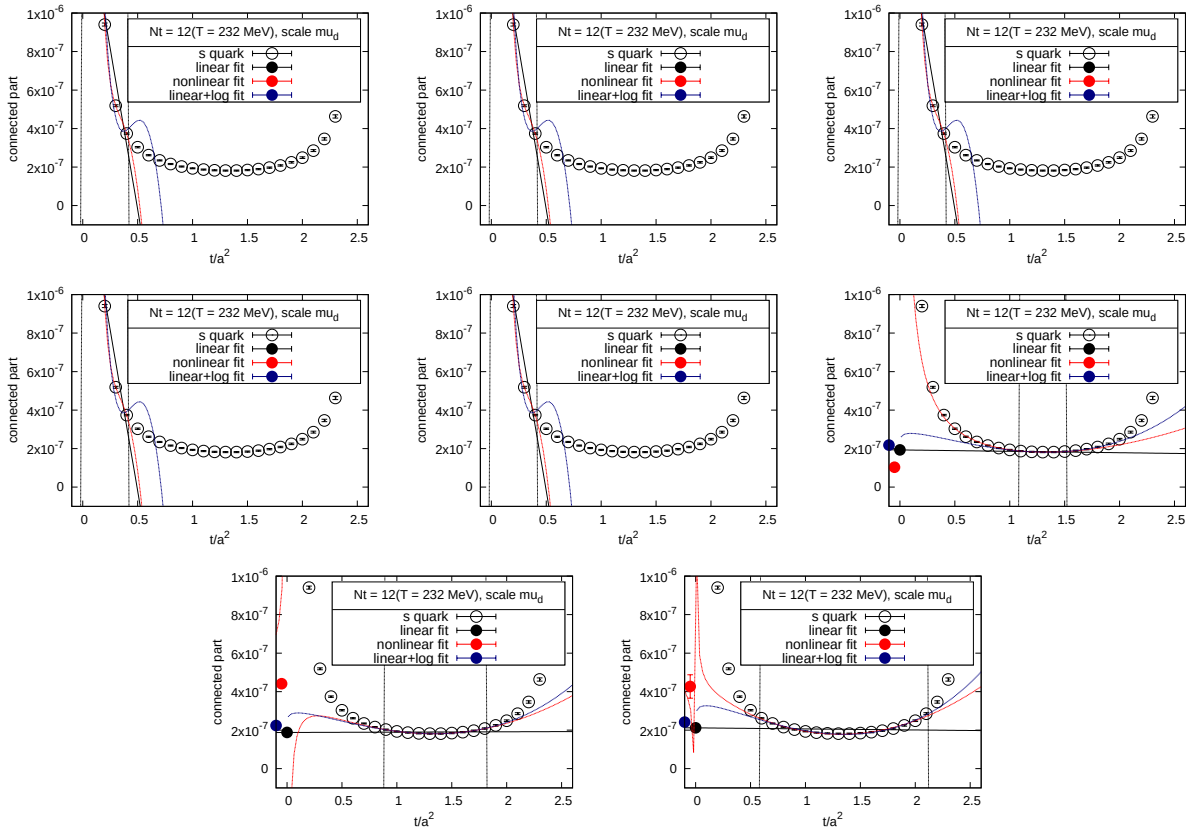

Figure C.48: The connected part of chiral susceptibility $\chi_s^{\rm conn}$ as a function of the flow-time. $N_t = 12$, μ_d. From top-left to the bottom: we vary the cut-off values of the linear fit as a, b, c, ..., h. The pair of dashed vertical lines indicates the window used for the fit at each cut-off. Black solid lines are the fit results of the linear fit and filled circles at $t = 0$ are the results extracted from the fits. Red and blue dashed lines and filled circle at $t \sim 0$ are the results of nonlinear and linear+log fit, respectively.

$N_t = 10$

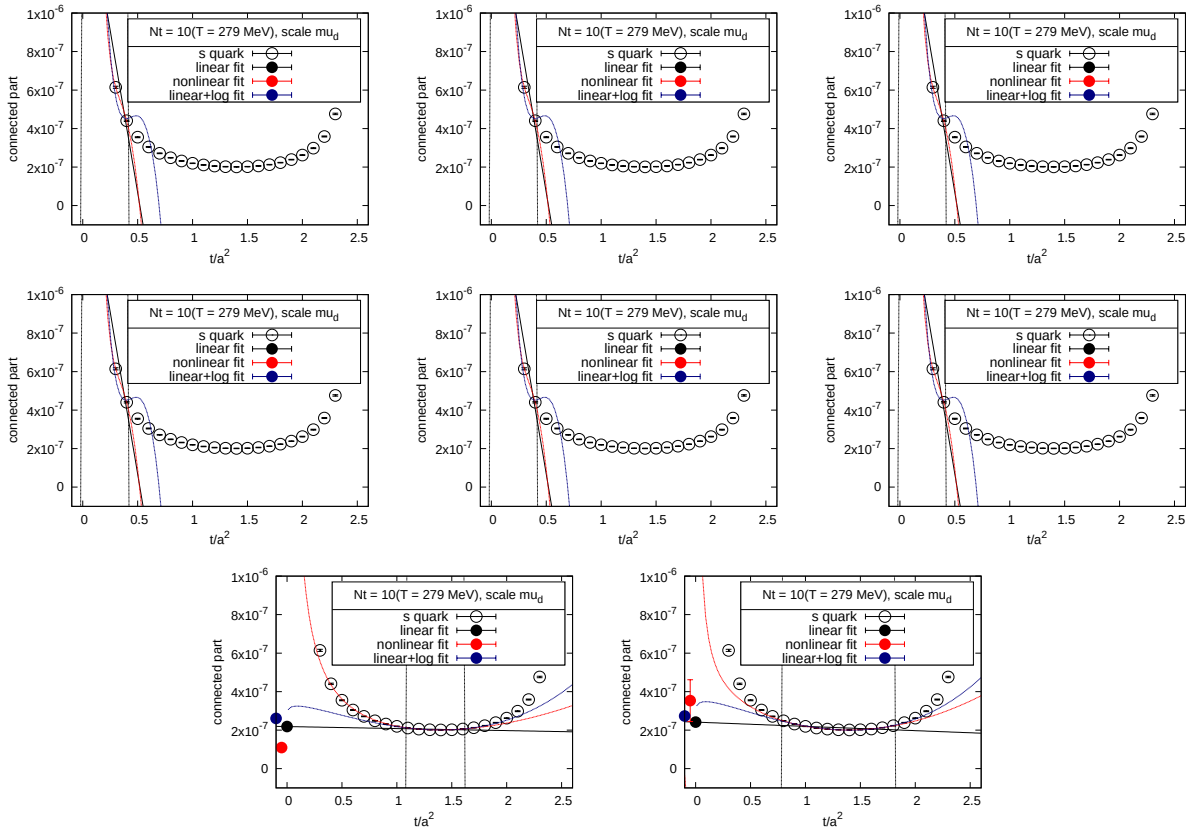

Figure C.49: The connected part of chiral susceptibility $\chi_s^{\rm conn}$ as a function of the flow-time. $N_t = 10$, μ_d. From top-left to the bottom: we vary the cut-off values of the linear fit as a, b, c, ..., h. The pair of dashed vertical lines indicates the window used for the fit at each cut-off. Black solid lines are the fit results of the linear fit and filled circles at $t = 0$ are the results extracted from the fits. Red and blue dashed lines and filled circle at $t \sim 0$ are the results of nonlinear and linear+log fit, respectively.

renewcommand108

$N_t = 10$

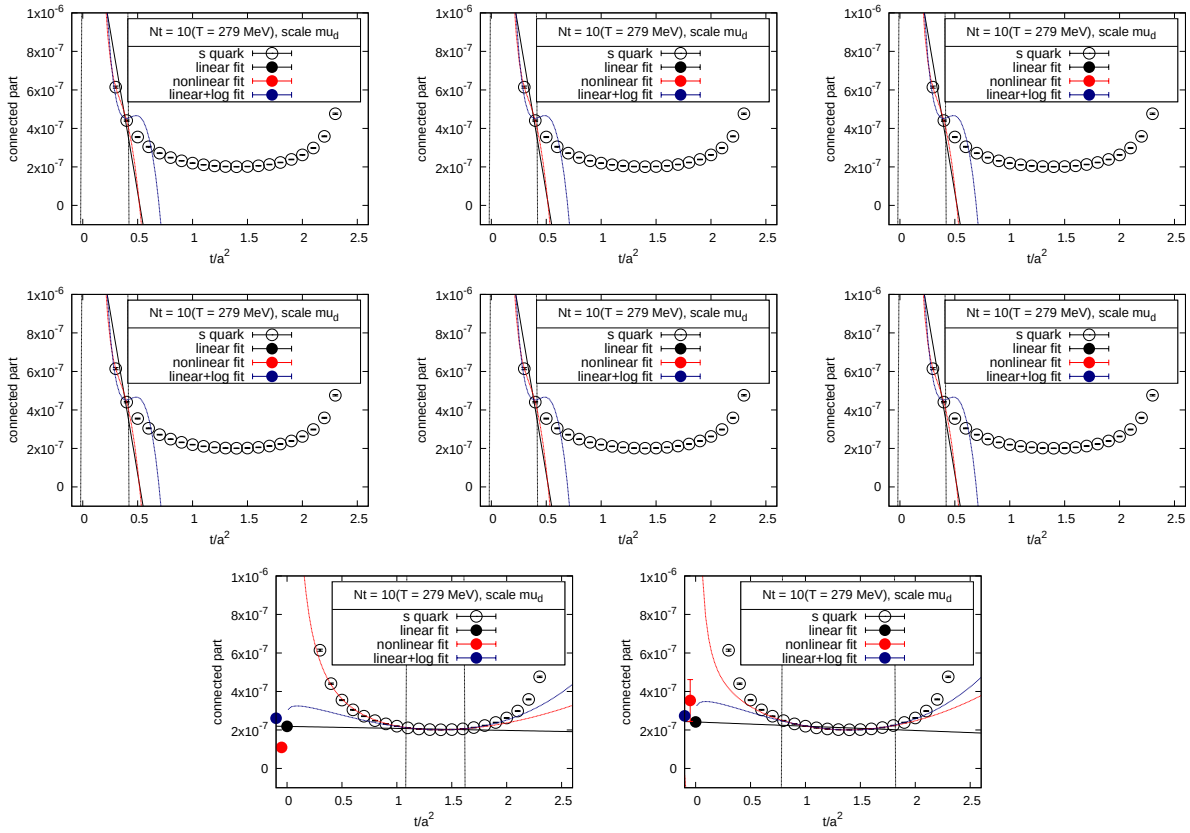

Figure C.50: The connected part of chiral susceptibility $\chi_s^{\rm conn}$ as a function of the flow-time. $N_t = 10$, μ_d. From top-left to the bottom: we vary the cut-off values of the linear fit as a, b, c, ..., h. The pair of dashed vertical lines indicates the window used for the fit at each cut-off. Black solid lines are the fit results of the linear fit and filled circles at $t = 0$ are the results extracted from the fits. Red and blue dashed lines and filled circle at $t \sim 0$ are the results of nonlinear and linear+log fit, respectively.

C.2.11 The connected part of chiral susceptibility , μ_0

$N_t = 16$

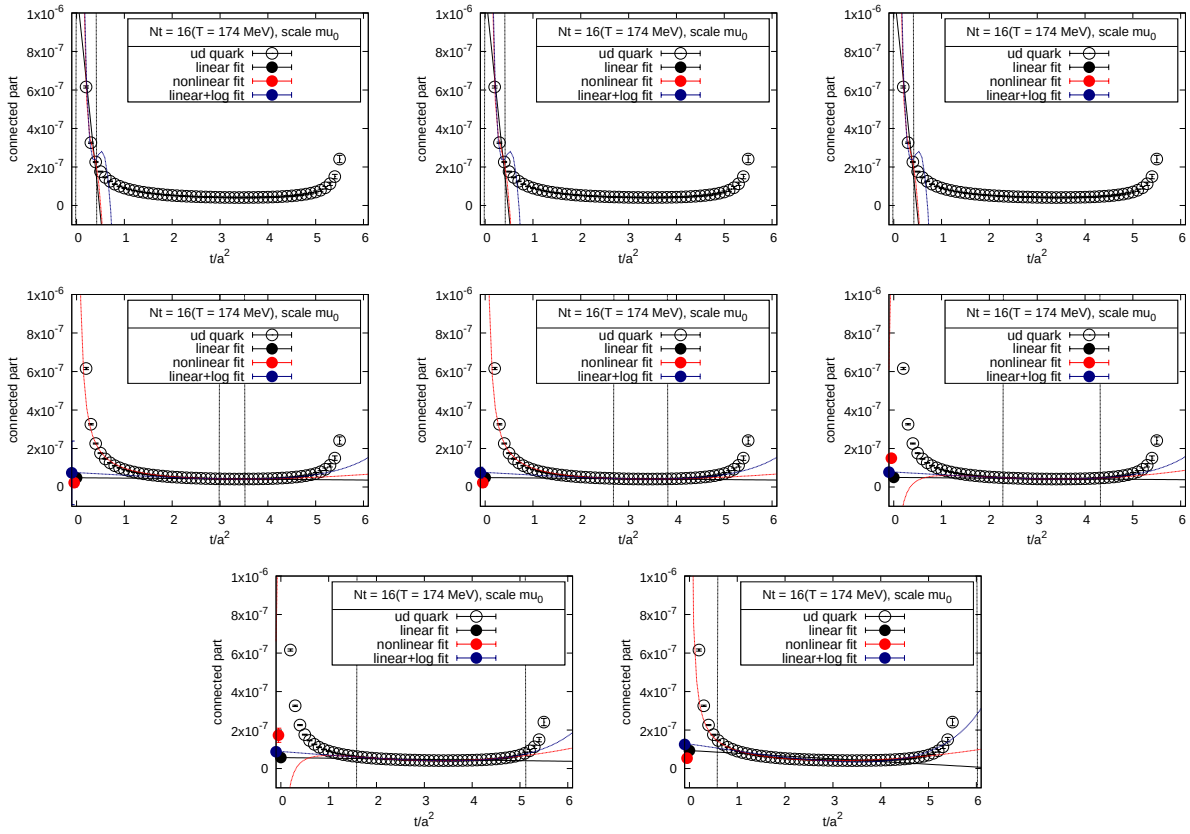

Figure C.51: The connected part of chiral susceptibility $\chi_{ud}^{\rm conn}$ as a function of the flow-time. $N_t = 16$, μ_0. From top-left to the bottom: we vary the cut-off values of the linear fit as a, b, c, ..., h. The pair of dashed vertical lines indicates the window used for the fit at each cut-off. Black solid lines are the fit results of the linear fit and filled circles at $t = 0$ are the results extracted from the fits. Red and blue dashed lines and filled circle at $t \sim 0$ are the results of nonlinear and linear+log fit, respectively.

$N_t = 14$

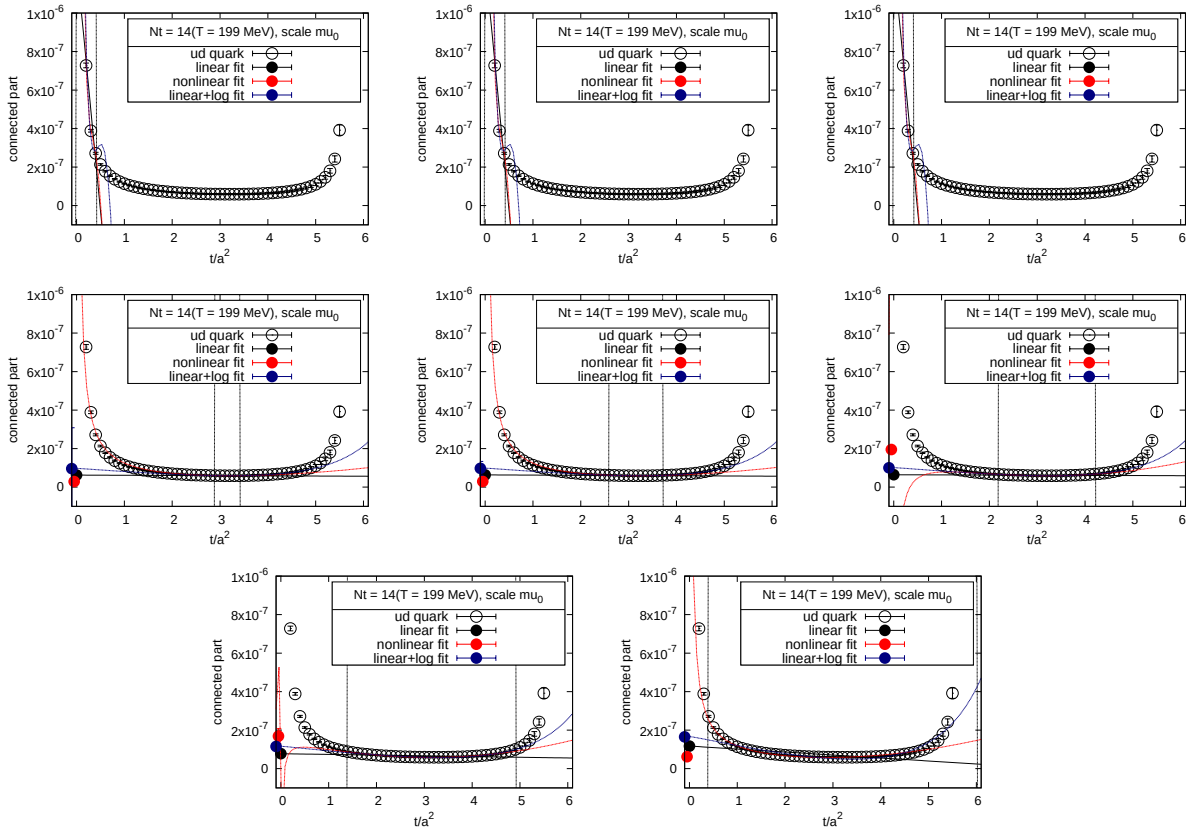

Figure C.52: The connected part of chiral susceptibility $\chi_{ud}^{\rm conn}$ as a function of the flow-time. $N_t = 14$, μ_0. From top-left to the bottom: we vary the cut-off values of the linear fit as a, b, c, ..., h. The pair of dashed vertical lines indicates the window used for the fit at each cut-off. Black solid lines are the fit results of the linear fit and filled circles at $t = 0$ are the results extracted from the fits. Red and blue dashed lines and filled circle at $t \sim 0$ are the results of nonlinear and linear+log fit, respectively.

$N_t = 12$

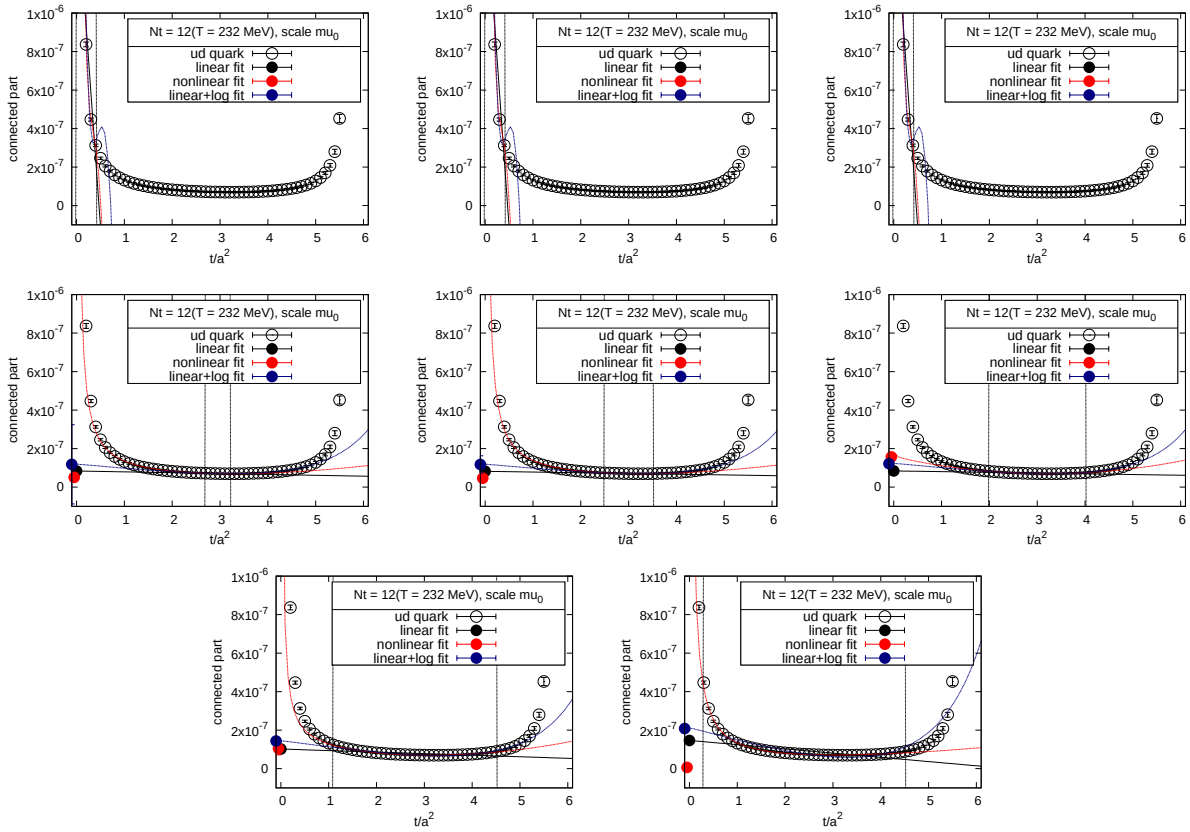

Figure C.53: The connected part of chiral susceptibility $\chi_{ud}^{\rm conn}$ as a function of the flow-time. $N_t = 12$, μ_0. From top-left to the bottom: we vary the cut-off values of the linear fit as a, b, c, ..., h. The pair of dashed vertical lines indicates the window used for the fit at each cut-off. Black solid lines are the fit results of the linear fit and filled circles at $t = 0$ are the results extracted from the fits. Red and blue dashed lines and filled circle at $t \sim 0$ are the results of nonlinear and linear+log fit, respectively.

$N_t = 10$

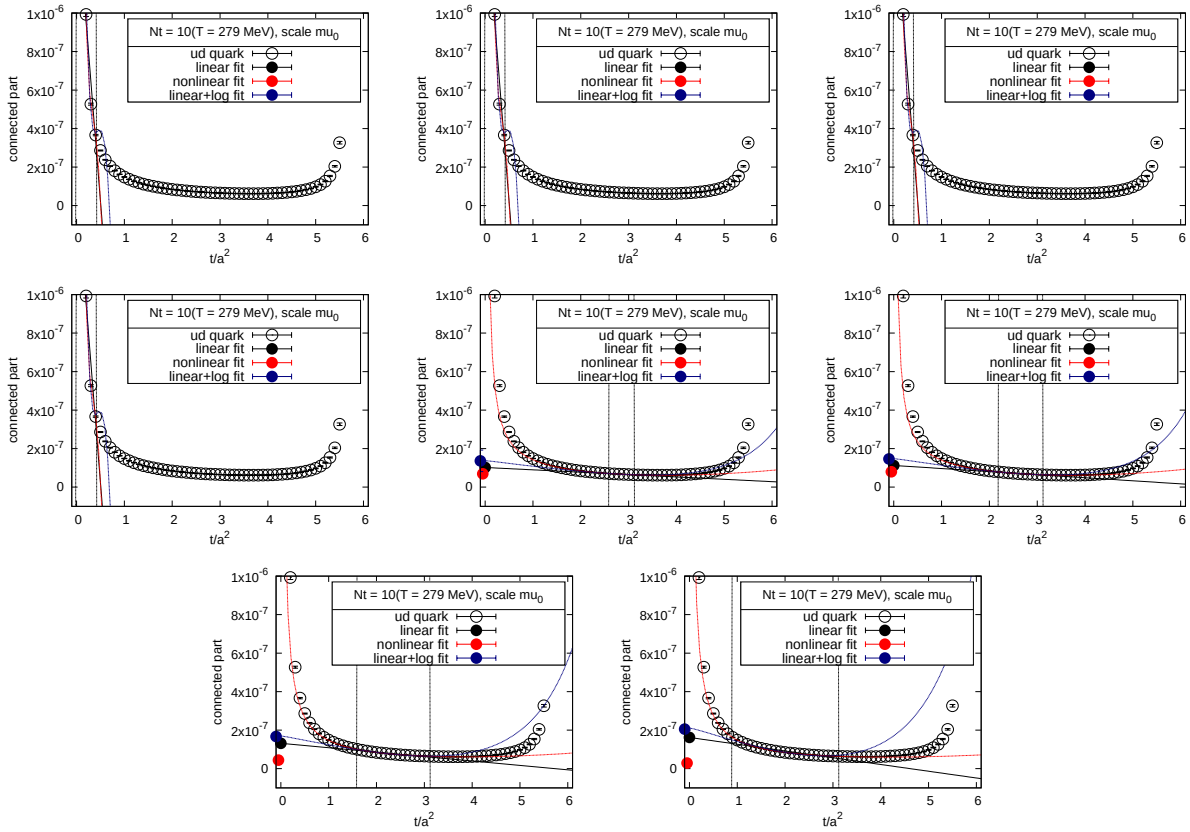

Figure C.54: The connected part of chiral susceptibility $\chi_{ud}^{\rm conn}$ as a function of the flow-time. $N_t = 10$, μ_0. From top-left to the bottom: we vary the cut-off values of the linear fit as a, b, c, ..., h. The pair of dashed vertical lines indicates the window used for the fit at each cut-off. Black solid lines are the fit results of the linear fit and filled circles at $t = 0$ are the results extracted from the fits. Red and blue dashed lines and filled circle at $t \sim 0$ are the results of nonlinear and linear+log fit, respectively.

$N_t = 8$

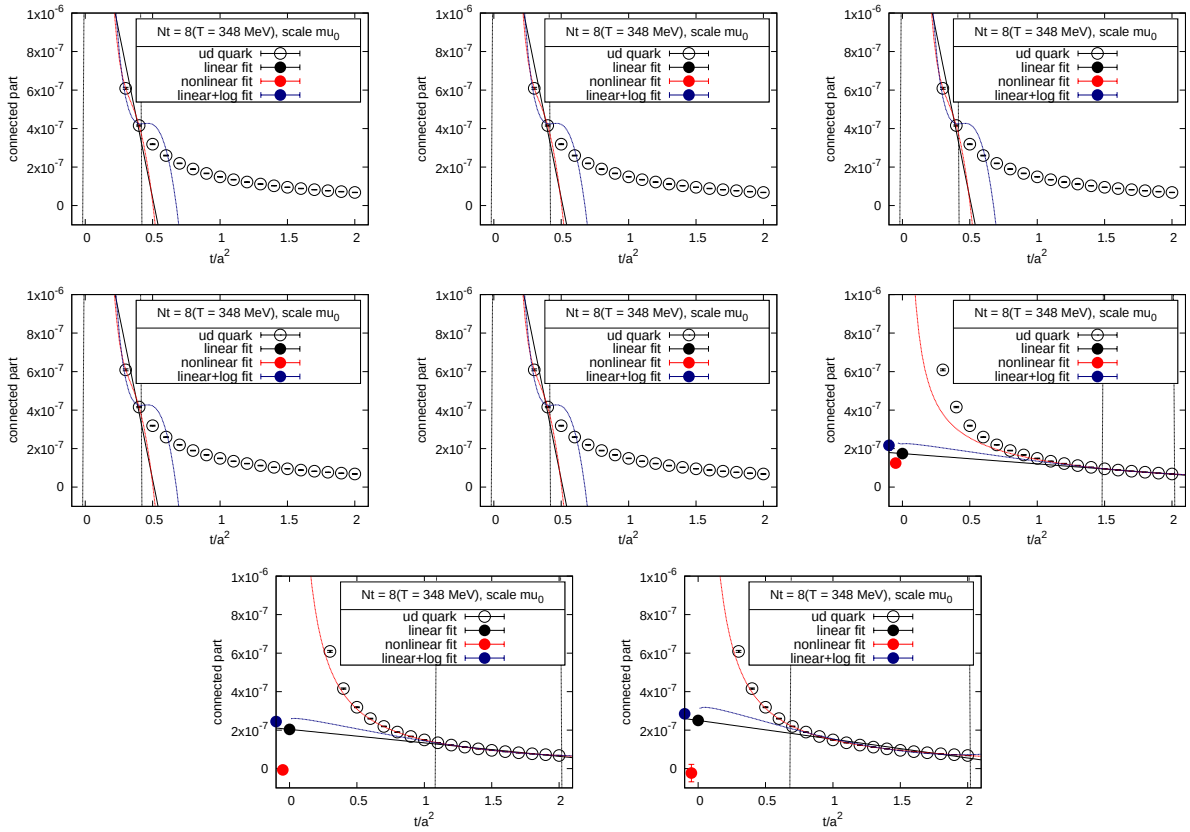

Figure C.55: The connected part of chiral susceptibility $\chi_{ud}^{\rm conn}$ as a function of the flow-time. $N_t = 8$, μ_0. From top-left to the bottom: we vary the cut-off values of the linear fit as a, b, c, ..., h. The pair of dashed vertical lines indicates the window used for the fit at each cut-off. Black solid lines are the fit results of the linear fit and filled circles at $t = 0$ are the results extracted from the fits. Red and blue dashed lines and filled circle at $t \sim 0$ are the results of nonlinear and linear+log fit, respectively.

C.2.12 The connected part of chiral susceptibility , μ_0

$N_t = 16$

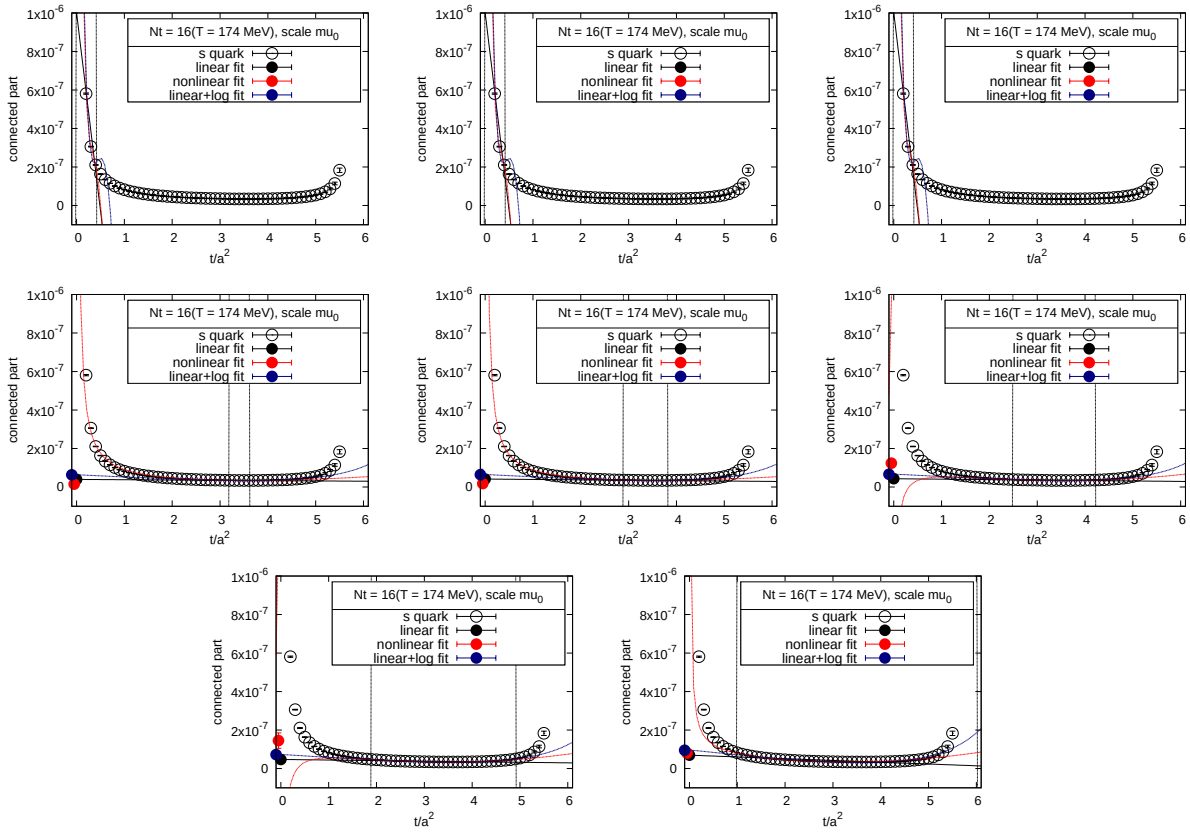

Figure C.56: The connected part of chiral susceptibility $\chi_s^{\rm conn}$ as a function of the flow-time. $N_t = 16$, μ_0. From top-left to the bottom: we vary the cut-off values of the linear fit as a, b, c, ..., h. The pair of dashed vertical lines indicates the window used for the fit at each cut-off. Black solid lines are the fit results of the linear fit and filled circles at $t = 0$ are the results extracted from the fits. Red and blue dashed lines and filled circle at $t \sim 0$ are the results of nonlinear and linear+log fit, respectively.

$N_t = 14$

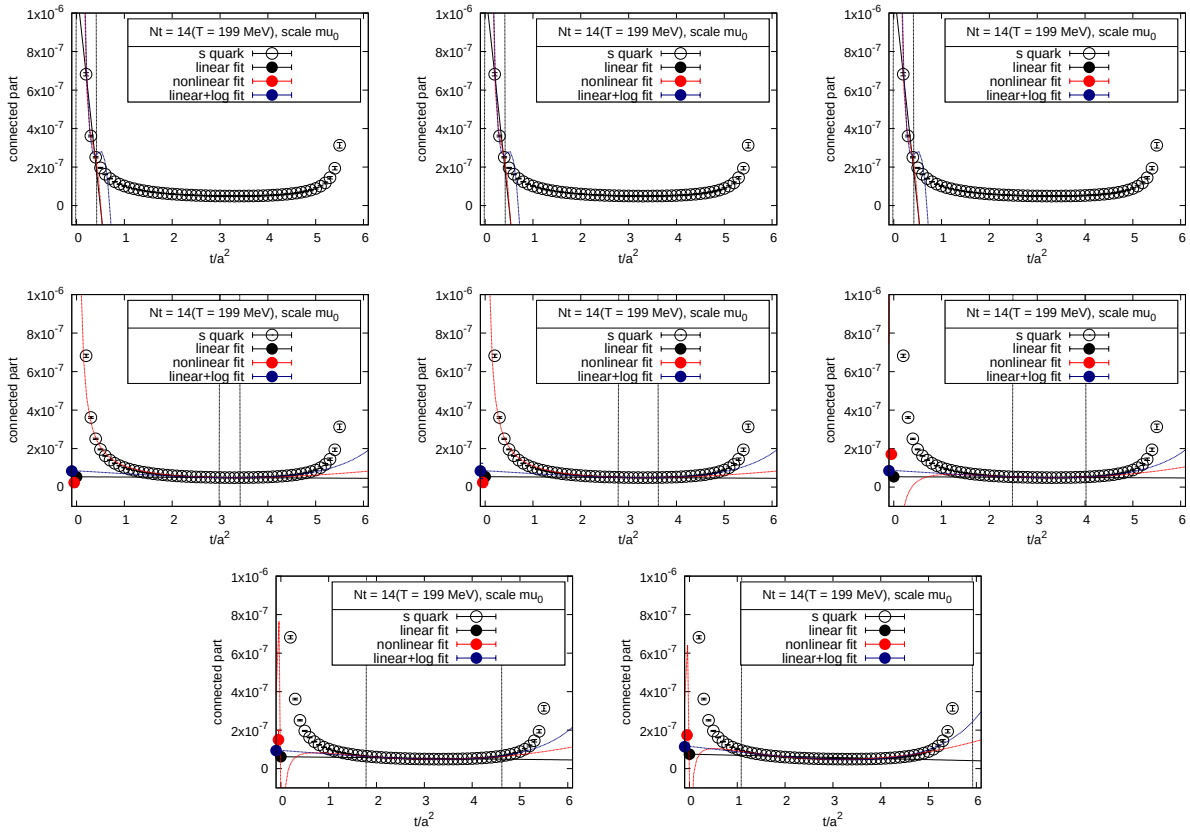

Figure C.57: The connected part of chiral susceptibility $\chi_s^{\rm conn}$ as a function of the flow-time. $N_t = 14$, μ_0. From top-left to the bottom: we vary the cut-off values of the linear fit as a, b, c, ..., h. The pair of dashed vertical lines indicates the window used for the fit at each cut-off. Black solid lines are the fit results of the linear fit and filled circles at $t = 0$ are the results extracted from the fits. Red and blue dashed lines and filled circle at $t \sim 0$ are the results of nonlinear and linear+log fit, respectively.

$N_t = 12$

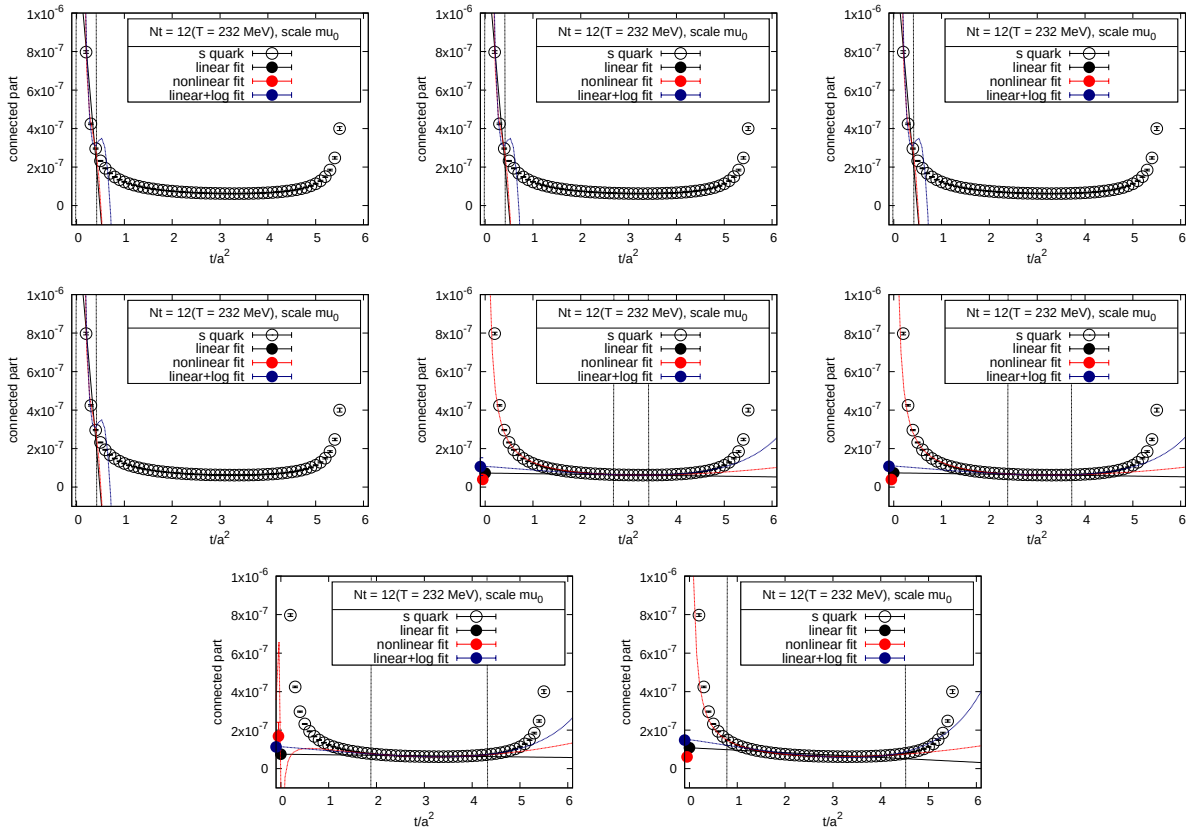

Figure C.58: The connected part of chiral susceptibility $\chi_s^{\rm conn}$ as a function of the flow-time. $N_t = 12$, μ_0. From top-left to the bottom: we vary the cut-off values of the linear fit as a, b, c, ..., h. The pair of dashed vertical lines indicates the window used for the fit at each cut-off. Black solid lines are the fit results of the linear fit and filled circles at $t = 0$ are the results extracted from the fits. Red and blue dashed lines and filled circle at $t \sim 0$ are the results of nonlinear and linear+log fit, respectively.

$N_t = 10$

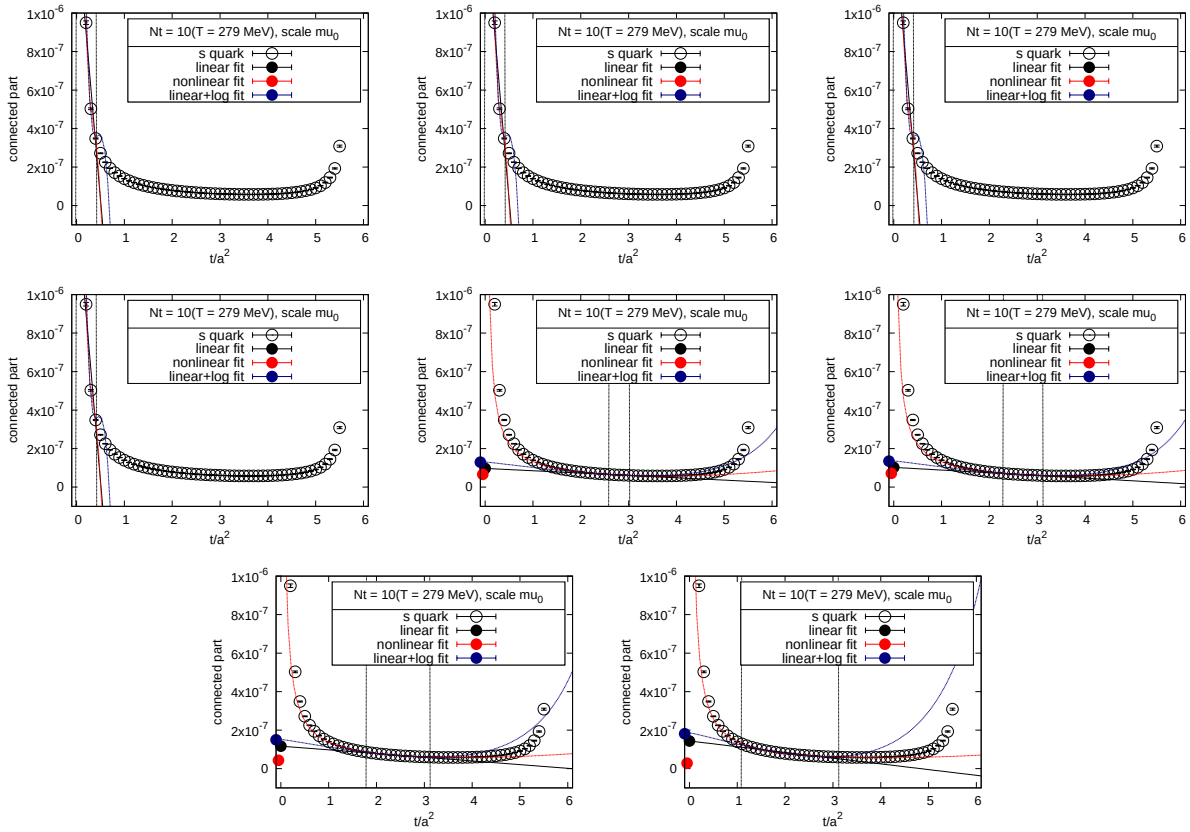

Figure C.59: The connected part of chiral susceptibility χ_s^{conn} as a function of the flow-time. $N_t = 10$, μ_0. From top-left to the bottom: we vary the cut-off values of the linear fit as a, b, c, ..., h. The pair of dashed vertical lines indicates the window used for the fit at each cut-off. Black solid lines are the fit results of the linear fit and filled circles at $t = 0$ are the results extracted from the fits. Red and blue dashed lines and filled circle at $t \sim 0$ are the results of nonlinear and linear+log fit, respectively.

$N_t = 8$

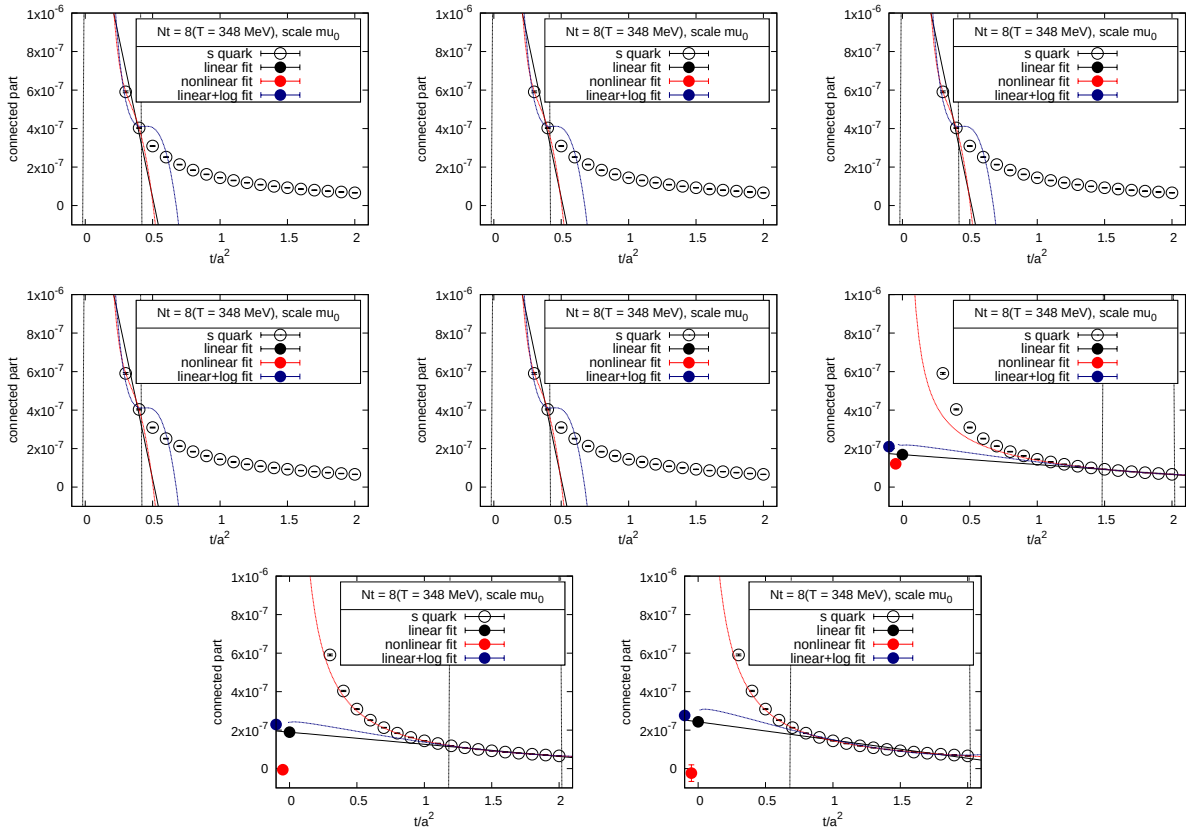

Figure C.60: The connected part of chiral susceptibility $\chi_s^{\rm conn}$ as a function of the flow-time. $N_t = 8$, μ_0. From top-left to the bottom: we vary the cut-off values of the linear fit as a, b, c, ..., h. The pair of dashed vertical lines indicates the window used for the fit at each cut-off. Black solid lines are the fit results of the linear fit and filled circles at $t = 0$ are the results extracted from the fits. Red and blue dashed lines and filled circle at $t \sim 0$ are the results of nonlinear and linear+log fit, respectively.

C.2.13 The $U(1)_A$ susceptibility $\chi_{ud}^{\pi-\delta}$, μ_d

$N_t = 16$

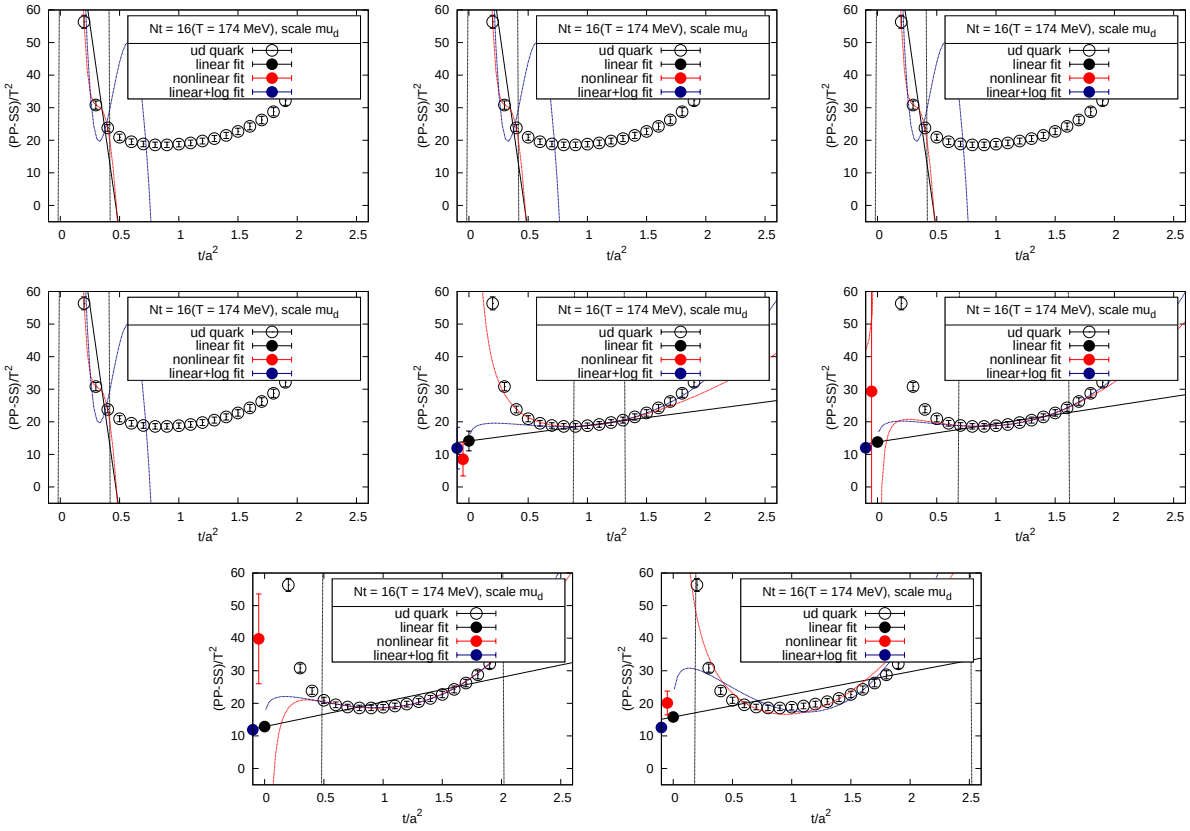

Figure C.61: The $U(1)_A$ susceptibility $\chi_{ud}^{\pi-\delta}$ as a function of the flow-time. $N_t = 16$, μ_d. From top-left to the bottom: we vary the cut-off values of the linear fit as a, b, c, ..., h. The pair of dashed vertical lines indicates the window used for the fit at each cut-off. Black solid lines are the fit results of the linear fit and filled circles at $t = 0$ are the results extracted from the fits. Red and blue dashed lines and filled circle at $t \sim 0$ are the results of nonlinear and linear+log fit, respectively.

$N_t = 14$

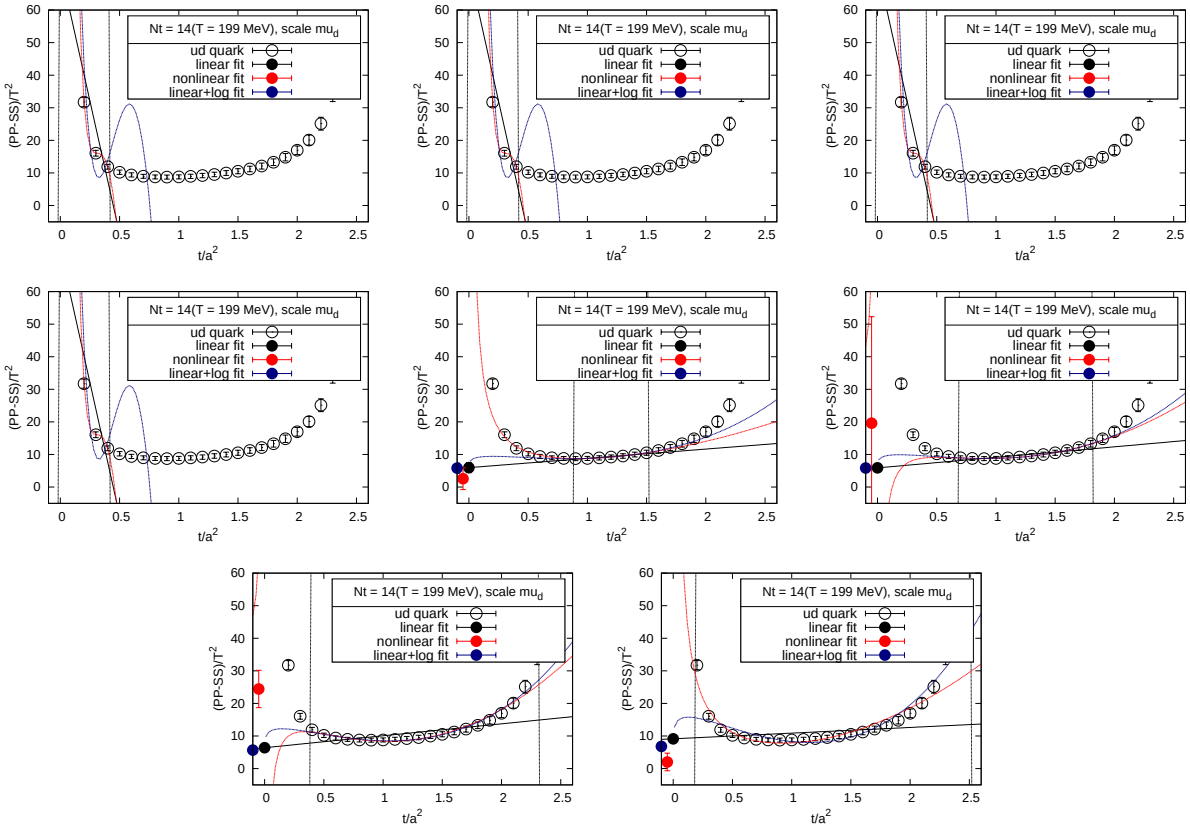

Figure C.62: The $U(1)_A$ susceptibility $\chi_{ud}^{\pi-\delta}$ as a function of the flow-time. $N_t = 14$, μ_d. From top-left to the bottom: we vary the cut-off values of the linear fit as a, b, c, ..., h. The pair of dashed vertical lines indicates the window used for the fit at each cut-off. Black solid lines are the fit results of the linear fit and filled circles at $t = 0$ are the results extracted from the fits. Red and blue dashed lines and filled circle at $t \sim 0$ are the results of nonlinear and linear+log fit, respectively.

$N_t = 12$

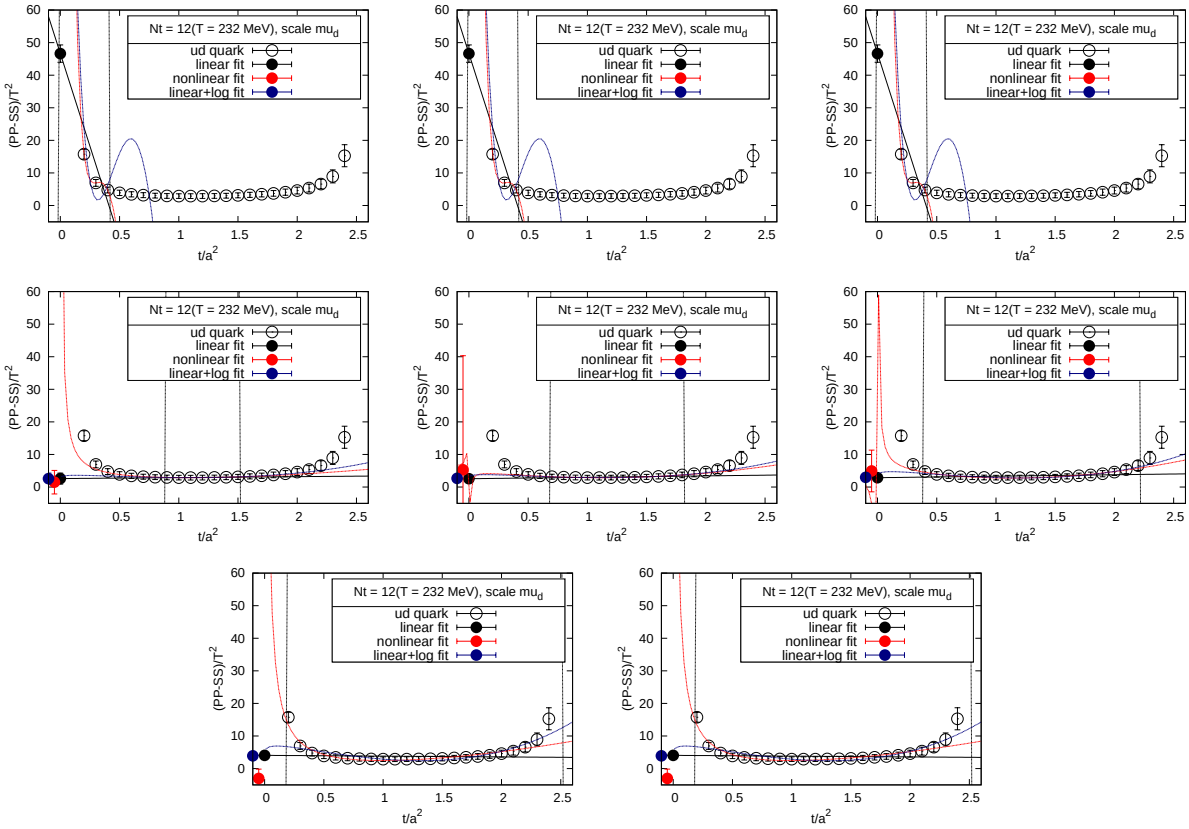

Figure C.63: The $U(1)_A$ susceptibility $\chi_{ud}^{\pi-\delta}$ as a function of the flow-time. $N_t = 12$, μ_d. From top-left to the bottom: we vary the cut-off values of the linear fit as a, b, c, ..., h. The pair of dashed vertical lines indicates the window used for the fit at each cut-off. Black solid lines are the fit results of the linear fit and filled circles at $t = 0$ are the results extracted from the fits. Red and blue dashed lines and filled circle at $t \sim 0$ are the results of nonlinear and linear+log fit, respectively.

$N_t = 10$

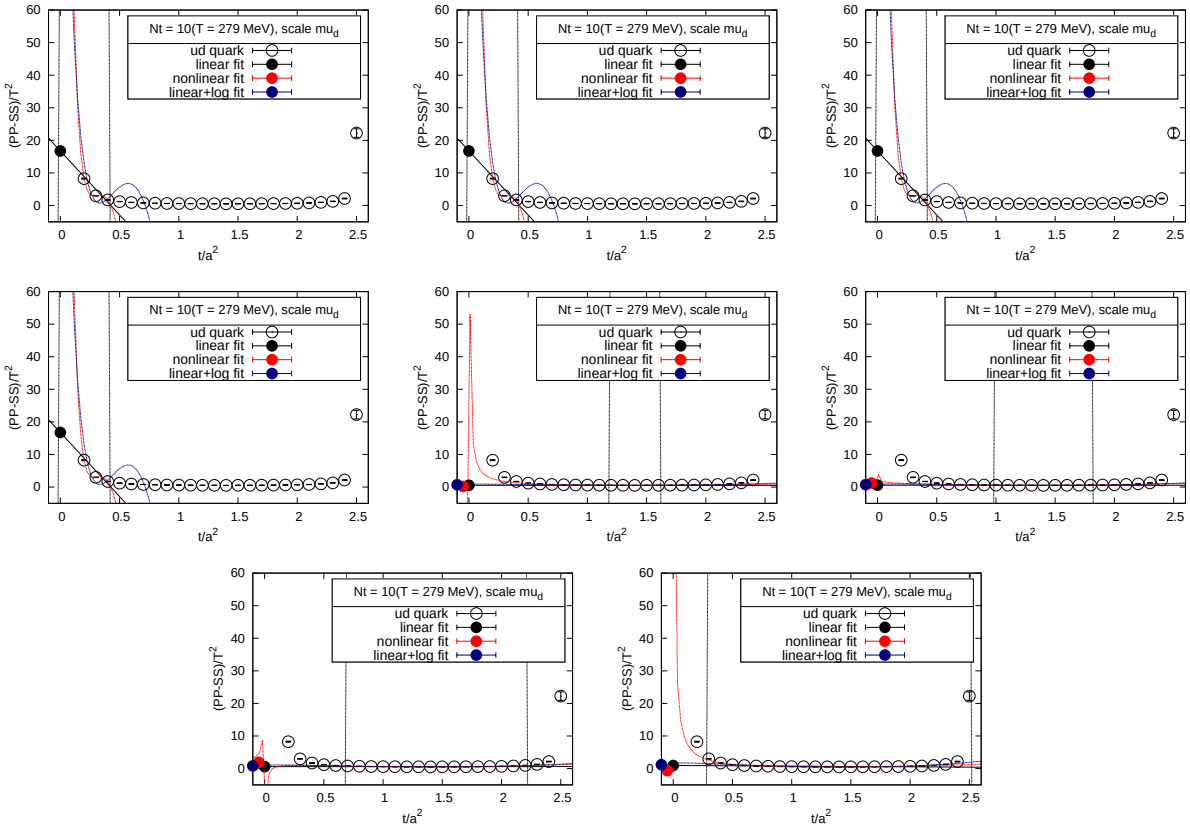

Figure C.64: The $U(1)_A$ susceptibility $\chi_{ud}^{\pi-\delta}$ as a function of the flow-time. $N_t = 10$, μ_d. From top-left to the bottom: we vary the cut-off values of the linear fit as a, b, c, ..., h. The pair of dashed vertical lines indicates the window used for the fit at each cut-off. Black solid lines are the fit results of the linear fit and filled circles at $t = 0$ are the results extracted from the fits. Red and blue dashed lines and filled circle at $t \sim 0$ are the results of nonlinear and linear+log fit, respectively.

$N_t = 8$

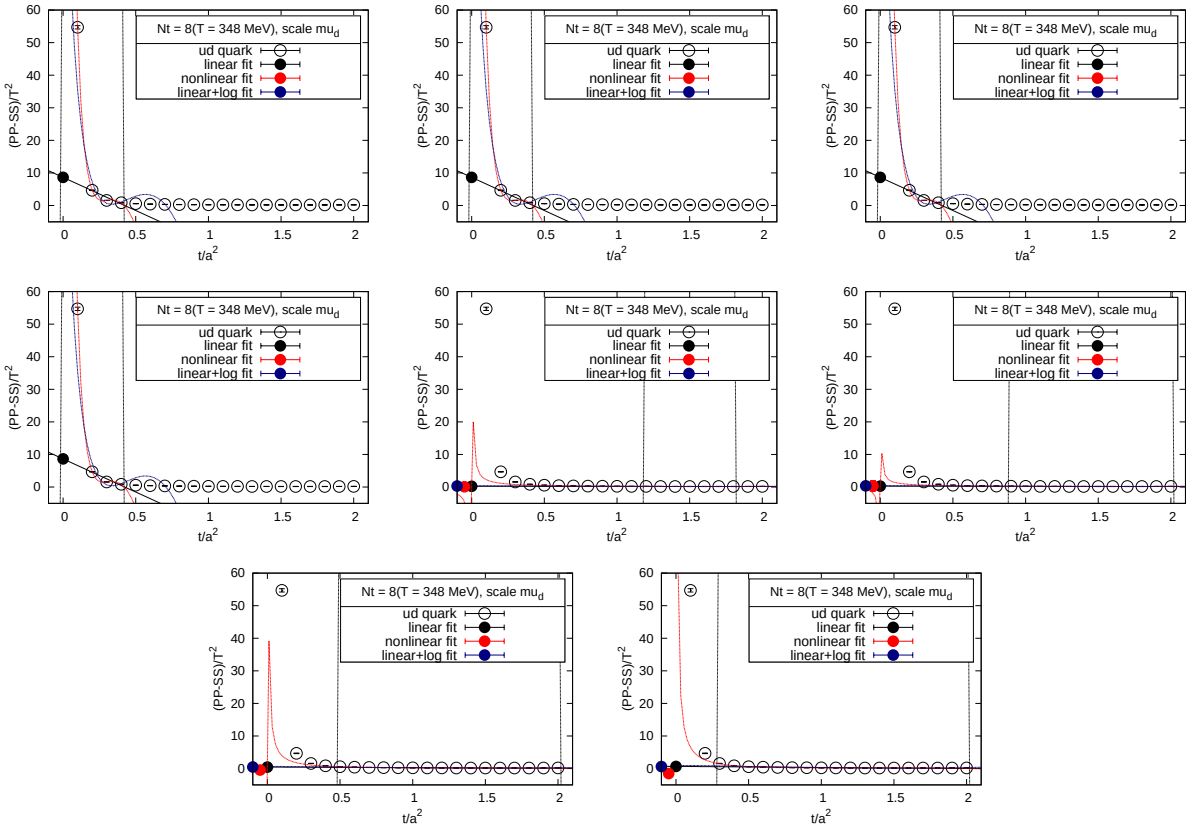

Figure C.65: The $U(1)_A$ susceptibility $\chi_{ud}^{\pi-\delta}$ as a function of the flow-time. $N_t = 8$, μ_d. From top-left to the bottom: we vary the cut-off values of the linear fit as a, b, c, ..., h. The pair of dashed vertical lines indicates the window used for the fit at each cut-off. Black solid lines are the fit results of the linear fit and filled circles at $t = 0$ are the results extracted from the fits. Red and blue dashed lines and filled circle at $t \sim 0$ are the results of nonlinear and linear+log fit, respectively.

C.2.14 The $U(1)_A$ susceptibility , μ_0

$N_t = 16$

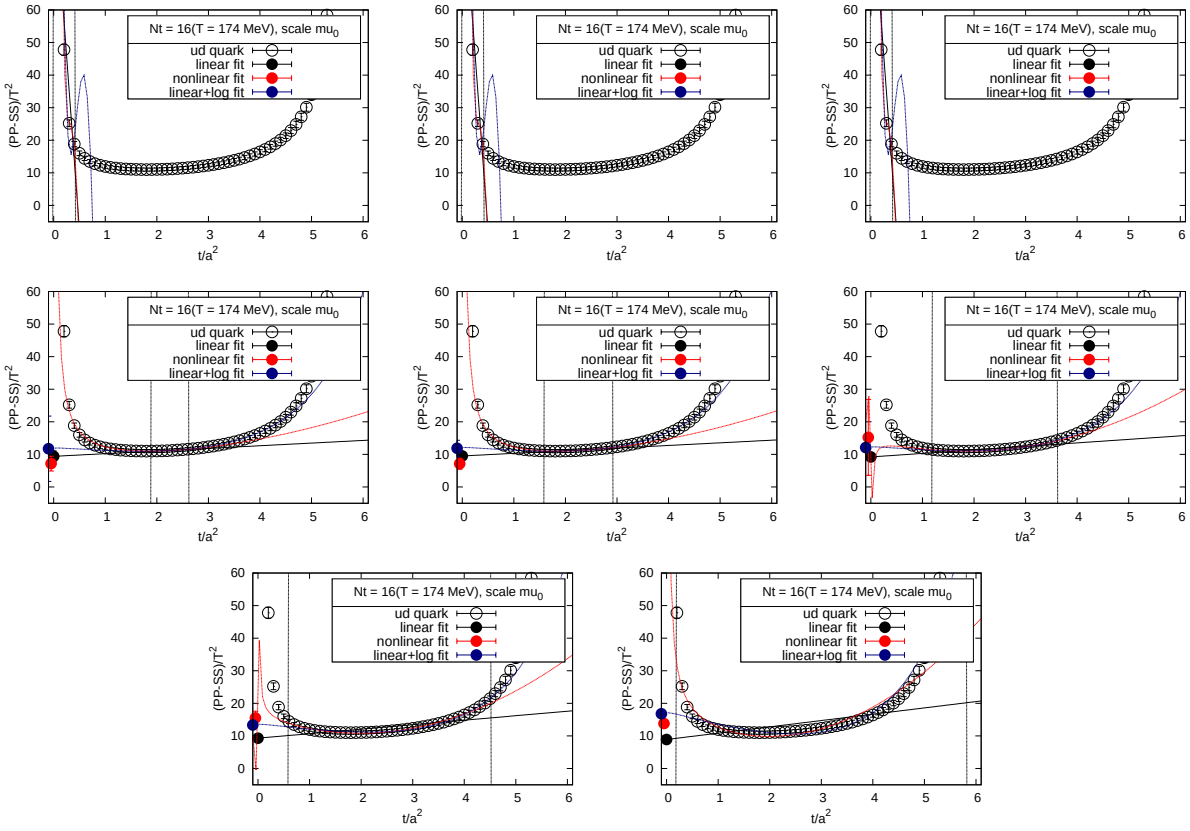

Figure C.66: The $U(1)_A$ susceptibility $\chi_{ud}^{\pi-\delta}$ as a function of the flow-time. $N_t = 16$, μ_0. From top-left to the bottom: we vary the cut-off values of the linear fit as a, b, c, ..., h. The pair of dashed vertical lines indicates the window used for the fit at each cut-off. Black solid lines are the fit results of the linear fit and filled circles at $t = 0$ are the results extracted from the fits. Red and blue dashed lines and filled circle at $t \sim 0$ are the results of nonlinear and linear+log fit, respectively.

$N_t = 14$

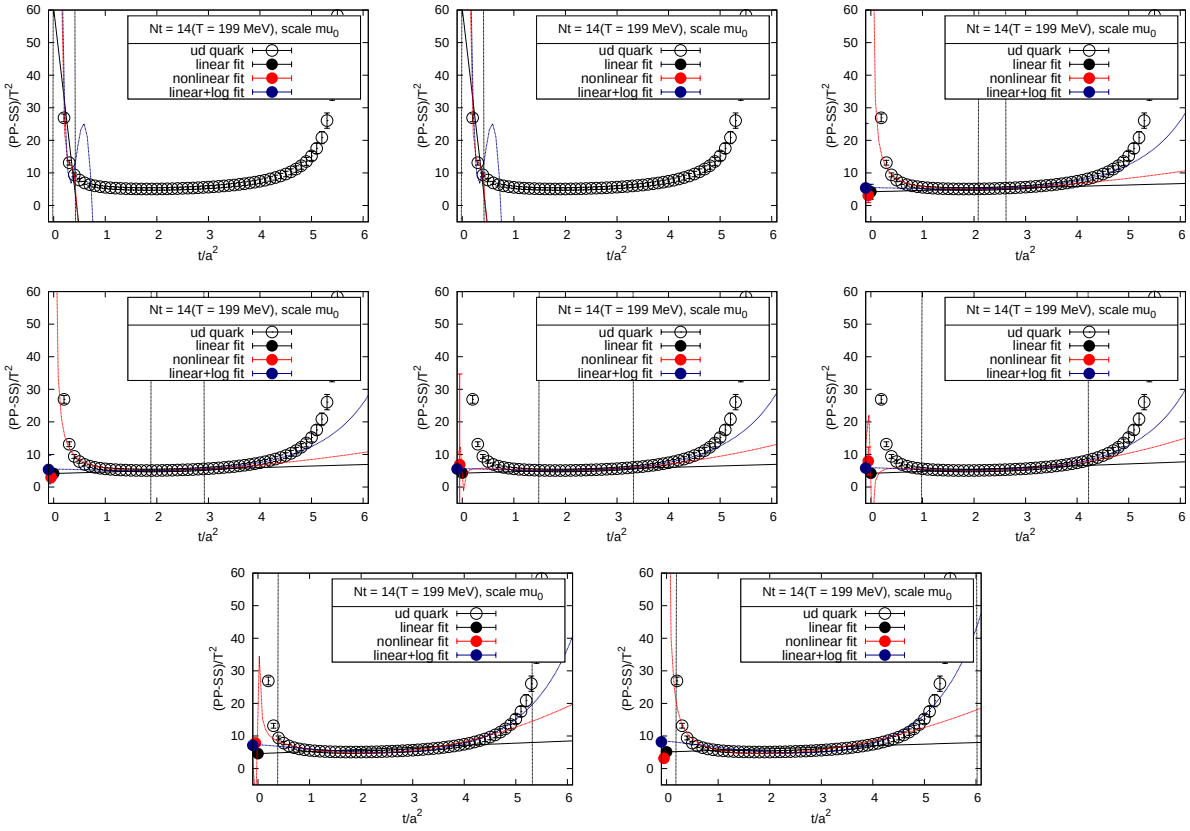

Figure C.67: The $U(1)_A$ susceptibility $\chi_{ud}^{\pi-\delta}$ as a function of the flow-time. $N_t = 14$, μ_0. From top-left to the bottom: we vary the cut-off values of the linear fit as a, b, c, ..., h. The pair of dashed vertical lines indicates the window used for the fit at each cut-off. Black solid lines are the fit results of the linear fit and filled circles at $t = 0$ are the results extracted from the fits. Red and blue dashed lines and filled circle at $t \sim 0$ are the results of nonlinear and linear+log fit, respectively.

$N_t = 12$

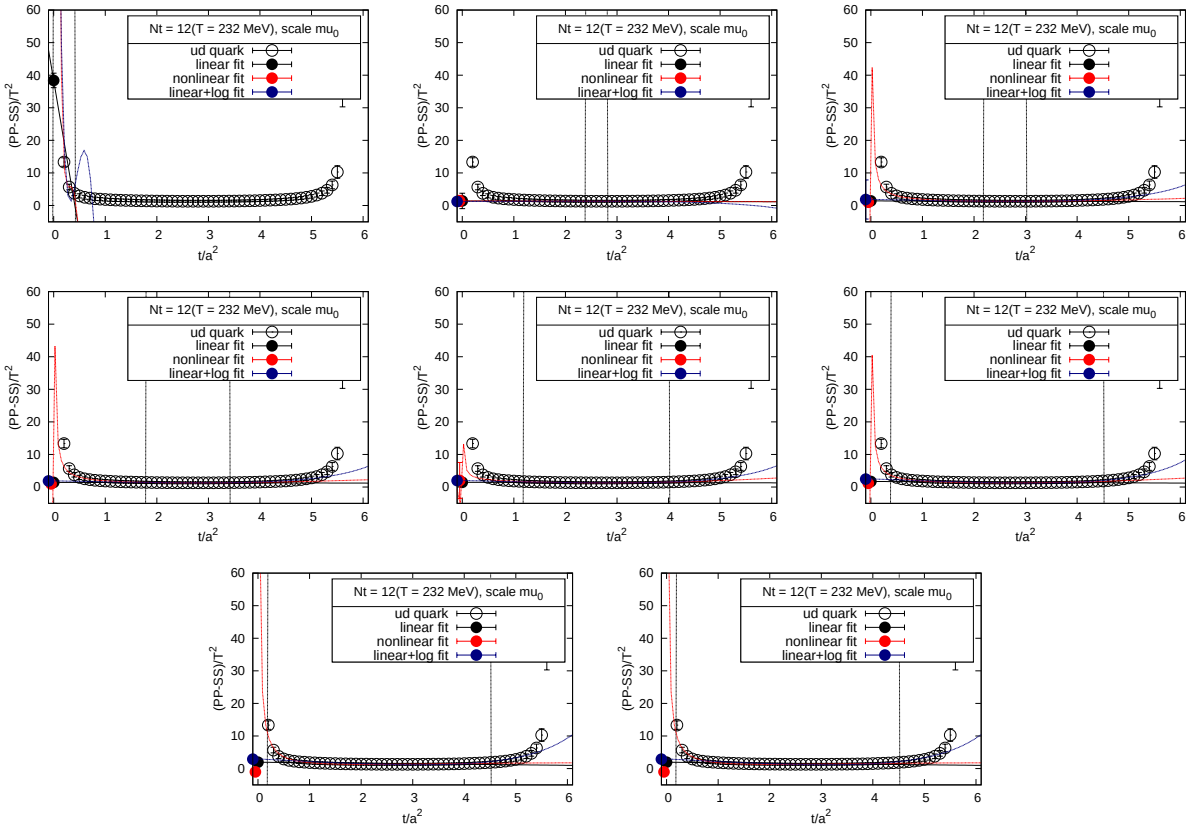

Figure C.68: The $U(1)_A$ susceptibility $\chi_{ud}^{\pi-\delta}$ as a function of the flow-time. $N_t = 12$, μ_0. From top-left to the bottom: we vary the cut-off values of the linear fit as a, b, c, ..., h. The pair of dashed vertical lines indicates the window used for the fit at each cut-off. Black solid lines are the fit results of the linear fit and filled circles at $t = 0$ are the results extracted from the fits. Red and blue dashed lines and filled circle at $t \sim 0$ are the results of nonlinear and linear+log fit, respectively.

$N_t = 10$

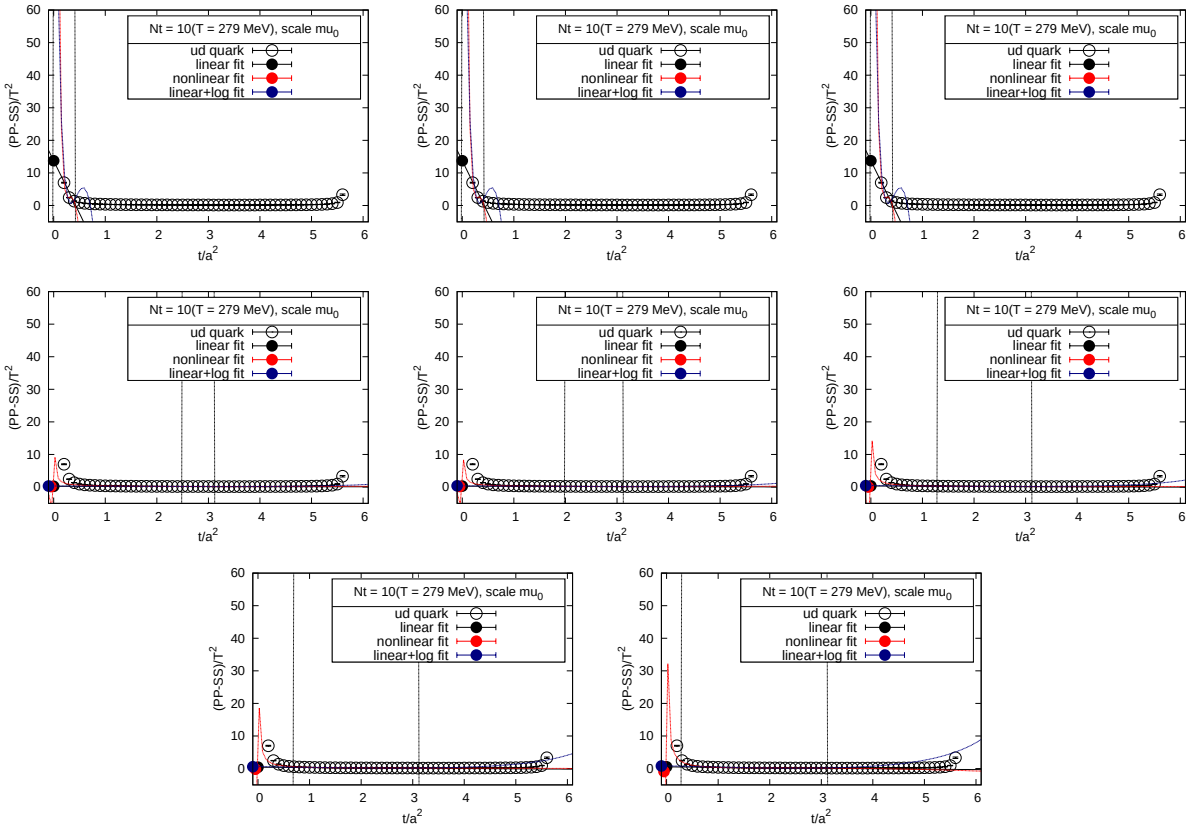

Figure C.69: The $U(1)_A$ susceptibility $\chi_{ud}^{\pi-\delta}$ as a function of the flow-time. $N_t = 10$, μ_0. From top-left to the bottom: we vary the cut-off values of the linear fit as a, b, c, ..., h. The pair of dashed vertical lines indicates the window used for the fit at each cut-off. Black solid lines are the fit results of the linear fit and filled circles at $t = 0$ are the results extracted from the fits. Red and blue dashed lines and filled circle at $t \sim 0$ are the results of nonlinear and linear+log fit, respectively.

$N_t = 8$

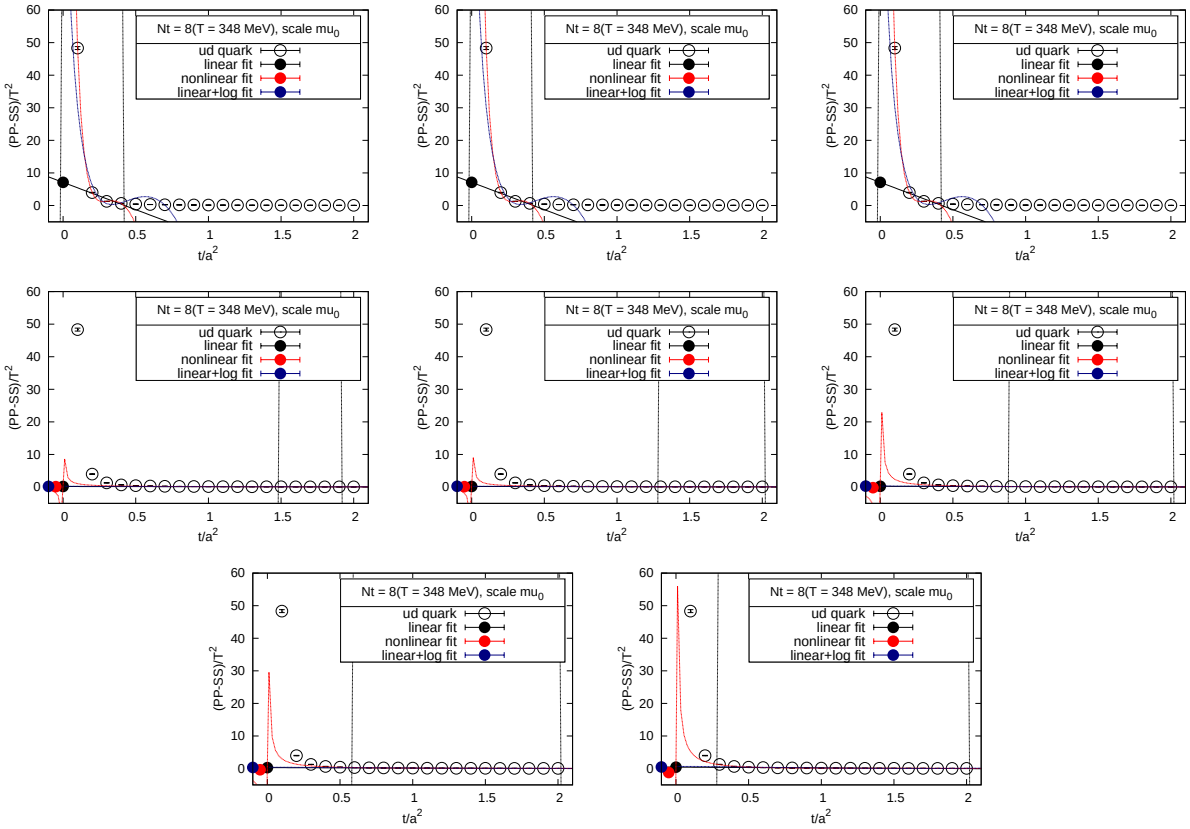

Figure C.70: The $U(1)_A$ susceptibility $\chi_{ud}^{\pi-\delta}$ as a function of the flow-time. $N_t = 8$, μ_0. From top-left to the bottom: we vary the cut-off values of the linear fit as a, b, c, ..., h. The pair of dashed vertical lines indicates the window used for the fit at each cut-off. Black solid lines are the fit results of the linear fit and filled circles at $t = 0$ are the results extracted from the fits. Red and blue dashed lines and filled circle at $t \sim 0$ are the results of nonlinear and linear+log fit, respectively.

Bibliography

[1] K. Fukushima and T. Hatsuda, Reports Prog. Phys. **74** (2011), arXiv:1005.4814.

[2] K. G. Wilson, Phys. Rev. D **10**, 2445 (1974).

[3] H. B. Nielsen and M. Ninomiya, Nucl. Phys. B **185**, 20 (1981).

[4] H. B. Nielsen and M. Ninomiya, Nucl. Phys. B **193**, 173 (1981).

[5] H. B. Nielsen and M. Ninomiya, Phys. Lett. B **105**, 219 (1981).

[6] K. G. Wilson, Quarks and Strings on a Lattice, in *13th Int. Sch. Subnucl. Phys. New Phenom. Subnucl. Phys.*, p. 99, 1975.

[7] Y. Iwasaki, (2011), arXiv:1111.7054.

[8] B. Sheikholeslami and R. Wohlert, Nucl. Phys. B **259**, 572 (1985).

[9] Y. Aoki, G. Endrodi, Z. Fodor, S. D. Katz, and K. K. Szabó, Nature **443**, 675 (2006), arXiv:0611014.

[10] S.-T. Li and H.-T. Ding, Chiral phase transition in (2 + 1)-flavor QCD on Nτ = 6 lattices, in *Proc. Sci.* Vol. LATTICE201, p. 372, Sissa Medialab, 2018.

[11] G. Aarts *et al.*, J. High Energy Phys. **2015**, 186 (2015), arXiv:1412.6411.

[12] A. Bazavov *et al.*, Phys. Lett. Sect. B Nucl. Elem. Part. High-Energy Phys. **795**, 15 (2019), arXiv:1812.08235.

[13] T. Bhattacharya *et al.*, Phys. Rev. Lett. **113**, 082001 (2014).

[14] Report No., , 2020 (unpublished), arXiv:2011.01499v1.

[15] R. Narayanan and H. Neuberger, J. High Energy Phys. , 4581 (2006), arXiv:0601210.

[16] M. Lüscher, Commun. Math. Phys. **293**, 899 (2009), arXiv:0907.5491.

[17] M. Lüscher, J. High Energy Phys. **2010** (2010), arXiv:1006.4518.

[18] M. Lüscher and P. Weisz, J. High Energy Phys. **2011** (2011), arXiv:1101.0963.

[19] M. Lüscher, J. High Energy Phys. **2013**, 123 (2013), arXiv:1302.5246.

[20] H. Suzuki, Prog. Theor. Exp. Phys. **2013**, 83 (2013), arXiv:1304.0533.

[21] H. Makino and H. Suzuki, Prog. Theor. Exp. Phys. **2014**, 63 (2014), arXiv:1403.4772.

[22] M. Asakawa, T. Hatsuda, E. Itou, M. Kitazawa, and H. Suzuki, Phys. Rev. D **90**, 011501 (2014).

[23] Y. Taniguchi *et al.*, Phys. Rev. D **96** (2017).

[24] T. Umeda *et al.*, Phys. Rev. D **85** (2012), arXiv:1202.4719.

[25] M. Shirogane *et al.*, (2020), arXiv:2011.10292.

[26] R. D. Peccei and H. R. Quinn, Phys. Rev. Lett. **38**, 1440 (1977).

[27] C. Bonati and M. D'Elia, Phys. Rev. D - Part. Fields, Gravit. Cosmol. **89** (2014), arXiv:1401.2441.

[28] L. Giusti, G. C. Rossi, and M. Testa, Phys. Lett. B **587**, 157 (2004), arXiv:0402027.

[29] M. Bochicchio, G. C. Rossi, M. Testa, and K. Yoshida, Phys. Lett. B **149**, 487 (1984).

[30] T. Endo, K. Hieda, D. Miura, and H. Suzuki, Prog. Theor. Exp. Phys. **2015**, 53 (2015), arXiv:1502.01809.

[31] Y. Taniguchi, K. Kanaya, H. Suzuki, and T. Umeda, Phys. Rev. D **95**, 054502 (2017), arXiv:1611.02411.

[32] T. Ishikawa *et al.*, Phys. Rev. D **78** (2008).

[33] Y. Iwasaki, Nucl. Phys. B **258**, 141 (1985).

[34] L. Levkova, T. Manke, and R. Mawhinney, Phys. Rev. D **73** (2006).

[35] T. Umeda *et al.*, Phys. Rev. D **79** (2009).

[36] R. Yanagihara, T. Iritani, M. Kitazawa, M. Asakawa, and T. Hatsuda, Phys. Lett. B **789**, 210 (2019).

[37] R. V. Harlander, Y. Kluth, and F. Lange, Eur. Phys. J. C **78**, 944 (2018), arXiv:1808.09837.

[38] Y. Taniguchi *et al.*, Phys. Rev. D **102**, 014510 (2020).

[39] K. Kanaya *et al.*, Study of 2 + 1 flavor finite-temperature QCD using improved Wilson quarks at the physical point with the gradient flow, 2019, arXiv:1910.13036.

[40] M. I. Buchoff *et al.*, Phys. Rev. D **89** (2014).

[41] Lattice QCD code Bridge++, http://bridge.kek.jp/Lattice-code/index_e.html.

[42] W. E. Caswell, Phys. Rev. Lett. **33**, 244 (1974).

[43] D. Jones, Nucl. Phys. B **75**, 531 (1974).

[44] R. Tarrach, Nucl. Phys. B **183**, 384 (1981).

[45] O. Nachtmann and W. Wetzel, Nucl. Phys. B **187**, 333 (1981).

[46] O. V. Tarasov, A. A. Vladimirov, and A. Y. Zharkov, Phys. Lett. B **93**, 429 (1980).

[47] S. A. Larin and J. A. Vermaseren, Phys. Lett. B **303**, 334 (1993).

[48] T. Van Ritbergen, J. A. Vermaseren, and S. A. Larin, Phys. Lett. B **400**, 379 (1997).

[49] F. Herzog, B. Ruijl, T. Ueda, J. A. Vermaseren, and A. Vogt, J. High Energy Phys. **2017**, 1 (2017), arXiv:1701.01404.

[50] P. A. Baikov, K. G. Chetyrkin, and J. H. Kühn, Phys. Rev. Lett. **118** (2017), arXiv:1606.08659.

[51] O. V. Tarasov, Rep. No. JINR-P2-82-900 (1982).

[52] S. A. Larin, Phys. Lett. B **303**, 113 (1993), arXiv:9302240.

[53] K. G. Chetyrkin, Phys. Lett. Sect. B Nucl. Elem. Part. High-Energy Phys. **404**, 161 (1997).

[54] J. A. Vermaseren, S. A. Larin, and T. Van Ritbergen, Phys. Lett. B **405**, 327 (1997), arXiv:9703284.

[55] P. A. Baikov, K. G. Chetyrkin, and J. H. Kühn, J. High Energy Phys. **2014**, 76 (2014).

[56] T. Luthe, A. Maier, P. Marquard, and Y. Schröder, J. High Energy Phys. **2017**, 1 (2017).